Investigation of Cu-Cu bonding for 2.5D and 3D system integration using self-assembled monolayer as oxidation inhibitor

Maria Lykova

Dissertation

Institut für Aufbau- und Verbindungstechnik der Elektronik
Fakultät Elektrotechnik und Informationstechnik
Technische Universität Dresden

Als Dissertation genehmigt von der Fakultät Elektrotechnik und Informationstechnik der Technischen Universität Dresden.

Vorsitzender:	Prof. Dr.-Ing. Thomas Mikolajick
Gutachter:	Jun.-Prof. Dr.-Ing. Iuliana Panchenko
	Prof. Dr.-Ing. Martin Schneider-Ramelow
	Prof. Tadatomo Suga
Weiteres Mitglied:	Prof. Dr.-Ing. habil. Thomas Zerna

Tag der Einreichung:	06.04.2021
Tag der Verteidigung:	13.12.2021

1. Auflage 2022

Warennamen werden in dieser Arbeit ohne Gewährleistung der freien Verwendbarkeit benutzt. Text, Abbildungen und technischen Angaben wurden sorgfältig erarbeitet und überprüft und stellen die Ansicht und Meinung des Autors dar. Trotzdem sind Fehler nicht völlig ausgeschlossen. Der Autor weist darauf hin, dass er für die Fehlerfreiheit keine Gewährleistung und für eventuelle Folgen aus Fehlern keine Haftung übernimmt.

© Maria Lykova, Dresden, 2022

Abstract

Cu-Cu bonding is one of the most promising fine-pitch interconnect technologies with solder elimination for 2.5D and 3D system integration. This bonding technology has been intensively investigated in the last years and is currently in application for miniaturized microelectronics products. However, Cu-Cu bonding has very high demands on the sur-face planarity and purity, and the bonding partners should be oxide-free. Oxidized Cu requires elevated bonding parameters in order to break through the oxide layer and achieve reliable Cu-Cu interconnects. Those bonding conditions are undesirable for many devices (e.g. due to the temperature/pressure sensitivity). Therefore, alternative technologies with a simple technique for Cu protection from oxidation are required.

Self-assembled monolayers (SAMs) are proposed for the Cu protection and the improvement of the Cu-Cu thermocompression (TC) and ultrasonic (US) flip-chip bonding technologies in this thesis. The experiments were carried out on Si dies with electroplated Cu microbumps and Cu layers. The thesis comprises the comprehensive characterization of the SAM for Cu protection, evaluation of technological parameters for TC and US flip-chip bonding as well as characterization of the Cu-Cu bonding quality (shear strength tests, fracture surface and microstructure analyses).

The storage at low temperatures (at -18 °C and -40 °C) confirmed the prolonged protective effect of the short-chain SAMs for the electroplated Cu without chemical-mechanical polishing. The influence of the low-temperature storage in air and the thermal SAM desorption in an inert gas atmosphere on the TC bonding quality was analyzed in detail. The approach of using US power to mechanically remove SAM and simultaneously start the US flip-chip bonding has not been systematically investigated before. The method provides the benefit of short bonding time, low bonding temperature and bonding in ambient air.

Both the TC and US flip-chip bonding results featured the shear strength that is approximately 30 % higher for the samples with SAM passivation in comparison to the uncoated samples. The presence of Si and Ti fracture surfaces after the shear strength tests is typical for the samples with the SAM passivation, which suggests a higher strength of such interconnects in comparison to the uncoated samples. The transmission electron microscopy (TEM) indicated no SAM traces at the central region of the Cu-Cu bonding interface after the US flip-chip bonding.

The results of this thesis show the improvement of the bonding quality caused by the application of SAM for Cu protection from oxidation in comparison to the commonly applied Cu pre-treatments. The found technological process window for the US flip-chip bonding in air offers high bonding quality at 90 °C and 150 °C, at 180 MPa, for the bonding duration of 1 s. The knowledge gained in this thesis is an important contribution to the understanding of the SAM performance on chips with electroplated Cu microbumps/layers and further application of the Cu-Cu fine-pitch bonding technology for microelectronic devices.

Kurzfassung

Das Cu-Cu-Bonden ist eine vielversprechende lötfreie Fine-Pitch-Verbindungstechnologie für die 2,5D- und 3D-Systemintegration. Diese Bondtechnologie wurde in den letzten Jahren intensiv untersucht und wird derzeit für miniaturisierte mikroelektronische Produkte eingesetzt. Allerdings, stellt das Cu-Cu-Bonden zum einen sehr hohe Anforderungen an die Oberflächenplanarität und -reinheit, und zum anderen sollten die Bondpartner frei von Oxiden sein. Oxidiertes Cu erfordert erhöhte Bondparameter, um die Oxidschicht zu durchbrechen und zuverlässige Cu-Cu-Verbindungen zu erzielen. Diese Bondbedingungen sind für viele sensible Bauelemente nicht geeignet. Aus diesem Grund sollten alternative Technologien mit einer einfachen Technik zum Schutz von Cu vor Oxidation gefunden werden.

In dieser Arbeit werden selbstorganisierte Monolagen (SAMs) für den Cu-Oxidationsschutz und die Verbesserung der Cu-Cu-Thermokompression- (TC) und Ultraschall- (US) Flip-Chip-Bondtechnologien untersucht. Die Experimente werden an Si-Chips mit galvanisch aufgebrachten Cu-Microbumps und Cu-Schichten durchgeführt. Die Arbeit beinhaltet die umfassende Charakterisierung der SAM für den Cu-Schutz, die Bewertung der technologischen Parameter für das TC- und US-Flip-Chip-Bonden sowie die Charakterisierung der Cu-Cu-Bondqualität (Scherfestigkeitstests, Bruchflächen- und Mikrostrukturanalysen).

Eine Lagerung bei tiefen Temperaturen (bei -18 °C und -40 °C) bestätigte die langanhaltende Schutzwirkung der kurzkettigen SAMs für das galvanisch abgeschiedene Cu ohne chemisch-mechanische Politur. Der Einfluss der Tieftemperaturlagerung an Luft und der thermischen SAM-Desorption in einer Inertgasatmosphäre auf die TC-Verbindungsqualität wird im Detail analysiert. Die Idee, mit Hilfe der US-Leistung SAM mechanisch zu entfernen und gleichzeitig das US-Flip-Chip-Bonden zu starten, wurde in der Literatur bisher nicht systematisch untersucht. Die Methode ermöglicht kurze Bondzeiten, niedrige Bondtemperaturen und das Bonden an Umgebungsluft.

Sowohl beim TC- als auch beim US-Flip-Chip-Bonden zeigt es sich, dass die Scherfestigkeit bei den Proben mit SAM-Passivierung um ca. 30 % höher ist als bei unbeschichteten Proben. Das Vorhandensein von Si- und Ti-Bruchflächen nach den Scherfestigkeitstests ist für die Proben mit der SAM-Passivierung typisch, was auf eine höhere Festigkeit solcher Verbindungen im Vergleich zu ungeschützten Proben schließen lässt. Die Transmissionselektronenmikroskopie (TEM) zeigt keine SAM-Spuren im zentralen Bereich der Cu-Cu-Grenzfläche nach dem US-Flip-Chip-Bonden.

Die Ergebnisse dieser Arbeit zeigen die Verbesserung der Bondqualität durch den Einsatz von SAM zum Schutz des Cu vor Oxidation im Vergleich zum üblicherweise angewandten Cu-Vorätzen. Das gefundene technologische Prozessfenster für das US-Flip-Chip-Bonden an Luft bietet eine hohe Bondqualität bei 90 °C und 150 °C, bei 180 MPa, bei einer Bonddauer von 1 s an. Die in dieser Arbeit gewonnenen Erkenntnisse sind ein wichtiger Beitrag zum Verständnis des SAM-Einflusses auf Chips mit galvanischen Cu-Microbumps, bzw. Cu-Schichten, und zur weiteren Anwendung der Cu-Cu-Fine-Pitch-Bondtechnologie in der Mikroelektronik.

Acknowledgements

The deepest gratitude I would like to express toward Jun.-Prof. I. Panchenko, who gave me the chance to start and accomplish the doctorate program under her supervision. I am very grateful for her patience, constructive criticism, scientific discussions, reviewing processes, continuous support, motivation and encouragement.

For reviewing the dissertation and essential scientific discussions, I would like to thank Prof. Dr. M. Schneider-Ramelow, especially regarding ultrasonic bonding, and Prof. T. Suga, particularly concerning thermocompression bonding. Moreover, this doctorate would not be possible without the guidance and support from Prof. Dr. K.-J. Wolter and Prof. Dr. K. Bock.

For a deep understanding of SEM and EBSD analysis, including critical and fruitful discussions of this thesis at different stages, I would like to thank Dr. M. Müller. For the excellent teamwork, practical tips and exchange of experience, I would like to thank L. Wambera, Dr. J. Meyer and S. Bickel. A great appreciation deserves O. Mudrievska for her high contribution within the scope of the student qualification work. Overall, I would like to express my deep gratitude to the whole staff of the Electronic Packaging Department of TU Dresden.

Moreover, I would like to acknowledge the staff of the Institute of Semiconductors and Microsystems of TU Dresden. For discussions and help in the fields of chemistry and spectroscopy, I would like to thank Dr. V. Neumann and Dr. U. Künzelmann. One of the most critical parts of this thesis, comprising XPS analysis, would not be possible without the support of Dr. M. Geidel, J. Reif and Dr. E. Langer. For the friendly cooperation during the work with the glove box system, I thank Dr. M. Franke and R. Körbitz.

For the breakthrough and the chance to see my topic from a different perspective, for the extraordinary support and unforgettable time of my research stay at the University of Tokyo, I would like to thank the research group of Prof. T. Suga, especially Dr. F. Mu, M. Yamamoto and M. Akaike.

For mask and wafer manufacturing, as well as for the possibility of performing ultrasonic bond experiments, for fruitful discussions and productive cooperation, I would like to acknowledge the staff of Fraunhofer IZM ASSID, especially Dr. J. Grafe, C. Rudolph, Dr. W. Steller, A. Schwarz, A. Shehzad, J. Krause and M. J. Wolf. Additionally, I would like to acknowledge the staff of Fraunhofer IZM in Berlin for participation in wafer manufacturing, fruitful discussions and great support. I am especially grateful to Prof. Dr. K.-D. Lang and Prof. Dr. M. Schneider-Ramelow for critical scientific discussions.

For the novel infrared ellipsometric (IRSE) analysis, as well as a joint publication, I would like to thank PD Dr. K. Hinrichs and I. Engler (Leibnitz-Institute für analytische Wissenschaften – ISAS). For the excellent TEM investigation, I would like to acknowledge F. Altmann and Dr. A. Graff (Fraunhofer IMWS). For crucial discussions regarding the ultrasonic bonder, I want to express my gratitude to R. Windemuth (Panasonic).

This work would not be possible without profound financial support from the Graduate Academy of TU Dresden.

Finally, I would like to thank my mother O. Lykova, my father O. Lykov and my sister K. Lykova for their firm support and belief in me through all the ups and downs of this journey. My special gratitude is devoted to the extraordinary support and persistent encouragement from M. Schubert.

Contents

List of Abbreviations ... IX
List of symbols ... X
1 Introduction ... 1
1.1 2.5D and 3D system integration ... 1
1.2 Aims of the thesis ... 3
2 State of the art in Cu-Cu bonding ... 5
2.1 Cu-Cu bonding technologies ... 5
2.2 Application of SAM for Cu-Cu bonding technologies ... 8
2.2.1 Characterization of SAM protective effect ... 8
2.2.2 Thermocompression and ultrasonic Cu-Cu bonding with SAM ... 10
3 Fundamentals of Cu-Cu bonding with SAM passivation ... 14
3.1 Cu material properties and Cu oxidation ... 14
3.1.1 Impact of Cu microstructure and Cu mechanical properties on Cu-Cu bonding ... 14
3.1.2 Types of Cu oxides ... 16
3.2 Description of SAM structure, its adsorption and desorption mechanisms ... 18
3.2.1 SAM structure and types ... 18
3.2.2 Adsorption and desorption mechanisms ... 22
3.3 US bonding process ... 26
3.3.1 Similarity between the US flip-chip bonding and wire bonding ... 26
3.3.2 The impact of the chip design on the US flip-chip bonding results ... 27
4 Materials and methods ... 29
4.1 Description and characterization of the samples ... 29
4.2 Passivation of the Cu surface with SAM ... 36
4.3 Characterization of SAM protective capability ... 36
4.3.1 Contact angle (CA) measurement ... 36
4.3.2 X-ray photoelectron spectroscopy ... 37
4.3.3 Infrared spectroscopic ellipsometry ... 40

4.4 Bonding techniques ... 42
4.4.1 Description of the used bonding equipment ... 42
4.4.2 Details of thermocompression and ultrasonic bonding processes ... 42
4.5 Characterization of the bonding quality ... 44
4.5.1 Shear strength test ... 44
4.5.2 Topography analysis ... 44
4.5.3 Microstructure analysis of the Cu-Cu bonding interface ... 45
4.5.3.1 Sample preparation and scanning electron microscopy analysis ... 45
4.5.3.2 Transmission electron microscopy analysis ... 48
5 Microstructure characterization of the Cu surface before bonding ... 50
5.1 Grain structure analysis of the Cu surface by electron backscatter diffraction ... 50
5.1.1 EBSD measurement ... 50
5.1.2 Data analysis and filtering procedure of EBSD data sets ... 51
5.1.3 Method for correction of sample orientation in cross-sections ... 52
5.1.4 Drift correction of EBSD measurements ... 55
5.2 Results and discussion ... 57
5.2.1 Characterization of bonding interface image quality before bonding ... 57
5.2.2 Characterization of the grain size before bonding ... 58
5.2.3 Characterization of grain orientation before bonding ... 62
5.2.4 Estimation of Young's modulus ... 65
5.3 Summary ... 66
6 Influence of SAM passivation on the protection of Cu from oxidation ... 68
6.1 Experiment description ... 68
6.2 Factors contributing to the prolongation of SAM protective effect ... 69
6.2.1 Results and discussion ... 69
6.2.1.1 Characterization of the Cu surface after etching ... 69
6.2.1.2 Influence of SAM chain length on SAM protective function after room temperature storage ... 72
6.2.1.3 Influence of room and low-temperature storage on the wettability of the Cu surface ... 74
6.2.1.4 Influence of room temperature storage on the chemical composition of the Cu surface ... 76

6.2.1.5 Influence of low-temperature storage on the chemical composition of the Cu surface 79
6.3 Summary 81
7 Investigation of Cu-Cu thermocompression bonding with SAM passivation 82
7.1 Experiment description 82
7.2 Influence of desorption conditions on Cu-Cu bonding quality 86
7.2.1 Results and discussion 86
7.2.1.1 Analysis of the chemical composition of the Cu surface 86
7.2.1.2 Characterization of the mechanical strength of the interconnects 93
7.3 Influence of storage conditions on Cu-Cu bonding quality 96
7.3.1 Results and discussion 96
7.3.1.1 Analysis of the chemical composition of the Cu surface 96
7.3.1.2 Characterization of Cu-Cu bonding interface 100
7.3.1.3 Characterization of mechanical strength of the interconnects 101
7.4 Summary 104
8 Investigation of Cu-Cu flip-chip ultrasonic bonding with SAM passivation 106
8.1 Experiment description 106
8.2 Inspection of the bonding tilt and its influence on the bonding area 108
8.2.1 Results and discussion 108
8.2.1.1 Characterization of the bonding tilt 108
8.2.1.2 Influence of the bonding tilt on the calculation of the bonding area 109
8.3 Characterization of the bonding interface by SEM and TEM analyses 111
8.3.1 Results and discussion 111
8.3.1.1 SEM analysis of Cu-Cu bonding interface 111
8.3.1.2 TEM analysis of Cu-Cu bonding interface 119
8.4 Characterization of shear strength tests and fracture surface analysis 123
8.4.1 Results and discussion 123
8.4.1.1 Die shear strength tests and fracture surface analysis 123
8.4.1.2 Microbump shear strength tests 128
8.4.1.3 Comparison of the shear strength of the SAM-protected interconnects with other pre-treatment methods from literature 131
8.5 Summary 132

9 Summary and outlook 134
Literature 137
List of figures 149
List of tables 157
Appendix 158
A.1 Additional information for EBSD measurements 158

List of Abbreviations

Abbreviation	Meaning
AES	Auger electron spectroscopy
BGA	ball grid array
BT	Benzenethiol
CA	contact angle
CMP	chemical-mechanical polishing
D2D	die-to-die
D2W	die-to-wafer
EBSD	electron backscatter diffraction
ECD	electrochemical deposition
EDX	energy dispersive X-ray
FIB	focused ion beam
HAGB	high-angle grain boundary
IMC	intermetallic compound
IPF	inverse pole figure
IRSE	infrared spectroscopic ellipsometry
LAGB	low-angle grain boundary
ND	normal direction
OSP	organic solderability preservative
PCB	printed circuit board
ppm	particles per million
PVD	physical vapor deposition
RD	rolling direction
SAM	self-assembled monolayer
SEM	scanning electron microscopy
SOH	standoff height
STEM	scanning transmission electron microscopy
TC	thermocompression
TD	transverse direction
TDS	thermal desorption spectroscopy
TEM	transmission electron microscopy
TS	thermosonic
TSVs	Through-Si-Vias
UHV	ultra-high vacuum
US	ultrasonic
XPS	X-ray photoelectron spectroscopy

List of symbols

Symbol	Unit	Meaning
A		transformation matrix
A_{EBSD}	mm^2	set area for EBSD measurement
A_{real}	mm^2	real area of EBSD measurement
BE	eV	binding energy
c_{ij}	GPa	elastic stiffness constant
d_{EBSD}	μm	grain diameter calculated by OIM Analysis software
d_{real}	μm	real grain diameter
E	GPa	Young's Modulus
$(h\ k\ l)$		indexing of crystal planes
h_{EBSD}	μm	height of a bump in EBSD measurement
h_{real}	μm	real height of a bump obtained from SEM image
$h\nu$	eV	photon energy
k		correction factor
KE	eV	kinetic energy
$\vec{r}_{crystal}$		vector of the crystal orientation
r_p		*p*-polarized component
$\vec{r}_{projected}$		projected vector into the TD plane
$\vec{r}_{RD}$		RD vector
r_s		*s*-polarized component
$\vec{r}_{sample}$		vector of the sample orientation
S	mm^2	bonding area
s_{ij}	$\frac{m^2}{N}$	elastic compliance constant
$\tan\psi$		amplitude ratio
$[u\ v\ w]$		indexing of crystal directions
α	$^\circ$	angle between the projected vector into the TD plane and vector RD
Δ		phase shift
$\varepsilon_{lateral}$		lateral strain
$\varepsilon_{logitudinal}$		logitudinal strain
ν		Poisson's factor
ρ		change in polarization
φ	eV	spectrometer work function

1 Introduction

1.1 2.5D and 3D system integration

During the last six decades, the size of electrical components kept shrinking while their functionality increased. According to Moore's Law from the 1960s, the number of transistors per chip should double every 18 months [1]. Due to numerous reasons, inter alia, lithographic limitations and heat dissipation problems, this tendency was acknowledged as nearing an end in 2016 [2]. The latest research is focused rather on diversification of electrical components or widening their functionalities, which is defined as the More than Moore approach. There is no reason to miniaturize smartphones, but there is a demand for more functionalities and lower fabrication costs. This can be achieved i.e. by using a chiplet, an integrated circuit block with its functionality, built on a bigger die together with other chiplets [3]. Chiplets are fabricated separately and can be assembled in more sophisticated integrated circuits upon request. 2.5D system integration offers a possibility of high-density connections of such side-by-side integrated chiplets or dies using Si interposer with Through-Si-Vias (TSVs) [4], [5].

Fig. 1-1 presents 2.5D integration of a logic die, connected to the substrate and the memory dies by TSVs and Cu microcontacts. The memory dies, in turn, are also integrated into 3D stacks using TSVs and microcontacts. Interposer is connected to the organic or ceramic substrate using C4 bumps. The connection between the substrate and the printed circuit board (PCB) is typically realized by ball grid array (BGA) balls. Such packaging provides miniaturization of die footprint, better accessibility of electrical components and, as a result, lower signal delay. Shorter interconnects due to the use of interposers cause a reduction of parasitic capacitances, which minimizes power consumption. They allow transmission of high bandwidth signals, reduce heat generation and enhance overall performance significantly. Therefore both, 2.5D and 3D integrations address ideally More than Moore requirements, potentially providing an increase in functionalities and lowering costs [6].

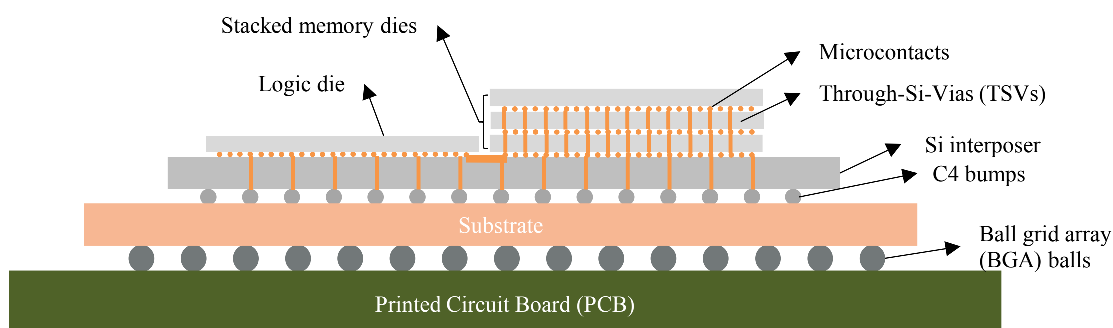

Fig. 1-1 Schematic cross-section view of a 2.5D integrated logic die and a 3D stack of memory dies, connected by TSVs and microcontacts (adapted from [5])

Nevertheless, implementation of such systems goes along with challenges, especially for die-to-die interconnection (see microcontacts in Fig. 1-1). Choice of materials for microcontacts upon increasing terminal density is one of them. Microcontacts for 3D systems are now in the range of 5 - 20 µm [1], [6]. The choice of pure Cu instead of solder joints is based on applicability for fine-pitch interconnects, higher electrical and thermal conductivities, outstanding mechanical properties, fewer fabrication steps, no reliability issues connected to intermetallic compounds (IMCs) and cost-efficiency.

The biggest challenge of implementing Cu as microcontact material for 2.5D and 3D systems is its oxidation within seconds of air exposure. Cu oxide increases contact resistance and hampers a reliable interconnect formation during Cu-Cu bonding.

As wafer production and bonding are performed not always by one fab, there is often a need for Cu protection during wafer storage and transportation time. A die can be etched or cleaned by plasma before bonding to remove oxides or temporary protective layers (i.e. organic solderability preservatives (OSP)). However, the OSP solution is not represented in literature in detail when it comes to scaling down the interconnects, possibly, due to contamination issues [7]. On the other hand, there is still a re-oxidation problem and renewed adsorption of organic contaminations during seconds of air exposure due to the high reactivity of Cu metal.

There is a variety of solutions to this problem, i.e. etching of Cu with formic acid directly in the bonding chamber, which requires a complex chemical control system in the bonder. Much more simple is a technique of Cu passivation with a protective self-assembled monolayer (SAM) and its subsequent desorption via thermal annealing *in-situ* before bonding [8], [9]. The technique of passivation is a simple immersion into organic solvent mixed with an active surfactant [10]. SAM is a densely packed (1…10) nm thin monomolecular layer. Fig. 1-2 shows a schematic illustration of SAM and its typical ordering on Cu surface. SAMs can be classified into short- and long-chain SAMs depending on the amount of C in their backbones.

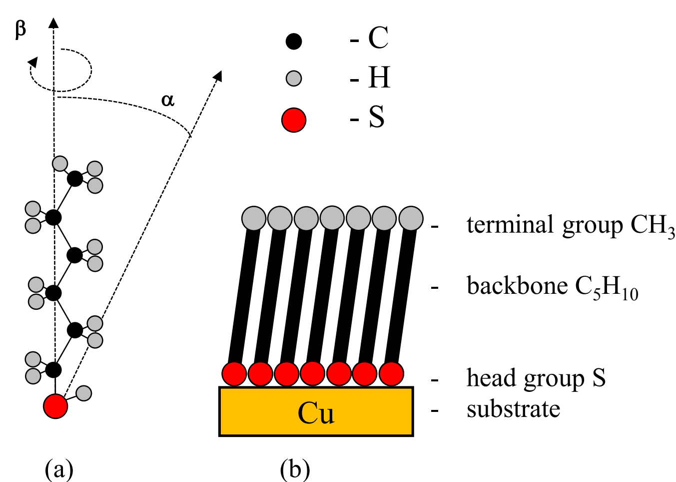

Fig. 1-2 Schematic presentation of one SAM chain of 1-hexanethiol (C6) with tilt angle α and twist angle β (a); schematic view of the ordered SAM chains on Cu surface and their structure (b)

The monolayer, however, degrades (oxidizes) upon exposure to air at room temperature. Therefore, the ways of prolongation of its functioning have been investigated. Long-chain

SAMs have been proven to be more long-lasting oxidation inhibitors. Their desorption is, however, much more complicated than the desorption of the short-chain ones [8]. One of the promising techniques is storage at low temperatures [11], which has not been investigated systematically for short-chain SAMs. Quality of bonding after such storage is also rather an unanswered question in the literature.

Furthermore, SAM passivation is commonly recommended for smooth sputtered surfaces [10]. The roughness of electroplated Cu microbumps usually exceeds the roughness of the sputtered surfaces. Therefore, there is a need for the characterization of SAM protective effect for electroplated Cu surfaces with higher roughness.

Thermocompression (TC) bonding, whereby SAM thermal desorption *in-situ* has been applied, is a well-established method for fine-pitch bonding. Another rather less investigated method is flip-chip ultrasonic (US) bonding [12]. This method applies additionally US power, which can be very beneficial, especially regarding bonding time (≤ 1 s). As SAM can be mechanically rubbed away from the surface, US bonding can open the new possibilities of Cu-Cu bonding in air, much shorter bonding time, as well as lower bonding temperature.

1.2 Aims of the thesis

The present thesis aims to empirically study the impact of SAM passivation towards improving Cu-Cu bonding technology for 2.5D / 3D integration systems. The main objectives of this research work are:

1. Characterization of SAM passivation as oxidation inhibitor for electroplated Cu, the influence of storage conditions on the chemical composition of the Cu surface
2. Investigation of TC Cu-Cu bonding technology with SAM passivation, the influence of desorption conditions and storage at low temperatures on the bonding quality
3. Investigation of Cu-Cu US flip-chip bonding with SAM passivation, characterization of the dependency between the bonding parameters and quality of formed interconnects

One of the general goals is to decrease the bonding parameters for Cu and simplify the bonding requirements while achieving a reliable Cu-Cu interconnect. Fig. 1-3 summarizes the main factors influencing Cu-Cu bonding technology, which will be analyzed in this study.

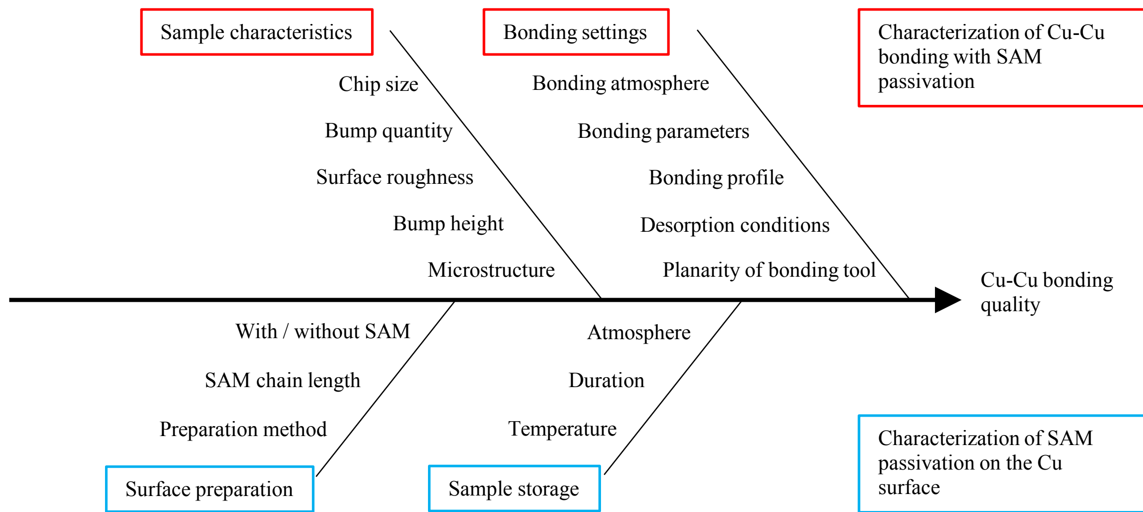

Fig. 1-3 Schematic overview of the influencing factors on the Cu-Cu bonding technology with SAM passivation

The next chapter presents state of the art in most intensively investigated Cu-Cu bonding technologies, investigations of SAM passivation and Cu-Cu bonding methods with SAM passivation.

2 State of the art in Cu-Cu bonding

2.1 Cu-Cu bonding technologies

Cu-Cu diffusion bonding can be classified in different ways according to bonding technology, interconnect form and pre-treatment method (Fig. 2-1). The main Cu-Cu bonding technologies are presented on the left of the diagram and will be discussed later on.

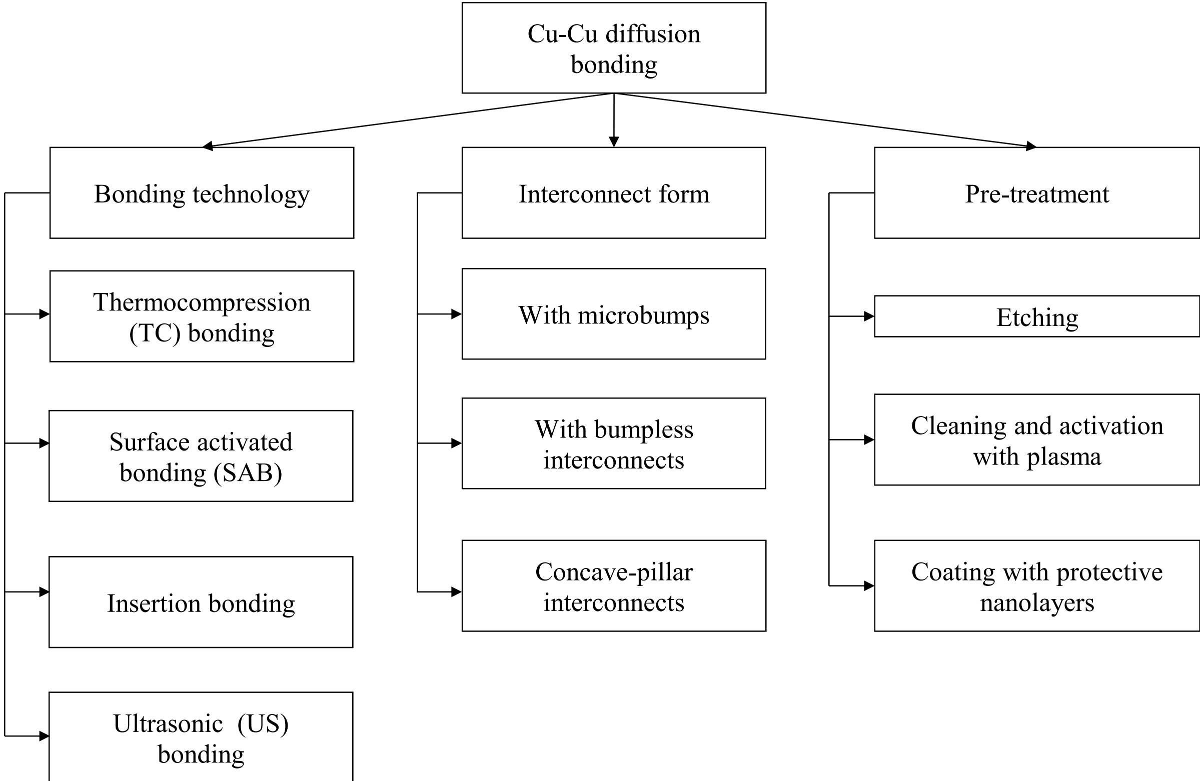

Fig. 2-1 Proposed classification of common bonding technologies, interconnect forms and Cu pre-treatment methods for diffusion bonding using Cu as interconnect material

TC bonding is one of the most established Cu-Cu bonding methods, which commonly applies high temperature and high pressure in order to deform the metal parts and cause the interdiffusion process. Interconnect form of the bonded test vehicles has a significant influence on the bonding force [6]. Cu microbump and Cu pillar have the same meaning in this thesis. Bonding of Cu microbumps (Fig. 2-2, (a)) using TC method or concave-pillar interconnects (Fig. 2-2, (c)) using insertion bonding requires (100…350) MPa of bonding pressure, whereas less than 2.5 MPa is enough for bumpless interconnects [13]–[15]. Cu-Cu TC bonding is typically performed at a temperature range (300…400) °C, additionally followed by annealing at the same temperatures [15], [16]. Annealing and bonding processes commonly take from 30 min to several hours. Such temperatures and durations can damage other thermally sensible components in the package. Thus, the importance of decreasing bonding temperature, pressure, duration and making possible bonding in air ambient have been of particular interest in the development of new technologies.

The dependency between interconnect form and bonding force derives from the need for local plastic deformation of the Cu surface. The higher the roughness and the bump height variation, the higher degree of deformation is needed. The roughness of Cu microbumps is normally higher ($R_a \geq 10$ nm) than of chemical-mechanically polished (CMP) surfaces ($R_a \leq 2$-3 nm) [17]–[19]. CMP is usually applied for bumpless interconnects, which are commonly used for wafer-to-wafer (W2W) bonding. Bumpless interconnects are common for hybrid bonding. Hybrid bonding is defined by the bonding of an insulator layer of one of the two wafers to the insulator layer on the other wafer and at the same time by direct metal-to-metal bonding of the metal pads located in the same plane with the insulator layers (Fig. 2-2, (b)). The hybrid Cu/SiO_2 bonding process requires a CMP process before bonding to obtain very low roughness of the SiO_2 and the Cu surfaces. The wafers are usually contacted in high vacuum and at low bonding pressure. This is followed by annealing step at (200…400) °C to perform hydrophilic SiO_2/SiO_2 bonding and Cu-Cu TC bonding processes [15], [20]. The resulting interconnection is strong and reliable, but has high requirements to the surface quality before bonding, bonding atmosphere and is not yet an optimal solution for die-to-die (D2D) or die-to-wafer (D2W) bonding.

Deformation of microbump contacts enables breaking through the oxide and contamination layers in air, causes an increase in grain dislocation density, grain boundaries and, hence, activation of interdiffusion mechanisms. Moreover, deformation during bonding hardens material, which increases its shear strength. Yamamoto et al. report that the shear strength of bonded Au films appears to be lower compared to Au microbumps [21]. The use of concave-pillar interconnect (Fig. 2-2, (c)) by insertion bonding enables bonding in air at 200 °C. This method requires, however, higher deformation compared to microbump contacts, which is achieved by applying a bonding pressure of 389 MPa [22]. Such a high bonding pressure can be disadvantageous considering the trend of thinning down of the electrical components [3]. Therefore, bonding with microbumps, illustrated in Fig. 2-2 (a), has been chosen for the development of new Cu-Cu bonding technology in this work.

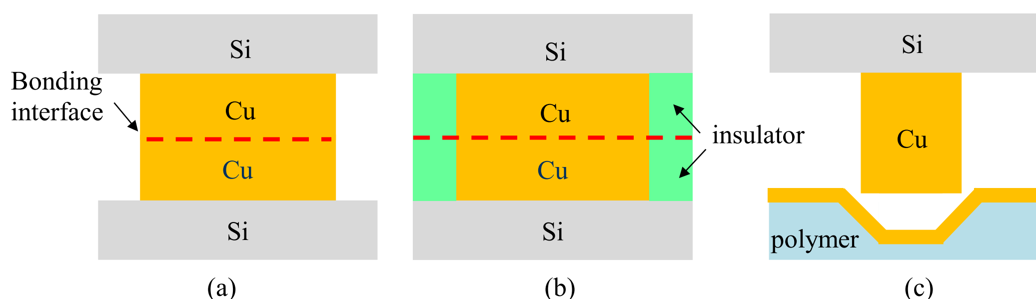

Fig. 2-2 Types of die topologies for Cu-Cu bonding: with microbumps (a), with bumpless interconnects (b) and concave-pillar interconnects (c)

Furthermore, Cu-Cu bonding requires surface pre-treatment to remove Cu oxide and organic contamination layer. Commonly used methods to remove Cu oxide are wet or dry etching. Wet etching can be carried out using acetic, citric, sulfuric, or hydrochloric acids [13], [23]–[26]. The drawback of this method is the reoxidation of Cu within seconds of air exposure before and during the bonding procedure. Dry etching is usually performed using N_2/Ar+H_2 or HCOOH

gas treatments *in-situ* before bonding [27]–[30]. This avoids Cu reoxidation but requires complex equipment with a control system of the chemical processes.

Another pre-treatment method is surface activation using Ar^+ ion bombardment in ultra-high vacuum (UHV) before bonding. Suga et al. were a pioneer research group in the development of this method for Cu-Cu bonding and achieved high interconnect quality at room temperature [31]–[34]. Such a method is commonly applied on smooth surfaces, such as bumpless interconnects. However, using an ultra-high vacuum is time-consuming and has a low throughput in microelectronics manufacturing. Yamamoto et al. report about the positive effect of Au surface pre-treatment with atmospheric pressure plasma [21]. Nonetheless, this method is still connected with the problem of re-oxidation before bonding when using Cu.

In order to protect Cu from oxidation, permanent coatings of the Cu surface with metallic nanolayers have been implemented. Researchers report about permanent passivations with Au [35], [36], Co/Au [37], Pd [38], Au/Ni [39], electroless Ni – immersion Au (ENIG) or electroless Ni – electroless Pd – Immersion Au (ENEPIG) [40], [41], Al [42], Al/Ni [43] and Ti/N [8]. For instance, 10 nm of Au sputtered layer has good protective properties against oxidation due to the inertness of Au and its high electrical and thermal conductivity. Nonetheless, such interconnects are reported to be unreliable due to several reasons. First, differences in interdiffusion coefficients ($D_{Cu} > D_{Au}$) cause faster diffusion of Cu into Au than Au into Cu. This causes Cu oxidation and the formation of Kirkendall voids at the Cu/Au interface. Second, intermetallic phases, that start to form above 200 °C, are reported to be brittle [39]. Sputtering of a thin Co diffusion barrier between Cu and Au would solve this problem [37] but will bring another one instead. Electrical resistances of Co, Ni, Al, Ti are much higher than the electrical resistance of Cu. Passivation with another noble film, Pd [38], would, unfortunately, collide with a similar challenge as Au, namely fast diffusion of Cu into Pd, which inhibits oxidation protection during long-term storage [44].

Self-assembled monolayers (SAMs) gained a lot of attention among temporary passivations for Cu in the last three decades. The most studied SAM systems are formed from alkanethiols (RSH), where R is an alkyl chain $-C_nH_{2n+1}$. Alkanethiols, also referred to as thiols or mercaptans, are readily adsorbed by certain metal surfaces in order to form alkanethiolates, also referred to as thiolates (i.e. RS-Cu). A short reference for the thiols or thiolates with a certain number of C atoms would be C2 for 1-ethanethiol, C3 for 1-propanethiol, C6 for 1-hexanethiol, etc. Chemical reaction (2-1) describes SAM adsorption on Cu. This is accompanied by cleavage (desorption) of one H atom from an adsorbed molecule [45]–[47]:

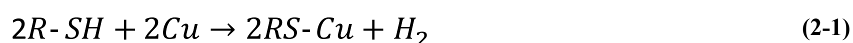

$$2R\text{-}SH + 2Cu \rightarrow 2RS\text{-}Cu + H_2 \quad \textbf{(2-1)}$$

Monolayers can be classified into short- and long-chain SAMs [48]. Short-chain SAMs have less than nine C atoms in their backbones. Long-chain SAMs have more than nine C atoms in their backbones, respectively [49].

SAMs have a variety of applications in nanotechnologies. It has been used for patterning in lithography [50], [51], as a diffusion barrier between low-K dielectric layers and metals [52],

[53], as corrosion inhibitor [54]–[56] and as a protective coating against Cu oxidation [57], [58].

The research group of Chuan Seng Tan at the Nanyang Technological University in Singapore intensively investigated the temporary passivation of Cu with SAMs before bonding [8], [9], [59]–[62]. The idea was to passivate the Cu surface with the monolayer and store it for several days in air while retarding the Cu oxidation process. After that, the sample pair is placed into a bonding chamber, which is purged with an inert gas. Before the bonding process starts, the samples are pre-heated *in-situ* for a certain time to activate the SAM desorption process. This procedure is followed by bonding of Cu surfaces, which allows decreasing of bonding temperature up to 250 °C. Nevertheless, there is an earlier mentioned problem of degradation of SAMs upon air exposure [8]. The next chapter addresses this problem in more detail.

Apart from TC bonding, other ways of bonding with SAM have been reported: wire bonding and flip-chip US bonding. In both cases beneficial is that ultrasonic rubbing in air is used instead of thermal desorption of SAM in an inert gas atmosphere. US flip-chip Cu-Cu bonding, in contrast to wire bonding, has not been investigated in detail and is not a widely spread method. US bonding will be used as a general term comprising US bonding of dies with microbumps with and without heating in this work later on.

The protective function of SAM as an oxidation inhibitor and its application for Cu-Cu bonding have been investigated by a number of researchers. Their findings are presented in detail in the next chapter.

2.2 Application of SAM for Cu-Cu bonding technologies

2.2.1 Characterization of SAM protective effect

There are several ways of prolongation of SAM functioning: storage in an inert gas atmosphere, using long-chain SAMs and storage at low temperatures in air conditions. Storage in an inert gas atmosphere is possible, but, for instance, a glove box system with strict oxygen control is complex and price intensive. Using long-chain SAMs results in difficulties of their desorption. Therefore, storage at low temperatures of the short-chain SAMs appears to have a potential for investigation.

Tab. 2-1 presents the main SAM terminology and chemical formulas used in this thesis. It is known that n-alkanethiols (R-SH), adsorbed on Cu surface, form thiolates (RS-Metal) [46], [63]. S-headgroup of SAM can in time oxidize and form sulfonates (R-SO_3-Metal) in air. Penetration of O atoms into the Cu surface through defects in SAM is designated as SAM degradation in this work. This and the formation of disulfides will be discussed in chapter 3.2.2 in detail.

Tab. 2-1 Common chemical formulas and terminology of used alkanethiols and their derivatives in this study ($R = C_nH_{2n+1}$) [10]

Formula	Name	Explanation
R-SH	alkanethiol, thiol, mercaptan	SAM substance
RS-Metal	alkanethiolate, thiolate	Product of thiol adsorption (chemisorption) on metal surface
$R\text{-}SO_3$-Metal	sulfonate	Product of thiolate oxidation
RS-SR	disulfide	Product of reaction between two thiols or thiolates

The protective effect of SAM before bonding has been investigated by a number of research groups. Tab. 2-2 shows the impact of SAM on the chemical composition of Cu surface after storage in air for various periods.

Many investigations have been performed for short-chain and long-chain SAMs on Au [10], [64]. Schoenefisch et al. have shown that a full transformation of thiolates to sulfonates on polished bulk polycrystalline Au occurs after storage at room temperature in air for one hour for short-chain thiolates (C3), for 24 hours for long-chain thiolates (C12) and seven days for C18 according to XPS measurements [65]. Willey et al. report about only 12 hours of the complete transformation from thiolates to sulfonates at similar conditions, but on a 100 nm Au sputtered layer [66]. Not many investigations have been conducted using SAM on Cu. Tab. 2-2 presents SAM aging on Cu at various storage conditions reported in the literature. Physical vapor deposition (PVD) is one of the deposition methods to produce thin films. This method comprises sputtering and evaporating of thin films. In this work, PVD Cu is referred to as a sputtered surface.

Tab. 2-2 Indication of chemical composition changes of the Cu surface depending on Cu type and storage conditions

Cu type	SAM type	Storage time	Storage temperature	Surface changes	Ref.
Cu PVD	C16	101 h (4 days)	room	XPS: oxide growth, sulfonates appear	[63]
		391 h (16 days)	room	XPS: oxide and sulfonates growth; thiolates still present	
Cu PVD	C6	3 days	room	CA: decrease Δ=40 °	[8]
			4 °C	CA: no changes	
Cu PVD	C6	7 days	room	CA: decrease Δ=30 °	[67]
			2 °C	CA: decrease Δ=15 °	
Cu bulk	C18	3 weeks	room	XPS: oxide growth, sulfonates not detected	[68]
		1 week	4 °C	XPS: oxide growth, sulfonates not detected	
		10 weeks	-30 °C	XPS: no oxide growth	

The SAM appears to be unstable after the deposition. Sum of different processes, connected to SAM oxidation, SAM disordering (presence of defects) and SAM desorption are usually labeled as SAM degradation. The evidence of SAM degradation is usually found by characterization of surface chemical composition, wettability (contact angle (CA)), SAM molecular orientation, etc. Literature reports a lower degradation rate of SAM on Cu at low temperatures. Paul et al. show that, though the number of sulfonates grows after 16 days of air exposure, the thiolate species are still detected on the Cu surface [63]. Lim et al. used

wettability tests to evaluate C6-SAM aging rate [8]. Wettability of metals like Cu is commonly evaluated by the sessile drop contact angle (CA) method [69]. As SAMs make Cu surface hydrophobic, which means that CA is higher than 90 °, a drastic decrease in hydrophobicity (by 40 °) after three days of air exposure at room temperature indicates SAM degradation. Meanwhile, no changes in CA are detected after storage at 4 °C that indicates a noticeable effect of low temperatures on SAM stability. Ghosh et al. report decrease of CA by 30 ° after storage at room temperature and by 15 ° after storage at 2 °C for seven days [67]. CA measurement is dependent not only on the chemical composition of the surface but also on its roughness and measurement conditions (humidity, atmosphere, etc.). Therefore, the results of CA tests have to be observed in combination with other characterization methods (XPS, IRSE). Liu and Hutt suggest that wetting properties can be even more sensitive to the changes in the chemical state of the surface than XPS [70]. Wettability data for the reference samples without SAM is usually absent. Moreover, CA for samples with SAM has been assessed only for several hours or days of storage.

Hutt et al. show that oxide growth on Cu can be almost terminated using long-chain SAMs (C18) and storage at -30 °C in air for 10 weeks using XPS [68]. Usually, SAMs are passivated on smooth sputtered surfaces. But in their work, bulk 0.25 mm thin Cu foils (99.9 %, Goodfellow) were used. The average roughness of a similar foil type (thickness 0.1 mm) is reported in [71] and is about 23 nm. Electroplated Cu for microbumps also has higher roughness than PVD Cu. Therefore, a question appeared, if rougher Cu surfaces can be protected by short-chain SAMs over a longer time scale.

Ghosh et al. report slowing of SAM degradation using storage at lower temperatures (2 °C) upon exposure to air, but the research group has not investigated the bonding quality after such storage of SAM coated samples [72]. The same can be claimed for the research of Ebbens et al. [73]. The next subchapter shows what has been highlighted in the literature about Cu-Cu bonding with SAM passivation.

2.2.2 Thermocompression and ultrasonic Cu-Cu bonding with SAM

Three Cu-Cu bonding technologies can be outlined by application of SAM passivation in literature reports: wire bonding, TC and US flip-chip bonding. In this work, US flip-chip bonding is also referred to as US bonding. Tab. 2-3 describes bonding parameters of these techniques, sample designs and evaluation methods.

Tab. 2-3 Wire, thermocompression and ultrasonic Cu-Cu bonding with SAM

Parameters / research groups	**Wire bonding** [54], [74], [75]	**TC flip-chip bonding** [57], [59]	**US flip-chip bonding** [12], [76]
Sample types	Pads and wire balls	Chips with pads	Chip with cone-shaped bumps to chip with electrodes
Wire ball/pad/bump size	Ball diameter: 40 µm Pad size (width×length): approx. 65×65 µm^2	Pad height: 5 µm, 10 µm, 50 µm, 100 µm	Bump diameter: 10 µm Bump height: 9 µm
Bonding area	approx. 0.001 mm^2	16 mm^2	0.95 mm^2
Pitch	approx. 80 µm	-	20 µm
Chip size	-	8×8 mm^2	5×5 mm^2; 7×7 mm^2
SAM type	C10, Benzotriazole	C6, C12	C6
Storage (temperature, time, atmosphere)	-	T_{room}; 3 days; air	0 h, 4 h, 24 h; air; T_{room}
Desorption (temperature, time, atmosphere)	-	250 °C; 10 min; N_2	-
Bonding paramaters (temperature, time, pressure, atmosphere)	145 °C; 35 ms; - ; air	250 °C; 1 h; 250 kPa; vacuum (~10-4 mbar)	T_{room}; 1 s; 127 MPa; air
Characterization methods	Shear strength test; wettability by CA; chemical composition by XPS; desorption by TDS	Shear strength test; wettability by CA; cross-sections by TEM; chemical composition by EDX and XPS	Shear strength test; chemical composition by AES; electrical test by four probe method; wettability by CA; cross-sections by SEM

Oxidation of Cu has always been a significant challenge concerning its application in wire bonding. Passivation of Cu wires with SAM leads to reaching the shear strength of 125 MPa while applying only 140 MPa of bonding pressure in air in a low-temperature range under 150 °C [54], [74], [75]. The bonding duration of 35 ms is reported to be enough to break through the monolayer and form a bond [77], [78].

Peng et al. have intensively investigated TC Cu-Cu bonding with SAM passivation. In this study, Cu wafers or Cu chips with polished pads [9] were passivated with 1-hexanethiol (C6) and stored for 3 days at room temperature in air. Afterward, the samples were placed into the bonding chamber, purged with N_2-gas. Pre-heating of samples is performed *in-situ* before bonding for 10 - 30 minutes at 250 °C to activate the desorption process of SAM molecules. Afterward, the TC bonding is performed at 250 °C for one hour in vacuum (Fig. 2-3). The cleanliness of Cu surfaces after the desorption process is assessed by XPS. Although the S-spectra before and after desorption are shown, there is no data about the presence of O or C on the Cu surface after pre-heating.

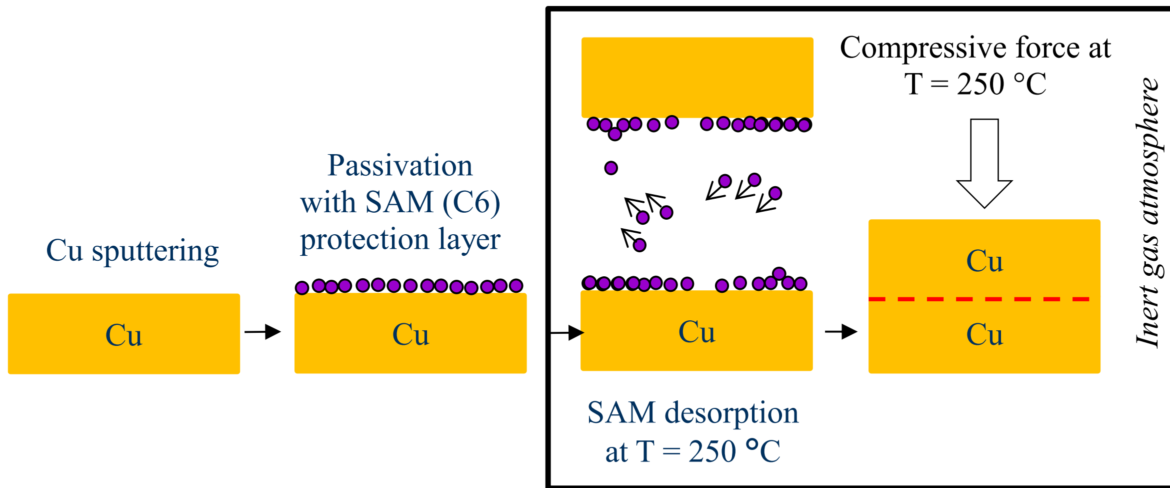

Fig. 2-3 Schematic view of Cu-Cu TC bonding with thermal SAM desorption

Considering observations of the previous subchapter, there is a high potential of termination of SAM degradation using storage at low temperatures. Nevertheless, there is not enough experimental data for Cu-Cu bonding after storage at low temperatures.

It was reported in the literature that SAM desorption is essential before bonding, otherwise, SAM serves as a diffusion barrier for Cu-Cu interconnect [8], [62]. Carbonell et al. have measured desorption temperature for SAM desorption of C10 using thermal desorption spectrometry (TDS) [75]. The temperature was constantly increased with a heating rate of 0.39 °C/s. Two desorption peaks were found as a result: at 95 °C and around 150 °C. The presence of two peaks has been explained by two-step SAM desorption. The first peak is formed as a result of sulfonates formation (S oxidation) and desorption. This causes decomposition of alkyl chains, adsorption of their fragments onto the Cu surface and desorption at higher temperatures. Although the maximum of the desorption peak for alkyl fragments is at approximately 150 °C, the intensity of the peak decreases slowly. This means that full desorption of C10 from the pure Cu surface occurs at temperatures higher than 250 °C. C6 radical has been desorbed at 97 °C and 187 °C according to TDS measurements of Kodama et al. [79]. After desorbing of C18 SAMs no S species were found after reaching 210 °C with a heating rate of 2 °C/min in [80].

TC bonding with SAM desorption implies several investigation gaps concerning the desorption procedure. Is Cu SAM- and oxide-free after annealing at constant temperature? This question has not been addressed systematically according to literature data.

Qiu et al. proposed ultrasonic bonding of Si-dies with cone-shaped Cu microbumps at room temperature in air ambient [12], [76]. Fig. 2-4 illustrates the experimental procedure. The quantity of microbumps is 12100. However, their results show lower shear strength for Cu/SAM in comparison to uncoated Cu interconnects.

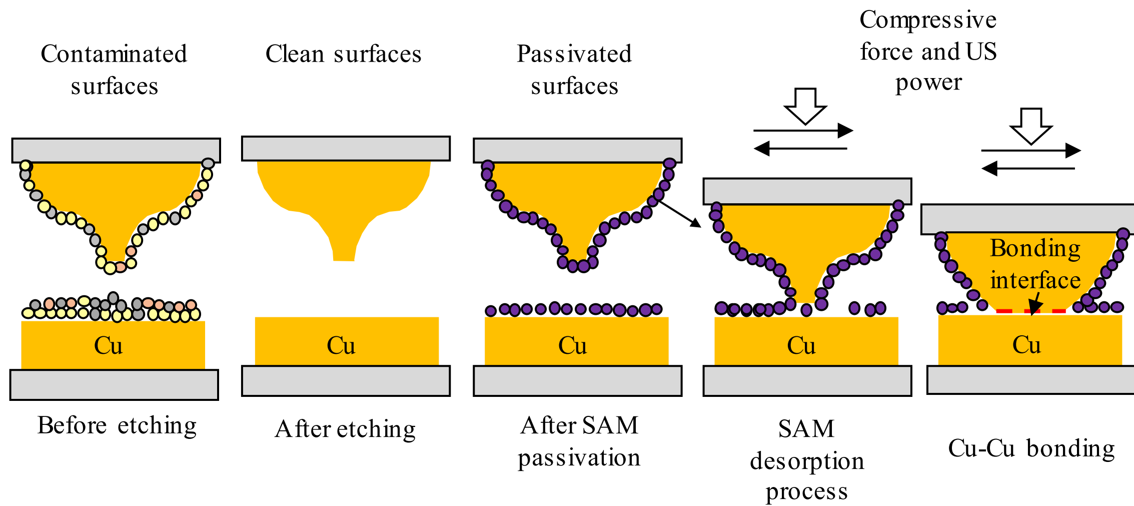

Fig. 2-4 Schematic representation of US bonding using SAM passivation of planar (on the bottom die) and cone-shaped (on the top die) bumps

Implementation of ultrasonic energy in the bonding process can make mechanical SAM removal in air possible, significantly decrease bonding time and temperature, at the same time exposing clear or barely contaminated Cu surfaces to bonding. However, there is a lack of published data about bonding profile, the influence of die design on the Cu-Cu bonding technology, surface roughness and parameter window for US Cu-Cu flip-chip bonding in general. The application of thermosonic bonding (TS) can have a positive impact on the bonding quality, while still maintaining the requirements for a low-temperature range.

Furthermore, there is not enough systematic analysis of shear strength for single interconnects, fracture surfaces after die shear tests, Cu-Cu bonding interface, as well as the influence of non-planarities between bonding stage and head.

It is important to summarize theoretical fundamentals about Cu metal properties and SAM coating, which will be described in the next chapter, before going into experimental description and results. TC bonding is a well-established method and its principles are well known in contrast to the less investigated and rarely used US flip-chip bonding. Thus, the next chapter will highlight the theory behind this process, as well.

3 Fundamentals of Cu-Cu bonding with SAM passivation

3.1 Cu material properties and Cu oxidation

3.1.1 Impact of Cu microstructure and Cu mechanical properties on Cu-Cu bonding

Cu and Au belong to the first subgroup of the periodic system and have high electrical and thermal conductivities. The precious metals have been used as established materials for metallic interconnects in microelectronic packaging. As interconnect density has been increasing, Al and Cu have gained noticeable attention as low-cost candidates. Excellent electrical, thermal and mechanical properties of Cu (Tab. 3-1) have been of specific interest for microelectronics as its reliability has an impact on the whole end-device.

Tab. 3-1 Comparison of the main properties of the commonly used metals in diffusion bonding

Characteristic	**Al** [81]	**Au** [82]	**Cu** [83]
Resistivity, 10^{-8} Ωm (20 °C)	2.67	2.2	1.69
Thermal conductivity, W/mK (0 - 100 °C)	237	318	401
Linear coefficient of thermal expansion, 10^{-6} K^{-1} (0 - 100 °C)	23.5	14.1	17
Melting point, °C	660.4	1064.4	1083
Young's modulus, GPa	70.6	78.5	129.8
Tensile strength (soft), MPa	(50…90)	130	224
Tensile strength (hard), MPa	(130…195)	220	314
Poisson's ratio	0.345	0.42	0.343

The lattice structure of Cu is face-centered cubic (fcc) [82, p. 54] and illustrated in Fig. 3-1 (a).

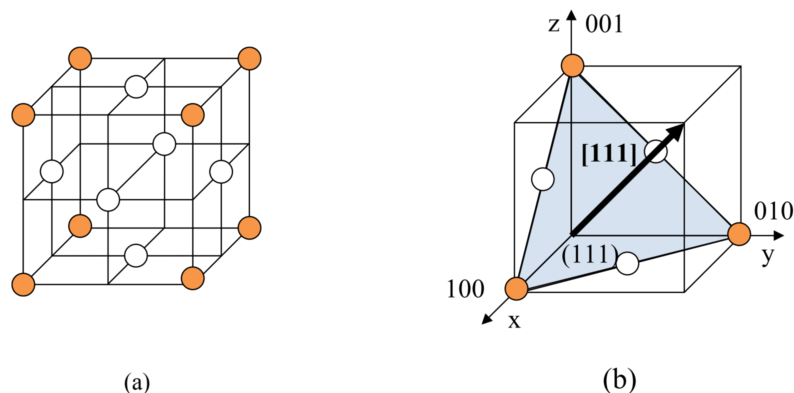

Fig. 3-1 Ordering of atoms in a face-centered cubic (fcc) elemental cell of Cu (a), Miller indices and (1 1 1) close-packed plane with [1 1 1] vector (b) (adapted from [84]**)**

Grains of any metal are separated by grain boundaries. There are low-angle (LAGB) and high-angle (HAGB) grain boundaries. Low angle grain boundaries feature misorientation angles lower than 5 ° [85] while high angle grain boundaries have misorientations higher than 5 ° (for fcc max. 65 °). Twin boundaries are not considered grain boundaries and feature very low grain boundary energy. They are typically generated by a stacking fault or by mechanical deformation. The twin boundary is planar as it is characterized by a crystallographic twinning plane. It features mirror symmetry between the original matrix and the twin [86]. The presence of twins influences the bondability of the samples [87]. The formation of twins makes Cu harder as planes slipping during the deformation becomes more difficult. This contributes to the mechanical strength of the future Cu-Cu interconnect [88]. Therefore, twin formation has to be investigated. Typical twin boundaries for electroplated Cu are formed by a 60 ° rotation around the <1 1 1> axis with {1 1 1} twinning plane (∑3 twin) [89]. Another twin is characterized by a 38.9 ° rotation around the <1 1 0> axis with {1 1 0} as a twinning plane (∑9 twin). Fig. 3-1 (b) presents the (1 1 1) plane and [1 1 1] vector.

Furthermore, mechanical properties are grain orientation dependent. Young's modulus or modulus of elasticity represents the relationship between the applied stress and the amount of corresponding strain. In other words, the higher Young's modulus is, the higher is the maximal stress at, which the material will respond elastically. The lower the elastic limit is, the less stress it is needed in order to cause a material fracture. Therefore, a higher Young's modulus fosters higher mechanical strength of the formed Cu-Cu interconnects after bonding. Young's modulus *E* for cubic crystal systems can be calculated for various orientations using equation (3-1) where [u v w] is a direction unit vector with a length of 1 and s_{ij} is elastic compliance constant [90].

$$E_{[uvw]} = (s_{11} - 2(s_{11} - s_{12} - \frac{1}{2}s_{44})(u^2v^2 + v^2w^2 + u^2w^2))^{-1} \qquad \textbf{(3-1)}$$

$$s_{11} = 1.49 \cdot 10^{-11}\ \frac{m^2}{N},\ s_{12} = -0.63 \cdot 10^{-11}\ \frac{m^2}{N},\ s_{44} = 1.33 \cdot 10^{-11}\ \frac{m^2}{N}$$

The energy backscatter diffraction (EBSD) method is commonly used to define the preferred crystallographic orientation (texture) of a material. Inverse pole figure (IPF) in this method is usually used to represent this texture. Fig. 3-2 shows Young's modulus, calculated using the formula (3-1)), overlaid on IPF texture plot for Cu where c_{ij} is elastic stiffness constant. The values correlate well with the literature [86].

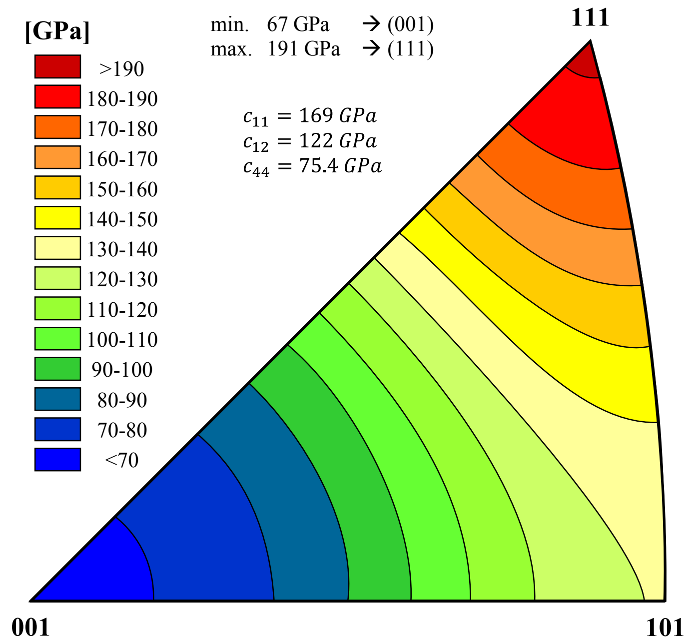

Fig. 3-2 Schematic view of IPF plot with the distribution of Young's modulus for cubic crystal system of Cu depending on crystal orientation

Grain size also influences the mechanical properties of Cu. Young's modulus and material's hardness tend to increase with decreasing grain size [91]. Higher Young's modulus and hardness values increase the shear strength of a bonded interconnect. Mobility of dislocations is restrained through a higher amount of grains and grain boundaries. Thus, more often changes in the directions of dislocation motion are needed to deform a material. Therefore, grain size and crystallographic orientation of the samples before bonding will be investigated in this thesis (chapter 5).

Having discussed Cu properties and microstructure, it is necessary to show the theoretical background for its oxidation process. Therefore, the types of Cu oxides and the mechanism of their formation are discussed in the next chapter.

3.1.2 Types of Cu oxides

There are two stable oxidation states of Cu: Cu_2O and CuO. Cu_2O is formed as soon as Cu is exposed to air. This layer sticks well on Cu, starts growing in form of islands and causes its reddish coloring. After long exposure times at room temperature CuO starts to grow. At elevated temperatures at 120 °C or higher, the surface appearance becomes darker. From 600 °C to 900 °C, CuO is formed, which color is black [84].

The behavior of Cu at room temperature in air can be described by chemical reactions (3-2) - (3-5). First Cu_2O layer forms in air [84], [92]:

$$4Cu + O_2 \rightarrow 2Cu_2O \tag{3-2}$$

$$2Cu + H_2O \rightarrow Cu_2O + H_2\uparrow \tag{3-3}$$

In the presence of humidity, Cu_2O reacts with water to form $Cu(OH)_2$ or CuO [84]:

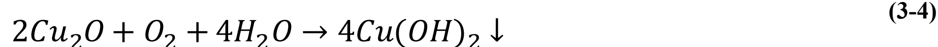

$$2Cu_2O + O_2 + 4H_2O \rightarrow 4Cu(OH)_2\downarrow \tag{3-4}$$

$$Cu_2O + H_2O \rightarrow 2CuO + H_2\uparrow \tag{3-5}$$

Fig. 3-3 presents a proposed model of Cu oxidation upon exposure to air [93].

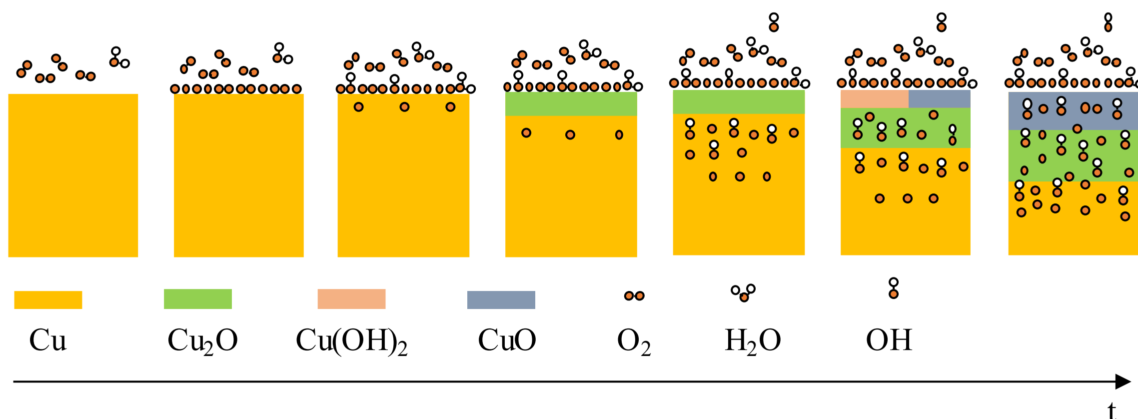

Fig. 3-3 Mechanism of Cu oxides growth according to [93]

According to [93], the oxidation process occurs towards the inner direction of Cu. Fig. 3-3 presents stages of the Cu oxide growth. First, O-containing compounds are adsorbed from air onto the Cu surface and start to penetrate in Cu in form of O- or OH-bindings. Second, Cu_2O is formed (detected after 10 min of air exposure) whereas O-containing compounds penetrate further. After that CuO and $Cu(OH)_2$ form after the reaction of O with Cu_2O. $Cu(OH)_2$ refers to a metastable oxidation state of Cu, which is in time transferred into CuO, too. Cu_2O with a thickness in the range of (1.2…1.8) nm is detected (XPS) already after the first 10 min of air exposure. After 500 h of air exposure, CuO is still not detected. CuO layer with a thickness of about 1.3 nm is detected at first after 700 h (29 days) of air exposure.

Conductivity and mechanical strength of the interconnect decrease with the oxidation of Cu. Higher bonding parameters and the inert gas atmosphere is needed to break through a thick oxide layer. Therefore, SAM passivation was chosen in order to protect Cu. It is important to understand SAM structure and types in order to choose the appropriate one. Adsorption and desorption mechanisms provide an understanding of SAM formation, as well as how it can be removed before bonding. Therefore, the next subchapter is devoted to these aspects.

3.2 Description of SAM structure, its adsorption and desorption mechanisms

3.2.1 SAM structure and types

SAM is an organic assembly formed by spontaneous adsorption of surfactants from an organic solvent on a certain substrate. Metals and metal oxides are usually used as a substrate because the adsorbates lower their surface tension [94]. As a result, closely packed SAM is formed. The monolayer can be adsorbed on the substrate surface through the liquid or the gas states. A substrate is immersed into the SAM-solution for 1 - 18 h for the adsorption from the liquid state [10], [19]. Isopropanol, ethanol or toluol are the most common solvents for SAMs. A SAM molecule typically consists of a head group, of a molecular backbone or chain and a terminal group schematically illustrated in Fig. 1-2 according to [49]. A head group must have a chemical affinity to a certain substrate in order to anchor to it. The SAM backbone provides lateral van der Waals interactions between the chains, which hold them in a "standing" state. The terminal group defines the monolayer surface properties. For instance, a $-CH_3$ or $-CF_3$ terminal groups provide hydrophobic, whereby -OH terminal groups provide hydrophilic properties to the surface [95].

Naturally, alkanethiols have all-trans conformation. All-trans conformation is a zig-zag form of hydrocarbon chain, which is caused by the rotation of C bonds. In this way, H atoms have minimal interaction with each other and the SAM molecule gains its minimal potential energy. The 3D model of 1-hexanethiol (C6) molecule is made in the software of Advanced Chemistry Development, Inc. (ACD/Labs) [96] and is presented in Fig. 3-4 (a). Knowing the lengths of the atomic bonds and the angles between them, as well as monolayer tilt to the Cu surface (12 ° [10]), the thickness of the SAM layer can be calculated. For example, the thickness of C6 SAM is approximately 0.8 nm.

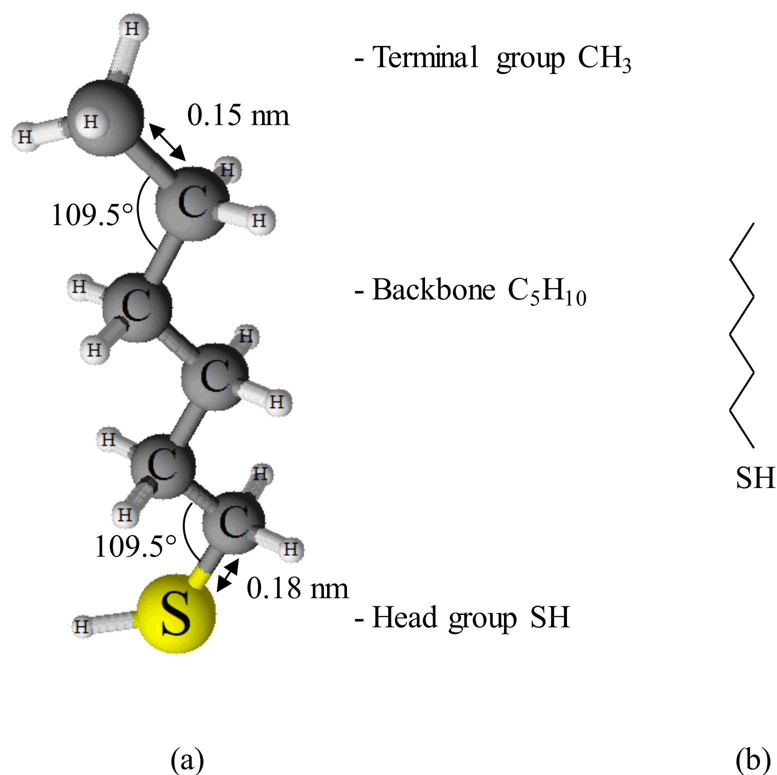

Fig. 3-4 3D Model of a 1-hexanethiol molecule with distances and angles between the atoms made in ACD/Labs software [96] **(a) and schematic symbol of 1-hexanethiol (b)**

Fig. 3-5 presents proposed SAM classification by head, backbone and terminal group types [95].

The first group is classified by a head group. In this work, alkanethiols are investigated because they and their derivatives are usually adsorbed by Au, Ag, Pd, Pt or Cu metals [97]. Alkanethiols belong to SAMs with a head group containing S compounds. Head groups with organosilicon compounds are formed on the hydroxylated metal oxides and are usually applied for patterning on transparent or non-conductive substrates [98]. Acid derivatives are adsorbed by metal oxides due to the chemical reaction between the acid and metal oxide, which results in salt formation [98]. The most common example for such a layer is Langmuir-Blodgett film.

The second group is classified by its terminal group. Commercially available SAMs usually contain $-CH_3$ terminal groups. These can be replaced or bound to various other end groups ($-CF_3$, -OH, etc.) with the help of special chemical processes and equipment [95]. Various terminal groups have different wettability. For instance, $-CH_3$ and $-CF_3$ make passivated substrate hydrophobic whereas -OH makes it hydrophilic.

The third group is classified by its backbone structure. Aliphatic and aromatic SAMs differ by their backbone structure. Both systems have their advantages and disadvantages. Aromatic systems are rigid and planar molecules, that are easy to modify using various end groups [99]. However, aromatic molecules with the same number of C atoms are reported to be more corrosive than aliphatic systems [100].

The fourth group of SAMs can be classified by their chain length. The length of a SAM backbone is defined by the number of C atoms in its backbone. If the quantity is higher than 9, then it is a long-chain thiol [48]. Monzo et al. investigated the corrosion of Cu stripes in mercaptan containing synthetic naphtha. The results revealed that only C2 and C3 cause Cu corrosion. Increasing the chain length almost terminates the corrosion of Cu by SAM species and transforms them into corrosion inhibitors [54], [100]. Long-chain SAMs are known for their better intermolecular interactions and, thus, their higher ordering and more long-lasting stability. Yet, SAMs with long-chain SAMs take a longer time to adsorb, as well as are more complicated to remove from the substrate [8].

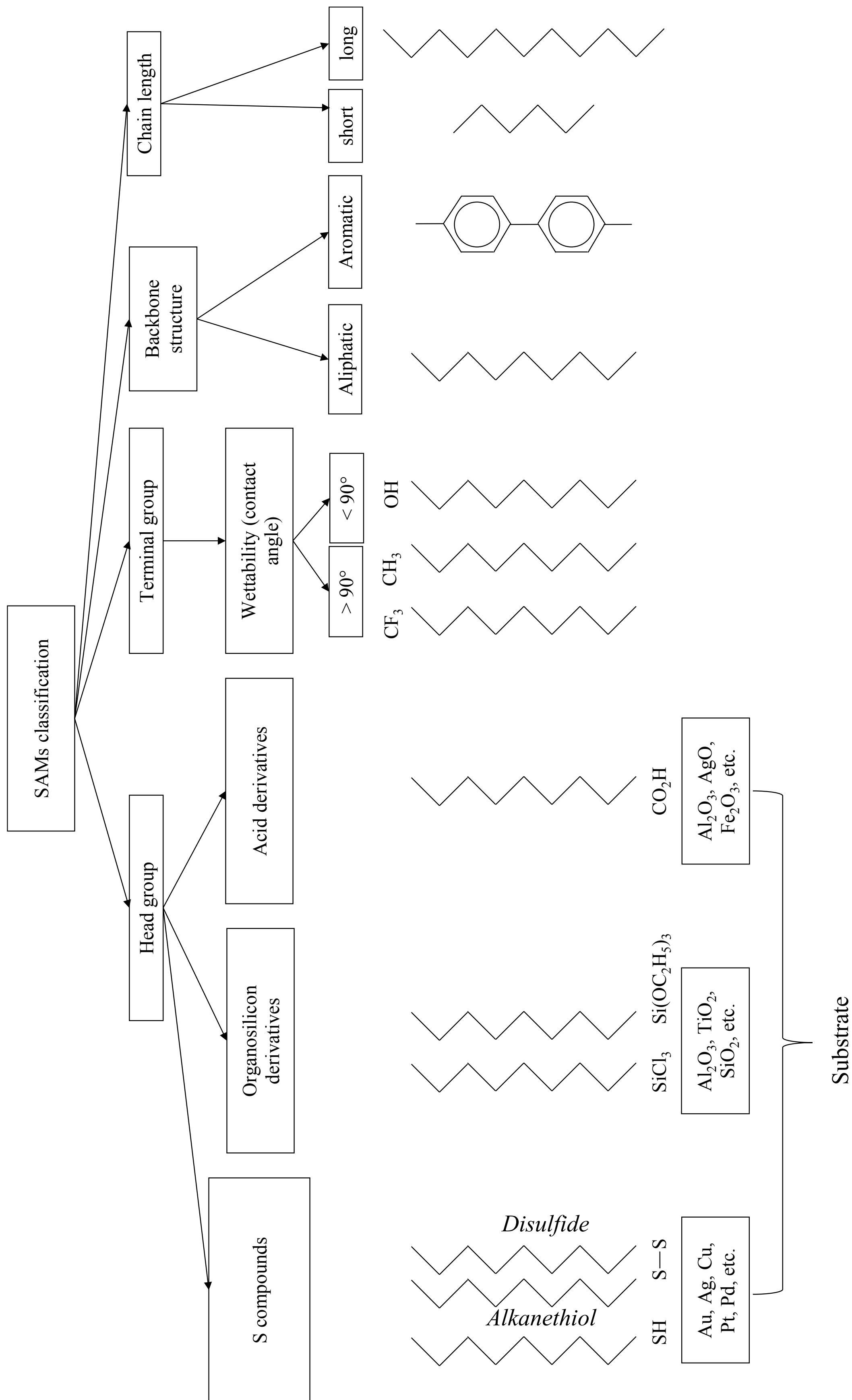

Fig. 3-5 Classification of SAM by head groups, terminal groups and by the molecular backbone structure (according to [95]**)**

Despite high intermolecular ordering, SAMs often contain extrinsic and intrinsic defects [10], [101]. Fig. 3-6 shows examples of such defects on the Au surface. Extrinsic defects are connected to the imperfections of the metal substrate. Grain boundaries, monoatomic step-edges [102], Au vacancy islands can impede the formation of ordered SAM structures. Impurities on the metal surface can be as harmful as impurities in the solvent or in the alkanethiols (the reagents), which already belong to the intrinsic defects. Another internal defect is caused by molecules with gauche conformations (Fig. 3-6, (a)). Thermodynamical phase transitions of SAMs from lying-down phase to standing-up phase belong to intrinsic defects. If SAM is adsorbed from different sides of a substrate, it can cause a defect on SAM crystal edges tilted in different directions.

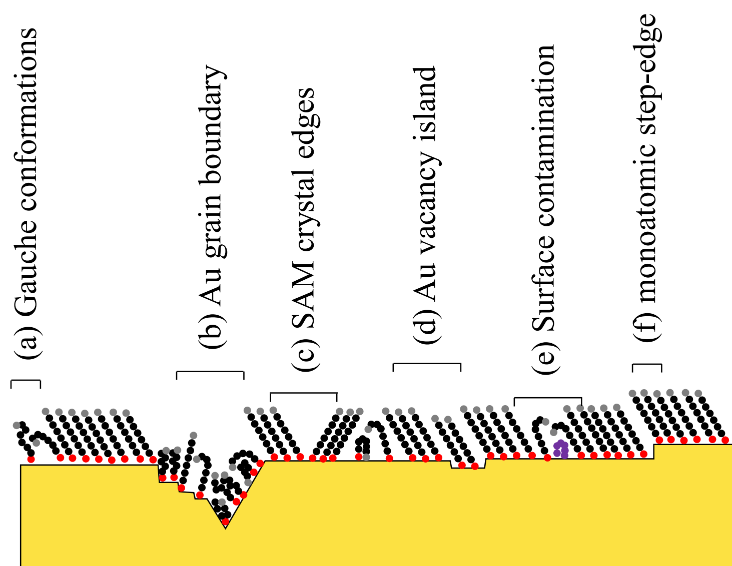

Fig. 3-6 Possible types of defects in SAM caused by (a) gauche conformations, (b) Au grain boundaries, (c) SAM crystal edges, (d) Au vacancy islands, (e) surface contaminations and (f) Au monoatomic step-edges (adapted from [10], [101]**)**

Having described SAM structure and types, it is important to understand the mechanisms of its adsorption and desorption, which is discussed in the following chapter.

3.2.2 Adsorption and desorption mechanisms

Fig. 3-7 shows that self-assembly is a combination of intermolecular and intramolecular forces. ΔE_{ads} is adsorption energy, ΔE_{hyd} is the energy between the hydrocarbons, referred to as the van der Waals forces, ΔE_{corr} reflects the corrugating potential of the substrate, ΔE_g is the energy of gauche defects, which are defined by disordered non-conformational molecules [98], [103].

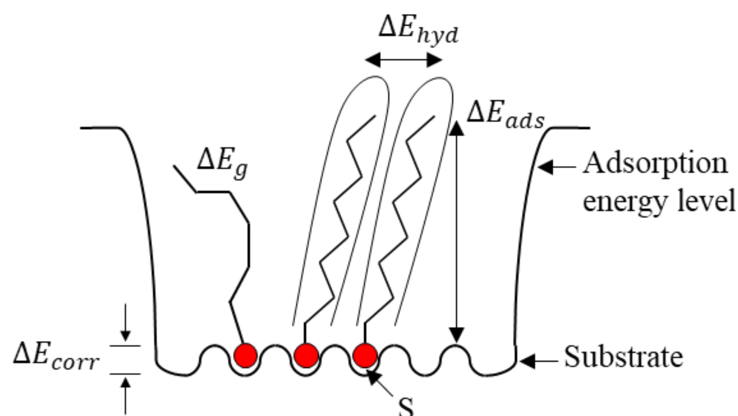

Fig. 3-7 Schematic illustration of intermolecular and intramolecular energies of the adsorbed SAM where ΔE_{corr} is corrugation substrate potential, ΔE_g is gauche defect energy or variation from the energy of a stretched chain, ΔE_{hyd} is the energy between the organic backbones, ΔE_{ads} is adsorption energy (according to [103]**)**

SAM adsorption theory is described in [98] and is based on a combination of diffraction measurement methods, atomic force and scanning probe microscopies.

Fig. 3-8 presents stages of SAM adsorption on the example of 1-hexanethiols on the Cu surface. SAM is commonly adsorbed on a substrate from the solution with a certain SAM concentration (1 – 10 mM). There are two adsorption types present during the process: physisorption and chemisorption. Physisorption describes weak adsorption between SAM and substrate, which is mainly governed by van der Waals forces. Chemisorption describes the formation of a strong chemical bond (formula (2-1)). There are several stages of SAM adsorption [104]. At first, separate SAM molecules are physisorbed on the substrate with a molecular axis parallel to the surface (Fig. 3-8, (a)). Such physisorbed molecules are mobile. This state is determined as a *lying-down* or *striped* phase, which is characterized by low density. Full coverage of the Cu surface with lying-down immobile chains (Fig. 3-8, (b)) is reported to be very fast, in the range of several minutes. The next step is straightening of the already chemisorbed and immobile SAM chains, which is defined as the *standing-up* phase of high-density hydrocarbon chains. During these processes, the islands of standing-up molecules grow, whereas the area with lying-down molecules shrinks (Fig. 3-8, (c)). This process takes a longer time, up to several hours. At the end a completed densely packed monolayer is formed (Fig. 3-8, (d)). The last stage of the process is the reorientation of chains due to intermolecular forces to make all-trans conformation.

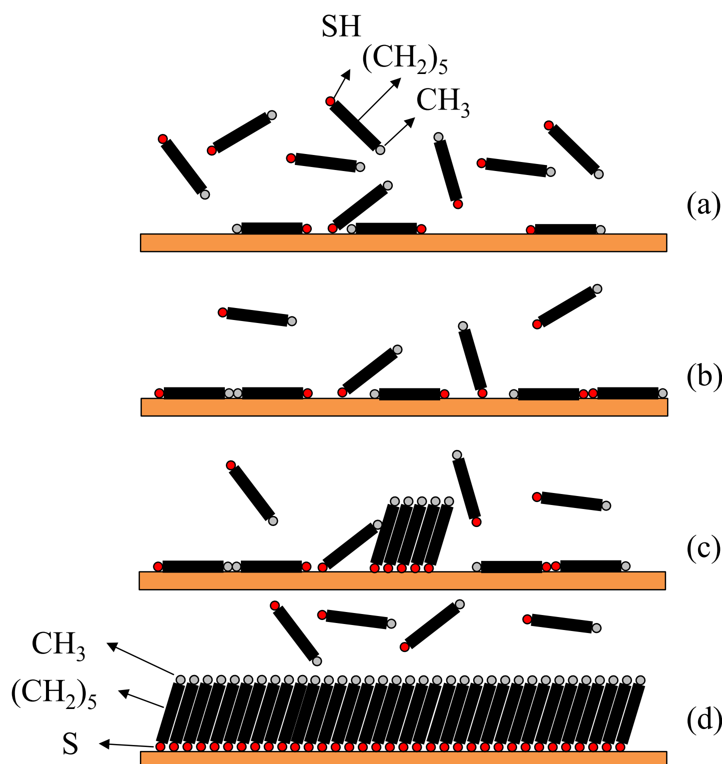

Fig. 3-8 Phases of C6 SAM formation on Cu surface: mobile phase (a), immobile lying-down or striped phase (b), the coexistence of stand-up and lying-down phases (c) and completed monolayer (d). Adapted from [104], [105]

Desorption of self-assembled monolayers has been widely investigated. Thermal desorption spectroscopy (TDS) has been performed in order to distinguish the temperature, at, which SAM desorption occurs. However, continuous heating rate (i.e. 2 °C min^{-1} [80]) during TDS measurements may also have an impact on the SAM desorption. This would explain why SAM does not spontaneously desorb upon application of its “desorption temperature”, provided by TDS. This would explain the need for annealing for a certain time at a constant temperature (i.e. at 250 °C for 30 min [8]) in order to fully remove SAM from the Cu surface, which has not been investigated in literature in detail.

Fig. 3-9 shows schematic drawings of SAM chemical compounds in chemisorbed and physisorbed states, used for explanations of adsorption and desorption mechanisms in more detail later on.

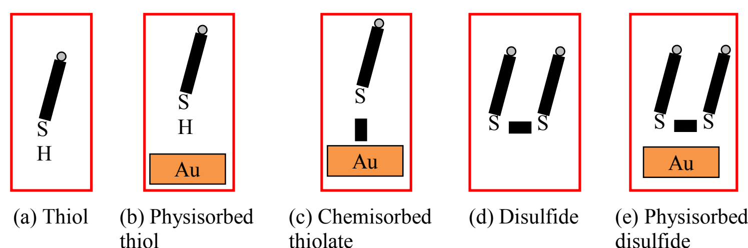

Fig. 3-9 Schematic representation of chemical compounds taking part in adsorption and desorption processes

Fig. 3-10 presents the SAM desorption model proposed by Nishida et al. [106], which was also confirmed by other researchers [80], [107]. It has been reported that alkanethiols can

transform to disulfides in solvents (Fig. 3-10, (a)). Not only chemisorbed alkanethiolates are detected on Au after the immersion process, but also disulfides and weakly bound alkanethiols, physisorbed on its surface (Fig. 3-10, (b)). Previous reports suggest that low amounts of such species (≥ 5 %) in alkanethiol solution do not impede the formation of closely packed monolayer and its properties. Therefore, it is important to pay attention to working with fresh solutions.

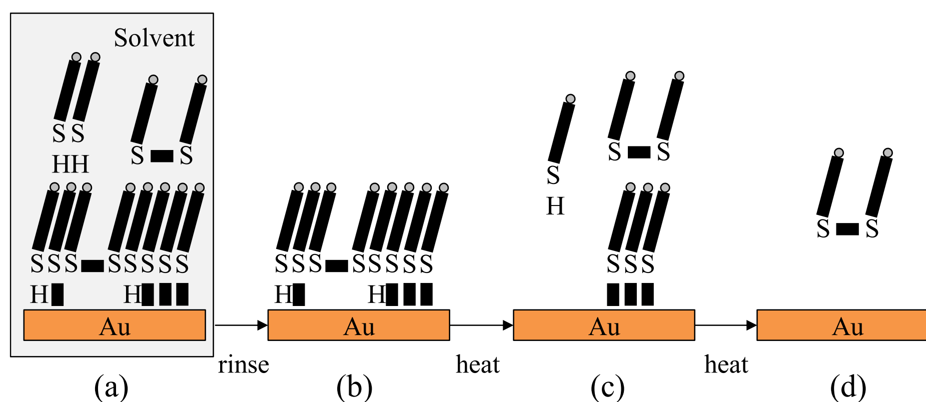

Fig. 3-10 The adsorption and desorption mechanisms of the alkanethiols on Au (according to [106], [107]**) showing the immersion of samples and the SAM adsorption from the solution (a), the rinsing of the samples with a solvent (b), the heating of the samples and the desorption of the weakly adsorbed species (c), the increasing temperature, the formation of disulfides and their desorption from the metal surface (d)**

According to [80], [106], the formation of thiolates on the metal surface can be assigned to a fast chemical reaction (3-6). The formation of disulfides on the metal surface is considered to be not only the result of adsorption from the solution but is also a result of a slow reaction of self-exchange between the thiolates (3-7).

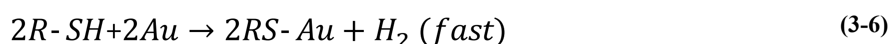

$$2R\text{-}SH{+}2Au \rightarrow 2RS\text{-}Au + H_2\,(fast) \quad \textbf{(3-6)}$$

$$RS\text{-}Au + RS\text{-}Au \rightarrow RS\text{-}SR + 2Au\,(slow) \quad \textbf{(3-7)}$$

After carrying out the TDS analysis three desorption peaks were detected: at approximately 37, 57 and 227 °C. The first peak is related to weakly adsorbed (physisorbed) monomers of alkanethiols and the second peak is assigned to physisorbed disulfides (Fig. 3-10, (c)). And the last peak at the highest temperature is assigned to desorption of disulfides (Fig. 3-10, (d)), which were formed from chemisorbed alkanethiolates after the start of the desorption process that is referred to as slow reaction (3-7).

Desorption energies for chemisorbed species are the same for different kinds of alkanethiols and are in the range of (124…128) kJ/mol. The activation energies for desorption of weakly physisorbed SAM species are reported to be 79 and 150 kJ/mol for C6 and C16 SAM, respectively. This means that C16 SAM species are harder to remove from the Cu surface before bonding, although this type of SAM should have better protection against oxidation. Therefore, short-chain (C6) SAMs have been chosen for most of the storage and bonding experiments in this thesis. In one of the storage experiments in air, the protective functions of C6 will be compared to C16 (chapter 6.2.1.2).

The choice of Cu surface preparation is as important as the choice of the bonding technique. The fundamentals of TC bonding are well known because it is an established bonding method [108]. US flip-chip bonding is a much less investigated method, especially for Cu-Cu interconnects. Therefore, the next chapter presents the theoretical background, needed to understand the results, idea and important considerations of US flip-chip bonding with SAM passivation.

3.3 US bonding process

3.3.1 Similarity between the US flip-chip bonding and wire bonding

TC and US bonding of metals in a solid-state is based on the deformation and the atomic diffusion processes. One of the ways to optimize the bonding parameters in TC bonding is to introduce a new form of energy. US power provides the possibility to decrease applied temperatures (150 °C) and pressures (150 MPa) of TC bonding [109]. US bonding is a low-temperature bonding method with short bonding times (≤ 2 s [19], [110], [111]), which comprises wire bonding and US flip-chip bonding. Wire bonding is an established bonding method, which has been intensively investigated in the literature [54], [112]. The wire bonding process, investigated by F. Osterwald in detail, comprises four phases of interconnect formation: pre-deformation phase, cleaning phase, deformation phase and volume interaction phase [113]. The same progression can be, possibly, valid or very similar to US flip-chip bonding of microbumps as well.

In the **pre-deformation phase**, only the "touch-down" force is applied to the wire without the application of US power. During the pre-deformation phase, it is important to set the optimal bonding pressure. Low deformation results in a small contact area, which can lead to the very high density of ultrasonic energy applied on the approaching asperities of the contacts. Too high ultrasonic density can lead to the destruction of an interconnect. Too high pre-deformation is also harmful. Increasing the dislocation density can harden metal too much so that no further deformation is possible. The higher is pre-deformation, the longer is the following cleaning phase.

The **cleaning phase** is a period, during, which US exposure does not cause deformation [113, p. 47]. The higher is the contamination level, the longer is the cleaning phase. The lower is ultrasonic energy, the longer is the cleaning phase [112]. Using too high US energy decreases the cleaning phase time. This is connected to the damping of US energy by contaminations. After breaking through the contamination layer, US energy reaches its set value, and deformation starts. During the cleaning phase, contaminations on the partner surfaces are displaced.

Higher bonding force after the cleaning phase decreases metal softening in contrast to higher US power [112]. During the **deformation phase,** the relatively clean surfaces come into contact. This causes the formation of microweldings, which, in turn, dampen the ultrasonic energy. During the deformation, metal hardens till it is incompressible. When critical deformation and maximum dislocation density are reached, US power starts to transform into

the rubbing heat. This leads to the activation of recovery and recrystallization processes. Afterward, the metal can deform again.

The **volume interaction phase** is characterized by appearing of a big area interconnect, which forms after diffusion processes through the grain boundaries of contact materials. The energy for the further diffusion processes is provided by the further supply of the US power. The deformation phase itself with microweldings is not enough for the formation of the high-quality interconnects. The reason is that induced dislocations cause tension in the contact area, which can cause cracks. In order to avoid such high tension in the contact area, the atoms have to go through the relaxation phase. This means that the volume interaction phase is accomplished mainly through the atomic interdiffusion of the contact surfaces.

Besides understanding the internal microstructural changes of Cu-Cu interconnect during US bonding, it is hard to underestimate the importance of chip design in US flip-chip bonding, which is discussed in the following chapter.

3.3.2 The impact of the chip design on the US flip-chip bonding results

Unlike the TC bonding method, one of the most important factors in US flip-chip bonding is chip design. There is no standardization for suitable chip designs, as the US flip-chip bonding has not been widely applied and investigated in the industry. Some of the important factors about chip design for US bonding from literature are summarized below [109]:

1. Microbump height
2. Microbump quantity
3. Chip size
4. Chip thickness

Arai et al. [114] report that 20 µm high bump are better than 5 µm and 40 µm high bumps. Too low height does not allow deformation in order to compensate the tilt variation problem. However, too high values of height cause increased ultrasonic damping, which results in the lower transfer of ultrasonic energy [115]. The heights of 8-10 µm were also reported to be used for thermosonic bonding [19], [116]. Yamatsu et al., who work with the same equipment, as used in this study, uses 20 µm high Cu microbumps with 15 µm of SnAg on top [117].

Microbump quantity is an important factor in flip-chip US bonding [109]. If the bonding head and stage are not planar, the distribution of bonding force is not uniform. If the distribution of force is not uniform, the bonding of the interconnects is not simultaneous. While some interconnects reach a good bond, other microbumps only come to the cleaning phase. When the latest microbumps come to the volume interaction phase, the former interconnects can be destroyed because of overbonding [112].

Thin chips have an advantage for US bonding due to the better transfer of US energy. A thicknesses of (100…350) µm are reported [115], [118], [119]. Handling of thin chips is more challenging compared to standard chips with a thickness range (650…700) µm. An appropriate amount of ultrasonic energy has to be applied depending on the chip thickness.

To sum up, TC and US bonding methods both have advantages and disadvantages. TC, for instance, is an established bonding method, where the most important processes are Cu-Cu interdiffusion and deformation caused by the application of heat and bonding pressure. SAM desorption in the inert gas atmosphere before TC bonding has to be investigated systematically. US bonding of dies has been less investigated but provides an additional influence factor (US energy), which can be used to remove SAM before bonding in air and form a contact within a second.

The following chapter presents the description and characterization of the used samples, passivation procedures, bonding equipment and characterization methods.

4 Materials and methods

4.1 Description and characterization of the samples

In this chapter the samples, used for further experiments, are described. Typically, both top and bottom dies have bumps, but in this study bumps on the top die and full Cu on the bottom die are used. This is done to exclude possible causes of alignment issues, which lead to false interpretations of the shear strength due to change in the bonding area. Schematic presentation of the top (flipped) and bottom (substrate) dies is highlighted in Fig. 4-1.

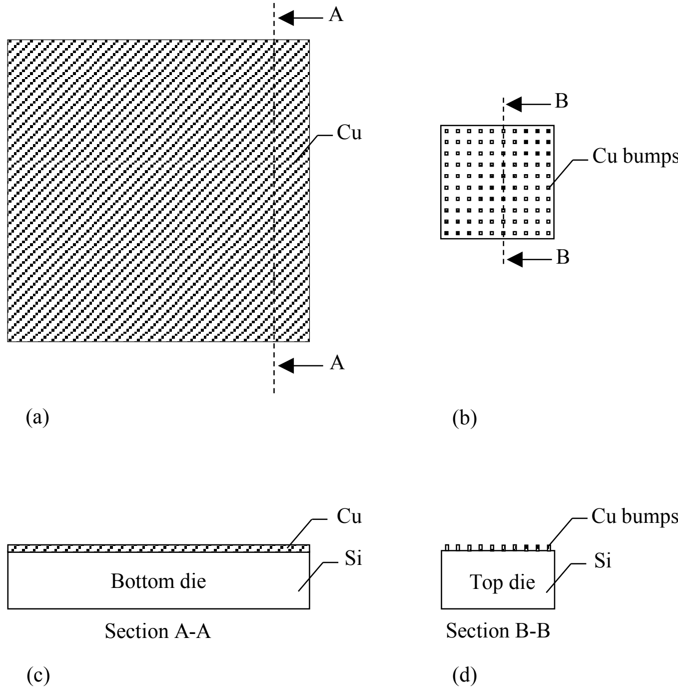

Fig. 4-1 Schematic top view of the bottom (a) and top (b) dies, cross-sectional view of the bottom (c) and top (d) dies

Two types of designs are developed for thermocompression (TC) bonding at 250 °C in Ar gas atmosphere (sample A) and ultrasonic (US) bonding at (30…150) °C in air (sample B). Characteristic parameters of samples A and B are shown in Fig. 4-2, Tab. 4-1, Tab. 4-2.

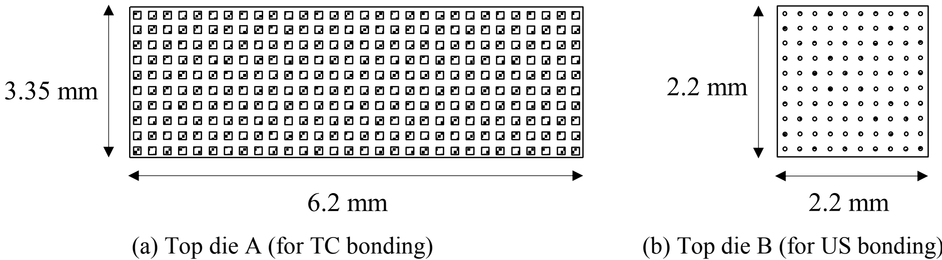

(a) Top die A (for TC bonding) (b) Top die B (for US bonding)

Fig. 4-2 Arrangements of bumps on the top dies A (a) and B (b)

The design of the top die A has a pitch of 130 μm and a bump size of 100×100 μm^2. It was chosen from the available test designs at the Fraunhofer Institute for Reliability and

Microintegration (Fraunhofer IZM, Berlin) in order to have a regular distribution of bumps across the chip area. Top die B design was developed at Fraunhofer IZM "All Silicon System Integration Center Dresden – ASSID" (Fraunhofer IZM-ASSID, Dresden). The aim was to develop a design suitable for fundamental US flip-chip bonding experiments, which comprise the sufficient microbump height, the low chip size, as well as the low number of microbumps. The effect of chip design on the bonding quality is explained in subchapter 3.3.2 in detail.

Tab. 4-1 Characteristic parameters of the designs and measured microbump properties for the top die A and top die B

Main top die parameters	(a) Top die A	(b) Top die B
Manufacturer	Fraunhofer IZM, Berlin	Fraunhofer IZM-ASSID, Dresden
Die size, mm^2	3.35 × 6.2	2.2 × 2.2
Bump size, μm^2 or bump diameter, µm	100 × 100	50
Bump form	square	round
Bump pitch, µm	130	150
Bump quantity	720	100
Bump matrix	18×40	10×10
Bonding area, mm^2	7.2	0.196
Planarization method	fly cutting at Fraunhofer IZM, Berlin	fly cutting at Fraunhofer IZM, Berlin
Roughness, nm	$R_a = 60 \pm 5.2$, $R_z = 439 \pm 31.1$	$R_a = 9 \pm 0.85$, $R_z = 110 \pm 8.1$
Meyer hardness, GPa	2.3 ± 0.3	2.68 ± 0.4
Young's modulus, GPa	104 ± 10.8	131.08 ± 10.4

Tab. 4-2 Characteristic parameters of the bottom die A and bottom die B

Bottom dies parameters	Bottom die A	Bottom die B
Manufacturer	Fraunhofer IZM-ASSID, Dresden	Fraunhofer IZM-ASSID, Dresden
Chip size, mm × mm	10 × 10	10 × 10
Cu thickness, µm	2	2
Cu type	ECD	ECD
Planarization method	CMP	-
Roughness	$R_a = 0.7 \pm 0.05$ nm, $R_z = 6 \pm 0.4$ nm	$R_a = 9 \pm 0.75$ nm, $R_z = 60 \pm 5.9$ nm
Meyer hardness, GPa	2.05 ± 0.09	2.2 ± 0.17
Young's modulus, GPa	109.9 ± 10.2	122.2 ±13.5

The average roughness values (R_a) and the maximum roughness values (R_z) are measured by confocal microscope µSurf (NanoFocus) with a lens 320-L ×50. The maximum vertical resolution of this lens is 4 nm. Estimation of roughness depends on the choice of cutoff wavelength according to evaluation standards of DIN EN ISO 4288 and ASME B46.1. If the estimated $R_a \leq 0.02$ µm, the total measurement distance should be $l_n \geq 0.4$ mm with a cutoff wavelength $\lambda_c = 0.08$ mm. This requirement is applicable for bottom dies and top die B. If

estimated $0.02 \leq R_a < 0.1$ µm, the total measurement distance should be $l_n \geq 1.25$ mm with a cutoff wavelength $\lambda_c = 0.25$ mm. This requirement is applicable for top die A. To guarantee such a high length for small microbumps, zig-zag measurement profiles have been used (Fig. 4-3). The lengths of the profiles are $l_n = 2.2$ mm for the top die A in Fig. 4-3 (a) and $l_n = 434$ µm for the top die B in Fig. 4-3 (b). Three microbumps for each top die type and three bottom die types per each bottom die type were measured. The roughness values of the microbump A ($R_a = 60 \pm 5.2$ nm) are much higher in comparison to the microbump B ($R_a = 9 \pm 0.85$), although both samples underwent the fly cutting at Fraunhofer IZM (Berlin). This can be caused by the differences between the fly-cutting procedures.

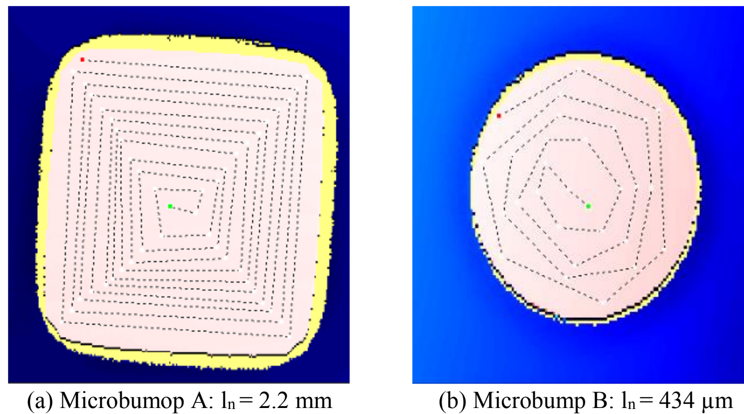

(a) Microbumop A: $l_n = 2.2$ mm (b) Microbump B: $l_n = 434$ µm

Fig. 4-3 Zig-zag measurement profiles of microbumps roughness of the microbump A (a) and microbump B (b) according to DIN EN ISO 4288 and ASME B46.1

Meyer hardness test by Bruker Nanoindenter PI88 with Berkovich tip was carried out by professorship Materials and Reliability of Microsystems at TU Chemnitz. It provided information about the initial hardness and Young's modulus of the samples by penetrating 200 nm of the Cu surface using the Berkovich tip. 15 points per each top die type and 25 points per each bottom die type were assessed.

Fig. 4-4 shows the arrangement of layers and layer thicknesses for the top and bottom dies.

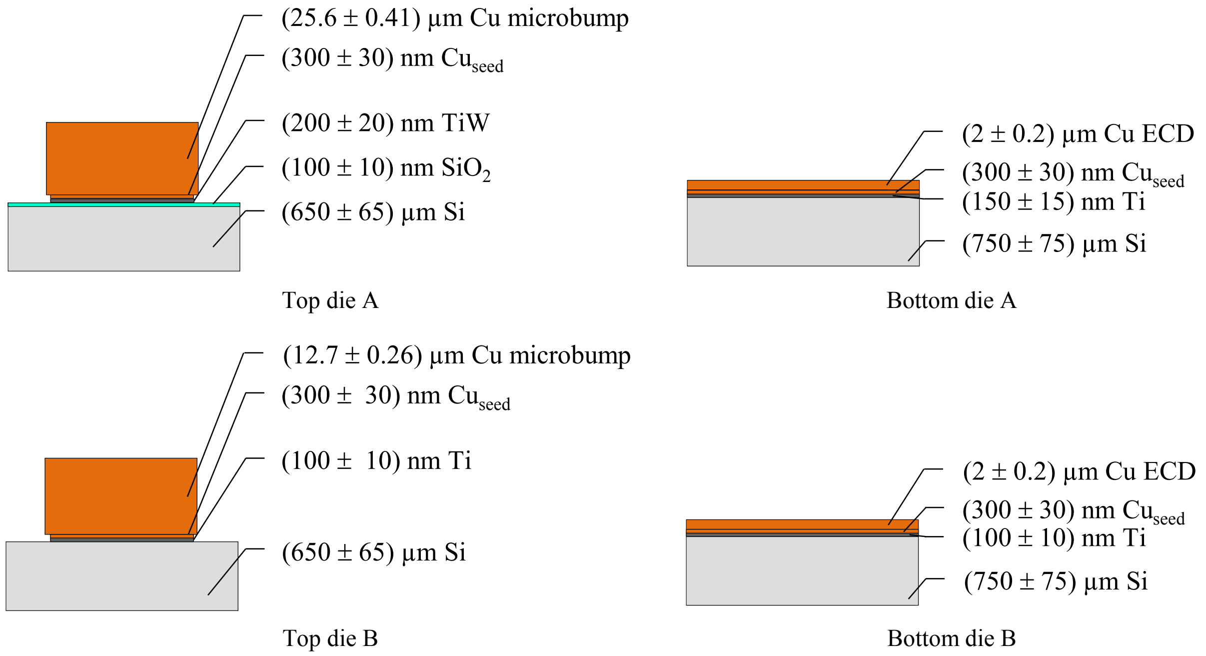

Fig. 4-4 Layer thicknesses of the top dies with Cu microbumps and bottom dies fully covered with Cu with standard deviations

Fig. 4-5 presents SEM images of Cu microbumps of top dies A and B from the top view and cross-section view.

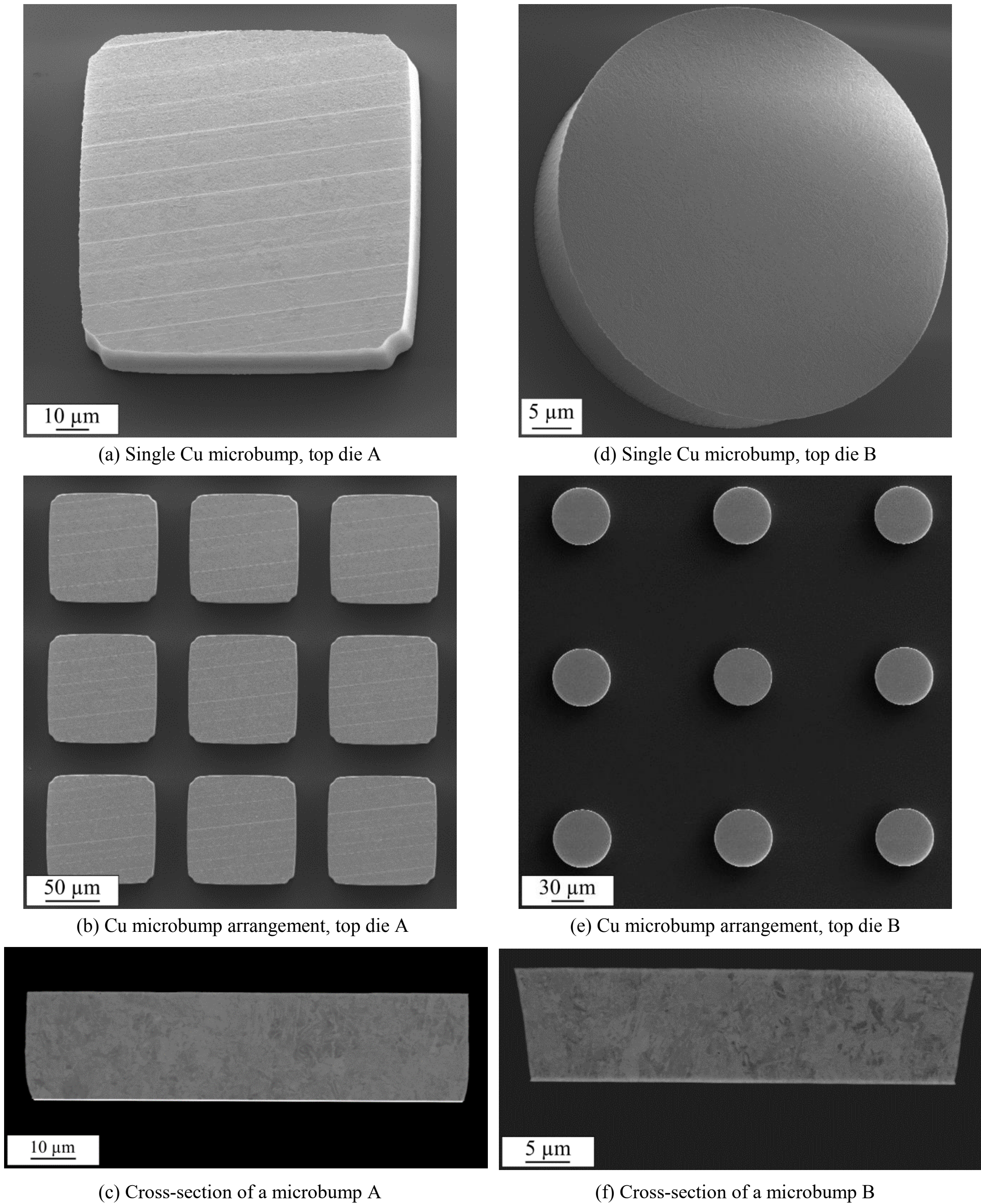

(a) Single Cu microbump, top die A
(d) Single Cu microbump, top die B
(b) Cu microbump arrangement, top die A
(e) Cu microbump arrangement, top die B
(c) Cross-section of a microbump A
(f) Cross-section of a microbump B

Fig. 4-5 SEM images of Cu microbumps from the top view (a, b, d, e) and of Cu microbumps from the cross-sectional view (c, f)

Fig. 4-6 highlights the fabrication of Cu microbumps using lithographic patterning and electroplating. A photoresist is deposited on the Cu seed layer (Fig. 4-6, (a)), followed by its patterning by application of a mask and exposure to ultraviolet light. Afterward, irradiated regions (in the case of the positive photoresist) are dissolved in a developing solution (Fig. 4-6, (b)). This process is followed by Cu electroplating till the target height is achieved (Fig. 4-6, (c)). Fig. 4-6 (d) shows the following resist stripping. The last fabrication steps are

etching of Cu seed and Ti layers, whereby different chemical etchants are used for each of the metals. Complete removal of the Cu seed layer is important in order to avoid short circuits. At the same time, the surface cannot be overetched, because this may have an essential influence on the side-wall profile. The dashed lines in Fig. 4-6 (e), (f) show how Cu seed and Ti etchants affect the form of a microbump. After transportation of samples to Fraunhofer IZM (Berlin), the area between the microbumps is filled with polymer (Fig. 4-6, (g)) and then the fly cutting procedure takes place (Fig. 4-6, (h)). Fly cutting is a crucial step in order to provide a uniform distribution of bump heights across a wafer or a chip and to decrease Cu roughness [120], [121].

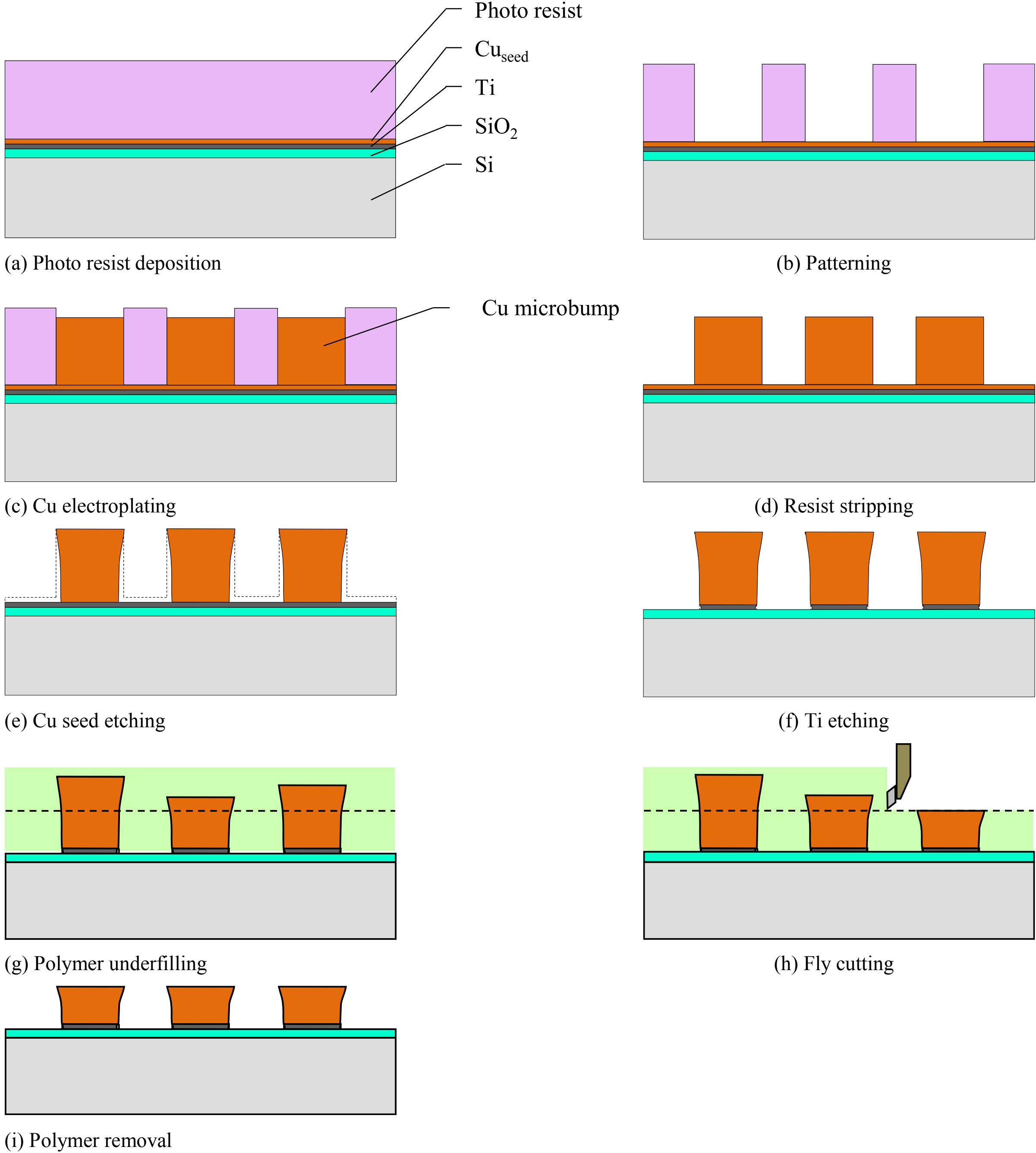

Fig. 4-6 Stages of through-mask plating to fabricate Cu microbumps (according to [122]) with a following fly cutting procedure

The distribution of microbump heights after fly cutting across each wafer and each chip is presented in Fig. 4-7 - Fig. 4-8. SEM images of Cu microbumps of the top dies A and B are

presented in Fig. 4-5. Wafer A shows a 1.2 µm difference of bump heights, whereas a single chip demonstrates a height deviation of (0.1 ± 0.04) µm. Microbumps of the wafer B differ in 0.8 µm, the height deviation across a single die is (0.1 ± 0.03). The wafers are diced into chips using the Stealth Dicing™ process (laser dicing). This process exhibits a clean Cu surface without defects in contrast to dicing with a normal saw using water.

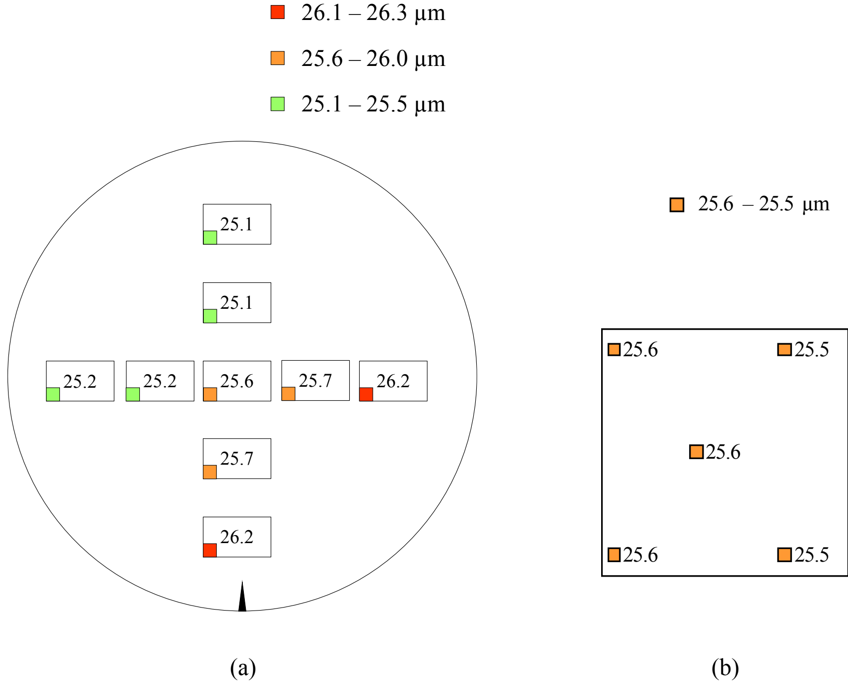

Fig. 4-7 Distribution of bump heights (in µm) on the wafer with samples A (a) and one chip (b) from the wafer middle

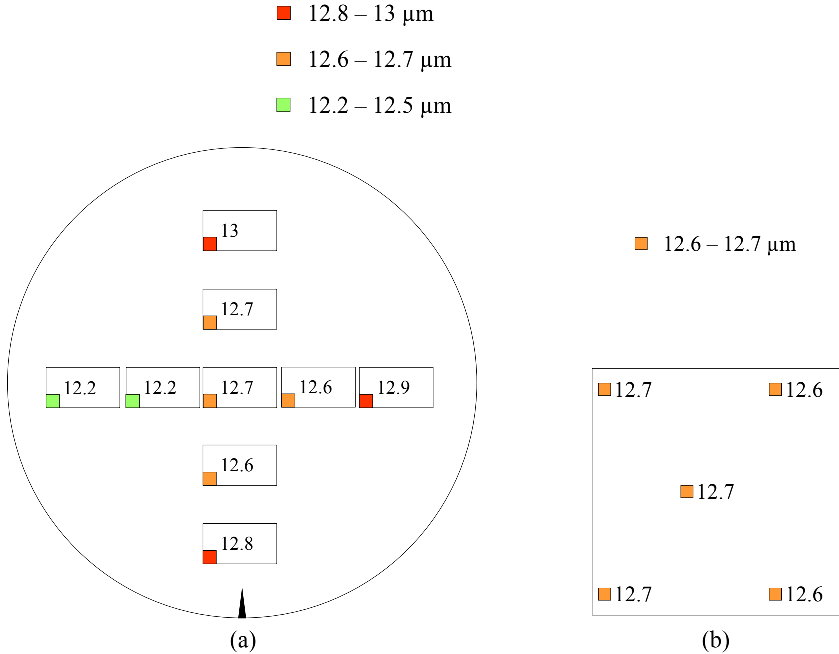

Fig. 4-8 Distribution of bump heights (in µm) on the wafer with samples B (a) and one chip (b) from the wafer middle

4.2 Passivation of the Cu surface with SAM

Passivation of Cu surface is performed in two different ways: in Ar gas atmosphere and air conditions.

In the first case, passivation is carried out in a glove box system Braun (Labstar) with oxygen content O < 0.5 ppm. The glovebox system was provided by the Institute of Semiconductors and Microsystems (Chair of Microsystems) at TU Dresden. All liquids are purged with Ar before the passivation. First, samples are etched with dilute H_2SO_4 10 % for (5…20) s, followed by rinsing with deionized water (DI water) and ethanol (Normapur, 99 %). After this, the samples are immersed for 2 h into the solution of 1-hexanethiol (C6, Sigma-Aldrich) or 1-hexadecanethiol (C16, Sigma-Aldrich) diluted with ethanol to the concentration of 1 mMol. It has been proved that two hours of immersion time is enough for a dense monolayer to form [54]. This was followed by taking out of the samples and rinsing them with ethanol to remove the unbonded S atoms on the Cu surface. The procedure was finished by drying the samples in the Ar gas atmosphere.

In the second case, passivation is performed in a laboratory clean room in air. The samples are etched with a dilute HCl 2 % (250 ml DI water and 15 ml HCl, 37 %, Sigma-Aldrich) for 3-5 min, followed by the rinse with 2-Propanol (Wako, 99 %). After that, the samples were immersed for 2 h into the solution of 1-hexanethiol (C6, Sigma-Aldrich) diluted in isopropanol to 1 mMol with the addition of 4 ml per liter of glacial acetic acid (Wako, 99.7 %) to etch away the Cu oxide formed during the air exposure [68]. The procedure is terminated by taking out the samples and rinsing them with isopropanol and drying them with N_2 gas.

In this study, two sample types are compared to each other: with SAM (SAM) and without SAM (no SAM) passivation. In the first case, a sample undergoes etching and passivation in the Ar gas atmosphere or air. In the second case, a sample is exposed only to etching in the same environment as passivation.

In order to characterize the SAM passivation effect on the chemical composition of the Cu surface, different techniques are used, which are described in the next chapter.

4.3 Characterization of SAM protective capability

Various techniques are used to investigate the SAM passivation quality and its degradation rate. Common methods to characterize SAM are the contact angle (CA) technique for surface wettability measurements, X-ray photoelectron spectroscopy (XPS) and infrared spectroscopic ellipsometry (IRSE) to yield chemical composition of the surface [61], [63], [74], [123].

4.3.1 Contact angle (CA) measurement

The sessile drop contact angle (CA) method provides information about the wettability of the surface. As Cu is a metal with high surface energy, clean freshly deposited Cu is hydrophilic. Knowing, that SAM passivated Cu surface becomes highly hydrophobic, that oxidized Cu surface exhibits hydrophilic properties, provides an instrument for characterization of the

passivation quality and degradation rate of SAM at various conditions. Fig. 4-9 shows the example of a water drop on a highly hydrophobic Cu surface, passivated with SAM.

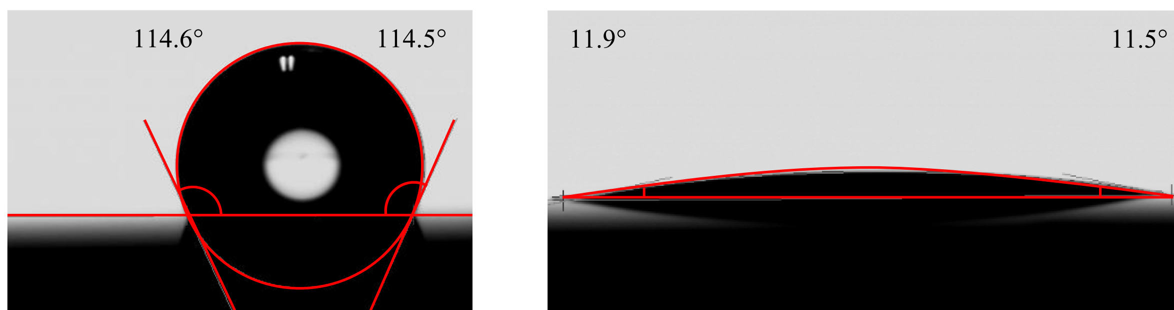

Fig. 4-9 A drop of liquid on the highly hydrophobic Cu surface with SAM (left) and the hydrophilic surface of freshly sputtered Cu surface (right)

The measurements were held using goniometer OCA-20 (DataPhysics). The volume of one drop was kept at 1 μm. Each sample was analyzed with 7 drops of deionized (DI) water. At least two samples were taken for each parameter set (14 drops). The maximal measured standard deviation is ±1.3 °. For these experiments, bottom dies fully covered with Cu were used (without microbumps).

4.3.2 X-ray photoelectron spectroscopy

X-ray photoelectron spectroscopy (XPS) yields information about the chemical composition of the surface. XPS provides precise data about the presence and state of SAM on the Cu surface. This is connected with a high surface sensitivity of the method, which penetrates only into (5…10) nm of a solid surface. Tab. 4-3 presents main measurement parameters of three XPS systems used in this study: Multiprobe® surface analysis unit (Omnicron NanoTechnology GmbH, Institute of Semiconductors and Microsystems, Chair of Semiconductor Technology, TU Dresden), PHI ESCA 5700 (Physical Electronics, Institute of Semiconductors and Microsystems, Chair of Microsystems, TU Dresden) and JPS-9200 (Jeol, School of Engineering, Department of Electrical Engineering and Information Systems, The University of Tokyo).

Tab. 4-3 Main measurement parameters of the used XPS systems

Parameters / XPS system	**Omnicron NanoTechnology**	**Physical Electronics**	**Jeol**
Target	Al	Al	Mg
Vacuum ($\times 10^{-7}$ Pa)	0.11	0.39	1.9
Filament current (mA)	20	19	10
Filament voltage (kV)	15	13	10

The surface of interest is bombarded by X-rays, which results in emitting of photoelectrons due to the photoelectric effect. The kinetic (KE) and binding energies (BE) can be measured in eV. These energies of the yielded intensity peaks usually correspond to certain atomic bindings seen on the surface.

Fig. 4-10 presents a wide XPS spectrum of the Cu surface where peaks correspond to chemical elements present on the surface.

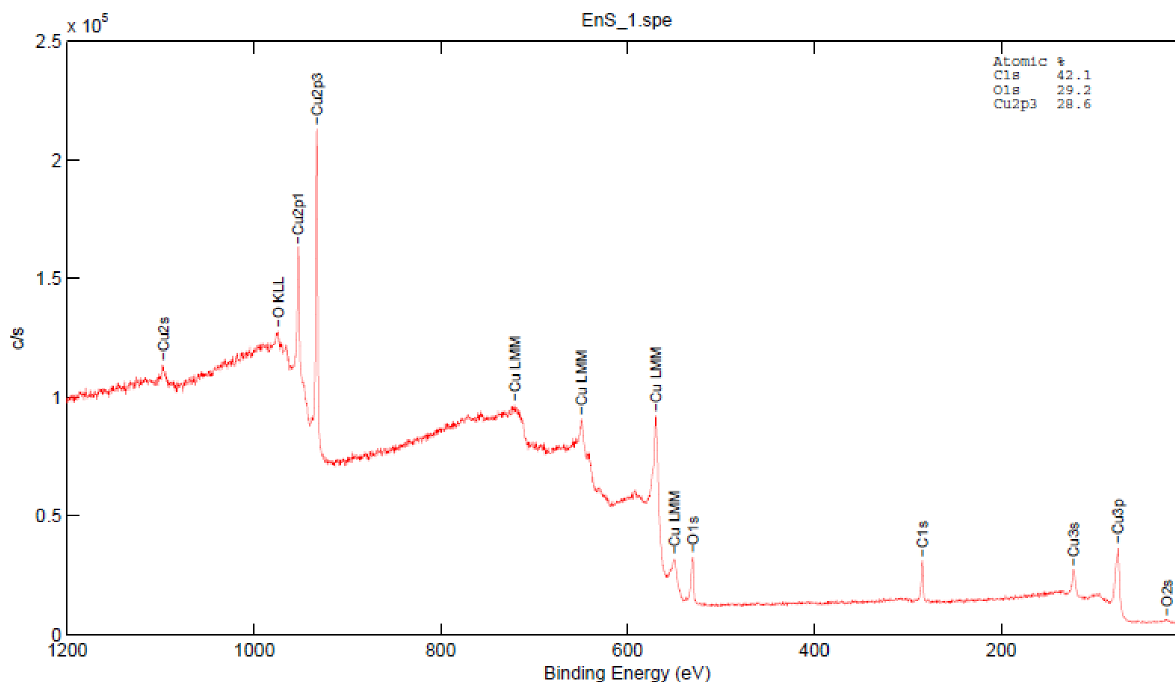

Fig. 4-10 Wide XPS spectrum of an exemplary Cu surface (*y*-axis represents intensity in counts/second)

Fig. 4-11 presents a narrow XPS spectrum of O1s, the range of, which is taken from the wide spectrum. The narrow spectra are measured with a smaller step to gain a higher resolution.

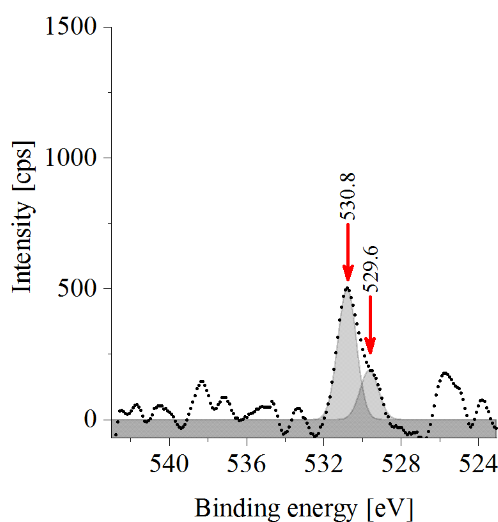

Fig. 4-11 Narrow XPS spectrum of O1s for an exemplary Cu surface

It is possible to layer-by-layer etch the Cu oxide from the Cu surface using *in-situ* Ar^+ ion bombardment in the XPS chamber. After each etching step the sample is irradiated with the X-ray and the chemical composition of the surface is yielded.

Identification of storage conditions, at, which SAM degradation and formation of Cu oxide is minimal, is one of the goals of this study. With the help of Ar^+ ion bombarding for different

samples it can be evaluated, how fast (in how many steps) Cu oxide is fully etched away from the Cu surface. One wide XPS spectrum and several narrow XPS spectra (i.e. for C, O, Cu, S) were acquired for each parameter set.

Tab. 4-4 - Tab. 4-6 summarize literature data regarding BE and KE values corresponding to certain chemical compounds. Apart from emitted photoelectron (which provides BE and KE values) after absorption of a photon, Auger electron is emitted for some elements due to relaxation processes of the excited ions, which remain after the photoemission process. Such characteristic Cu $L_3M_{4,5}M_{4,5}$ (Cu LMM) energy for Cu can provide more precise information about Cu and Cu oxide peak positions in comparison to the standard Cu spectra.

BE and KE energies for solid surfaces are connected by the equation (4-1), where $h\nu$ is the photon energy (1486.6 eV for AlKα and 1253.6 eV for MgKα) and φ is spectrometer work function [124]. Since the work function is usually included in the BE or KE energies, provided by the software, it is easy to convert one type of energy into another for comparative analysis.

$$KE = h\nu - BE - \varphi \qquad \textbf{(4-1)}$$

BE values of emitted photoelectrons are the same for AlKα and MgKα source anodes. That is why most of the spectra for chemical compounds are shown using BE. The Auger energies can be presented by KE or BE values in literature. However, in this case, KE is the same and BE varies for different source anodes. Therefore, both KE and BE energies are calculated for Cu LMM spectra in Tab. 4-4.

The peaks from an XPS spectrum are always assigned to a reference they correspond to. In such a way the reference peak positions, for example of adventitious C contamination, can be estimated and compared to the results of this study.

Tab. 4-4 Binding energies of Cu LMM and corresponding to it O1s and S2p bindings with references

Chemical compound	KE (eV)	BE (eV) Al Kα	BE (eV) Mg Kα	BE (eV)			Ref.
	Cu LMM			O1s	C1s	S2p	
Cu	918.6	568	335		284.6		[125]
	919	567.6	334			162.3	[54]
	918.1	568.5	334.9		285	162.5	[68]
	918.6	568	334.4		284.6		[126]
Cu_2O	916.6	570	337				[125]
	917.2	569.4	335.8				[54]
	916.5	570.1	336.5	530.4			[126]
	917.6	569	336		285		[127]
CuO	917.8	568.8	335.2	529.6			[126]
$Cu(OH)_2$	916.7	569.9	336.3	531.3			[126]

Tab. 4-5 presents the assignment of C compounds to binding energies.

Tab. 4-5 Peak positions assigned to molecules in the XPS spectra of C 1s

Chemical compound	C1s	Ref.
	BE(eV)	
C	284.29	[128]
C-C	285	[127], [129]
C-C, C-H	284.8	[130]
C=O	287.6-287.8	[130]
C-O-C	288.4-289.1	[130]
C-O-Cu	286.3	[128]

Tab. 4-6 additionally describes XPS binding energies (peak positions) for S in SAM molecules (on Au or Cu) and apart from them.

Tab. 4-6 Binding energies of S bindings with references

Chemical compounds	S2p	Ref.
	BE (eV)	
S2p	163.8-164	[131], [132]
$C_8H_{17}SCu$ (S2p3/2)	162.4	[133]
$C_8H_{17}SCu$ (S2p1/2)	163.6	[133]
$C_{18}H_{37}SAu$ (S2p3/2)	162	[134]
$C_{18}H_{37}SAu$ (S2p1/2)	163.2	[134]
R-SO_3-Metal	>166	[62], [125]
$CuSO_4$	167.05	[135]

In order to get a realistic picture of the chemical state of the surface of the samples, the XPS process was divided into two steps. First, X-rays irradiated Cu surface and its chemical state was determined. The provided information is further defined as the "initial state" of the Cu surface. In this state adventitious carbon contamination layer covers all of the surface compounds and impedes analysis of the real chemical composition of the Cu surface. Therefore, the process requires a second step of Ar^+ ion bombardment with low energy (500 eV for 2 min) to remove the organic contamination layer [136]. This step is defined further as "the cleaning step" after, which the sample surface is examined with XPS again.

The standard deviation error for the measurements of atomic concentrations by XPS is approximately 10 %. The Cu2p spectrum contains two peaks, $Cu2p_{1/2}$ and $Cu2p_{3/2}$. Calculations of Cu atomic concentration are made, based on the intensity of $Cu2p_{3/2}$ later on in this work.

4.3.3 Infrared spectroscopic ellipsometry

Ellipsometry in a visible spectral range has been widely used to investigate the layer thickness and structure. Infrared spectroscopic ellipsometry (IRSE) is a relatively new [137], [138] surface characterization technique. Since many organic compounds cannot be detected easily in a visible spectral range, IRSE became a proper method for the investigation of thin (monomolecular) organic films. This method complements XPS analysis providing more details on the degradation behavior of different types of SAMs on Cu surface.

The ellipsometric data describes changes in polarization of reflected light, which gets an elliptical form, due to its interaction with the molecule-covered sample surface. Fig. 4-12 shows field components parallel E_{pi} and perpendicular E_{si} to the incident plane of the electromagnetic wave and field components of the reflected electromagnetic wave E_{pr} and E_{sr}.

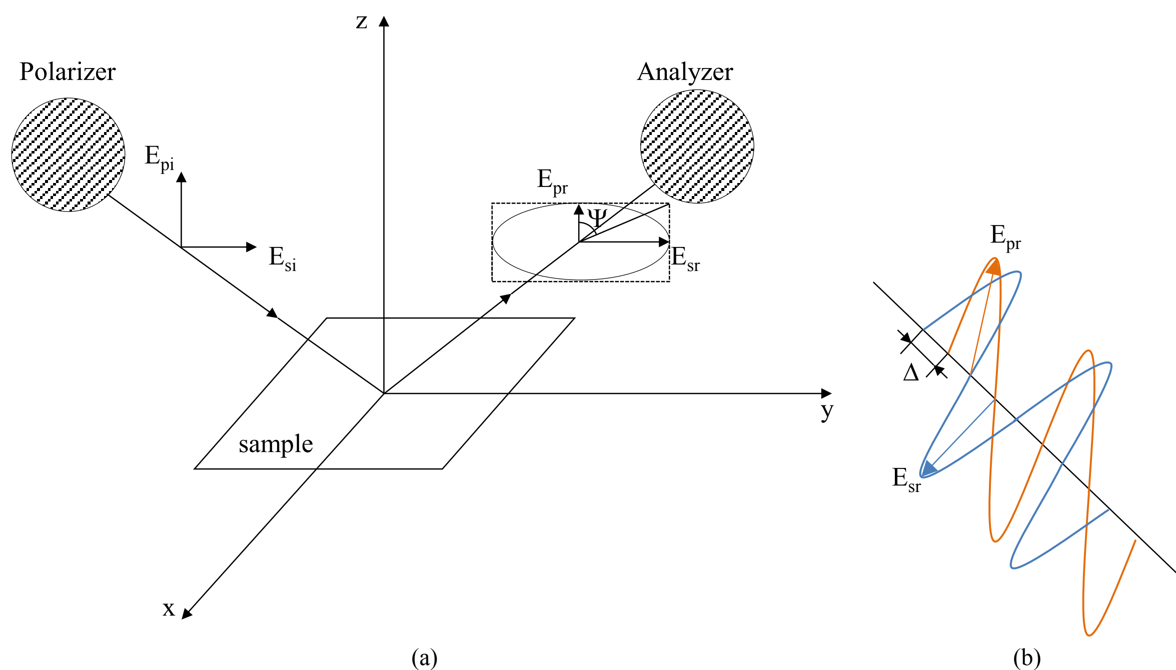

Fig. 4-12 Characteristic parameters of the ellipsometric measurements: orthogonal field components of the incident electromagnetic wave (E_{pi}, E_{si}), reflected electromagnetic wave (E_{pr}, E_{sr}), angle Ψ and phase shift Δ of the elliptically polarized wave (adapted from [137]**)**

The changes in polarization are expressed by the quantity ρ in equation (4-2)*, which* is defined by the amplitude ratio tan ψ and the phase shift Δ of the *p*- and *s*-polarized components (r_s and r_p) of the reflected electromagnetic wave.

$$\rho = \frac{r_p}{r_s} = \tan\psi\, e^{i\Delta} \tag{4-2}$$

The detected spectrum usually contains a certain arrangement of adsorption peaks at certain frequencies [48]. Tab. 4-7 describes assignments of peaks for a hydrocarbon chain of SAM layer. These can be assigned to the discrete molecular groups. The change of intensity of these peaks for the same sample (for example, before and after air exposure) can give information about the change in molecular orientation and chemical composition of the surface.

The measurements are performed in air by an ellipsometer, connected to an FTIR spectrometer Bruker IFS 55 equipped with liquid nitrogen cooled Mercury Cadmium Telluride (MCT) detector. The incidence angle is set to 80 °. The measurement resolution is set to be approximately 2 cm^{-1}. This method does not require a vacuum. Nevertheless, metals with high surface tension are complicated to characterize. This is caused by the reactivity of such metal surfaces and immediate adsorption of organic contaminations from the air, which increases the signal noise.

Tab. 4-7 Peak positions of C-H stretching modes for thiols and thiolates adsorbed on the metal, where $\nu_s(CH_2)$ is CH_2 symmetrical and $\nu_a(CH_2)$ is CH_2 asymmetrical vibration modes, $\nu_{a,ip}(CH_3)$ is CH_3 asymmetrical in-plane vibration mode, $\nu_{s,FR}(CH_3)$ are CH_3 asymmetrical vibration modes connected to Fermi resonance interactions

Thiols and thiolates adsorbed on Au or Cu	C-H stretching modes in cm^{-1}					Ref.
	$\nu_s(CH_2)$	$\nu_{s,FR}(CH_3)$	$\nu_a(CH_2)$	$\nu_{s,FR}(CH_3)$	$\nu_{a,ip}(CH_3)$	
$C_6H_{13}S$/Au	2852	2878	2921	2939	2966	[48]
$C_6H_{13}S$/Cu	2855	2878	2929	-	2964	this work
$C_{16}H_{33}S$/Au	2850	2879	2918	2938	2965	[48]
$C_{16}H_{33}S$/Au	2856	2881	2926	2942	2968	[64]
$C_{16}H_{33}S$/Cu	2849	2878	2918	2937	2964	this work
$C_{22}H_{45}S$/Au	2851	2878	2918	2937	2965	[11]
$C_{22}H_{45}S$/Au	2850	2879	2918	2937	2965	[48]
No SAM/Cu	2855	2878	2927	-	2963	this work
C22^a (crystalline)	2855	-	2924	-	-	[48]
C8^b (liquid)	2851	-	2918	-	-	[48]

^{a} Thiol C22 was measured in the crystalline state
^{b} Thiol C8 was measured in a liquid state

4.4 Bonding techniques

4.4.1 Description of the used bonding equipment

In order to conduct TC bonding in an inert gas atmosphere a formic acid bonder (Alpha DesignCo., LTD., the University of Tokyo) was used. Cu-Cu ultrasonic bonding was carried out in air with the help of flip-chip bonder FCB3 (Panasonic, Fraunhofer IZM ASSID). The characteristic parameters of each bonder can be found in Tab. 4-8. Parameters for FCB3 bonder are presented for the US bonding, viz. using US bonding head.

Tab. 4-8 List of the main parameters for bonders used in this thesis

Bonding parameters / Bonders	Alpha Design	FCB3 (US configuration)
Force maximal, N	3000	300
Temperature stage max., °C	400	150
Temperature head max., °C	400	250
Bonding head size, mm × mm	10 × 10	7 × 7
Atmosphere	Ar	air
Bonding accuracy (xy), µm	±3 / 3σ	±3 / 3σ
Heating rate (stage), °C/s	2	0.1
Heating rate (head), °C/s	2	75

4.4.2 Details of thermocompression and ultrasonic bonding processes

TC bonder Alpha Design (The University of Tokyo) with an inert gas atmosphere, constructed on the demand of the School of Engineering, was used in this study. First, the chips are placed on the bonding stage: the bottom die is face-up, the top die is placed on the bottom

die center face-down. Second, the chamber is closed and the air is pumped out till the pressure is 0.09 MPa. Further, Ar gas is introduced into the vacuum chamber (till the pressure becomes 0.1 MPa). After that, the chamber is constantly purged with Ar during the whole bonding procedure.

Fig. 4-13 Alpha Design TC bonder with Ar-gas atmosphere in the bonding chamber

The height of the chips is set manually in the bonding software, together with adjusting the bonding parameters. For the SAM desorption procedure, the stage is heated for 30 min, the chips lie on each other without the application of external bonding pressure. After this pre-heating procedure, the bonding head drives down onto the chip stack, and the bonding force and temperature are applied. The heating rate of the stage is 2 °C/s.

The flip-chip bonder FCB 3 (Panasonic) has two bonding modes (TC and US), however, no possibility of a controlled inert gas atmosphere in the bonding chamber. The equipment was used for US bonding experiments is presented in Fig. 4-14. The process begins with placing a top die into the tray (face-up) and a bottom die on the preheated stage ($T_{stage}=T_{bond}$). The top die is picked up and flipped by a vacuum tool. Afterward, the bonding head picks up the chip from the vacuum tool and places it on the bottom die. Further, the bonding head applies force and heating onto the top die. The recognition of a chip height is done also by the camera of the bonder. The ultrasound frequency is 60 kHz. Maximal amplitude reaches 1.5 – 2 µm. The heating rates of the bonding head and the heating plate are approximately 75 °C/s and 0.1 °C/s, respectively. T_{room} is considered to be the temperature of 30 °C in this study. This is done to fix T_{room} (or make it constant) so that the bonding results are comparable to each other.

Fig. 4-14 FCB 3 bonder (Panasonic)

4.5 Characterization of the bonding quality

4.5.1 Shear strength test

One of the most important characteristics of the joint quality is the shear strength between the top and bottom dies. Chapter 7 describes TC bonding using SAM passivation. These experiments were conducted at The University of Tokyo where a shear tester PTR-1100 (RHESCA Co., LTD.) was used. The maximum load of the used tool is 50 kgf. The shear strength test was done with a speed of 20 µm/s. A special clamping tool with 500 µm high holders was used to fix the dies. Chapter 8 describes US bonding using SAM passivation. In the following investigation, a shear tester Condor Sigma (XYZtec) at TU Dresden was used. The shear height is 65 µm, which is 10 % of the top die thickness for all of the samples. The shear tool with a maximum force of 200 kgf was used. The width of the shear chisel equaled 1 cm for both shear testers for the die shear tests. 100 gf tool was used during the shearing of separate microbumps (chapter 8.4). The shear height equaled 1.2 µm, which is 10 % of the microbump height (sample type B). The width of the shear chisel was always higher than the width of the sheared die or microbump.

4.5.2 Topography analysis

The importance of planarity between the head and stage in Cu-Cu bonding is hard to underestimate as it directly influences the bonding yield. Hence, the planarity of the bonded chips, height and roughness of the Cu microbumps were measured by µSurf (Nanofocus, TU Dresden) and LEXT OLS4100 (Olympus, The University of Tokyo) confocal microscopy. The main parameters for both devices are listed in Tab. 4-9.

Tab. 4-9 Characteristic parameters of the lenses for the analysis of the surface roughness and topology

	µSurf	**LEXT OLS4100**
Lense	800 S; 320 S	MPLFLN5x; MPLFLN10x
Working distance, mm	3.1; 0.66	20; 1
Field of view, µm	800×800; 320×320	2560×2560; 640×640
Numerical aperture	0.46; 0.8	0.15; 0.6

4.5.3 Microstructure analysis of the Cu-Cu bonding interface

In order to investigate the interconnect bonding quality, the cross-section characterization by scanning electron microscopy (SEM) or transmission electron microscopy (TEM) methods is one of the best choices for direct observation of the Cu-Cu bonding interface. A description of both of these methods is presented in this subchapter.

4.5.3.1 Sample preparation and scanning electron microscopy analysis

Before the cross-sectioning procedure, the samples have to be embedded into the epoxy resin mixture. Epoxy resin (SpeciFix, Struers) is mixed with a curing agent (SpeciFix-20, Struers) to a proportion of 7:1 with the addition of thinning agent TEK-MEK (T-E-Klebetechnik) with a concentration of 1 drop per 10 g of the mixture for its better infiltration. The solution should be evacuated for approx. 2 min right after mixing to remove air bubbles trapped in the solution during mixing. Graphite powder (Graphite Flake, Alfa Aesar) is added in the proportion of 1:4 to the received solution in order to avoid the charge accumulation on the samples exposed to the electron beam using SEM imaging. After slowly mixing the solution, it should stand (5…10) min without disruption. The samples are placed orthogonally into the polymer form onto the adhesive tape (Fig. 4-15, (a)). Next, the polymer form with the sample is filled with the epoxy mixture to half of the sample height. The following vacuum step (≤ 0.4 bar) for 30 s provides penetration of the mixture in the narrow area between the microbumps. After that, the form is filled till it is full. Curing is completed in (8…12) hours. Fig. 4-15 (b) shows cured epoxy resin mixture taken out of the form, grinded and polished till the target cross-sectional plane and painted with Ag varnish for SEM observations.

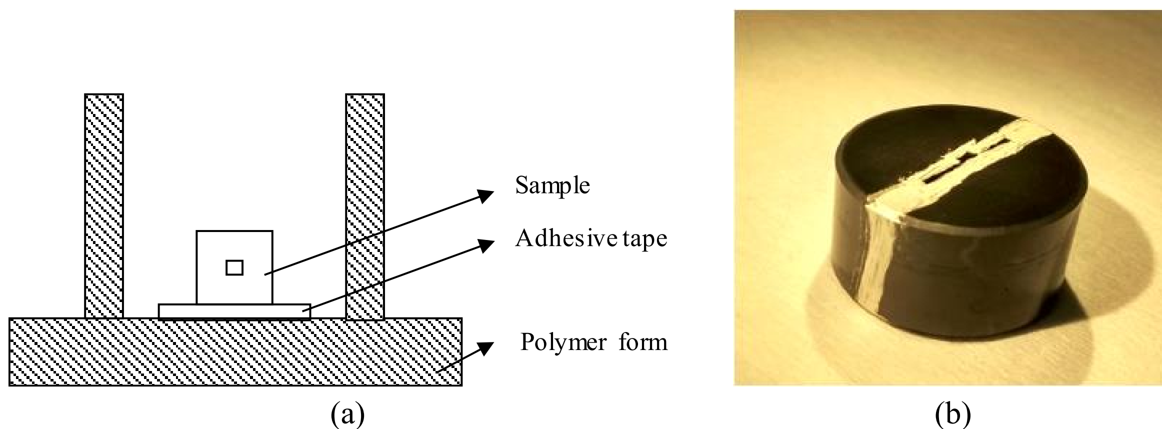

Fig. 4-15 Cross-sectional view of sample fixation in the polymer form (Ø25 mm) before filling it with epoxy resin mixture (a); epoxy resin sample with graphite powder after curing, grinding, polishing and painting it with Ag conductive varnish for SEM inspections (b)

The sample in the cured epoxy mixture is taken out of the form and exposed to grinding and polishing procedures (TegraPol, Struers). The target plain is found with the help of grinding steps. In order to reveal the real microstructure, polishing and fine polishing steps are done after the coarse grinding procedure. Scratches, coming from these steps, can inhibit the analysis of Cu-Cu bonding interface quality. Suspension residuals on the sample surface can also hamper SEM analysis. Therefore, the development of a suitable preparation receipt (Tab. 4-10) and thorough cleaning of samples after each step is crucial in achieving a good quality SEM image.

Tab. 4-10 Main parameters for the grinding and polishing

Parameters / preparation steps	1, 2, 3, 4 – grinding	5 — polishing	6 — polishing	7 — polishing	8 — fine polishing	9 — etching
Cloth	Grinding paper	MD-Dur	MD-Dac	MD-Nap	MD-Chem	MD-Chem
Abrasive material	SiC	DiaDuo	DiaDuo	DiaProNap-R	MasterMet2	$FeCl_3$ - solution 0.05 %
Particle size	P500 – 31 µm (Struers) P1200 – 15.3µm (Hermes) P2000 – 10 µm (Struers) P1200/P2500 – 6.5 µm (Buehler)	6 µm	3 µm	1 µm	0.02 µm	–
Lubricant	DI water	–	–	DI water and soap water	DI water	DI water
Rotation speed	100 rpm 100 rpm (40…100) rpm (40…100) rpm	150 rpm	150 rpm	150 rpm	120 rpm	120 rpm
Pressing force	manually	20 N	20 N	20 N	10 N	10 N
Duration	till target plane is achieved	(5…7) min	8 min	5 min	1 min	30 s

The imaging of the cross-sections of the Cu-Cu interconnects was made by SEM with a field-emission gun (Zeiss Supra 40VP). The main parameters for the SEM imaging are listed in Tab. 4-11.

Tab. 4-11 Parameters for SEM imaging of the cross-sections of the Cu-Cu interconnects

Parameters	Value
Accelaration voltage, kV	20
Working distance, mm	5
Detector types	AsB, SE2
Scan Speed	8
Noise reduction	Line average, N=10
Aperture	30 µm
Collector voltage	300V

4.5.3.2 Transmission electron microscopy analysis

Transmission electron microscopy (TEM) is used to obtain a high-resolution analysis of the Cu-Cu bonding interface and to determine its chemical composition. The TEM investigations are performed at Fraunhofer Institute for Microstructure of Materials and Systems (Fraunhofer IMWS). Special preparation is needed to cut out a TEM lamella. First, the space between the bumps is filled with underfill, which is cured afterward. Second, the Si layer of the top die is grinded to the dashed line in Fig. 4-16 (a). These two steps are carried out at Fraunhofer IZM-ASSID. Next, the samples are sent to Fraunhofer IMWS where TEM-lamella can be cut out from the top side (Fig. 4-16, (b)). Samples with SAM passivation bonded at 200 MPa at 150 °C are used for TEM analysis.

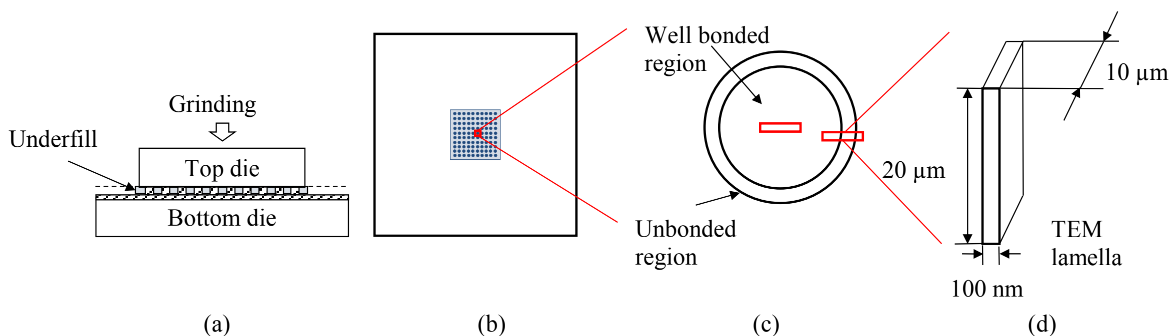

Fig. 4-16 Cross-section view of the top and bottom dies with a grinding direction after underfilling (a), top view of the top and bottom dies after grinding (b), magnified top view of one of the bumps with unbonded and well-bonded regions (c) and magnified view of the TEM lamella (d)

Bump edges have a high possibility to have a lower interconnect quality than bump center. Therefore, TEM-lamellae from both regions has to be investigated. TEM lamellae are cut out from bumps using focused ion beam (FIB) technology (Fig. 4-16, (d)). Their approximate location and size are presented in Fig. 4-16.

TEM-analysis is carried out by Titan G2 60-300 (Thermo Fisher Scientific, formerly FEI) with an image Cs corrector, X-FEG electron gun and Super-X detector with an acceleration

voltage of 300 kV. The images, produced by scanning transmission electron microscope (STEM), are made using a high angle annular dark-field (HAADF) detector.

Having described the techniques to characterize the formed interconnect after bonding, it is important to obtain detailed information about the Cu microstructure analysis of the used samples before bonding. Electron backscatter diffraction (EBSD) analysis has been used for this purpose. The method description and its settings are extensive and contain several analytical know-how. Therefore, a separate chapter for both, the method description and measurement results, is presented next.

5 Microstructure characterization of the Cu surface before bonding

5.1 Grain structure analysis of the Cu surface by electron backscatter diffraction

5.1.1 EBSD measurement

The electron backscatter diffraction (EBSD) technique is used to carry out microstructural and crystallographic characterizations of the samples used for the bonding process. The focus of this analysis is the evaluation of the Cu grain size and the characteristic grain orientation (texture) in the initial state before bonding. EBSD data acquisition was carried out with a DigiView IV EBSD camera and the TSL OIM Data Collection 5.3 software (EDAX Inc.). Parameters, used for all measurements, are summarized in Appendix A.1. Tab. 5-1 provides an overview of all investigated sample types and associated number of measurements. The sample arrangement and associated definition of the sample coordinate system are schematically given in Fig. 5-1 (a).

Tab. 5-1 Overview of the EBSD measurements in the initial state for all investigated sample types

Sample type	Bonding technology	Investigated surface	Number of measurements	Measurement area (Step size)	Mag.
Top Die A (with fly cutting)	TC	cross-section	10 bumps (in a row)	108×34 μm^2 (0.1 μm)	700x
Top Die B (with fly cutting)	US	cross-section	10 bumps (in a row)	61×21 μm^2 (0.1 μm)	1250x
Bottom Die A (ECD Cu after CMP)	TC	top view	2x (fine) 2x (coarse)	50×50 μm^2 (0.1 μm) 250×250 μm^2 (0.5 μm)	1250x 250x
Bottom Die B (ECD Cu)	US	top view	2x (fine) 2x (coarse)	50×50 μm^2 (0.1 μm) 250×250 μm^2 (0.5 μm)	1250x 250x

Tab. 5-1 indicates that the sample arrangement differs between top and bottom dies, which is exemplarily shown in Fig. 5-1 (b), (c). This choice for the bottom dies was made due to the relatively thin Cu layer of 2 μm, which limits possible measurement area in cross-sections in comparison to the top view. However, it is necessary to change the sample direction of the analysis due to these differences in the sample arrangement. Therefore, the relevant direction, parallel to the Cu deposition, is RD ([100]) for cross-sections and ND ([001]) for top view measurements (Fig. 5-1, (b), (c)). Direct comparison between both top and bottom dies, especially of the corresponding grain sizes, is not possible due to the above-described differences in sample arrangement. The two arrangement types show different parts of the microstructure and likely feature different dimensions.

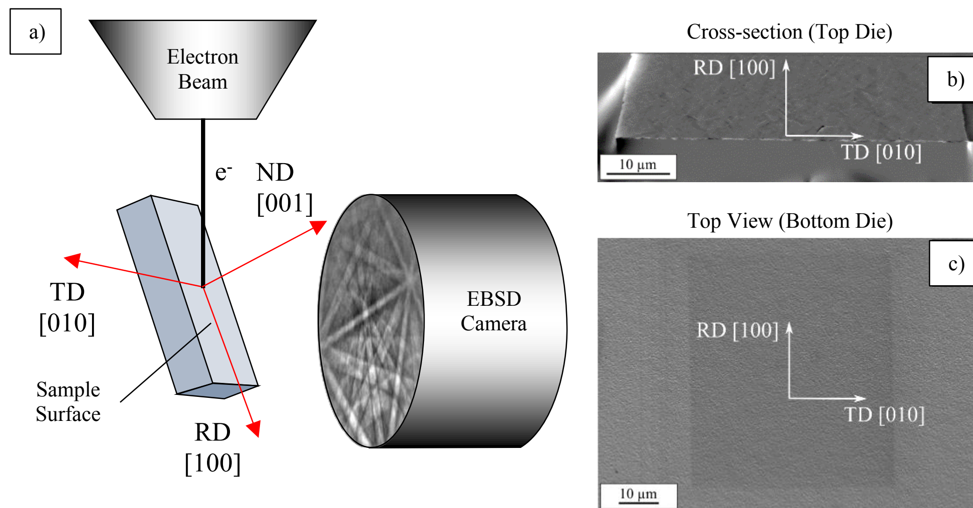

Fig. 5-1 Sample arrangement for EBSD measurements: (a) schematic representation of the EBSD measurement setup with inserted sample coordinate system defined by normal (ND), rolling (RD) and transverse (TD) direction, (b) sample orientation for the cross-sectional view of a microbump, (c) sample orientation for the top view of the bottom die (fully covered with Cu)

5.1.2 Data analysis and filtering procedure of EBSD data sets

After the acquisition, the measured dataset is analyzed with a TSL OIM Analysis 5.3 software (EDAX Inc.). However, indexing covers all data points even if there is no real pattern (for example in the epoxy mold) or if they belong to a different phase (Ti or Si). This means that a lot of data points are falsely indexed as Cu, as shown for the raw dataset in Fig. 5-2 (a). Filter and cleanup procedures (Fig. 5-2) are typically applied in order to remove these wrong indexed points before the analysis.

The first filter is characterized by the image quality (Fig. 5-2, (b)). The image quality (IQ) map shows the difference between good diffraction patterns (bright points) and bad diffraction patterns (dark points) as a measure of contrast between actual Kikuchi-lines and the pattern background. The bad patterns are mostly situated in the area of the epoxy mold since this material is amorphous. This allows filtering whereby only points with good image quality (IQ > 500) are considered in the dataset. However, crystalline materials, such as Si and Ti, are not necessarily affected by that. Since a simultaneous energy-dispersive X-ray (EDX) spectroscopy mapping (using an EDAX Octane Elect Plus detector) was carried out during each EBSD measurement for selected elements (C, O, Si, Ti and Cu), it is possible to use the EDX signal as a filter in order to exclude data, originating from Si wafer. All points with more than 20 counts for Si are, thereby, removed (Fig. 5-2, (c)). This filter is only applied for the cross-sections and is rather useless for the top view measurements. The last filter is applied in order to remove individual single points, not belonging to a certain grain. Therefore, all grains with a grain size of only 1 point and an orientation difference, higher than 5 ° towards all neighboring points, are excluded from the measurement (Fig. 5-2, (d)). However, this filter makes a final cleanup procedure necessary in order to fill up the removed data points inside the Cu surface. Therefore, a grain dilation procedure (single iteration) is carried out, which includes all of these points (size: 1 pixel, deviation > 5 °) into the respective surrounding grain. The result of this final step reveals the dataset, used for further analysis (Fig. 5-2, (e)).

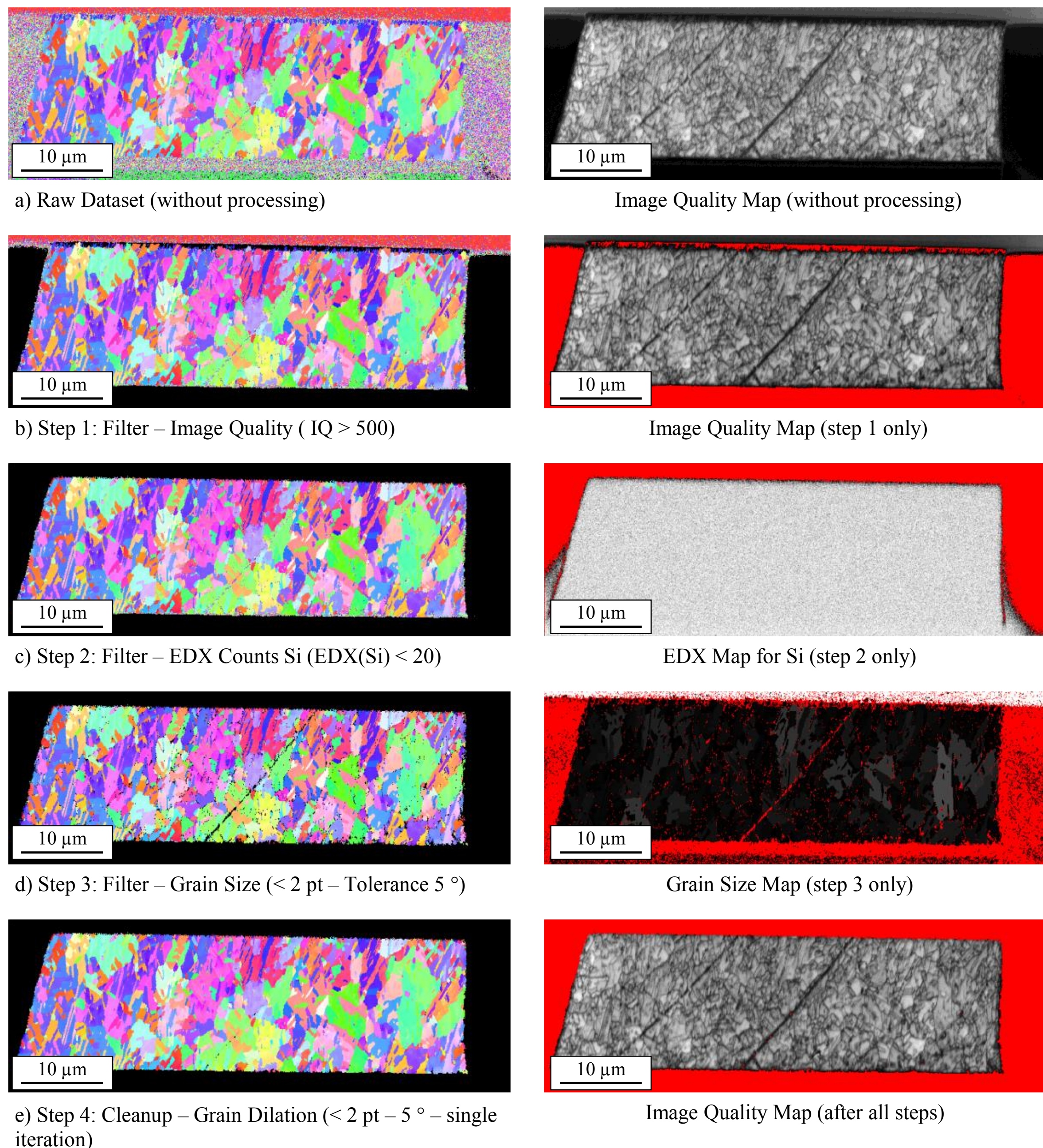

Fig. 5-2 Processing of an EBSD measurement for analysis (IPF map with accumulated filter progress in the left column; IQ map with red highlighting of excluded data points from the raw dataset in the right column): IPF map of the raw dataset (a); image quality filter (IQ > 500) (b); EDX filter for Si (EDX_{Si} < 20 counts) (c); grain size filter, which excludes grains with a size of 1 point and more than 5 ° deviation from adjacent points (d); cleanup grain dilation whereby single points with more than 5 ° deviation are included into the neighboring grain (e)

5.1.3 Method for correction of sample orientation in cross-sections

A novel method for the correction of sample orientation in cross-sections has been applied and has not been described in the literature before. It is necessary to know the exact sample orientation during the measurement in order to determine correct grain orientation along a specific sample direction, for example, the direction of Cu electroplating, which is perpendicular to the wafer surface. While this is well known for the top view measurements, orientation may differ from the ideal position in cross-sections (Fig. 5-3). Molding, as well as manual grinding and polishing processes during cross-section preparation, may introduce an

additional tilt between desired and actual cross-section planes, resulting in a rotation around TD (Fig. 5-3, (a)). Further tilt may originate from a non-planarity between the cross-section plane and the sample's backside used for mounting on the SEM sample holder. However, the latter is usually corrected during the EBSD sample positioning by additional tilting of the sample holder. Another type of misalignment, illustrated in Fig. 5-3 (b), is caused by the use of the tilted sample holder, which requires a manual positioning of the sample. This introduces an additional rotation around ND, which is also visible in a real measurement (Fig. 5-2, (a)) and is not correctable by the SEM stage.

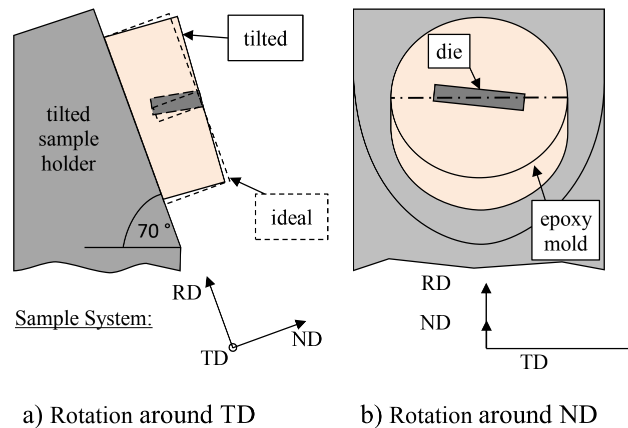

Fig. 5-3 Deviation from the ideal cross-section plane during EBSD measurements: manual sample preparation may introduce a rotation around RD (a); manual sample alignment on tilted sample holder introduces a rotation around ND (b)

It is necessary to estimate and correct the sample alignment since this influences the accuracy of the orientation analysis in specific sample directions. This is possible by measuring the orientation of the Si single crystal of the (001) oriented wafer, visible in the upper part of the measurement in Fig. 5-2 (a). The resulting unit cell is given in Fig. 5-4 (a). Its orientation is not perfectly aligned with the sample coordinate system, since the [001] direction of the crystal is not parallel to the RD vector. However, it is possible to calculate the necessary rotations around ND and TD to correct the total mismatch, determined for each example (Fig. 5-4).

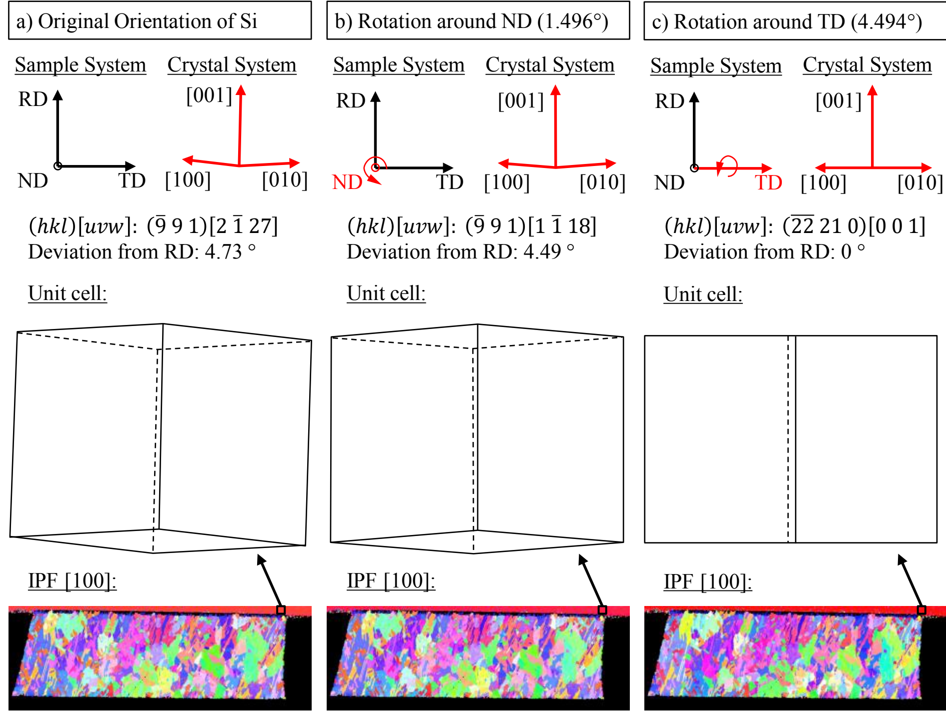

Fig. 5-4 Correction of the sample misalignment of an EBSD measurement by rotating a Si single crystal into its ideal position given by (001) wafer orientation: initial misalignment (a), correction by rotation around ND (b), correction by rotation around TD (c)

Therefore, the [0 0 1] vector of the crystal orientation ($\vec{r}_{crystal}$) has to be transformed from the crystal coordinate system into the sample coordinate system using the following equation [89]:

$$\vec{r}_{sample} = A^T \cdot \vec{r}_{crystal} \tag{5-1}$$

Transformation matrix A for the (h k l) [u v w] notation is given by:

$$A = \begin{bmatrix} \frac{u}{N_1} & q & \frac{h}{N_2} \\ \frac{v}{N_1} & r & \frac{k}{N_2} \\ \frac{w}{N_1} & s & \frac{l}{N_2} \end{bmatrix}$$

with

$$N_1 = \sqrt{u^2 + v^2 + w^2}$$

$$N_2 = \sqrt{h^2 + k^2 + l^2}$$

$$(q, r, s) = (h, k, l) \times (u, v, w)/(N_1 N_2)$$

The resulting vector ($\vec{r}_{crystal}$) or [x y z] should be parallel to RD or [100] (sample coordinate system) for a perfect alignment. This vector has to be projected in the ND plane by setting the respective vector component to zero [x y 0] in order to calculate the necessary rotation around

ND. Calculation of the rotation around TD is similar via projection into the TD plane ([x 0 z]). The respective angles can now be calculated via dot product of the projected vector and RD (both unit vectors) as follows:

$$\cos(\alpha) = \frac{\vec{r}_{projected} \cdot \vec{r}_{RD}}{|\vec{r}_{projected}| \cdot |\vec{r}_{RD}|} \quad \textbf{(5-2)}$$

Fig. 5-4 (b), (c) shows the correction of the unit cell by individual rotations with both calculated angles. These rotations can be easily applied to each data point in the respective EBSD measurement by rotating the complete dataset via OIM Analysis software. Deviations in the range of (0.6…6.6) ° were detected and corrected using these calculations. However, the accuracy of this correction is limited by the tolerances of the wafer orientation and by the accuracy of the EBSD measurement. The extracted average orientation of the Si single crystal in Fig. 5-4 (a) exhibits a scatter of ±0.6 °. This is in the range of the typical accuracy of 1 ° for EBSD. The accuracy of the alignment of the wafer surface, parallel to (001), is not exactly known but should be in the range of the accuracy of the flat or notch position, which is typically ±0.5 ° [139]. Further inaccuracies are introduced by the rounding associated with the (h k l) [u v w] notation, even with reals instead of integer values. The resulting discrepancies become visible if the calculated rotation around ND is used to correct the actual image. Fig. 5-5 shows that the calculated rotation of 1.5 ° is larger compared to the rotation of 1 °, determined by manual image rotation. However, this difference is in the range of the discussed inaccuracies.

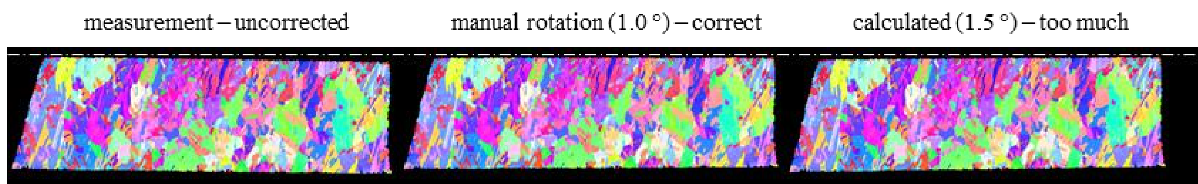

Fig. 5-5 Correction of the image alignment by rotation around ND, calculated rotation is not perfect and approx. 0.5 ° larger compared to manual image correction

5.1.4 Drift correction of EBSD measurements

EBSD measurements are often influenced by drift due to relatively long acquisition times. This causes significant distortion of the measured geometries due to the shifting of the measurement positions (Fig. 5-6). Drift can originate from various sources, such as stage movement, beam instabilities and charge accumulation. Fig. 5-6 (a), (b) shows an undistorted SEM image of a Cu microbump and the respective EBSD measurement. It becomes obvious that the measurement is distorted, which is visible by a slight displacement to the left (x-drift) and the increased bump height (y-drift). This suggests that the image drifted slightly to the left and the bottom during data acquisition (Fig. 5-6, (b)). The drift in the given example causes different step sizes in x- and y-direction, as well as a smaller step size in comparison to the preset of the measurement (0.1 µm – equal for both directions). Since a measurement has no internal drift correction, it is stretched to the fixed rectangular measurement area, which causes a visible distortion. Fig. 5-6 (c) shows another example for drift during the EBSD measurement of a bottom die in the top view. Dark area marks the actual measurement area (darkening is

caused by scanning by electron beam). The image is already tilt corrected, which allows direct measurements. This sample shows that the real measurement area increased, which is visible by the increased height compared to the preset.

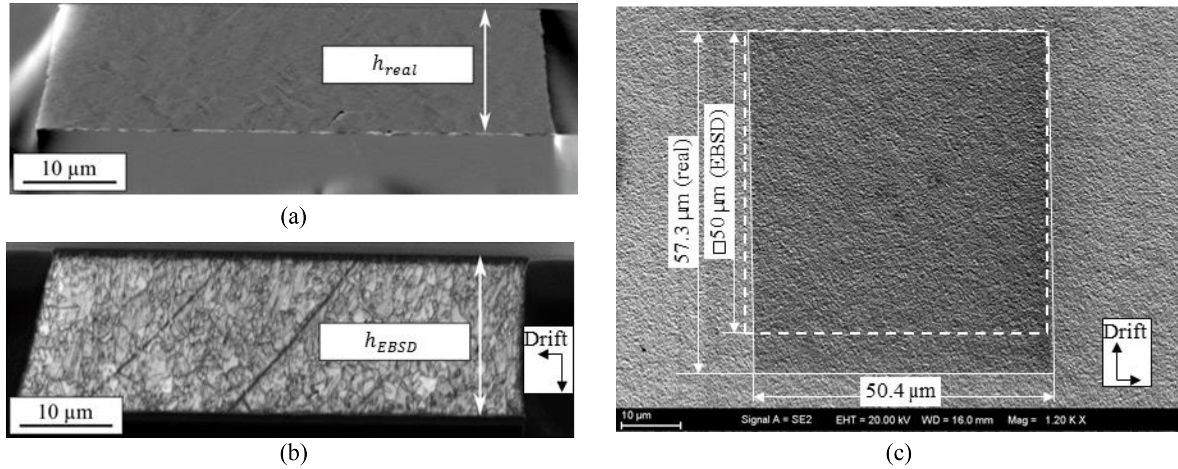

Fig. 5-6 Drift during EBSD measurements: SEM image of a cross-sectioned Cu microbump (a), IQ image of the respective EBSD measurement showing drift in x and y direction (b), Drift during a top view measurement obtained from a tilt corrected SEM image (c)

It becomes necessary to correct the drift, especially for the accuracy of grain sizes, since it is not possible to achieve drift-free measurements. It is assumed that the drift is constant for the whole measurement for this approach. From Fig. 5-6 it becomes obvious that especially drift in the y-direction is of relevance. This is due to the scanning of the electron beam line by line. This causes a negligibly small drift between neighboring points of a single line. However, the drift accumulates while scanning a single line and therefore causes a much larger distance between adjacent lines, which represents the real step size in the y-direction. Therefore, only change of the step size in the y-direction and its influence on the size of each measurement point is considered for correction.

Fig. 5-6 (c) shows that the real area A_{real} of the EBSD measurement (approx. 50.4 × 57.3 µm) differs from the area A_{EBSD} (50 × 50 µm), set for the measurement. It is possible to calculate a correction factor k for each measurement by comparing both rectangular areas. If only the drift in the y-direction is taken into account, the correction factor is simply the ratio between the heights of the real measurement area and the height of the preset area (5-3):

$$k = \frac{A_{real}}{A_{EBSD}} \approx \frac{h_{real}}{h_{EBSD}} \tag{5-3}$$

This can also be applied for the measurements of cross-sections where h_{real} is real height of a bump, obtained from the SEM image, and h_{EBSD} is the height of a bump in the EBSD measurement (Fig. 5-6 (a), (b)). This correction factor can be used to correct grain area values, extracted from the distorted EBSD measurement, assuming constant drift. Since the respective grain diameter is calculated by the OIM Analysis software from the determined grain area by assuming an ideal circle, it is possible to correct these values as follows:

$$d_{real} = \sqrt{\frac{4 \cdot k \cdot A_{EBSD}}{\pi}} = \sqrt{k} \cdot d_{EBSD} \quad \textbf{(5-4)}$$

This drift correction has been applied for all measurements to achieve more accurate grain sizes. Maximum drift, present in the measurements, used for analysis, does not exceed 34 % of the measurement height.

5.2 Results and discussion

5.2.1 Characterization of bonding interface image quality before bonding

Cu surface in the top view [0 0 1] has to be characterized in order to provide information about the bonding interface before bonding. Nevertheless, sample surface properties in the top view are not always suitable for EBSD analysis. Fig. 5-7 presents IQ and IPF images of the bottom dies A and B in comparison to the top die B. Different kinds of Cu surfaces are represented: ECD Cu surface after CMP (bottom die A), ECD Cu surface without CMP (bottom die B) and ECD Cu surface after fly cutting (top die B). The scale of IQ is common for all of the presented samples. IQ average value is presented for each of the samples in the right upper corner. The results suggest that Cu after CMP has the highest IQ (3919.67) whereas Cu surface after fly cutting obtains the lowest one (1765.57). This is connected to the fly cutting procedure, which introduces defects into the Cu surface (dark diagonal lines in IQ image). These defects result either in small grains or in wrong indexed points (see IPF image), which falsifies the results drastically. Since both top die A and top die B were exposed to fly cutting to decrease the differences of microbumps heights, reliable measurements of top die microbumps in the top view are not possible. Therefore, only cross-sectional views are characterized for the top dies further in this thesis. Bottom dies with and without CMP (as plated Cu) provide reliable results, although samples with CMP have higher IQ, possibly, due to lower surface roughness.

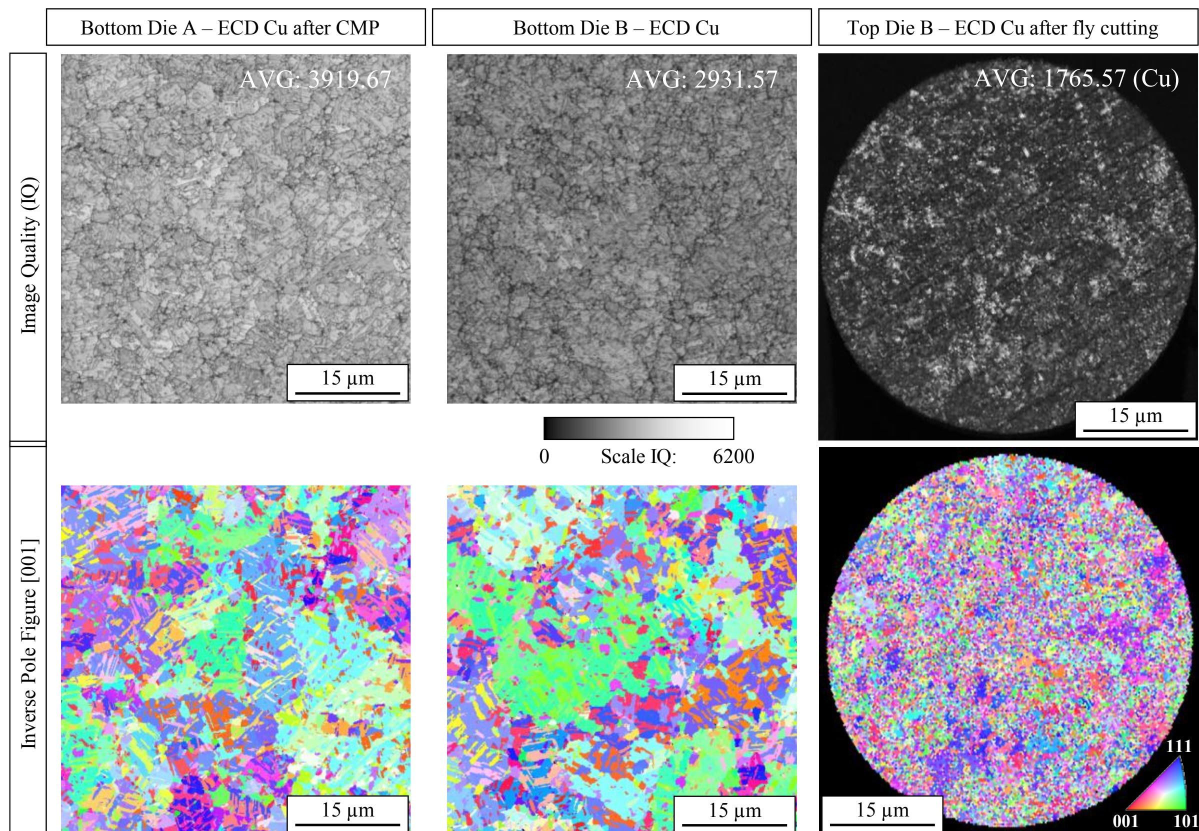

Fig. 5-7 Influence of the surface pre-treatment on the image quality (IQ)

5.2.2 Characterization of the grain size before bonding

The distribution of grain size for the samples before bonding is presented and characterized in this chapter. The presence of twins has an important impact on the grain size characterization, the definition of, which has been explained in chapter 3.1.1. Fig. 5-8 - Fig. 5-9 show grain size distributions excluding and including twins. It is obvious that the average grain diameter is higher after excluding twins and that each grain contains many twin boundaries. The average twin fraction for top and bottom dies equals 0.7±0.03. Therefore, the distribution of grain sizes after the exclusion of twins also differs. The distribution of grain sizes is characterized separately by grain number and by grain area. Average and standard deviation values for each distribution type are figured out.

Two diameter types, by grain number and by grain area, show different distribution tendencies. Calculation of diameter by grain number appears to be strongly affected by the step size and wrong indexed grains. The corresponding graphs do not show a peak, the maximum is situated always at minimal diameter. This can be caused by either too high step size (0.1 µm or 0.5 µm) or by too many wrong indexed points. On contrary, calculation of diameter by grain area often delivers peaks, especially for grain sizes without twins, and, thus, appears to provide a better representation of the grain size distribution. The grain size distributions by area show that the average grain diameter does not necessarily correlate with the peak positions. The peak position represents the grain size that dominates the measured area (covers most of the area).

The top dies are represented in the cross-section view in Fig. 5-8. Bottom dies are presented in the top view in Fig. 5-9 - Fig. 5-10. The measurement results show that the grain size is higher for the top view, which can be explained by the higher aspect ratio of the measurement area. Comparison between the two kinds of views is complicated or impossible. The grains are cut in different planes in the cross-section view, which influences the grain size distribution. The top view provides direct information on the bonding interface before bonding. Top view is also a better platform for the representation of big and small grains. The measurement area 50×50 μm^2 is better to gather information about the small grains whereas 250×250 μm^2 area provides a more precise characterization of the large grains.

The distributions of grain sizes (by area, excluding twins) for top dies A and B in Fig. 5-8 look similar. Although the average grain size is higher for the top die A (9.9 µm in comparison to 7.1 µm of the top die B), the peak positions lie closer and are at 8.5 and 7.1 µm for the top dies A and B, respectively. Also, the maximal grain size is higher for the top die A (23 µm) in comparison to the top die B (15 µm). This can be explained by the differences in the measurement areas, which are higher for the top die A due to larger microbumps.

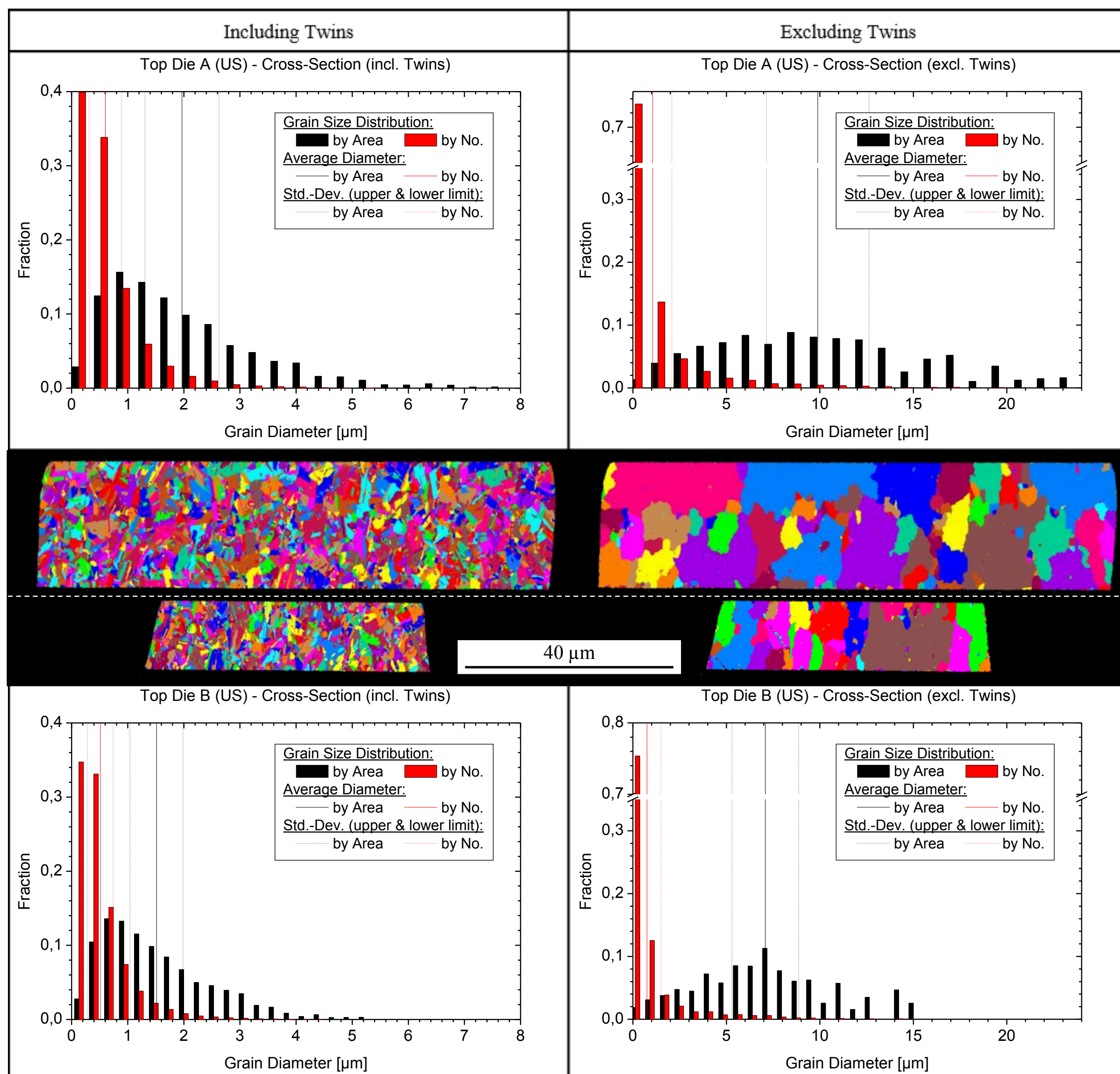

Fig. 5-8 Grain size distribution and unique grain maps for of the top die A for TC bonding and top die B for US bonding

Bottom die B exhibits a slightly lower average grain size (by area, excluding twins) in comparison to the bottom die A (Fig. 5-9, Fig. 5-10). Bottom die A features an average grain size of 17.2 µm whereas bottom die B is characterized by the average grain size of 15.3 µm for 250 × 250 μm^2 measurement area. A similar trend can be detected for 50 × 50 µm measurement areas where the average grain size by area equals 18.6 µm and 16.7 µm for the bottom die A and the bottom die B, respectively. Such a result was expected as only a thin Cu layer has been removed using CMP for the bottom die A. As already mentioned, Cu with CMP (bottom die A) provides a higher IQ in comparison to ECD Cu without CMP, which is shown in Fig. 5-7. This suggests better recognition of grains and orientations on the surfaces with lower roughness and possible increase of the measured grain sizes.

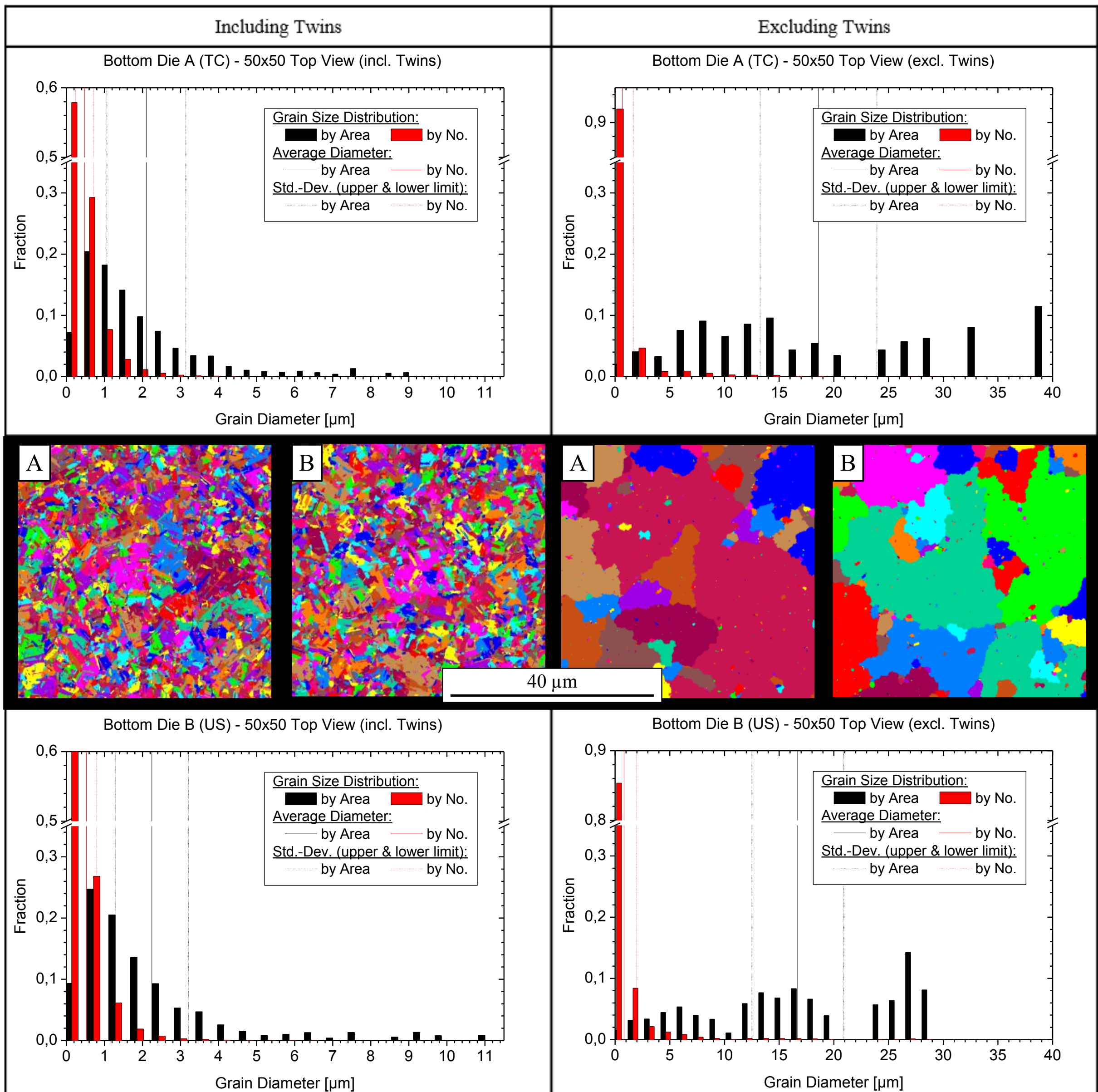

Fig. 5-9 Grain size distribution and unique grain maps for 50 × 50 µm^2 measurement areas of bottom die A (ECD Cu after CMP) for TC bonding and bottom die B (ECD Cu) for US bonding

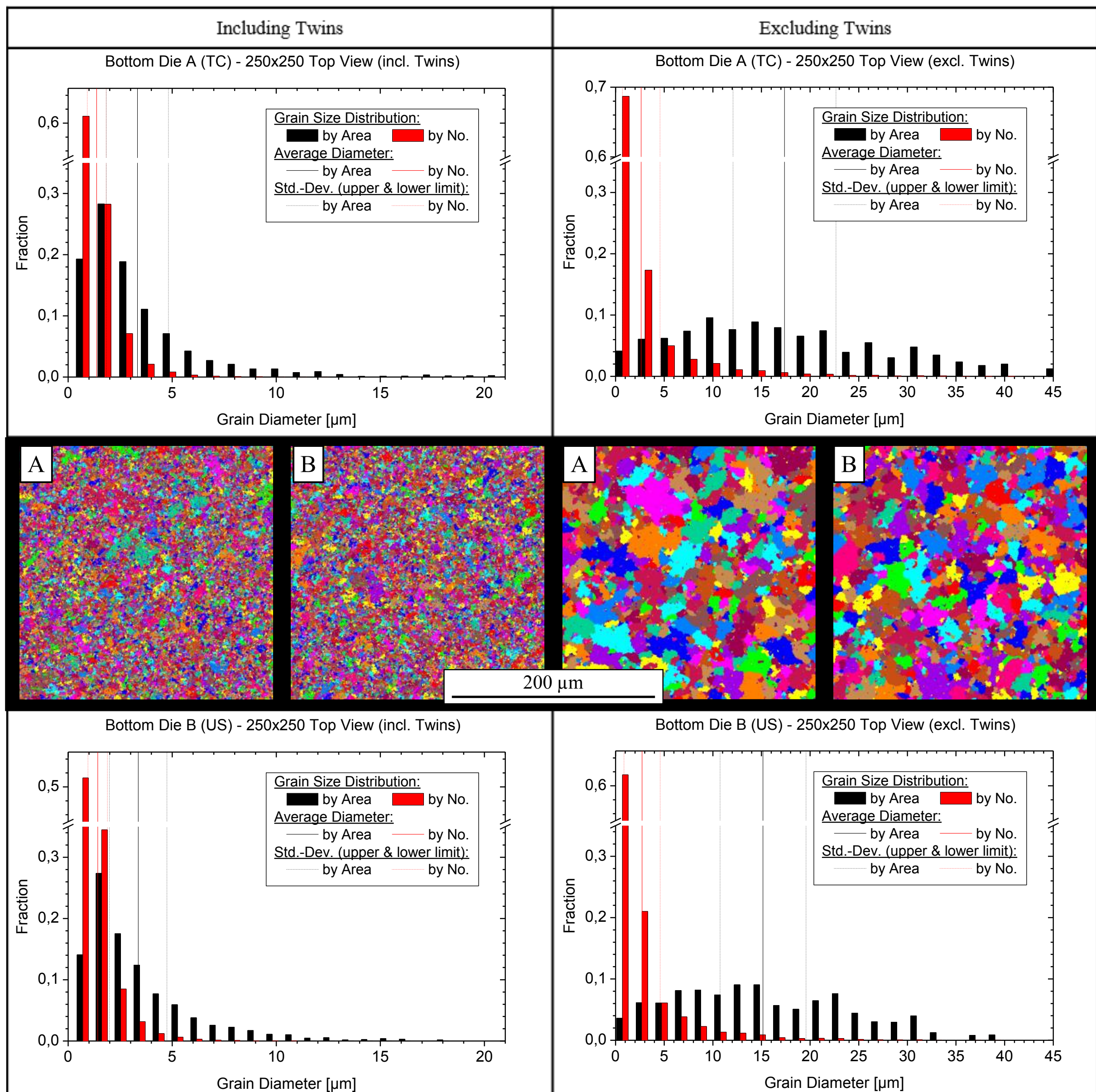

Fig. 5-10 Grain size distribution and unique grain maps for 250 × 250 µm² measurement areas of the bottom die A (ECD Cu after CMP) for TC bonding and bottom die B (ECD Cu) for US bonding

5.2.3 Characterization of grain orientation before bonding

Grain orientation directly influences mechanical properties of the Cu interface before bonding, which can make a significant impact on the mechanical strength of the formed Cu-Cu interconnects (discussed in chapter 3.1.1).

Fig. 5-11 shows an example of twin formation from the original orientations {0 0 1} and {1 1 1} by rotation of the Cu elemental cell by 60 ° in OIM Analysis software. Typical orientations of the 1st – 3rd orders are marked in the presented IPF texture plots. As discussed in chapter 3.1.1, typical twin boundaries for Cu are formed by 60 ° rotation around <1 1 1> axis. Twins can be formed from different orientations. In this study most of the twins come from {0 0 1} and {1 1 1} original orientations. Indication of planes by {h k l} integer is inexact (rounded).

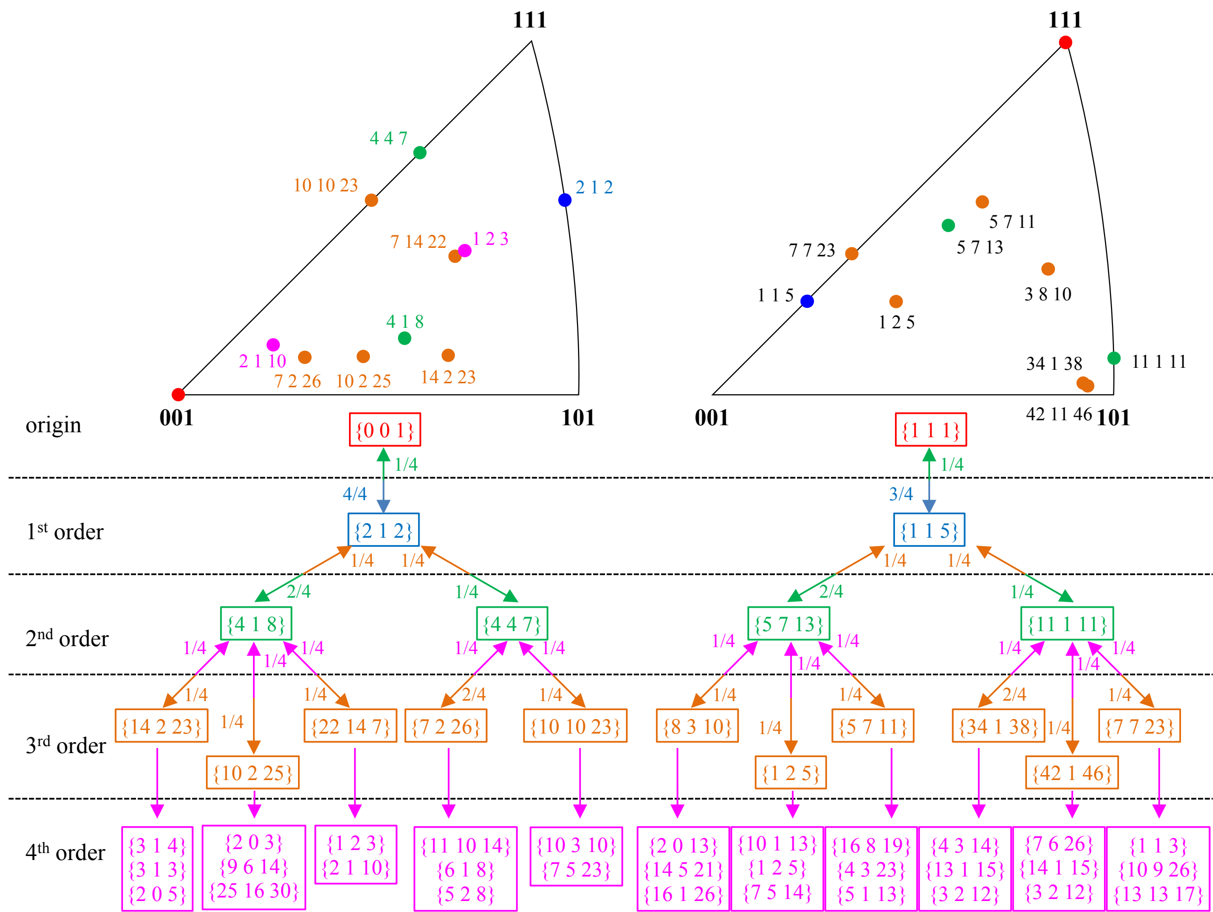

Fig. 5-11 Positions of twins of the 1st – 3rd orders (4th order is not shown) in the IPF plots and schematic representation of twin formation till the 4th order from the original {0 0 1} and {1 1 1} orientations

Fig. 5-12 shows characteristic textures of the top and bottom dies. All of the acquired IPF plots are presented in the appendix of this thesis in Fig. A. 2 - Fig. A. 4.

Top die A features a preferred orientation of {0 0 1} with twin orientations {2 1 2} of the 1st order, {1 1 3} (similar to {4 4 7}) and {1 0 2} (similar to {4 1 8}) of the 2nd order. Seven out of ten (7/10) IPF plots feature only twin orientations without coloring of the original orientations (Fig. 5-12, (a)). Three of ten (3/10) IPF plots feature green or yellow coloring of {1 0 1} orientation along with the above mentioned twins (Fig. 5-12, (b)). As these twins belong to {0 0 1} orientation and {1 0 1} is similar to {10 3 10}, is suggested that the twins originate from the orientation {0 0 1} for the top die A.

Top die B features a strongly varying texture between {0 0 1} and {1 1 1} orientations. Characteristic {0 0 1} texture is shown in Fig. 5-12 (d), which is detected for 4/10 of the measured microbumps and exhibits corresponding twins {2 1 2} and {1 0 2}. Typical {1 1 1} orientation is presented in Fig. 5-12 (e), which is indicated for 2/10 of the measured microbumps and exhibits corresponding {1 1 4} (similar to {1 1 5}) and {1 0 1} (similar to {11 1 11}) twins.

Along with differences in electroplating procedures, Cu thickness can be the reason for different orientations of the top die A (25.6 µm) and the top die B (12.6 µm). The original orientation can transform into any other orientation through the formation of twins and depends

on the Cu thickness [85]. Furthermore, IPF plots indicate mostly twin structures for the top die A, whereas top die B exhibits both the original orientations ({0 0 1} and {1 1 1}) and the twins. Stangl [140] reports that the amount of twins increases over the Cu layer thickness, which leads to the continuous change in its texture with each additional 100 nm. The results correlate well with the results of this EBSD analysis.

Bottom dies exhibit {0 0 1} preferred orientation with {2 1 2} and {3 1 3} twin structures (Fig. 5-12, (c), (f)). The bottom dies differ by the absence and presence of the CMP treatment. Additionally, the slight yellowish coloring of the {1 1 1} orientation is indicated for the bottom die B, which will be discussed in the next subchapter 5.2.4. Both bottom dies exhibit both original and twin orientations in contrast to the top die A (only twin structures), which can be also explained by the lower metal thickness of the bottom dies (2 µm).

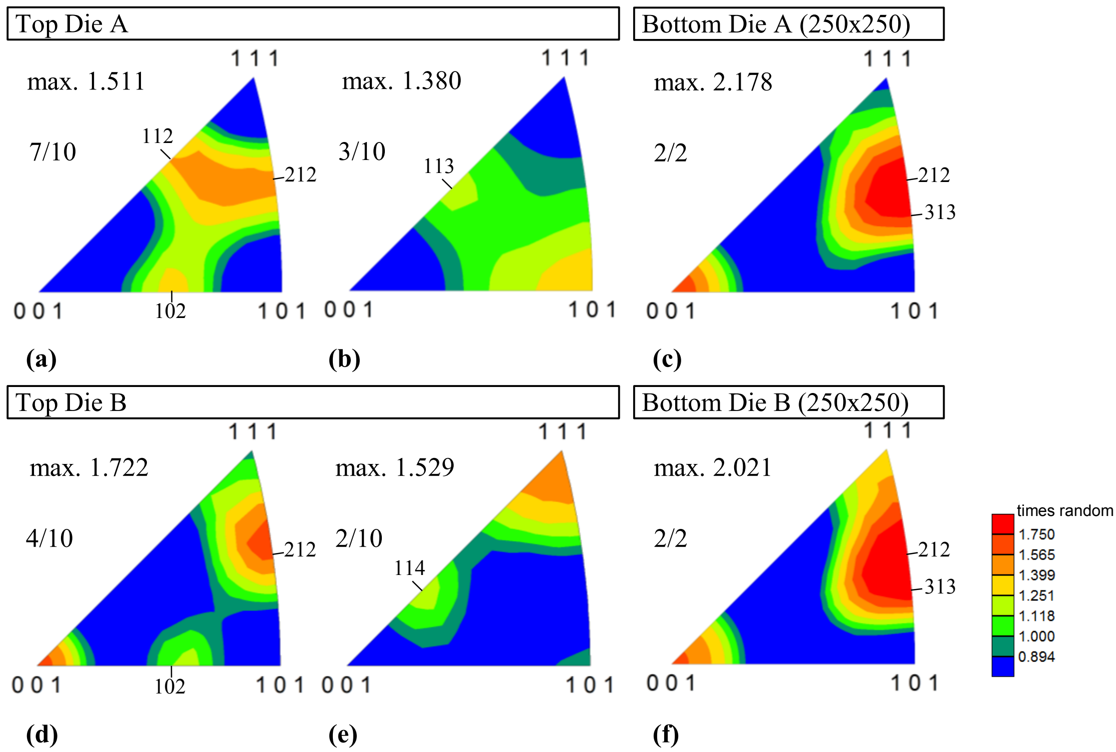

Fig. 5-12 Characteristic texture plots showing the qualitative distribution of grain orientations for top die A (a, b), top die B (d, e), bottom die A (c) and bottom die B (f)

Fig. 5-13 shows grain boundaries characterization for the top and bottom dies. The distribution of grain boundaries is similar for both types. ∑3 twins, which were described in chapter 3.1.1, are dominating among other grain boundaries with the fraction range (0.570…0.705). The next preferred orientation belongs to the ∑9 twin boundary. Bottom dies have almost no low angle grain boundaries (LAGB) in contrast to the top dies, which can be caused by the cross-sectioning of the top dies and correlates well with other literature results [85], [141].

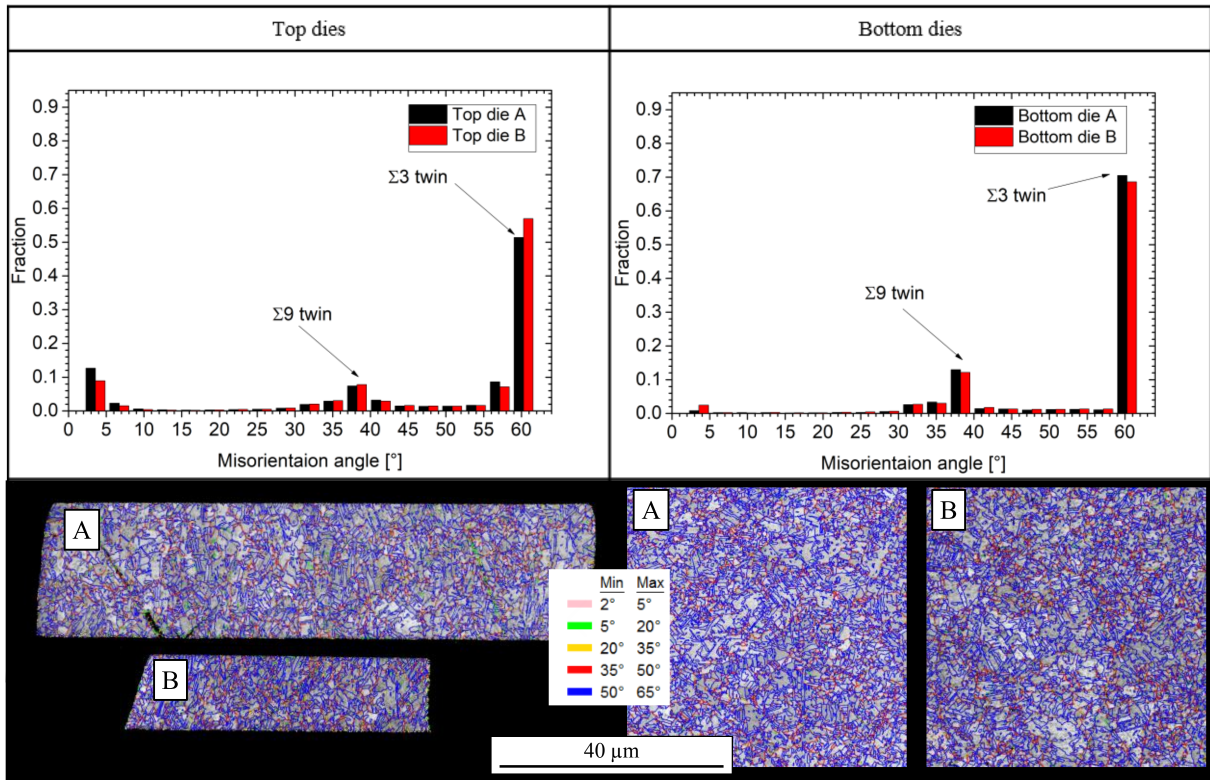

Fig. 5-13 Characterization of grain boundaries for top die A and top die B, bottom die A and bottom die B before bonding

5.2.4 Estimation of Young's modulus

Chapter 3.1.1 described the influence of Cu Young's modulus on the strength of the future Cu-Cu interconnect and its dependence on Cu grain orientation. Nanoindentation measurements, mentioned in chapter 4.1, provided Meyer hardness and Young's modulus average values for each sample. Fig. 5-14 presents the calculated distribution of Young's modulus depending on the Cu texture (chapter 3.1.1), laid over the IPF plots of the investigated samples. Calculated Young's modulus varies between 66.7 MPa for {0 0 1} texture and 191.1 MPa for {1 1 1} texture, which is confirmed by literature [86]. Young's modulus measurements in chapter 4.1 have shown higher values for top die B ((131.08±4) GPa) in comparison to top die A ((104±10.8) GPa). The results correlate well with calculated values as the presence of {1 1 1} orientations can be the reason for the increase in the average Young's modulus of the top die B.

As already mentioned, bottom dies differ by the presence (A) and absence (B) of the CMP step. Bottom dies B without CMP present higher Young's modulus (122.2±13.5) GPa in comparison to bottom dies A (109.9±10.2) GPa. EBSD measurements show also a yellowish coloring of the {1 1 1} direction with the highest Young's modulus only for the bottom die B. The bottom die A have slightly bigger grains than the bottom die B, but this can be the result of the differences in surface roughness values (better IQ for the bottom die A, less falsely detected grains). The difference in Young's modulus values can be also explained by the CMP slurry chemistry, certain substances of, which can decrease surface hardness and Young's modulus [142].

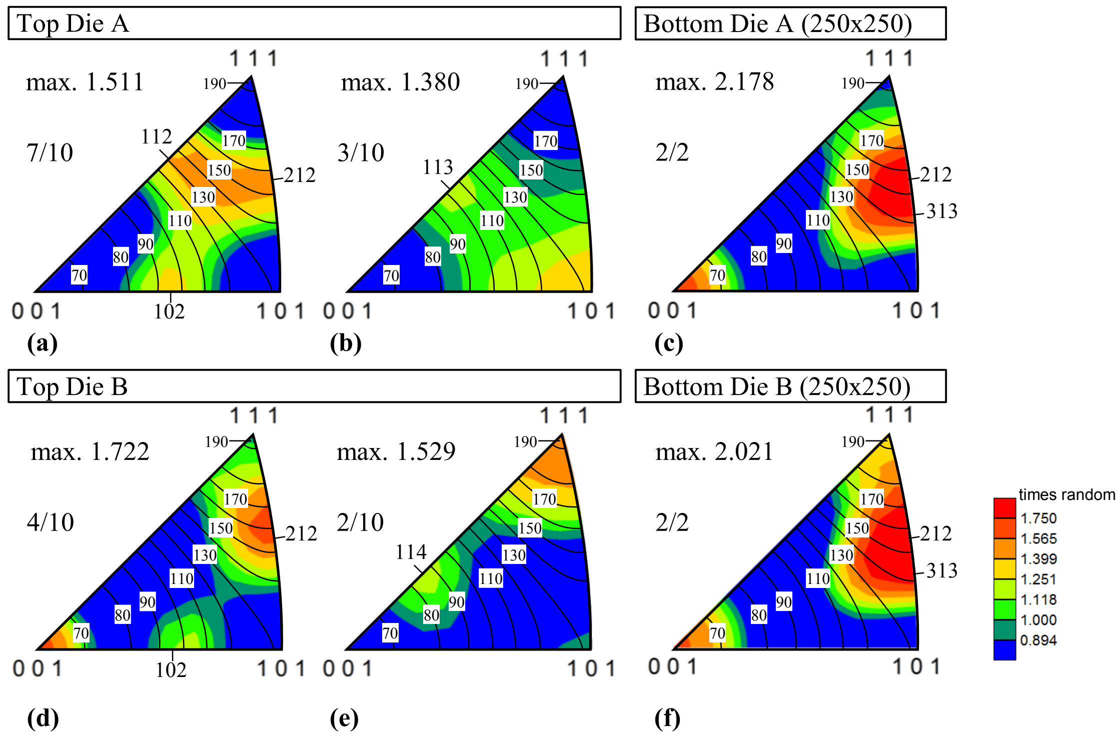

Fig. 5-14 Typical textures for the top die A (a, b) and top die B (d, e), bottom die A (c) and bottom die B (f) with the corresponding Young's modulus overlay

5.3 Summary

EBSD analysis of the samples, used for Cu-Cu bonding, was conducted in order to characterize Cu surface microstructure before bonding. The results can be summarized as follows:

1. Average grain sizes by number and by area, including and excluding twins for the top and bottom dies, have been determined.
2. Characterization of the average grain size by area provides more reliable results in comparison to the grain size by number. The average grain size by area excluding twins is 9.9 µm for the top die A (cross-section), 7.1 µm for the top die B (cross-section), 17.3 µm for the bottom die A and 15.2 µm for the bottom die B (top view, 250×250 µm^2)
3. All of the samples feature the domination of ∑3 twin boundaries in Cu microstructure with a fraction in the range of (0.570…0.705).
4. Top die A texture originates most probably from the {0 0 1} texture, which is represented by corresponding twins. Top die B varies strongly between {0 0 1} and {1 1 1} textures, which are detected in the IPF plots along with corresponding twins.
5. The difference between the orientations of the two samples correlates to the difference in their Cu thicknesses, as the amount of twins increases with Cu thickness.
6. Both bottom dies feature {0 0 1} texture whereas the bottom die B indicates additionally the {1 1 1} texture.

7. The measured Young's modulus values are well comparable to the calculated values from the corresponding textures. The differences between the measured values can be explained using textures and the calculated Young's modulus values.
8. Higher Young's modulus of the top die B ((131.08±4) GPa) in comparison to the top die A ((104±10.08) GPa), acquired using nanoindentation, correlates to the presence of {1 1 1} texture in some of the microbumps of the top die B.
9. Higher Young's modulus of the bottom die B ((122.2±13.5) GPa) in comparison to the bottom die A ((109.9±10.2) GPa) correlates to the presence of {1 1 1} texture for the bottom die B.

Having characterized the microstructure of Cu before bonding, the SAM passivation effect on Cu surface properties can be characterized and the ways of improvement of this technique can be discussed in the next chapter.

6 Influence of SAM passivation on the protection of Cu from oxidation

6.1 Experiment description

SAMs can be used as inhibitors of Cu oxidation. Nevertheless, the monomolecular coatings also start to degrade within a day if stored in air at room temperature [65]. In this work degradation of SAM is considered to be its disordering, oxidizing and desorption. Characterization of SAMs at conditions, by, which the protective effect can be prolonged, is one of the aims of this study and is presented in this chapter.

Though it is advisable to use smooth surfaces for well SAM ordering [10], the roughness of electrochemically deposited (ECD) Cu microbumps (R_a = 9 ± 0.85 nm) exceeds the roughness of physically vapor deposited (PVD) (R_a = 1 ± 0.3 nm) or ECD Cu with chemical-mechanical polishing (CMP) (R_a = 0.7 ± 0.05 nm). In this work low roughness is defined as $R_a \leq 1$ nm. In order to apply SAM passivation for Cu-Cu bonding in 3D / 2.5D integration, it is necessary to investigate SAM protective effect on Cu ECD microbumps. This chapter highlights factors influencing SAM protective effect, which imply observation of H_2SO_4 10 % cleaning effect on Cu surface, analysis of the influence of SAM chain length and storage conditions.

Fig. 4-1 presents experimental setup implying variable parameters and evaluation methods of SAM passivation. C16 SAM represents long-chain molecules and is involved only in one investigation using infrared spectroscopic ellipsometry (IRSE). This experiment is carried out to confirm that long-chain SAMs protect Cu from oxidation for a longer period in comparison to short-chain SAMs (represented by C6). However, long-chain SAMs are hard to remove from Cu before bonding (see subchapter 3.2.2). C6 has been chosen for further experiments to find out, at, which conditions short-chain SAM protective function can be prolonged. All pre-treatments, including SAM passivation, described in this chapter, were carried out in a glove box system with an inert gas atmosphere (see chapter 4.2).

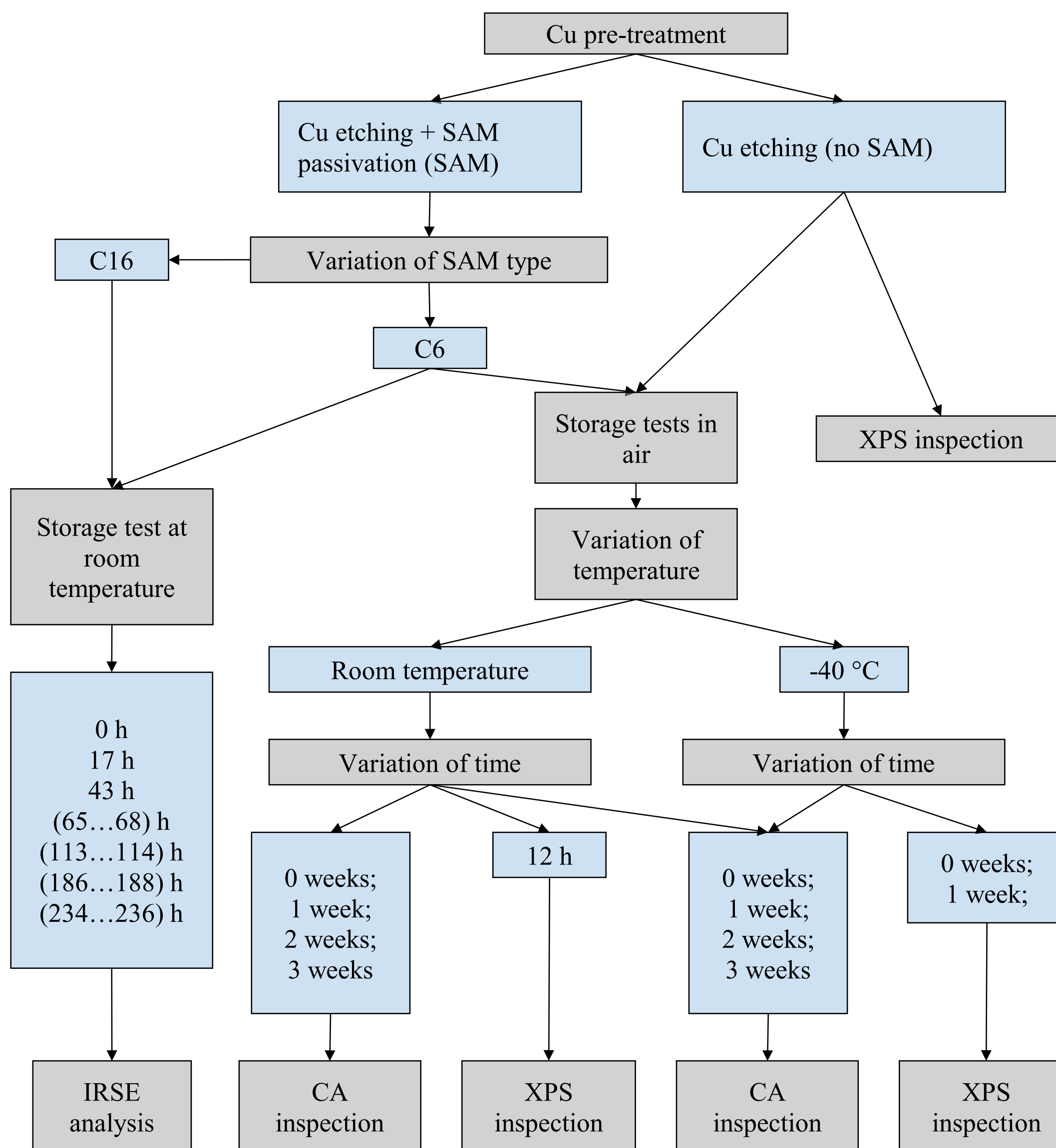

Fig. 6-1 Experimental setup for characterization of SAM protective effect depending on its chain length, storage temperature and time

Having presented the experimental plan, the results of the experiments can be reported and discussed in the next chapter.

6.2 Factors contributing to the prolongation of SAM protective effect

6.2.1 Results and discussion

6.2.1.1 Characterization of the Cu surface after etching

The etching procedure is precedential for each passivation process. Etching by H_2SO_4 10 % for (5…20) s is one of the standard etchants used to clean Cu from oxides and contamination layer. However, it is important to assess the effectiveness of H_2SO_4 10 % on the removal of Cu oxide before SAM passivation. As discussed in chapter 4.3.2, XPS analysis in this study is

usually divided into two measurements: in the initial state and after the cleaning step. The low-energy cleaning step is usually enough to remove the C-containing contamination layer on Cu (in this case 600 eV for 2 min). To remove Cu oxide additional Ar^+ ion bombardment at higher energy (2 keV) was carried out for varied time intervals: for 20 s, 40 s and 80 s. The purpose is to compare the number of bombardment steps in order to fully remove O content on samples before and after etching with H_2SO_4 10 %. This experiment was performed by the Multiprobe® surface analysis unit (Omnicron NanoTechnology GmbH). Si chips with PVD Cu were used for this purpose. Fig. 6-2 reflects atomic concentrations of C1s (a), O1s (b) and $Cu2p_{3/2}$ (c) on samples before and after etching with H_2SO_4 10 % for (5…10) s. The thickness of the Cu oxide layer cannot be estimated accurately, because of the overlapping of Cu2p signals of oxidic and metallic Cu. However, there is information from literature about the formation of 1.21 nm of Cu_2O already after 10 min and 1.31 nm of CuO after 700 h of air exposure at room temperature [93]. Density functional theory (DFT) has been applied in addition to XPS measurements to obtain this information.

Fig. 6-2 (a) shows almost no C content (< 3 at.%) after the first cleaning step (Ar^+ ion bombardment for 2 minutes at 600 eV). This proves that the adventitious organic contamination layer is removed for both chips, with and without etching. Considering atomic concentrations of O1s (Fig. 6-2, (b)), O content is almost completely removed on the etched sample after the cleaning step (1 at.%). In contrast, O is still present on Cu (5 at.%) even after four Ar^+ ion bombardment steps for the untreated sample. The lower the O content, the higher is the percentage of Cu (Fig. 6-2, (c)). To sum up, the results suggest the full removal of Cu oxide from the Cu surface by H_2SO_4 10 %.

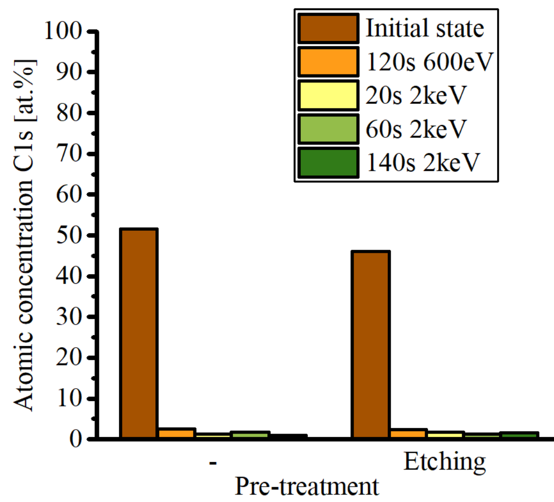

(a)

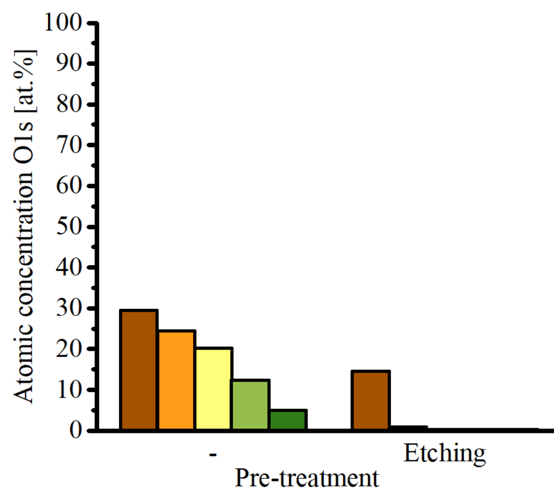

(b)

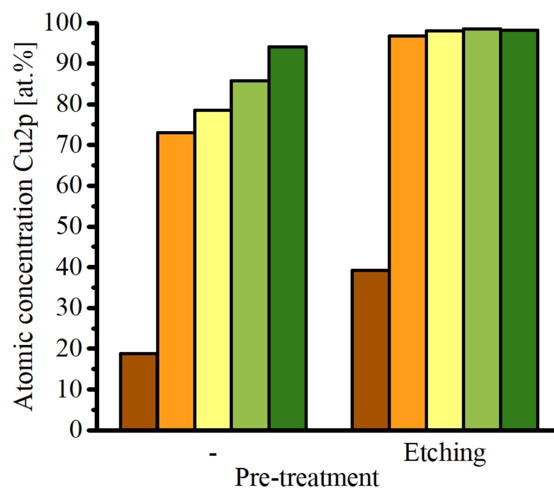

(c)

Fig. 6-2 Atomic concentrations of C1s (a), O1s (b) and Cu2p$_{3/2}$ (c) on Cu surface without (-) and with H_2SO_4 10 % etching (Etching) in the initial state (initial state), after Ar^+ ion bombardment for 2 min at 600 eV (cleaning step), after 20 s at 2 keV (20s 2keV), after 60 s at 2 keV (60s 2keV) and after 140 s at 2keV (140s 2keV)

Proving the complete oxide removal after Cu surface etching has been a significant step, which can serve as reliable basics for further characterization, which imply an analysis of the chain length and low-temperature storage impact and will be discussed in the next subchapter.

6.2.1.2 Influence of SAM chain length on SAM protective function after room temperature storage

Infrared spectroscopic ellipsometry (IRSE) is applied to characterize the influence of SAM chain length on its protective function as an oxidation inhibitor for Cu. Long-chain thiols are usually those having more than nine C atoms in a chain [48]. Sputtered Cu surface passivated with *n*-alkanethiolates can be characterized by four absorption bands in infrared spectrum summarized in Tab. 4-7 (chapter 4.3.3): CH_2 symmetrical $\nu_s(CH_2)$ and CH_2 asymmetrical $\nu_a(CH_2)$ vibration modes, CH_3 asymmetrical in-plane vibration mode $\nu_{a,ip}(CH_3)$, CH_3 asymmetrical vibration mode influenced by Fermi resonance interactions $\nu_{s,FR}(CH_3)$ [48], [64]. CH_3 asymmetrical out-of-plane vibration mode $\nu_{a,op}(CH_3)$ cannot be detected because of the signal noise [48].

The sample type, used for this experiment, is a (13 × 13) μm^2 Si die (750 µm thick) with Ti (150 nm thick) and sputtered Cu (2 µm thick) on top with an average surface roughness of approximately 2 nm. Two types of SAM passivation are used: using 1-hexanethiol (C6) and 1-hexadecanethiol (C16). The preparation is carried out in a glove box with an inert gas atmosphere ($O_2 < 0.5$ ppm). Fig. 6-3 presents IR absorption bands of methyl (CH_3) and methylene (CH_2) groups for such samples: with C6-SAM (C6); with C16-SAM (C16); without SAM (no SAM); without SAM after storage for two weeks in laboratory cleanroom in air at room temperature (no SAM, 2 weeks).

The spectra highlight that CH_2 peak positions of C16 are detected at slightly lower frequencies (wavenumbers) in comparison to the other sample types (Fig. 6-3). Furthermore, amplitude ratios of CH_2 are higher for samples without SAM and increase after the two weeks of storage. Apart from this, vibration mode $\nu_{a,ip}(CH_3)$ has a higher amplitude ratio for the samples with SAM passivation.

The experiment comprises storage of samples with C6-SAM, C16-SAM and samples without SAM (etched before storage) at room temperature in air. Fig. 6-4 shows the influence of storage time on the SAM aging/degradation rate for short- and long-chain alkanethiolates. To highlight the differences in the absorption lines all spectra were divided by the corresponding spectra of Cu/SAM stored for 17 h. The results show that $\nu_s(CH_2)$ and $\nu_a(CH_2)$ for both SAM types increase in amplitude ratios with storage time. Band amplitudes of C6-SAM have a higher growth rate and are becoming more similar to the spectra of samples without SAM. Furthermore, $\nu_a(CH_2)$ vibration modes for C16 show absorption bands at lower frequencies (2918 cm^{-1}) even after 236 h in air. The growth of a peak $\nu_a(CH_2)$ for this sample type is also detectable.

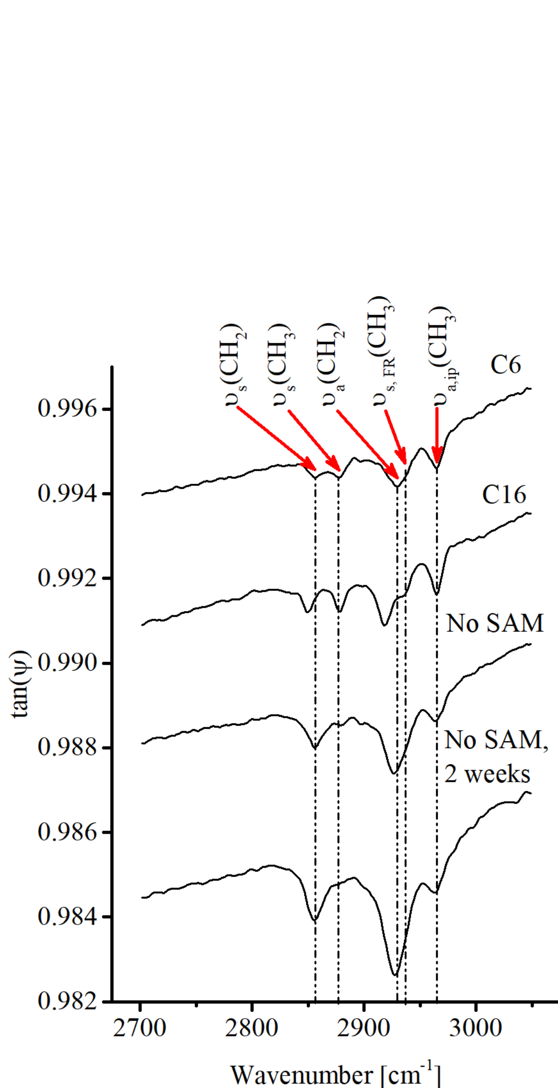

Fig. 6-3 IRSE spectra of Cu with C6-SAM (C6), C16-SAM (C16), without SAM (no SAM) and without SAM after storage for two weeks at room temperature in air (no SAM, 2 weeks)

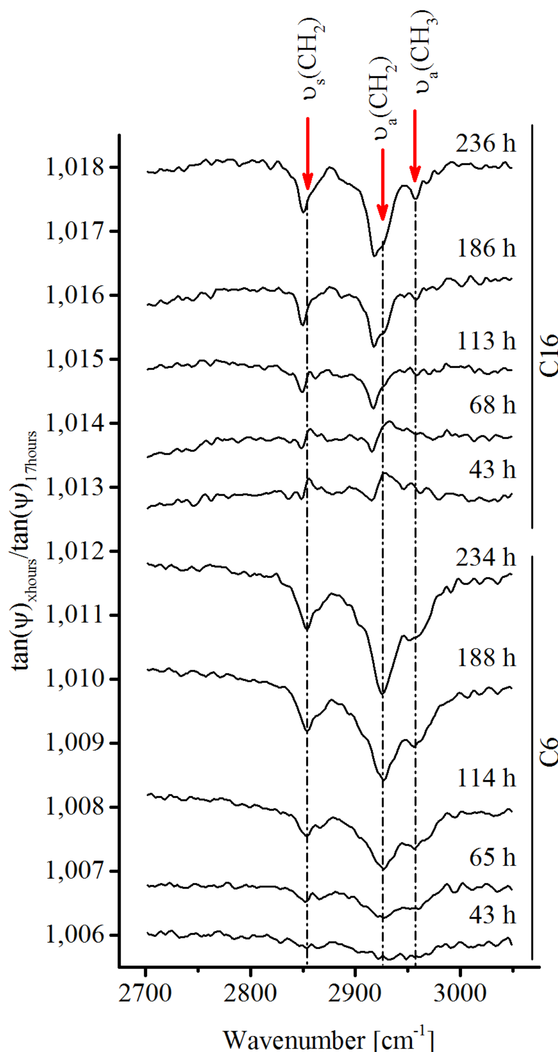

Fig. 6-4 Referenced IRSE spectra of Cu with C6-SAM (C6), C16-SAM (C16), after storage for 43 - 236 h at room temperature in air divided by IRSE spectra of Cu with C6 or C16, respectively, stored for 17 h in same conditions

The IRSE investigation aimed to compare the influence of SAM chain length on its degradation rate. Keeping this in mind, it is important to consider peak positions for C6 and C16 (Fig. 6-3). CH_2 absorption bands for C16 are found at lower wavenumbers than C6 in the initial state (Tab. 4-7). Shifting of C16 absorption bands towards lower frequencies indicates better monolayer ordering and its similarity to the crystalline structure [48].

Cu surface with SAM passivation can be differentiated from an uncoated surface by $\nu_{s,FR}(CH_3)$ vibration modes. Detection of this mode is a characteristic feature of the presence of SAM on the Cu surface as CH_3 binding is a terminal group of each alkyl chain. These terminal groups are very well ordered and, therefore, easily detectable before the storage tests.

In order to interpret the results of IRSE measurements, it is important to understand the orientation of SAM chains and transition dipole moments of their vibrations relatively to the xyz-coordinate system (Fig. 6-5). The orientation of an alkyl chain is defined by three angles:

Θ, Φ and Ψ (Fig. 6-5, left). The right figure side shows that the transition dipole moment of $\nu_s(CH_2)$ is oriented along the bisector of the HCH angle in the HCH plane perpendicularly to the CCC molecular axis and lying in the CCC plane. The transition dipole moment of $\nu_a(CH_2)$ vibration is directed along HH methylene group perpendicularly to the CCC plane. $\nu_s(CH_3)$ vibration has a transition dipole moment oriented parallel to the diagonal of the pyramid formed by the methylene group, oriented along with the terminating CC bond [143].

The growth of methylene (CH_2) band amplitude for both SAM types takes place during the storage tests (Fig. 6-4). Only projections of the transition dipole moments of molecular vibrations in the z-direction are found in the IR spectrum due to the selection rule in infrared spectroscopy for thin films on a metallic surface. Therefore, the increase of $\nu_s(CH_2)$ and $\nu_a(CH_2)$ band amplitudes is most probably connected to monolayer tilting (tilt angle Θ). Horn et al. claim that this is caused by the change of the chemical state of the Cu surface, i.e. its oxidation or oxidation of SAM [64].

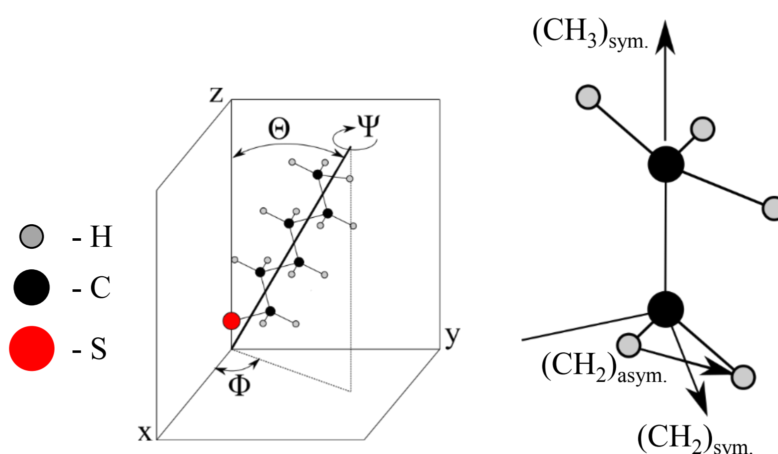

Fig. 6-5 Schematic view of the orientation of C6 SAM (left) and the transition dipole moments of some of the CH_2 and CH_3 vibrations (right). Θ, Φ and Ψ angles define the orientation of the C6 chain as follows: initially, a CCC backbone is normal to the surface and parallel to the z-x plane; then the chain is tilted by the angle Θ relative to the z-axis, then the chain is twisted by the angle Ψ and rotated around the z-axis by the angle Φ (adapted from [143]**)**

These results suggest that Cu with C16 SAM oxidizes slower in comparison to Cu with C6 SAM. This is derived by less ordering and a higher number of defects in short-chain SAMs in comparison to long-chain SAMs, which is confirmed by literature [48]. As long-chain SAMs are more complicated to remove before bonding, the ways of lifetime prolongation for short-chain SAMs (storage at -40 °C) were investigated.

6.2.1.3 Influence of room and low-temperature storage on the wettability of the Cu surface

The previous chapter reviewed long-chain SAMs considering their degradation rate in comparison to short-chain SAMs. Long-chain SAMs are complicated to remove before bonding due to the necessary increase in annealing time and temperature [57]. Thus, the ways of prolongation of short-chain SAMs lifetime were investigated. The protective effect of SAM has been investigated in literature at 5 °C and -30 °C since it is well known that SAM quality is temperature dependent [57], [67], [68].

The wettability of the Cu surface can be very sensitive to the changes in its chemical composition. Sung et al. reported a correlation of XPS data and CA measurements [45]. A decrease of CA values as a function of annealing time in air ambient is accompanied by the growth of O fracture on Cu coated with 1-hexadecanethiol (C16) measured by XPS. Therefore, the CA technique is chosen for test experiments of sample storage at different conditions. Laibinis et al. suggest that thicker SAMs inhibit Cu oxidation for longer periods than the thinner species [46]. In this publication, both XPS and CA techniques have been used to evaluate the degradation rate of SAMs containing 18 C atoms.

In this thesis, wettability properties are assessed by the sessile drop contact angle (CA) technique. If the CA is higher than 90 °, the surface is supposed to be hydrophobic. If CA is lower than 90 °, the surface is hydrophilic [69]. Cu surface is highly hydrophilic instantly after Cu deposition, less hydrophilic after oxidation in the oven (CA≈43 °) and Cu has CA values of approximately (90…100) ° after adsorbing volatile organic contamination layer due to storage in air [144]. Cu is highly hydrophobic (CA > 115 °) immediately after the passivation with SAM [45], [75]. Considering this, a mechanism of SAM behavior, based on the wettability of the passivated and stored Cu surface, can be suggested.

Sputtered Cu samples with (SAM) and without SAM (no SAM) passivation were stored for one, two and three weeks at room temperature and -40 °C in air for comparison. Fig. 6-6 (a) presents the influence of storage time on the surface wettability (CA) at room temperature. The results reveal that Cu with SAM has high hydrophobicity (116 °) directly after the preparation. This value drops to 84 ° after the first storage week. This can be caused by the SAM degradation, characterized by Cu oxidation and sulfonate formation [46], [65]. After the next two weeks, CA increases up to 95 °. This can be caused by the re-adsorption and growth of the adventitious C contamination layer on Cu formed in air. CA of samples without SAM is 105 ° in the initial state and also reduces down to 95 ° after three weeks of storage. This can be caused by etching with H_2SO_4 10 % before storage. The drying effect is typical for this acid, which increases Cu hydrophobicity. Fig. 6-6 (b) shows samples stored at -40 °C and reflects near to constant values of CA during three weeks. CA is 105 ° for samples without and 116 ° for samples with SAM coating, which suggests SAM stability and protection of Cu during this time.

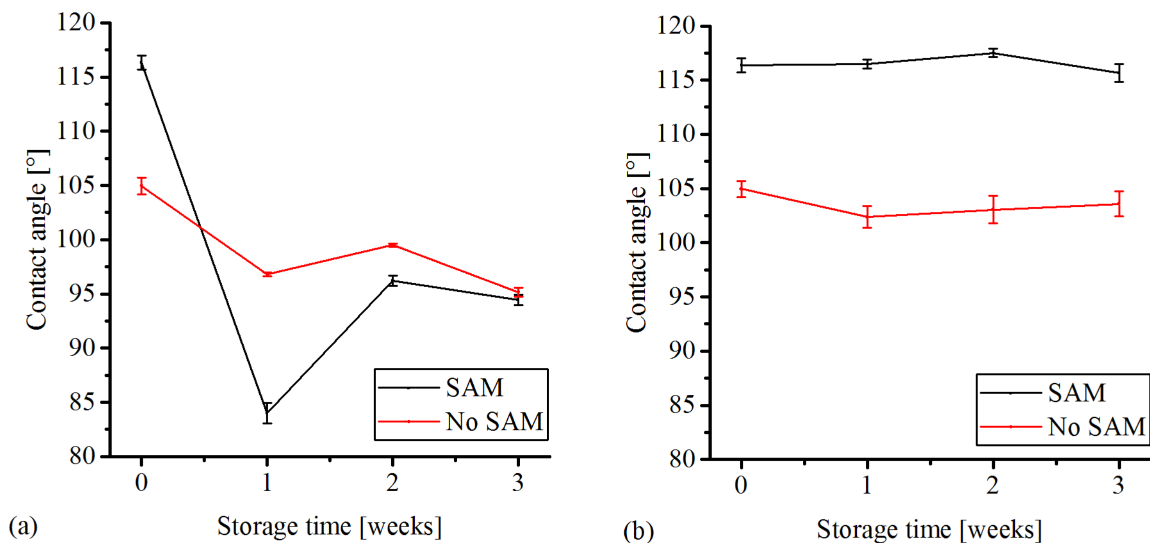

Fig. 6-6 Influence of storage at room temperature (a) and -40 °C (b) in air on the wettability (contact angle) of the samples with SAM (SAM) and without SAM (no SAM) passivation

6.2.1.4 Influence of room temperature storage on the chemical composition of the Cu surface

In order to obtain more precise information about the chemical composition of the Cu surface at different storage conditions, with and without SAM, it has been analyzed by XPS.

Fig. 6-7 - Fig. 6-9 show C1s, O1s and S2p XPS spectra of PVD Cu with and without SAM stored at room temperature for 12 h. These XPS measurements were performed by PHI ESCA 5700 (Physical Electronics). Cu LMM spectra were omitted because of the similarities of the results for samples with and without SAM. These measurements were carried out using an Al-Kα X-ray source. Peak assignments can be found in chapter 4.3.2.

Fig. 6-7 (a) and (c) show that the peak intensity at 285 eV (C-C binding) is higher for the coated sample. The sample without SAM (Fig. 6-7, (c)) reflects an additional peak at 289 eV (C-O-C binding), which is not typical for the sample with SAM. A low amount of C is detected after the cleaning step on both samples (Fig. 6-7, (b), (d)), but a still higher amount is detected on the passivated surface (Fig. 6-7, (b)).

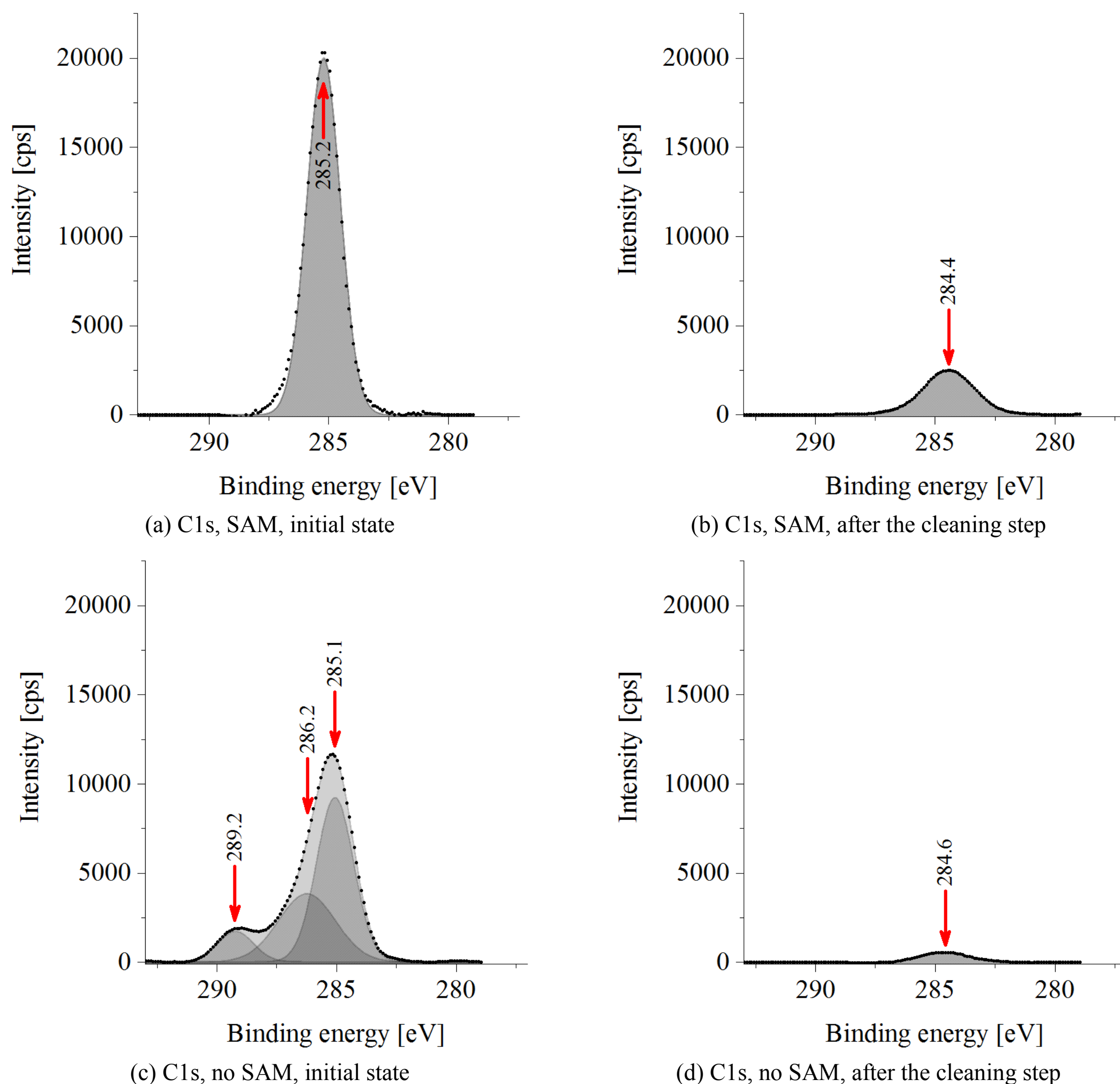

Fig. 6-7 XPS spectra of C1s for the samples with (SAM) and without SAM (no SAM) passivation after 12 hours at room temperature in air in the initial state (a, c) and after the cleaning step (b, d)

O1s XPS spectra (Fig. 6-8, (a), (c)) exhibit peaks at 531-533 eV (Cu_2O, $Cu(OH)_2$) in the initial state whereby O content is higher for the uncoated Cu surface. Fig. 6-8 (b) shows that O is barely seen for the SAM sample after the cleaning step. Cu without SAM shows peaks at 532 eV ($Cu(OH)_2$) and 530 eV (Cu_2O) and has a higher O content (Fig. 6-8, (d)) in comparison to the sample with SAM.

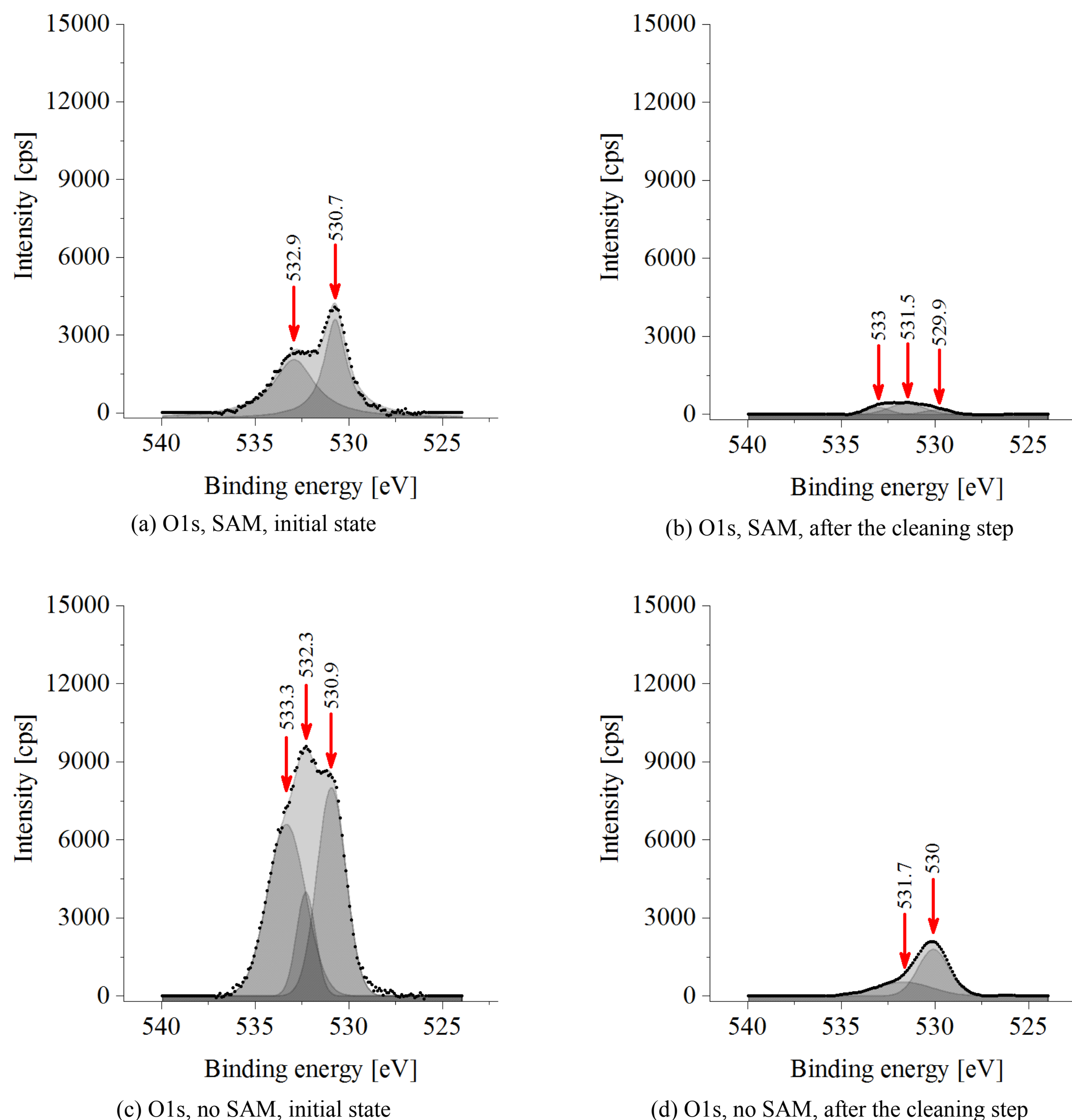

(a) O1s, SAM, initial state

(b) O1s, SAM, after the cleaning step

(c) O1s, no SAM, initial state

(d) O1s, no SAM, after the cleaning step

Fig. 6-8 XPS spectra of O1s for the samples with (SAM) and without SAM (no SAM) passivation after 12 hours at room temperature in air in the initial state (a, c) and after the cleaning step (b, d)

Analyzing S2p spectra, one peak at 162.8 eV is detected for the passivated sample (Fig. 6-9, (a)) that is completely removed after the cleaning step (Fig. 6-9, (b)). This peak position is assigned to thiolates (see Tab. 4-6). No sulfonates (products of SAM oxidation) are detected, the peaks of, which would appear starting from 166 eV.

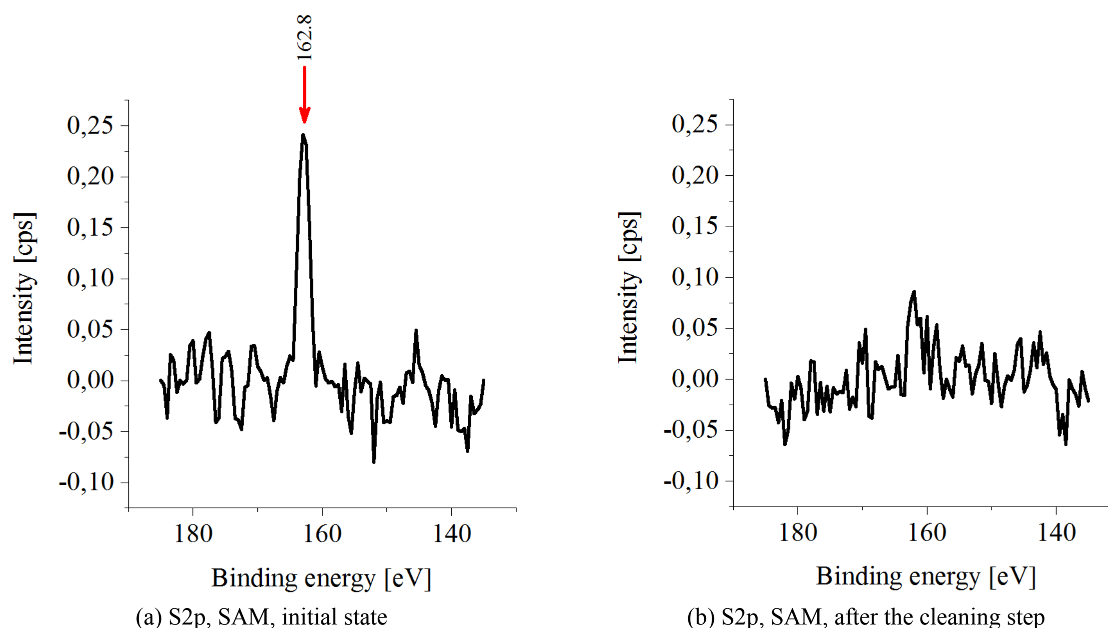

(a) S2p, SAM, initial state (b) S2p, SAM, after the cleaning step

Fig. 6-9 XPS spectra of S2p for the samples with (SAM) passivation after 12 hours at room temperature in air in the initial state (a) and after the cleaning step (b)

The assigning of XPS peaks is listed in Tab. 4-5 - Tab. 4-6 (chapter 4.3.2). Fig. 6-7 (a), (c) shows that the sample without SAM shows adsorption of C-O-C bindings at 289.2 eV (Tab. 4-5) after 12 hours of storage in air, which is not detected on samples with SAM. This suggests that, at least during 12 hours of air exposure, the SAM layer hampers the growth of not only oxides but also of the oxygen-containing organic layer [8].

Nevertheless, O content is detected on both surfaces in the initial state with a higher percentage on the unprotected Cu (Fig. 6-8, (a), (c)). O bindings on Cu/SAM are almost completely removed after the cleaning step (Fig. 6-8, (b)). An additional peak at 530 eV, assigned to Cu_2O, appears on the sample without SAM after the cleaning step (Fig. 6-8, (d)). A barely detectable peak at the same binding energy is detected on Cu/SAM. This suggests the start of Cu oxidation and its higher rate on the unprotected sample.

S2p spectra (Fig. 6-9, (a)), nevertheless, presents no peak at around 168 eV (sulfonate binding), which suggests that SAM was not oxidized during 12 hours of air exposure. This reflects the oxidation process of samples with SAM already mentioned in literature [45], [63], [75]. Cu oxidation happens before the transformation of thiolates to sulfonates. But still, the presence of SAM can retard or even terminate this oxidation process by inhibiting O penetration.

6.2.1.5 Influence of low-temperature storage on the chemical composition of the Cu surface

Characterization of SAM protective capability on a relatively rough surface of as-plated Cu (R_a = 10 nm) and assessing the SAM protective effect during the storage at low temperature (-40 °C) were carried out using XPS atomic concentration measurements.

Fig. 6-10 presents atomic concentrations of O1s, Cu2p, S2p and C1s for the samples before and after storage at -40 °C. All samples were for at least 2 h on air due to their transportation to the XPS chamber.

Fig. 6-10 (a) reveals approximately two times higher percentage of O on the samples without SAM in comparison to samples with SAM passivation either before, or after the storage test. Noteworthy is that O concentration is larger than 20 at.% on the unprotected samples and almost completely removed (< 3 at.%) for Cu/SAM after the cleaning step (for 120 s at 500 eV). Thus, the percentage of detected Cu in the initial state is lower for the uncoated samples in comparison to coated samples (Fig. 6-10, (b)). Bare Cu surface is seen for Cu/SAM (> 95 at.%). Only 72 at.% for Cu without SAM and 98.6 at.% for Cu with SAM coating are detected after the cleaning step. Percentage of S (4 at.%) on Cu/SAM stays unchanged after one week of air exposure at -40 °C (Fig. 6-10, (c)). C and S containing bindings are almost completely removed after the cleaning step for all of the samples (Fig. 6-10, (c), (d)).

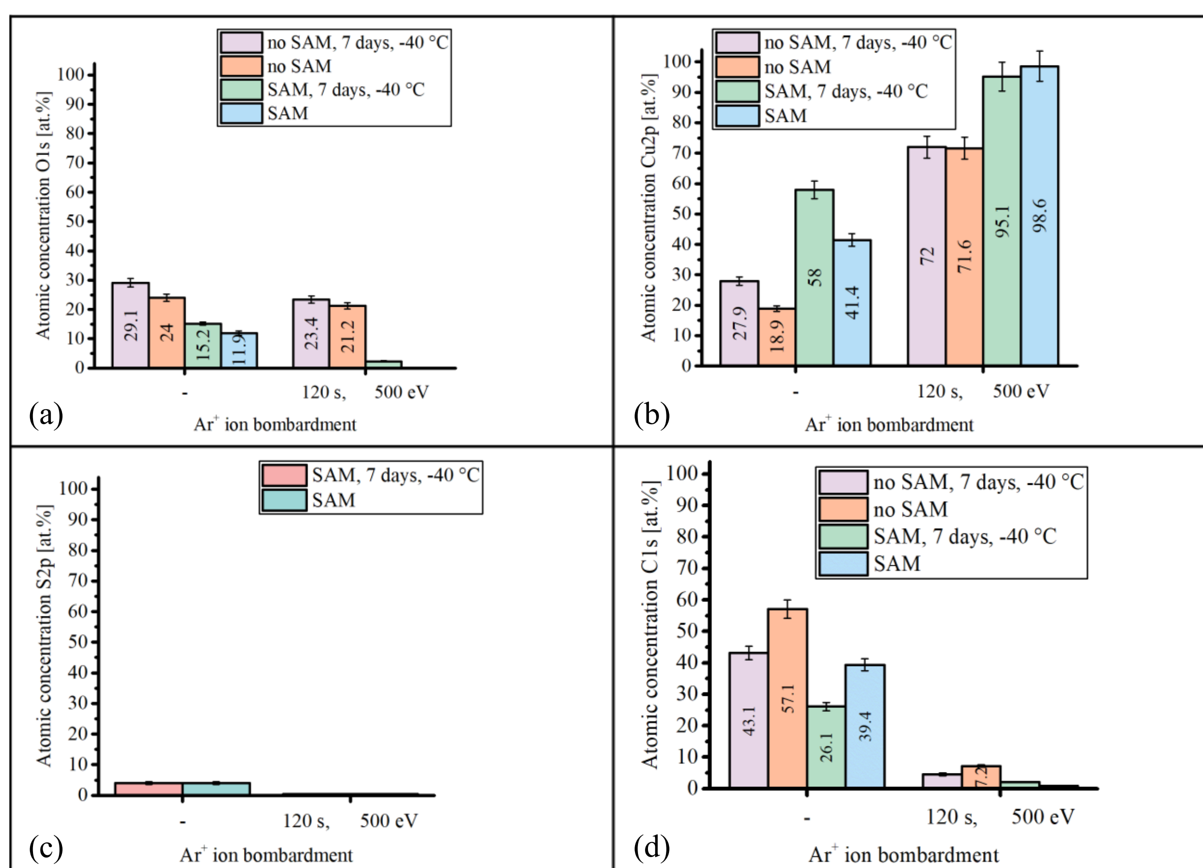

Fig. 6-10 Atomic concentrations of O1s (a), Cu2p (b), S2p (c) and C1s (d) for the samples with (SAM) and without SAM (no SAM) before and after storage for 7 days at -40 °C (7 days, -40 °C) before and after the cleaning step (Ar^+ ion bombardment)

As it has already been mentioned, SAMs have a better ordering upon lowering storage temperature [11], which can be very useful for the prevention of O penetration to the Cu surface. Due to the transportation time to the XPS vacuum chamber, all samples adsorbed an organic contamination layer in form of O-H, O-C and C-C bindings. Thus, Cu with SAM also exhibits O content in the initial state. After the cleaning step O is still present on the unprotected samples

and is absent for Cu/SAM, which suggests that SAM coating protects Cu from oxidation during one week at -40 °C. The amounts of Cu, C and S confirm the above-mentioned statement and the accuracy of the results. Based on IR spectroscopy measurements, Nuzzo et al. propose a theory of building up two chains per unit cell upon cooling, which results in higher monolayer density and coverage [11]. At lower temperatures (up to -193 °C) IR SAM peak intensities increase. The change in monolayer density comes supposedly from the disappearance of gauche conformations.

6.3 Summary

Characterization of the impact of SAM on the prevention of Cu oxidation has been presented in this chapter. The conditions for a long-term SAM lifetime have been discussed. The results can be summarized as follows:

1. A higher atomic concentration of Cu oxide is detected for Cu without passivation in comparison to Cu with SAM after 12 hours of storage at room temperature in air. No sulfonates (products of SAM oxidation) and negligibly low oxidation of Cu are detected for Cu/SAM, which confirms that Cu oxidizes before the sulfonates are starting to form and that SAM retards this oxidation process.
2. The length of the SAM chain influences the rate of Cu oxidation or the duration of its protection. The degradation rate of long-chain C16 SAM is slower compared to short-chain C6 SAM due to the higher ordering of the long-chain SAMs and lower amount of defects. The results also show that SAM degradation is a gradual process.
3. Storage of electroplated Cu (R_a = (8…10) nm) with short-chain (C6) SAMs at -40 °C for one week has shown a considerable effect on SAM stability in air conditions. No degradation of the monolayer or oxidation of Cu could be detected on Cu/SAM in contrast to samples without SAM. This confirms the suitability of SAM passivation for electroplated Cu microbumps, which can be a useful technique in 2.5D / 3D integration processes.

The discussed in this chapter improvement methods for the short-chain SAM protective function can be implemented to optimize the Cu-Cu bonding technologies. Therefore, the results of TC bonding with SAM after storage at low temperature (-18 °C), as well as SAM desorption conditions are presented and discussed in the next chapter.

7 Investigation of Cu-Cu thermocompression bonding with SAM passivation

7.1 Experiment description

TC bonding with SAM has already been investigated in the literature using SAM *in-situ* thermal desorption in the inert gas atmosphere (subchapter 2.2.2). The desorption conditions, however, have not been investigated in detail. For instance, it has not been investigated, if the Cu surface is free from oxides after the desorption procedure. Furthermore, shear strength tests have been carried out whereas the distribution of fracture surface types remains unknown. Therefore, the characterization of SAM desorption conditions and their influence on Cu-Cu bonding quality is addressed in subchapter 7.2.

The previous subchapter 6.2.1.5 discussed the influence of storage at -40 °C on SAM protective effect for electroplated Cu with an average roughness of (9 ± 0.75 nm). The results have shown a very positive effect on the preservation of the protective function of SAM. Subchapter 7.3.1.1 presents the characterization of the effect of storage at -18 °C on the chemical composition of ECD Cu. This temperature has been chosen to meet the requirements of industrial mass production where a simple freezer is in common use. Investigation of Cu-Cu bonding quality after such low storage tests has not been investigated systematically in literature. Hence, subchapters 7.3.1.3 and 7.3.1.2 comprise a detailed analysis of the shear strength, distribution of fracture surfaces as well as characterization of bonding interface of the bonded dies after the storage at -18 °C.

Fig. 7-1 presents a scheme of the experiments and assessment methods of the results in order to give the answers to the questions stated above.

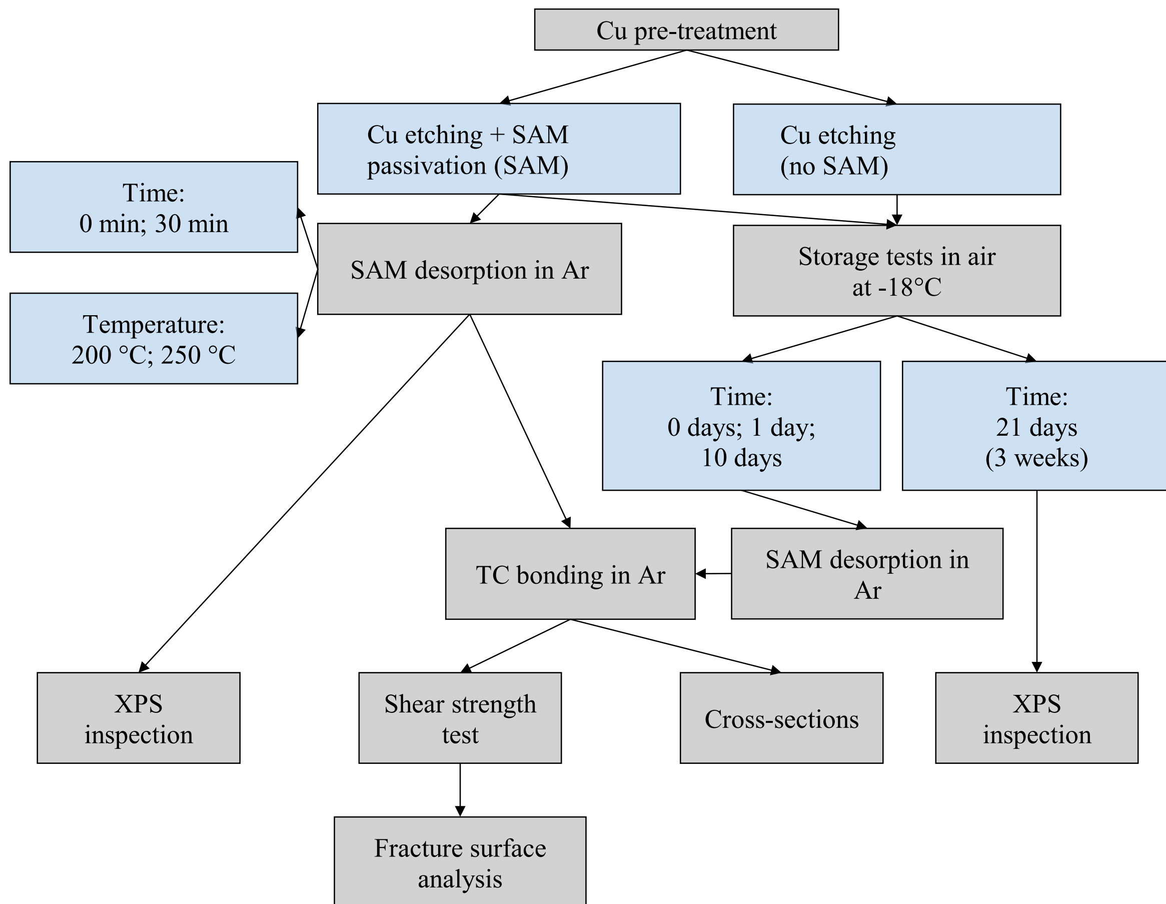

Fig. 7-1 Experimental setup for the investigation of the influence of desorption and storage conditions on the quality of Cu-Cu interconnects

The bonding parameters, which were kept constant are listed in Tab. 7-1.

Tab. 7-1 Parameters for TC bonding used in this chapter

Bonding parameter	Value
Set bonding pressure, MPa	40
Set bonding temperature, °C	250
Bonding time, min	30
Bonding area, mm^2	7.2
Sample pair (described in chapter 4.1)	top die A and bottom die A

Fig. 7-2 presents a bonding profile for the set bonding temperature and set bonding force on the Alpha Design bonder (subchapter 4.4.1). Temperature profile starts 2 s later than force profile in order to avoid additional oxidation before bonding.

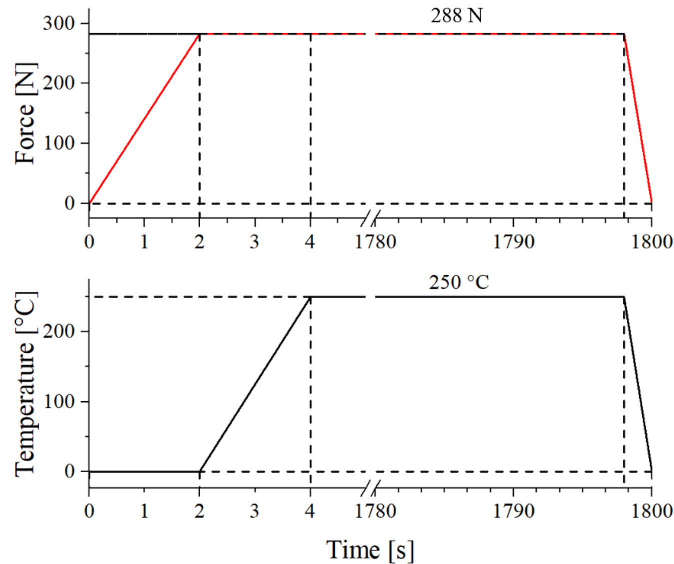

Fig. 7-2 Set bonding profile for TC bonding in Ar in Alpha Design bonder

Fig. 7-3 presents a part of the cross-section of bonded dies with only one bump. The Cu microbump is situated on the top die and the bottom die is fully covered by an electroplated Cu layer.

Fig. 7-4 shows typical types of fracture surfaces after shear strength tests: Si fracture (a); Ti fracture (b); Cu fracture (c) and no contact (d).

Normally, die-to-die bonding is characterized by high deviations in shear strength [12], [111], [114]. Consequently, it is important to analyze the fracture surface of the sheared chips to make more reliable conclusions. For instance, fracture, which occurs through Si (Fig. 7-4, (a)) or an adhesive layer of Ti or Ta (Fig. 7-4, (b)), is evidence of a strong interconnect [145], [146], as it suggests that Cu-Cu shear strength is higher. Fracture at TiW/Si (or Ti/Si in chapter 8) interface is referred to as “Ti” fracture in this study. The non-planar fracture close to the bonding interface is named “Cu fracture” in this study (Fig. 7-4, (c)). Cu fracture suggests lower mechanical strength of the interconnect. If the bumps are not in contact with the bottom die (e. g. due to tilt issue, not enough bonding force, etc.), the fracture surface is named as “no contact” whereby no interconnect is formed (Fig. 7-4, (d)). Fig. 7-5 shows parts of bottom dies A after shear strength tests with Si and Ti fractures (Fig. 7-5, (a)) and Si, Ti, Cu and “no contact” fractures (Fig. 7-5, (b)) using LEXT OLS4100 confocal microscope. These fracture types are characterized by SEM and EDX in chapter 8 more detailed.

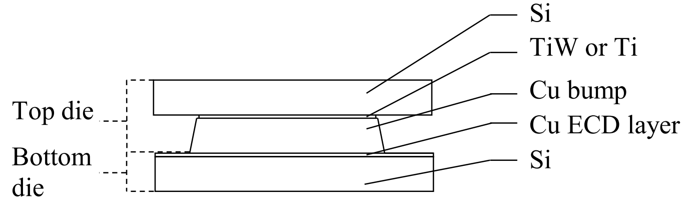

Fig. 7-3 Schematic layer stack of the bonded interconnect

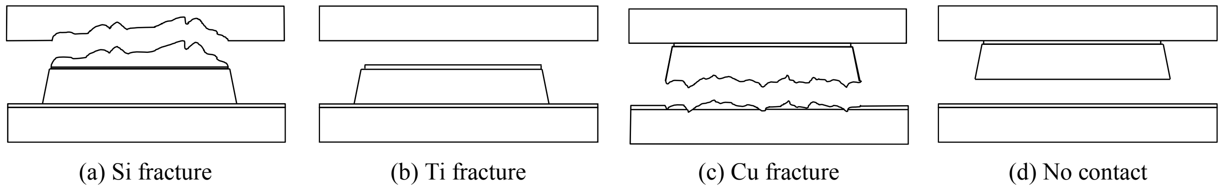

Fig. 7-4 Types of fracture surfaces in schematically presented cross-sections

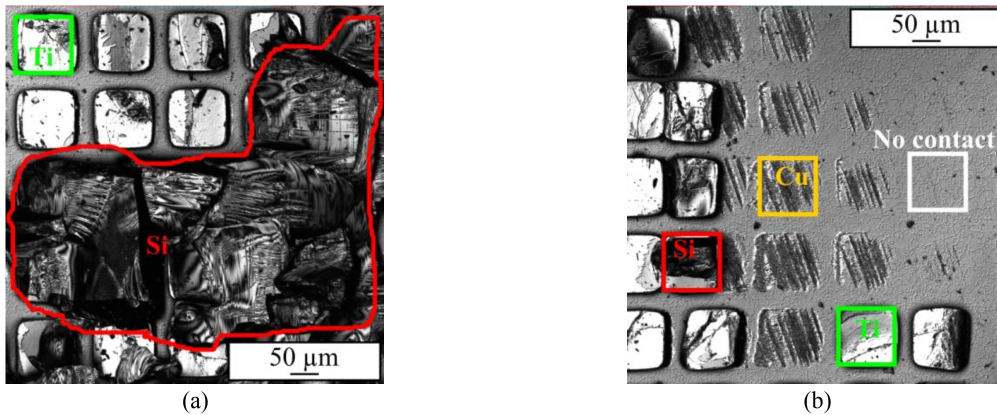

Fig. 7-5 Types of fracture surfaces after shear strength tests on the bottom dies A: Si and Ti fracture surfaces (a); Si, Ti, Cu fracture surfaces and no contact (b)

Fig. 7-6 shows a schematic view of a bonded sample pair with an orientation mark in the corner *c* (left image). The image at the right side is a bottom die after the shear strength test in the given orientation, made by confocal microscope LEXT OLS4100. “No contact” area near the corner *b* is detected for most of the bonded sample pairs, which suggests light non-planarity of the bonding tool.

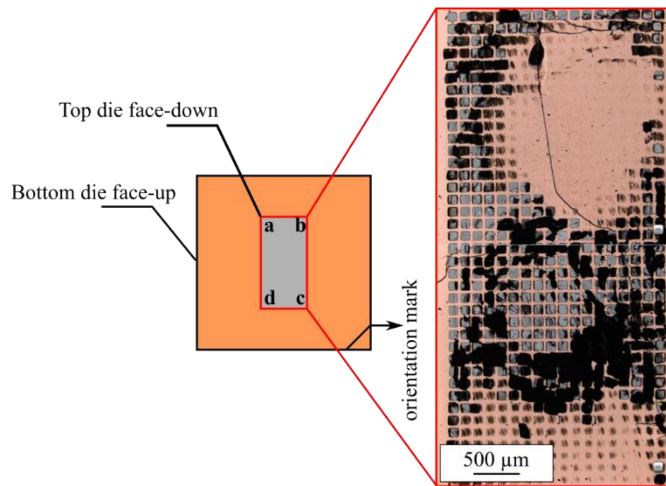

Fig. 7-6 Schematic top view of a bonded sample pair with orientation mark (left image) and a confocal microscope image of a bottom die after the shear strength test (right image)

Shear strength in MPa is calculated by dividing the shear strength in N by the initial bonding area (7.2 mm^2). "No contact" area was not subtracted from the initial bonding area during the calculation of shear strength in MPa. A similar procedure is used in shear strength evaluation in different research studies [15].

7.2 Influence of desorption conditions on Cu-Cu bonding quality

7.2.1 Results and discussion

7.2.1.1 Analysis of the chemical composition of the Cu surface

This subchapter presents XPS spectra of C1s, S2p, O1s and Cu LMM components on the Cu surface covered with SAM after three desorption conditions in the Ar gas atmosphere. These measurements were carried out using the JPS-9200 (Jeol) XPS system. Pre-annealing of the test samples at 200 °C or 250 °C for 30 min influences the stability of SAMs on the Cu surface and causes desorption. Samples without desorption procedures were analyzed for comparison. All of the samples could experience up to 1 h of air exposure due to transportation to the bonder as well as up to two days storage in a vacuum desiccator. Further, XPS analysis was performed twice for each sample: in the initial state and after the cleaning step by Ar^+ ion bombardment (chapter 4.3.2). All spectra were referenced to C1s adventitious carbon contamination peak set at 285 eV. Assigned peaks from the literature are listed in chapter 4.3.2. Fig. 7-7 - Fig. 7-10 show XPS spectra of C1s, O1s, S2p and CuLMM before and after the desorption process at 200 °C and 250 °C for 30 min. The results are summed up in Fig. 7-11, which presents the distribution of atomic concentrations of these elements on the Cu surface.

Fig. 7-7 shows XPS spectra of C1s spectra for the samples with SAM passivation before and after desorption (pre-annealing) procedure. C-C peak intensities at 285 eV in the initial state (Fig. 7-7, (a), (c), (e)) decrease with increasing temperature of desorption. The decrease in C

peak intensity is connected to sequential SAM desorption. No C-O bindings are detected around 287.6-289.1 eV.

S2p spectra of Cu/SAM sample without desorption in the initial state show only one peak at 162.8 eV (Fig. 7-8, (a)). S2p spectra of the Cu surface after the cleaning step (Fig. 7-8, (b)) exhibit a doublet of two peaks at 162 and 163 eV, which correspond to $S2p_{3/2}$ and $S2p_{1/2}$, respectively. These can be assigned to thiolate species. Due to organic contamination, the doublet of peaks is not detected in the initial state. After the desorption process at 200 °C, the S2p spectrum exhibits a doublet of peaks even before the cleaning step (Fig. 7-8, (c), (d)). Samples pre-annealed at 250 °C exhibit peaks at 163, 164 and 165 eV after the cleaning step (Fig. 7-8, (f)). The high binding energy peak at 164 eV can be assigned to unbound alkanethiols or S atoms. This means that thiol chains are still present on the Cu surface, but are not bound to it anymore. Binding energy >166 eV is usually assigned to the oxidized S. Such species were not detected before and after desorption at different temperatures on the Cu surface.

Types of Cu oxide are described in chapter 3.1. O1s XPS spectra show no peaks for Cu/SAM surface without desorption before and after the cleaning step (Fig. 7-9, (a), (b)). The amount of O increases with desorption temperature (Fig. 7-9, (c) - (f)). O spectrum shows a definite peak at 530.8 eV, which can be assigned to Cu_2O (Fig. 7-9, (d)) for the desorption at 200 °C after the cleaning step. The peak at 529.6 eV can be assigned to CuO but is negligibly small as it lies within the measurement error range. Peak position at 530.8 eV (Fig. 7-9, (f)) is also found on the 250 °C sample after the cleaning step. This suggests the presence of Cu_2O species on the Cu surfaces of pre-heated samples at both 200 °C and 250 °C.

Considering Cu LMM spectra (Fig. 7-10), no evidence of CuO species is detected, as they usually lie approximately 1 eV higher than the Cu peak. Cu_2O peak is commonly detected at the distance of approximately 2 eV from the Cu peak. Fig. 7-10 (a), (b) shows Cu LMM spectra before the desorption process, before and after Ar^+ ion bombardment at 500 eV for two minutes. Cu peak at 335.4 eV increases significantly after the removal of the adventitious C contamination layer. Fig. 7-10 (c) – (f) indicate that Cu_2O peak at 337.2-337.5 eV increases with temperature, followed by the decrease of Cu peak intensity at 335.3-335.4 eV. This suggests oxidation of Cu surface during the desorption process, dependent on process temperature and duration.

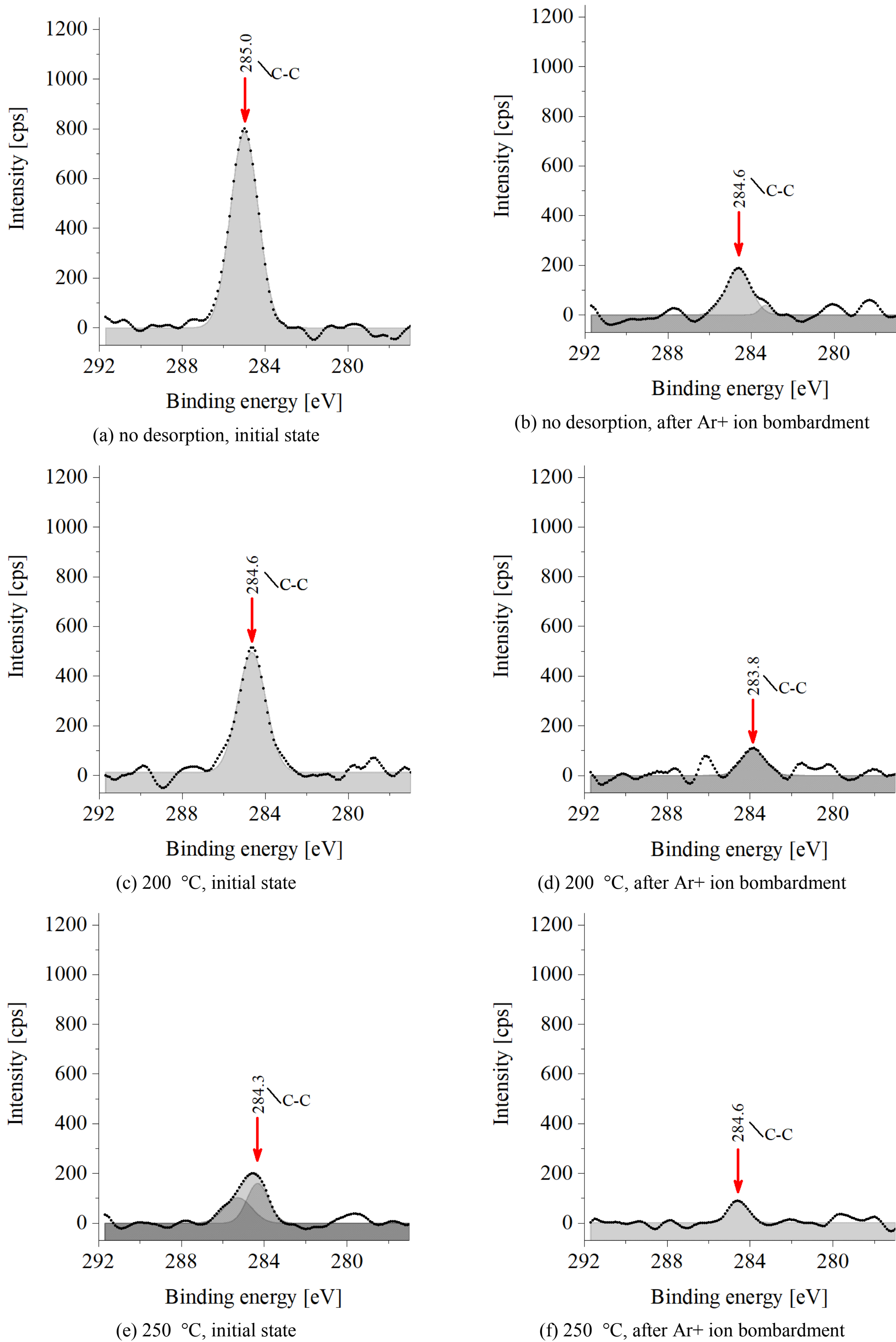

Fig. 7-7 XPS spectra of C1s before and after SAM desorption procedure at 200 °C and 250 °C for 30 min

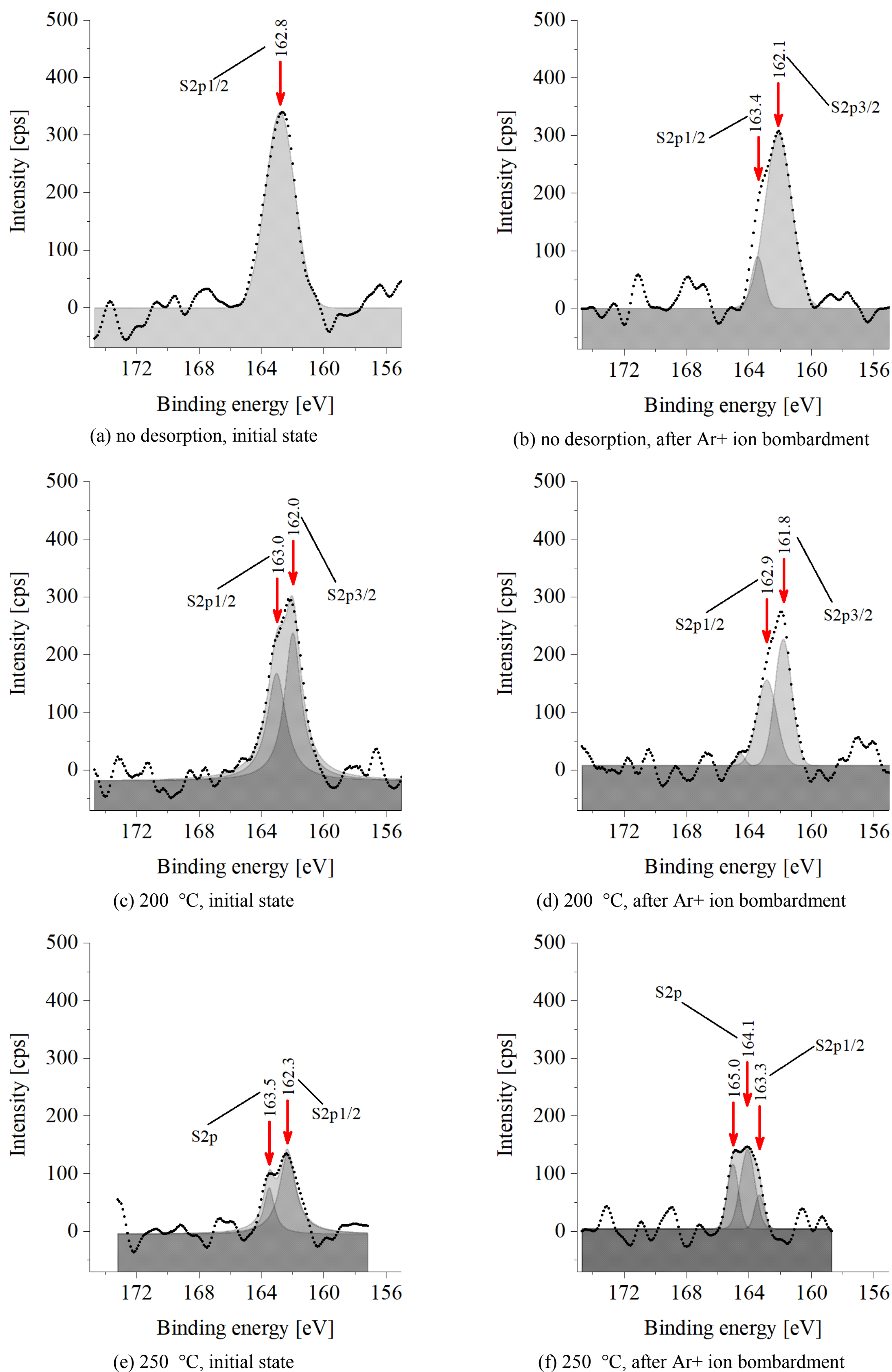

Fig. 7-8 XPS spectra of S2p3/2 before and after SAM desorption procedure at 200 °C and 250 °C for 30 min

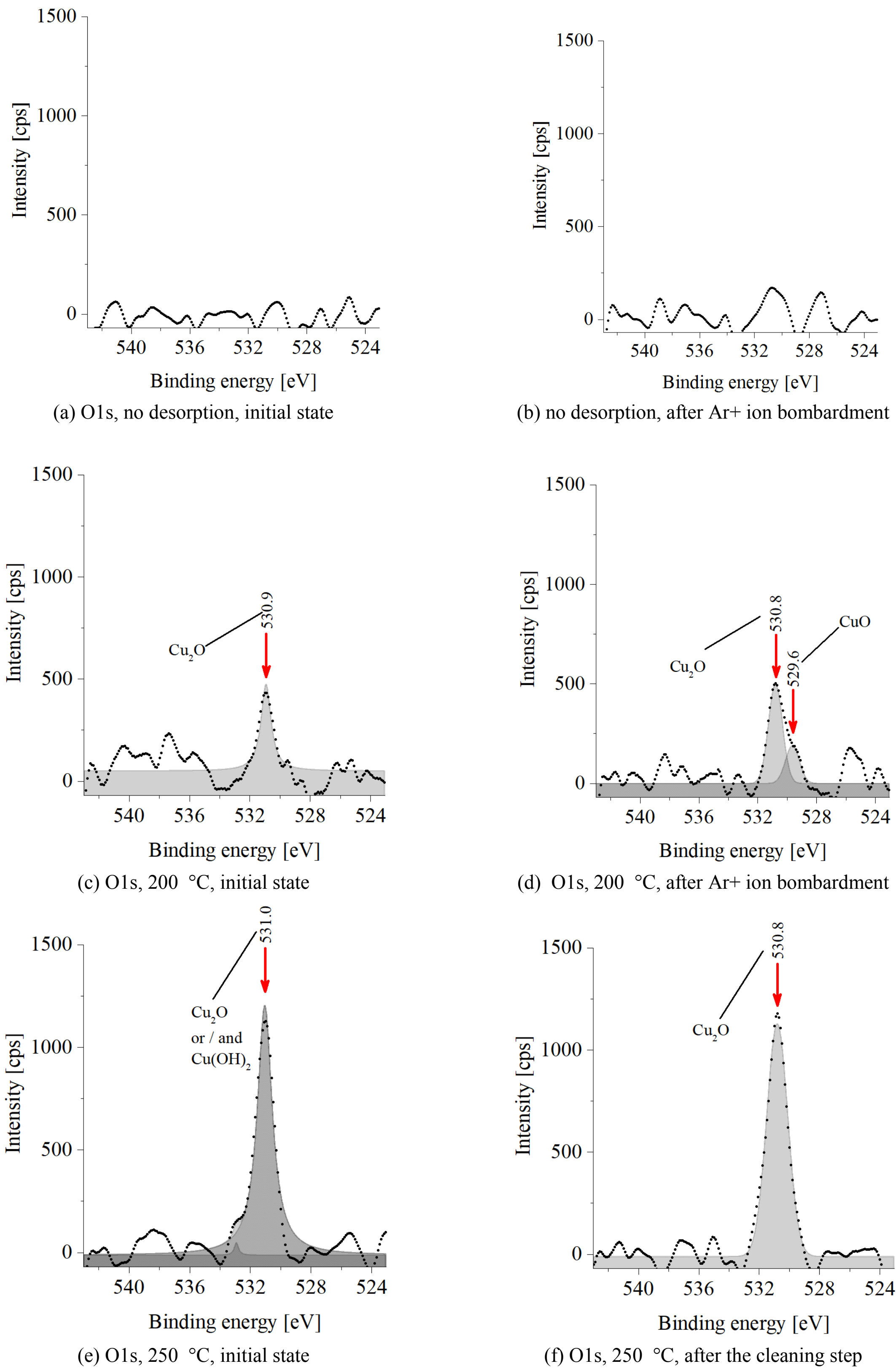

Fig. 7-9 XPS spectra of O1s before and after SAM desorption procedure at 200 °C and 250 °C for 30 min

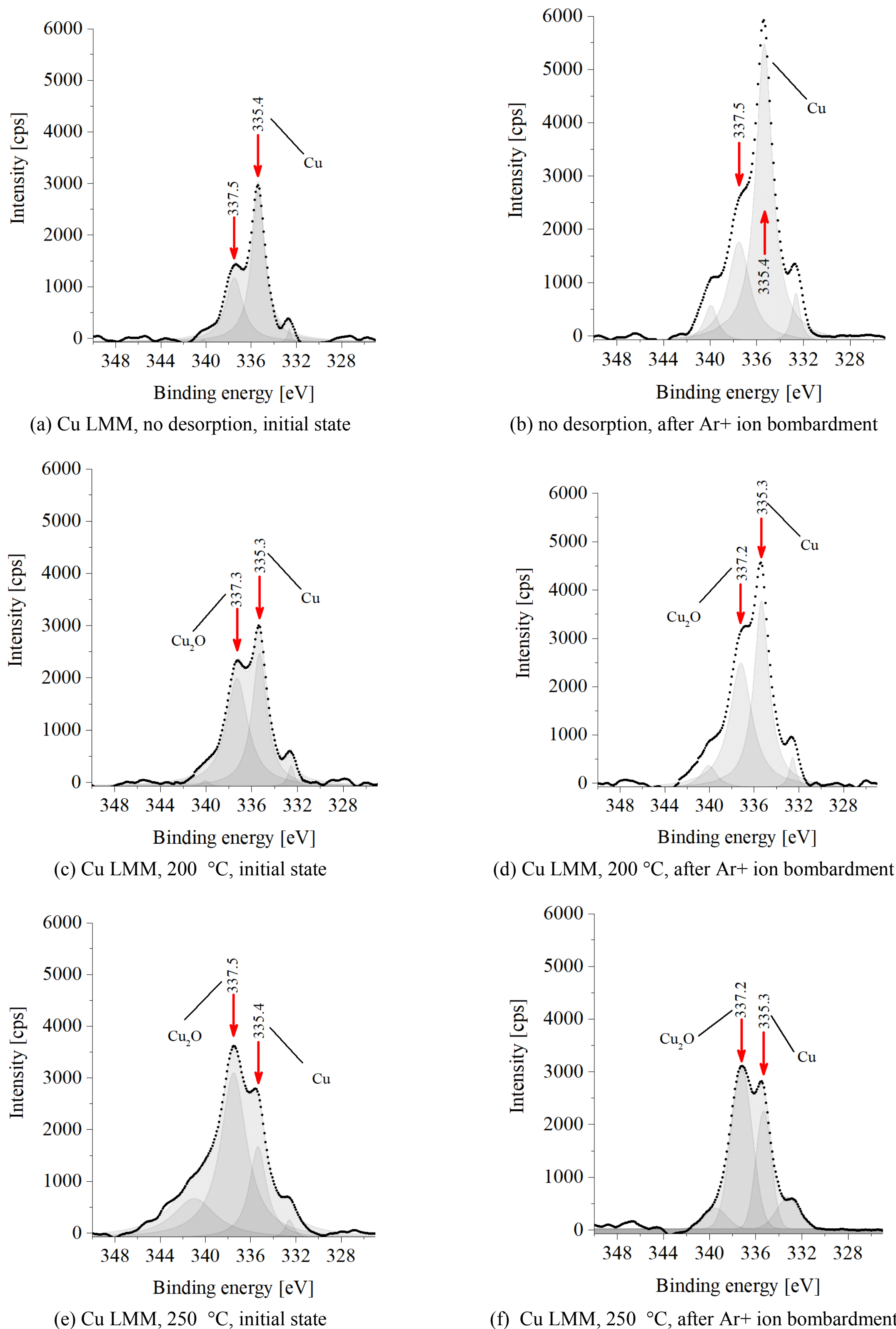

(a) Cu LMM, no desorption, initial state

(b) no desorption, after Ar+ ion bombardment

(c) Cu LMM, 200 °C, initial state

(d) Cu LMM, 200 °C, after Ar+ ion bombardment

(e) Cu LMM, 250 °C, initial state

(f) Cu LMM, 250 °C, after Ar+ ion bombardment

Fig. 7-10 XPS spectra of Cu LMM before and after SAM desorption procedure at 200 °C and 250 °C for 30 min

Fig. 7-11 shows the general trend for atomic concentrations for C1s, O1s, S2p and CuLMM on the Cu surface before and after desorption procedures at 200 °C and 250 °C. Fig. 7-11 (a) show that the adventitious C contamination layer is almost completely removed (≤ 5 at.%) after the cleaning step with Ar^+ ion bombardment. The results of atomic concentration analysis in

Fig. 7-11 (b) show that the amount of thiolates (concentration of S) on the Cu surface decreases with increasing desorption temperature. Nevertheless, even after 30 min at 250 °C the thiolates are only partially removed from the Cu surface (S < 5 at.%).

At 200 °C the ratio of O equals 6 at.% (Fig. 7-11, (c)). The temperature of 250 °C causes an increase of O ratio up to 16 at.%, which is evidence of Cu oxide presence. The percentage of Cu after the cleaning steps decreases with temperature due to the mentioned oxide growth (Fig. 7-11, (d)).

The graphs indicate that the percentage of C and S decreases and the amount of O and Cu increases with pre-annealing temperature. O percentage may increase because of possibly not ideal inert gas atmosphere in the bonding chamber during annealing. No O content controlling system was used. The amount of Cu increases because of SAM desorption and better recognition of Cu atoms by XPS.

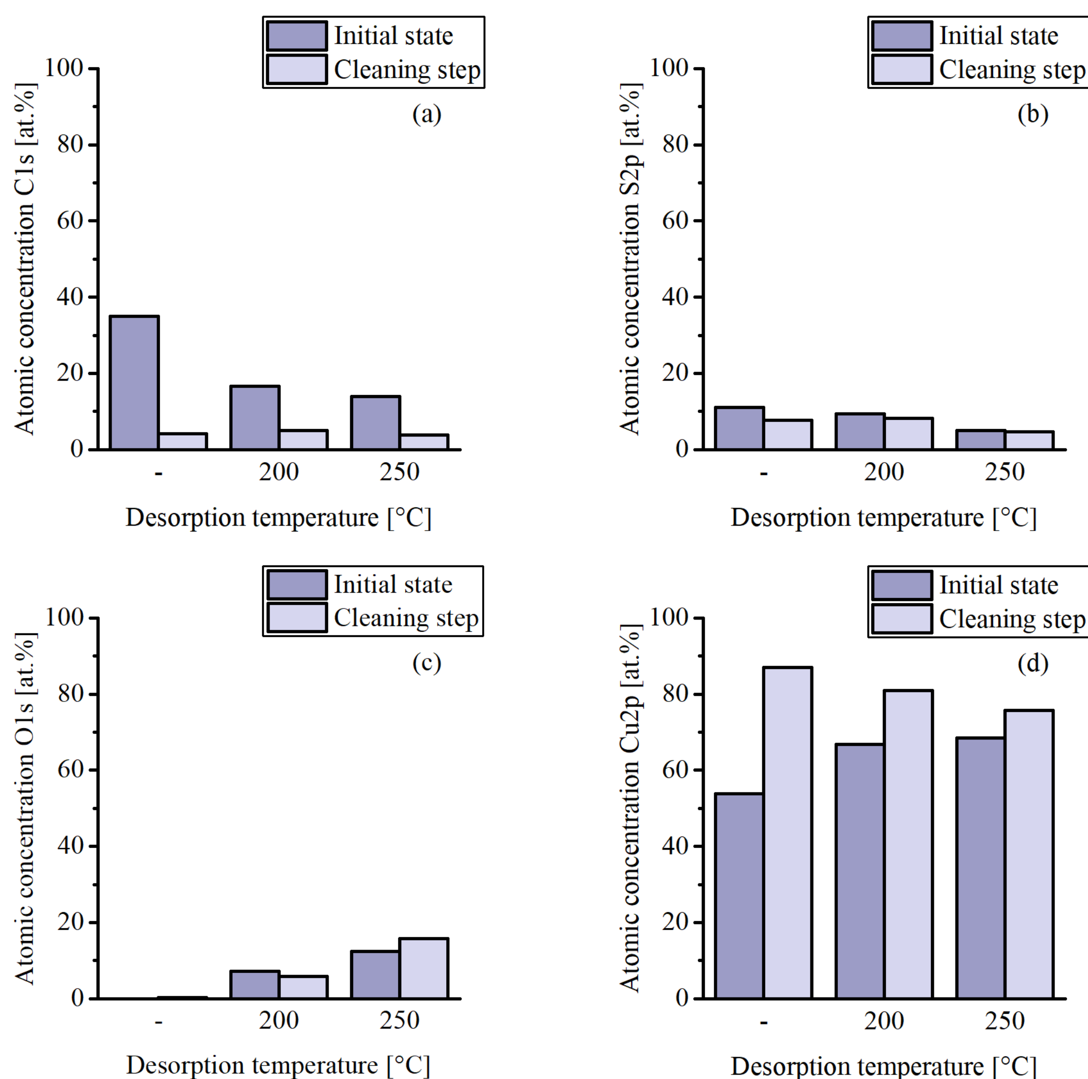

Fig. 7-11 Atomic concentrations of C1s (a), S2p (b), O1s (c) and Cu2p (d) of the samples with SAM before and after desorption at 200 °C and 250 °C

The chemical composition of the Cu surface before bonding shows that none of the chosen desorption temperatures remove SAM completely. Partial SAM desorption is visible for 200 °C and even more significantly for 250 °C. Nevertheless, rising temperature leads to Cu oxidation due to not ideal inert gas atmosphere or impurities in Cu. Characterization of Cu-Cu bonding quality is a necessary next step in order to distinguish the optimal desorption temperature.

7.2.1.2 Characterization of the mechanical strength of the interconnects

Shear strength tests were carried out after the bonding procedure (details in 4.4.2 and 7.1). Fig. 7-12 presents the results of the shear strength tests and fracture surface analyses. Three samples pairs per parameter set were bonded: two sample pairs for shear strength tests and one sample for cross-section analysis with SEM. Each shear strength value corresponds to the distribution of fracture surface types throughout a die in the graph below.

Oxide growth (due to the increase of desorption temperature) influences the shear strength. The lowest shear strength values exhibit bonding pairs with the desorption procedure at 250 °C. The highest values achieve bonding with 200 °C desorption. Interestingly, samples without SAM desorption can also be bonded with relatively high shear strength values ((37…46) MPa). Nevertheless, <10 % of Si fractures is observed for such samples, which is at least 10 % less in comparison to other samples. Therefore, 200 °C was chosen as an optimal temperature for the desorption process for the further experiments.

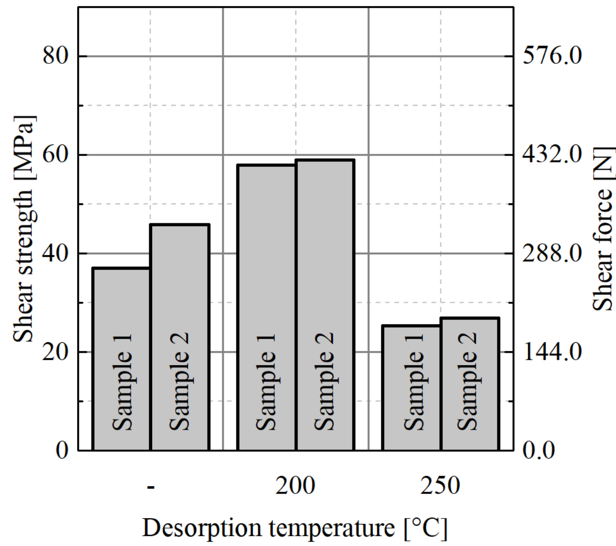

(a)

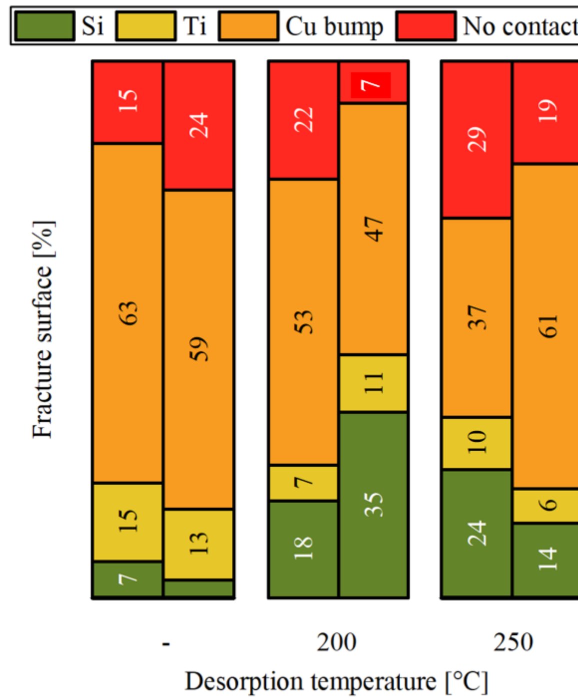

(b)

Fig. 7-12 Influence of desorption temperature on the shear strength (a) and fracture surface (b) of the bonded samples

The achieved shear strength for 200 °C desorption for 30 minutes equals (57…59) MPa. Peng reports achieving 12 MPa after pre-annealing of wafers at 250 °C *in-situ* to desorb SAM, bonding at 350 °C for 1h in a vacuum and annealing at 350 °C in N_2 for wafer-to-wafer bonding [147]. There are two fracture surfaces in his study: between Cu and TaN and on the Cu-Cu bonding interface. One wafer provides a mixture of these fracture surfaces, with better quality on the edges and worse in the wafer center. Fig. 7-12 shows that the percentage of Cu fractures alters between (47…53) % after the desorption at 200 °C. No contact area occupies 8-22 %. Finally, Si and Ti fractures can be assigned to (25…46) % of all bonds depending on the bonding temperature and pressure.

The research group of Tan et al. achieved (56…82) MPa after Cu-Cu bonding with SAM desorption at 250 °C for 10 min. Bonding took 1h at 250 °C in vacuum (this study: 250 °C, 30 min in Ar) [59]. Higher time for the bonding perhaps could not bring the higher shear strength because of the Cu oxidation due to too high pre-annealing temperature. The fracture surface was not observed in their study.

The research group mentioned above obtains one of the most intensive studies about SAM as a corrosion inhibitor for Cu-Cu bonding on a wafer level [8], [9], [60]. Desorption temperature in their reports is kept at 250 °C and time is fixed to (10…30) min. These studies show that 250 °C is enough to remove C6 from the Cu surface so that no S species can be detected by XPS after the annealing step. The presence of O species on the Cu surface has not been verified. The group reports that the Cu-Cu interconnect has poor bonding quality if SAM is not desorbed from the Cu surface. In this thesis, C6 is almost completely removed from the Cu surface after annealing at 250 °C for 30 minutes (atomic concentration of S < 5 at.%), but the amount of Cu oxide increases up to 16 at.% during this time. This can be caused by the not ideal inert gas atmosphere (the presence of O residuals) in the bonding chamber. The research group did the SAM passivation in the inert gas atmosphere on freshly sputtered Cu wafers. In this study, Cu was exposed to air after the deposition and was etched prior to passivation. This could cause the accumulation of some amount of O in the Cu grain boundaries, which desorbed and oxidized Cu during the pre-annealing procedure.

The shear strength of the samples without SAM desorption shows a better result than after the desorption process at 250 °C. This may be caused by the lower Cu oxidation of the pre-etched samples without SAM desorption in comparison to the samples with SAM desorption at 250 °C. The results show that the samples without SAM desorption can also be bonded. The start of the Cu-Cu self-diffusion is probably possible due to the breakage through the monolayer. Nevertheless, aging and reliability tests of such interconnect have to be performed before broad applications in semiconductor production.

The shear strength of interconnects without SAM desorption is lower than that of the interconnects pre-annealed at 200 °C. In this case, SAM is partially desorbed, but the amount of Cu oxide is still low (6 at.%).

Cu gets oxidized after annealing at 200 °C without the evidence of sulfonate formation (SAM oxidation). Fig. 7-13 proposes a model of SAM partial desorption during pre-annealing of samples in the Ar gas chamber. Schematic representation of SAM chemical compounds, used in this model, has already been shown in Fig. 3-9. The chamber has a not ideal inert gas atmosphere, which means that oxygen is present there. Defect places start to oxidize first. Second, physisorbed SAMs (weakly bonded) start to desorb. The freed space on the Cu surface gets readily oxidized. Disulfides are formed and desorbed in the last turn. In the end, a surface with a percentage of 9 at.% (in the initial state) of SAM residuals and also a low percentage of O bindings (6 at.%) is used for TC bonding in Ar. The S percentage before desorption is 11 at.% (in the initial state), which suggests that after 30 min at 200 °C a low amount of SAM was removed. Increasing annealing temperature to 250 °C leads to further SAM desorption but also

causes a higher amount of O (16 at.%) on Cu. This shows that the TC method of SAM desorption before bonding in the Ar-gas atmosphere needs to be optimized.

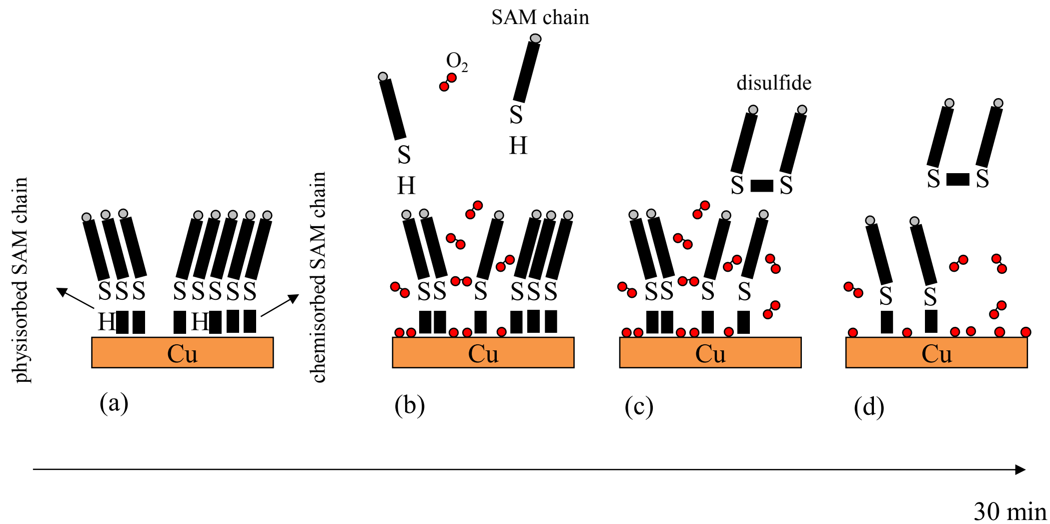

Fig. 7-13 Proposed schematic model of SAM desorption at 200 °C for 30 minutes with such stages: initial state (a), desorption of physisorbed SAMs and oxidation of free surface (b), formation and desorption of disulfides (c), the state of the Cu surface with partial SAM desorption after 30 minutes (d)

This subchapter aimed to make a coarse analysis about how long and at, which temperature SAM can be desorbed. The optimal solution appears to be desorption of 1-hexanethiol adsorbed on Cu surface at 200 °C for 30 min. During this time partial SAM desorption takes place, whereas the amount of Cu_2O is still low (6 %). This is proved by the analysis of the chemical composition of the surface, shear strength of the interconnects and their fracture surface.

The idea of SAM passivation without desorption provides high shear strength and can be even more attractive for industry because of the time saving and less exposure to the elevated temperature. Nevertheless, the long-term reliability (e.g. by aging tests) for such interconnects (without SAM desorption) should be investigated.

The method of SAM thermal desorption at 200 °C for 30 minutes for D2D bonding is probably not cost-effective but the idea of SAM desorption for W2W bonding has a high potential.

7.3 Influence of storage conditions on Cu-Cu bonding quality

7.3.1 Results and discussion

7.3.1.1 Analysis of the chemical composition of the Cu surface

Fig. 7-14 - Fig. 7-16 show C1s, O1s and CuLMM spectra for samples with and without SAM after 3 weeks storage at -18 °C in the initial state and after the cleaning step. The assigning to peaks was made according to Tab. 4-5 - Tab. 4-6.

C1s was referenced to 285 eV (C-C binding) in the initial state (Fig. 7-14, (a)). The spectrum also shows additional peaks at 286.2 eV (C-O-Cu), 289.0 eV and 290 eV (C-O-C) for the sample without SAM. Even after the cleaning step, the peak at 288 eV does not disappear (Fig. 7-14, (d)). Though the C-C compound has a higher intensity, there is no C-O-C detected on the Cu/SAM sample in both states.

O1s exhibit barely detected Cu oxide peaks at 532.9 eV (C-O-Cu, [128]) and 530.1 eV (Cu_2O), which corresponds to (3…4) at.% of O on the Cu/SAM surface. After the cleaning step a peak at 530 eV is almost comparable with the measurement error. On contrary, the sample without SAM exhibit definite Cu oxide peaks at 534.0 eV, 531.6 eV ($Cu(OH)_2$) and 530.1 eV in the initial state (Fig. 7-15, (c)), which suggests that a high amount of C and H containing bindings were adsorbed on the Cu surface. After the cleaning step the major peak shifts to 530.4 eV, which is evidence of Cu_2O. The atomic concentration of O is two times higher for the sample without SAM coating and equals 10 at.% after the cleaning step (Fig. 7-17, (c)). Cu LMM spectra exhibit a higher peak at (337.0…337.1) eV without SAM in comparison to Cu with SAM (Fig. 7-16). This peak is assigned to Cu_2O.

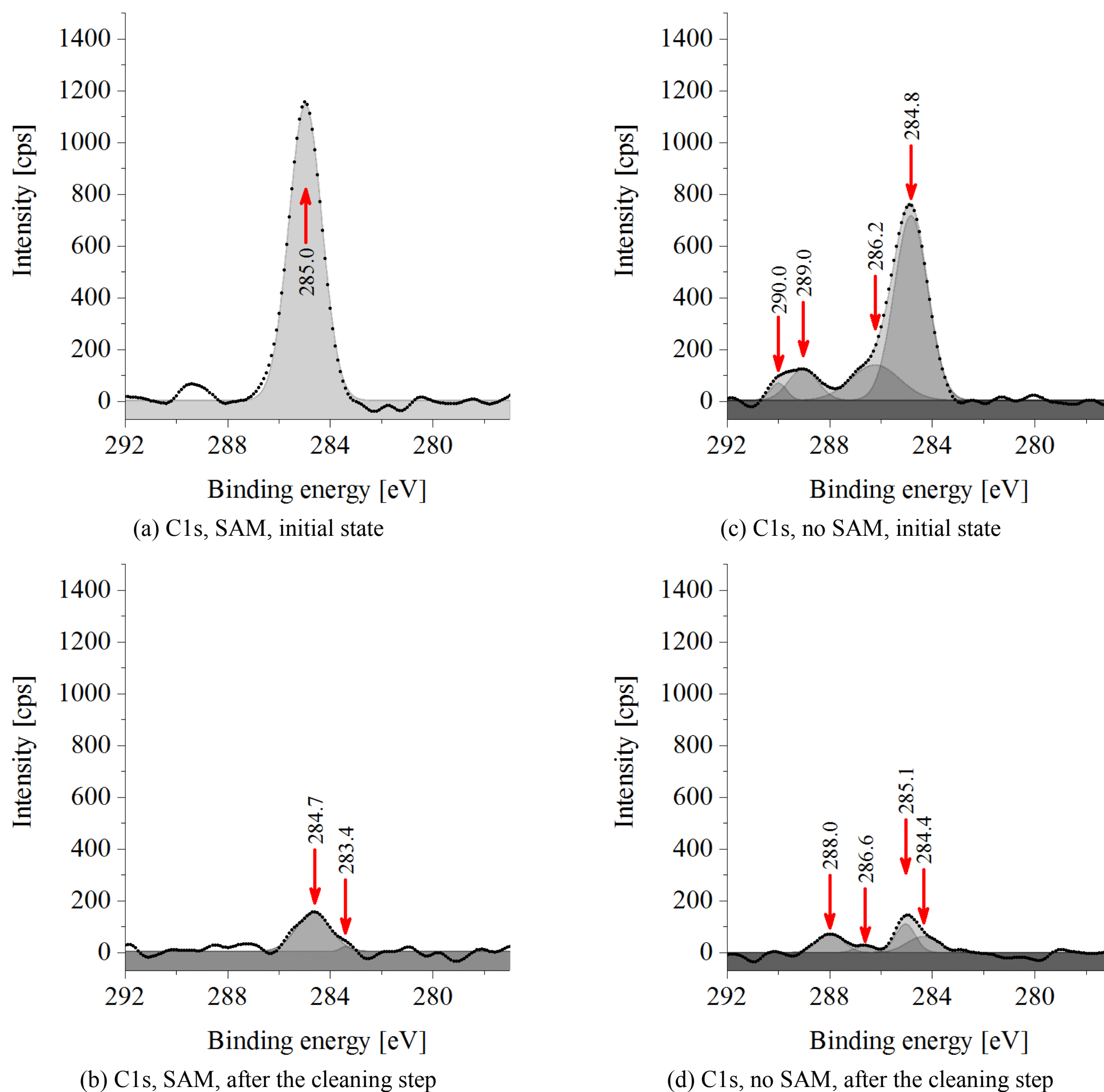

Fig. 7-14 XPS spectra of C1s for the samples with and without SAM passivation after 3 weeks of storage at -18 °C in air

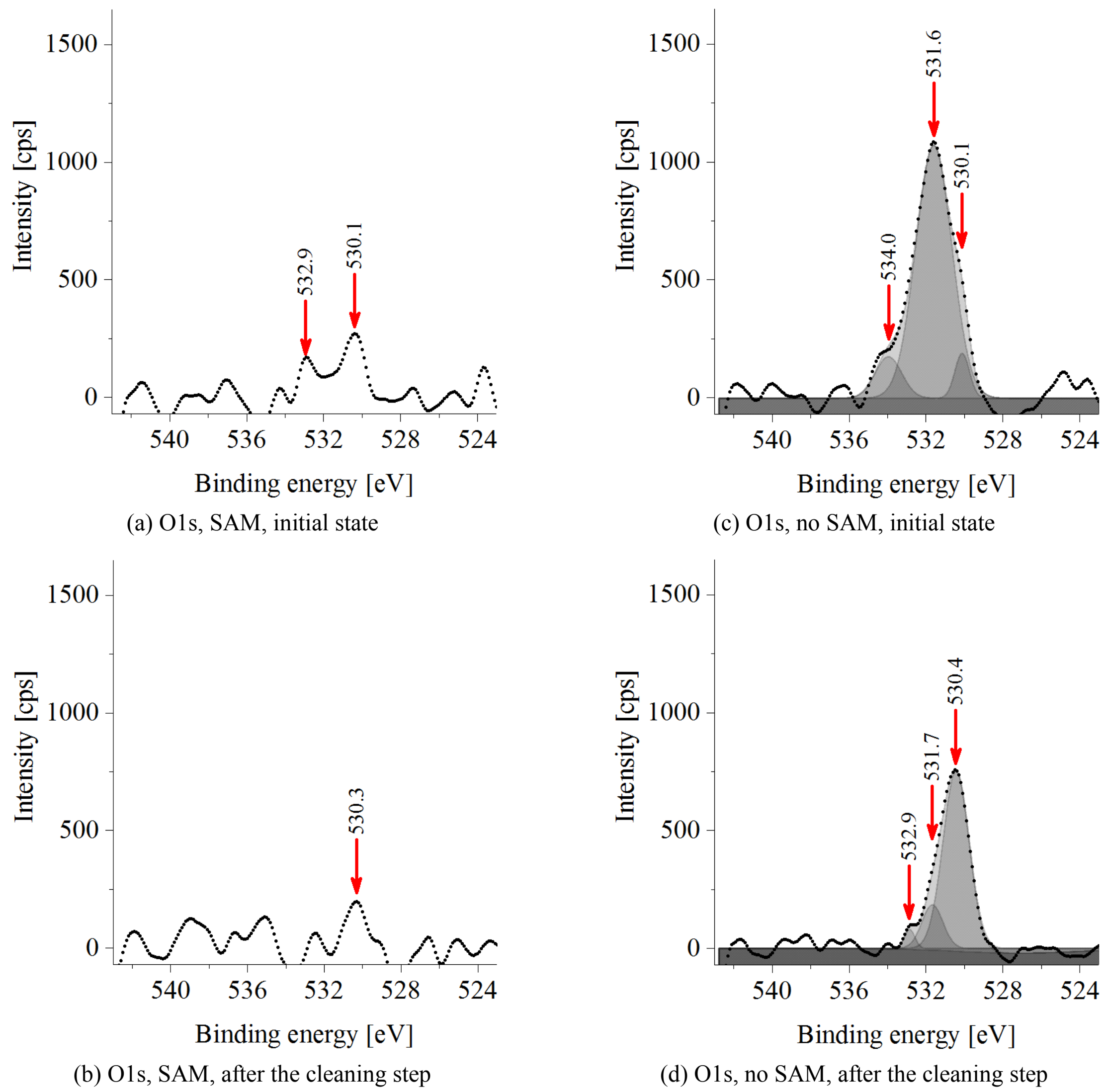

Fig. 7-15 XPS spectra of O1s for the samples with and without SAM passivation after 3 weeks of storage at -18 °C in air

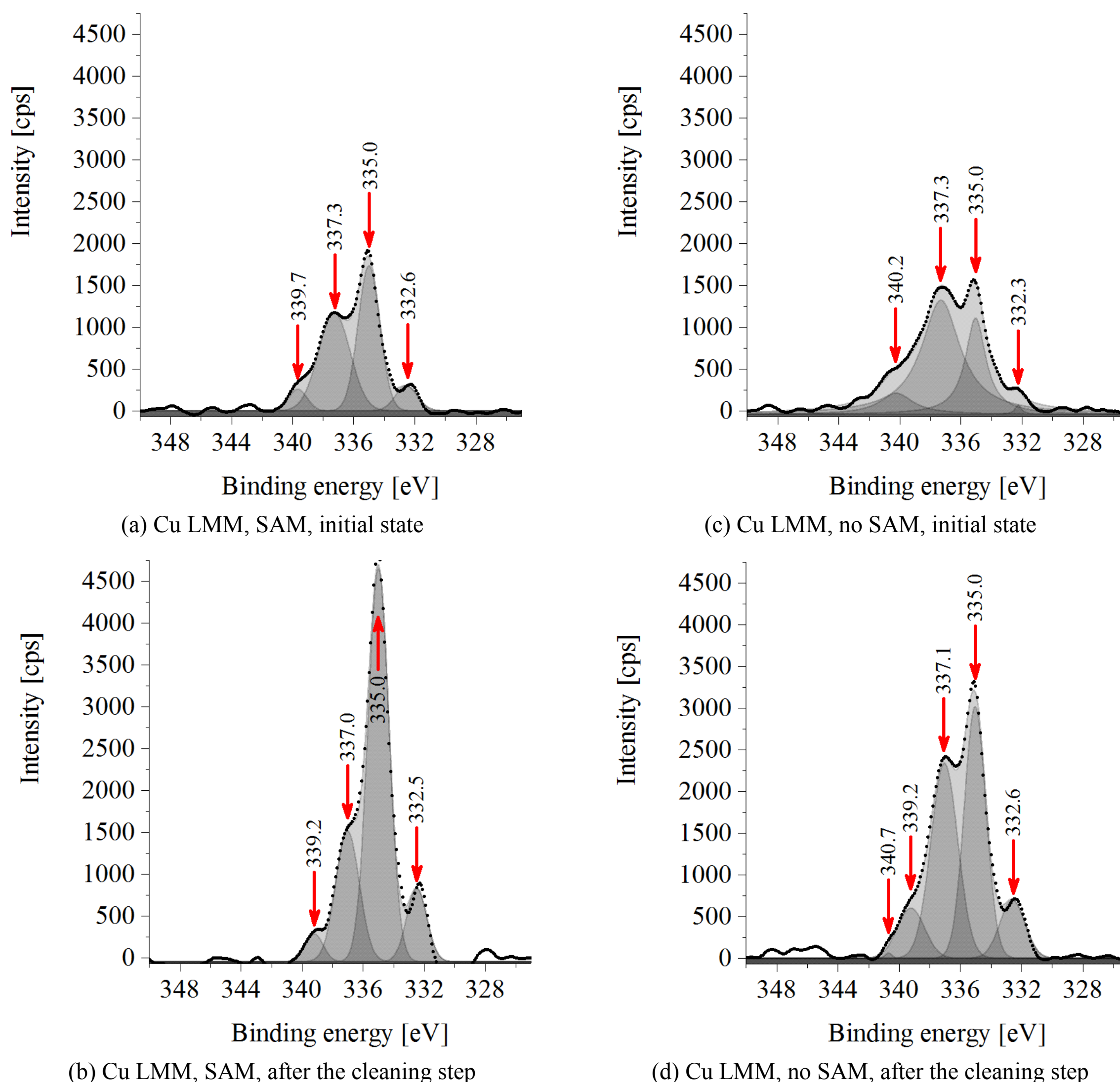

Fig. 7-16 XPS spectra of Cu LMM for the samples with and without SAM passivation after 3 weeks of storage at -18 °C in air

Fig. 7-17 presents the atomic concentrations of C1s, Cu2p and O1s after the storage for three weeks at -18 °C. Fig. 7-17 (a) shows that C content is higher on the passivated sample and decreases significantly after Ar^{+} ion bombardment for both sample types (with/without SAM). Fig. 7-17 (b) shows an increase in Cu content after the cleaning step for both sample types. Fig. 7-17 (c) shows that the samples with SAM exhibit 4 at.% of atomic concentration of O1s in the initial state in contrast to the unprotected samples, which are characterized by 27 at.% of O. The atomic concentration of O stays almost the same for Cu/SAM (3 at.%) before and after the cleaning step. The percentage of O for not passivated samples is 27 at.% in the initial state and drops to 10 at.% after the cleaning step. This is evidence of a significantly higher amount of Cu oxide on the unprotected Cu surface and almost oxide-free Cu/SAM surface after 3 weeks of storage in air conditions at -18 °C.

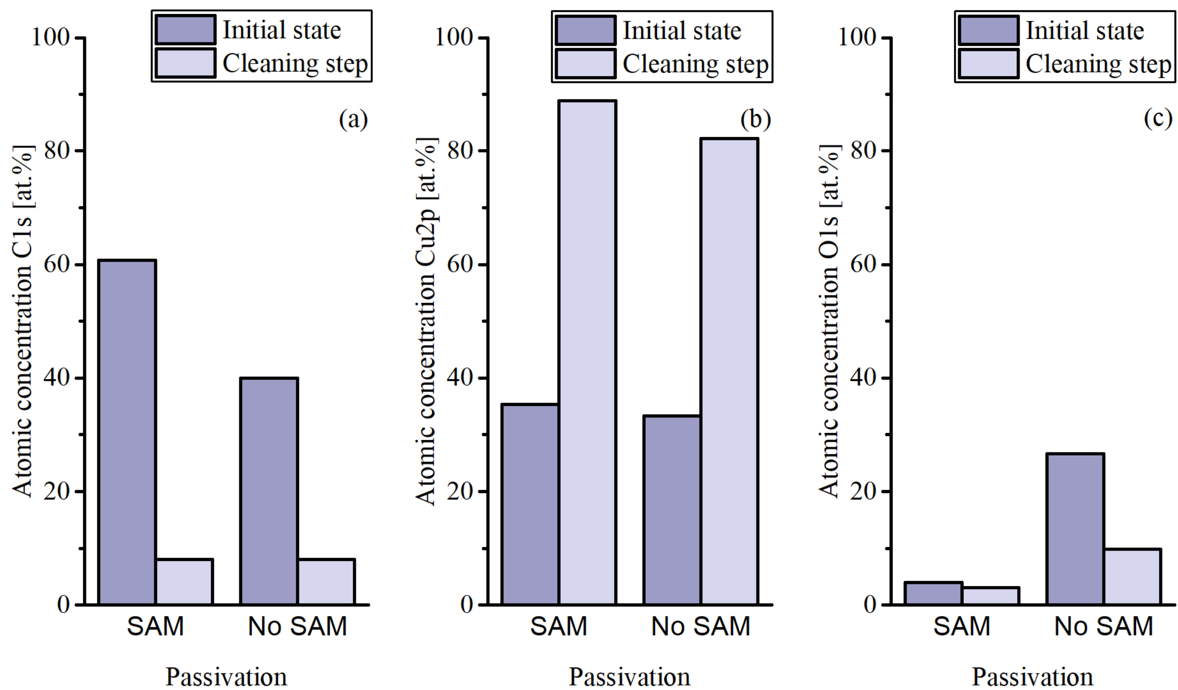

Fig. 7-17 Atomic concentrations of C1s (a), Cu2p (b) and O1s (c) of Cu surface with SAM (SAM) and without SAM (no SAM) passivation after 3 weeks storage at -18 °C in air

Comparing the samples with SAM after the pre-annealing procedure at 250 °C and samples without SAM, stored at -18 °C for three weeks, the amount of O is 16 at.% and 10 at.%, respectively. Although these values lay close to each other, there are some definite variations in concentrations of Cu and C. The presence of peaks at (288…289) eV suggests the presence of $CuCO_3$ on the stored unprotected sample, which is barely or not detected on the pre-annealed samples without SAM. The concentration of C is higher on the stored sample surface in comparison to the pre-heated one. This is caused by the longer air exposer of the stored chip and the inert gas environment of the pre-heated chip.

These results suggest that storage in a conventionally available freezer at -18 °C can also prolong the protective effect of short-chain SAMs compared to -40 °C (subchapter 6.2.1.5).

7.3.1.2 Characterization of Cu-Cu bonding interface

Fig. 7-18 presents common types of bonding interfaces of Cu-Cu interconnects bonded after storage at -18 °C in Ar inert gas atmosphere in the bonding chamber with an additional pre-annealing step (described in chapter 4.4.2) in order to desorb SAM. Samples without SAM also underwent pre-annealing at 200 °C for 30 min before bonding to make bonding results comparable. Cross-sectioning is made for one sample pair at each storage duration (0 days, 1 day, 10 days). This analysis is carried out for both passivated and uncoated sample pairs. Nearly 80 % of all of the Cu-Cu interconnects (6 cross-sections, 21 bumps per each cross-section) have a combination of thin delamination (Fig. 7-18, (c)) and the seamless bonding interface (Fig. 7-18, (a)) regions. Around 15 % of the interconnects show no bonding (Fig. 7-18, (d)). A bonding interface with nanovoids (Fig. 7-18, (b)) means that interdiffusion started, but there are still many voids seen along the interface. No significant differences are

detected between the cross-sections of the interconnects with and without SAM. Only one plane was observed in the cross-sections for each sample type, which cannot deliver statistical accuracy but can provide qualitative information.

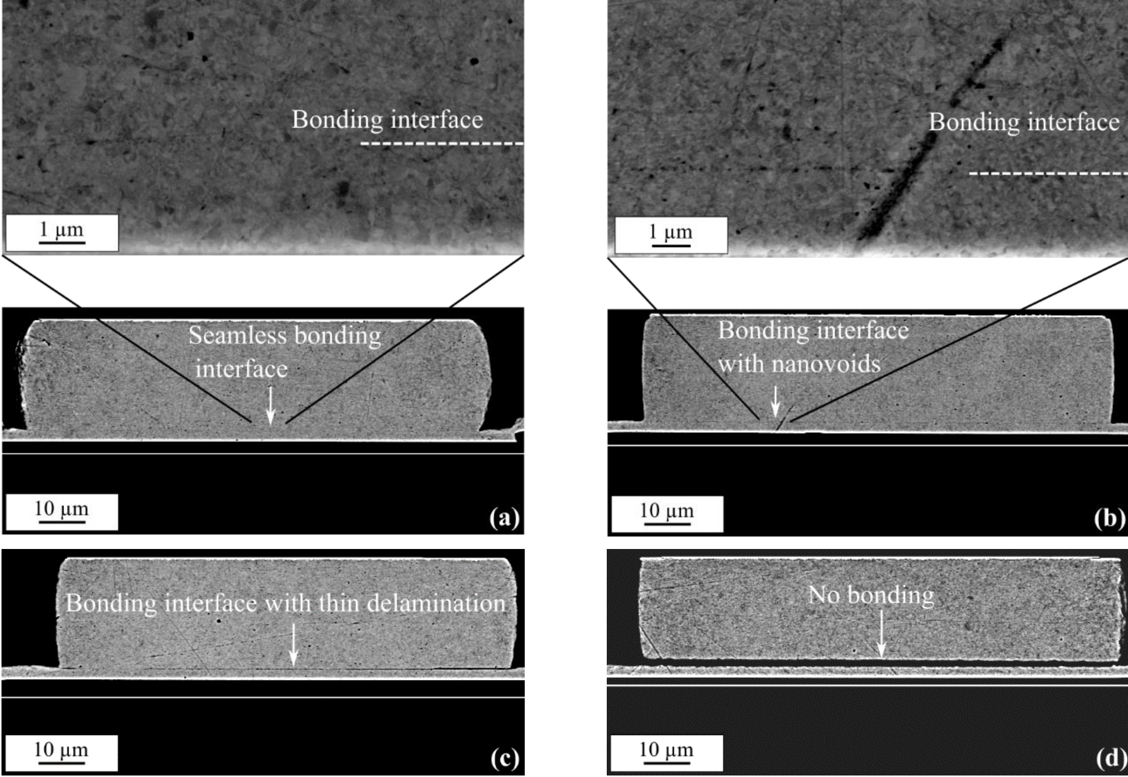

Fig. 7-18 Bonding interface types on SEM images of cross-sections of Cu-Cu interconnects after TC bonding in Ar inert gas atmosphere: seamless bonding interface (a), bonding interface with nanovoids (b), bonding interface with thin delamination (c), no bonding (d)

7.3.1.3 Characterization of mechanical strength of the interconnects

Fig. 7-19 and Fig. 7-20 show shear strength of samples with and without SAM, dependent on the storage time at -18 °C in air. Shear strength for both interconnect types, with and without SAM, decreases with storage time. The mean die shear strength is 34 % higher for the Cu/SAM after 10 days of storage at -18 °C in comparison to the samples without the SAM coating. Storage time does not influence the fracture surface of the samples with SAM. On contrary, for the samples without the protective coating, the amount of Si and Ti fractures decreases and the amount of Cu and "no contact" fractures increases with storage time. This is evidence of the Cu surface oxidation during the storage time and is the cause of lower interconnect quality in the case of bonding without SAM.

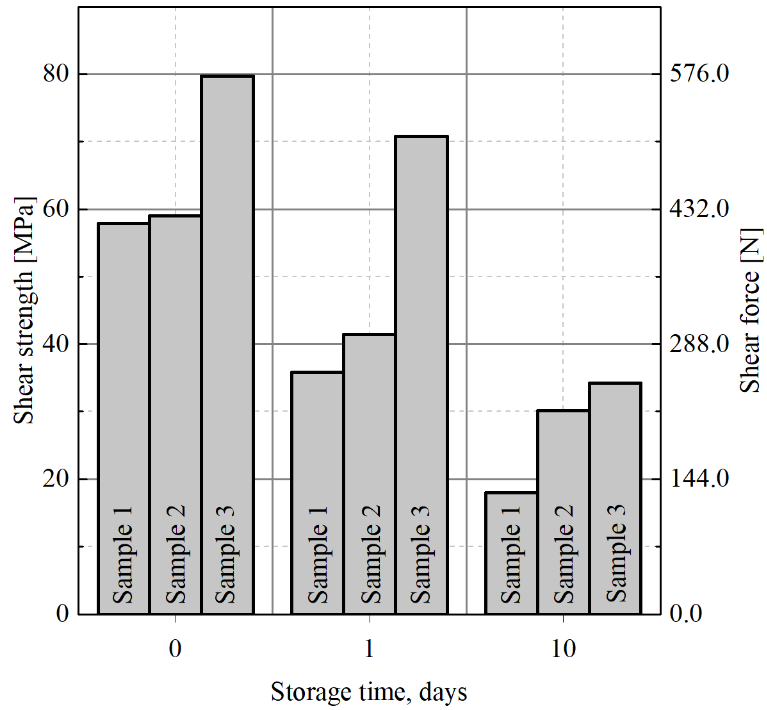

(a)

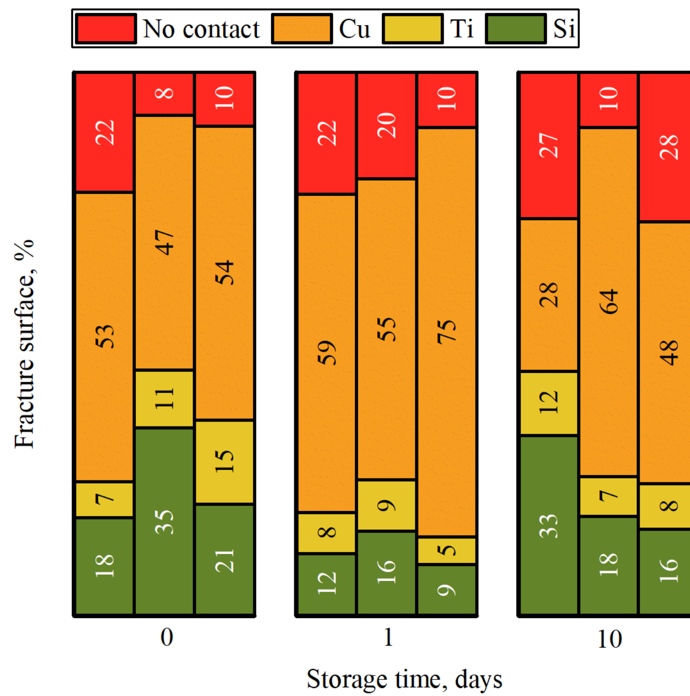

(b)

Fig. 7-19 Shear strength (a) and fracture surfaces (b) after TC bonding of samples with SAM in Ar after different storage times at -18 °C: 0, 1 and 10 days

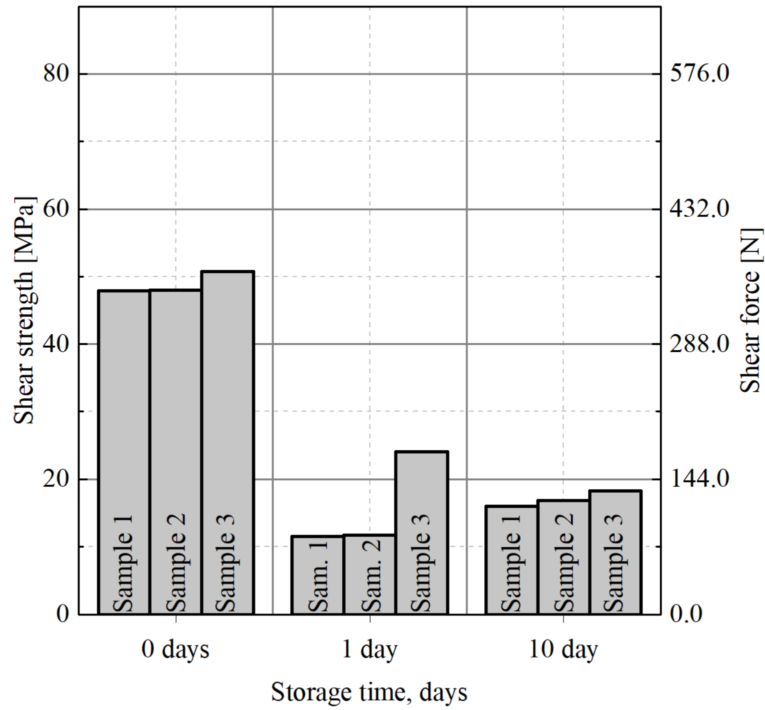

(a)

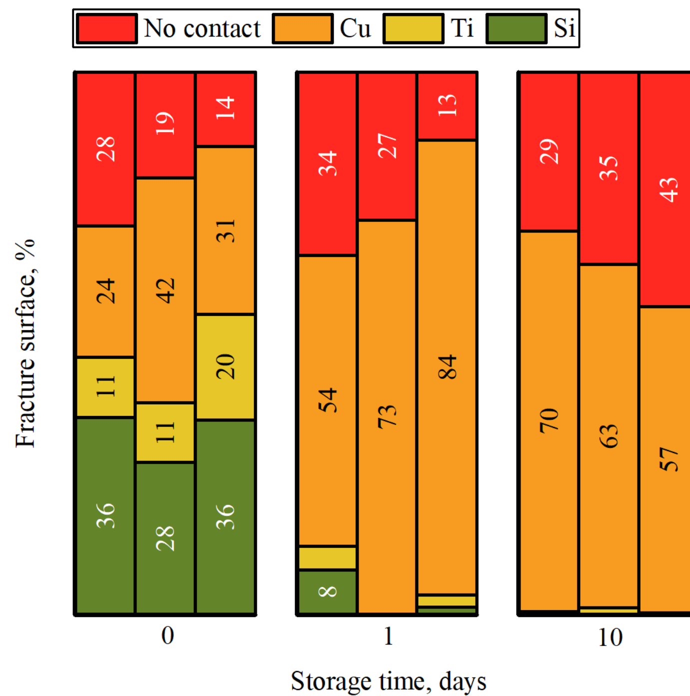

(b)

Fig. 7-20 Shear strength (a) and fracture surfaces (b) after TC bonding of samples without SAM in Ar after different storage times at -18 °C: 0, 1 and 10 days

Shear strength of samples with SAM reaches 80 MPa in comparison to freshly etched samples with 51 MPa. After storage for 1 day at -18 °C, the values for Cu/SAM can still reach 71 MPa, whereas the etched Cu does not exceed 24 MPa. The shear strength of the samples with SAM with storage for 1 day and without storage is comparable to the literature values of the not stored samples with SAM [59], [148].

The percentage of fracture surface types after the shear test does not change significantly with storage time for samples passivated with SAM: (9…35) % Si fractures, (5…12) % Ti fractures, (28…64) % Cu fractures, (8…28) % “no contact” areas. Si and Ti fractures, on contrary, almost disappear after the first storage day at -18 °C for samples without SAM, which, subsequently, causes a decrease of their shear strength. The percentage of the “no contact” area is (14…43) % and is higher for unprotected samples in comparison to Cu/SAM. Although the “no contact” area is mostly caused by bonding tool non-planarity, oxidized surface decreases the possibility of an interconnect formation. The finding proves that short-chain SAM passivation (C6) can impede oxide formation on the Cu surface during storage in air and, therefore, endorse Cu-Cu interconnect formation.

7.4 Summary

This chapter presents Cu-Cu TC bonding in an inert gas atmosphere using SAM. The first aim was to investigate desorption conditions for the monolayer. The second aim was to analyze how the storage of the samples with and without SAM influences the later bonding quality. The main conclusions are:

1. The optimal parameters for SAM desorption from Cu appear to be 200 °C and 30 min. During this time oxidation of Cu is negligibly low (6 at.%) and SAM is partially desorbed.
2. XPS analysis confirmed that oxidation of Cu is preferred to the S oxidation of the monolayer, that is why no S oxidation species were detected.
3. The shear strength of samples with SAM reaches max. 80 MPa, which is comparable with the literature result and is 35 % more than for the samples freshly etched before bonding. The samples without SAM coating reach max. 51 MPa after etching.
4. Samples with SAM stored for 3 weeks at -18 °C show a lower amount of O (3 at.%) on the Cu surface in comparison to the unprotected samples with 10 at.% after Ar^+ ion bombardment.
5. Although the shear strength decreased with storage time, the degradation was successfully retarded by short-chain SAM (C6). Within 24 hours at -18 °C in air it is still possible to achieve shear strengths in the range of 36-71 MPa.
6. The mean die shear strength is 34 % higher for the Cu/SAM after 10 days of storage at -18 °C in comparison to the samples without the SAM coating.
7. Almost complete absence of Si and Ti fractures after the first day of storage at -18 °C suggests Cu oxidation of the uncoated samples. The percentage of Si and Ti fractures remains unchanged even after 10 days of storage in air for Cu/SAM samples, which highlights a better interconnect quality in comparison to the samples without SAM passivation.

8. The method can be improved using the storage at lower temperatures, i.e. at -30 °C (discussed in chapter 6), in an inert gas atmosphere [73], or using better O control of the inert gas atmosphere in the bonding chamber.

In order to avoid the necessity of the inert gas atmosphere in the bonding chamber and propose an alternative bonding technology in air without the need of SAM thermal desorption, US flip-chip bonding with SAM passivation is described in the next chapter.

8 Investigation of Cu-Cu flip-chip ultrasonic bonding with SAM passivation

8.1 Experiment description

Fundamentals of ultrasonic (US) bonding are discussed in chapter 3.3. This method is chosen because of the possibilities of decreasing bonding temperature and time in air ambient, while partially removing the SAM layer via US rubbing. This method can be used for the exposure of clean Cu surfaces to bonding without essential re-oxidation in air at low bonding parameters. In this approach, no additional thermal desorption of SAM in an inert gas atmosphere is needed. Fig. 8-1 presents the experimental setup. A low-temperature range of (30…150) °C for Cu-Cu bonding is a parameter set of interest in today's microelectronic packaging technologies. The suitable bonding pressure range of (135…180) MPa was distinguished during the pre-experiments. The top die type B and the bottom die type B have been used in these experiments, the detailed description of, which can be found in chapter 4.1. The details of the US bonding process (including equipment) in these experiments are provided in chapter 4.4.2.

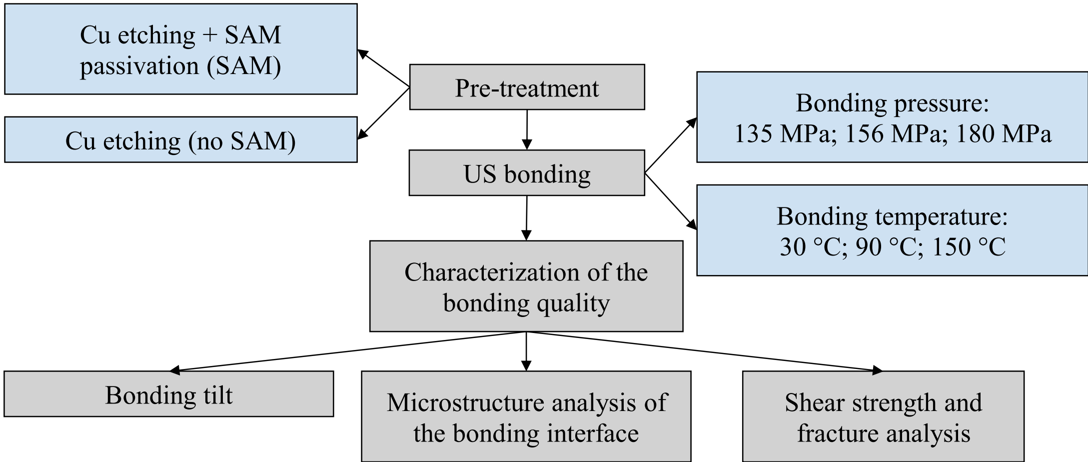

Fig. 8-1 Schematic overview of experiments for Cu-Cu US bonding with SAM passivation

Samples with and without SAM passivation were used for US bonding. Details of Cu etching and passivation are given in chapter 4.2. Parameters for Cu-Cu bonding in air were chosen in a low-temperature range. This technology is of particular interest for temperature sensible components, as low bonding parameters for US flip-chip Cu-Cu bonding in air have not been investigated widely before. State of the art in Cu-Cu bonding is presented in chapter 2. The quality of the formed interconnects was evaluated by SEM and TEM analysis of the cross-sections, shear strength and fracture surface analyses. Tab. 8-1 presents set and measured bonding parameters by integrated sensors into the bonder FCB3.

Tab. 8-1 Set and measured bonding parameters

Bonding parameter	Set value	Measured value
Power, W	6	6
Contact load, N	5	3.6
Bonding force, N	28.5; 33.3; 38	26.5 30.6; 35.2
Bonding pressure, MPa	145; 170; 194	135; 156; 180
Bonding temperature head, °C	30; 90; 150	-
Bonding temperature stage, °C	30; 90; 125	30.8; 89.4; 124.8

There are no sensors installed for the temperature measurement of the US bonding head of the FCB3 bonder. The results of the thermocouple measurements between the dies are also not reliable enough due to a very short bonding time and the presence of US vibration. Stage and head temperatures are kept at constant levels at 30 °C, 90 °C and 125 °C / 150 °C, respectively. Ramping of temperature is not applied.

Fig. 8-2 demonstrates exemplary measured bonding profiles, acquired by sensors of the bonder FCB 3. Measured bonding forces are (1.08…1.09) times lower than the set values. The choice of such a bonding profile for the US flip-chip Cu-Cu bonding is explained in [117] and discussed in chapter 8.2.1.2.

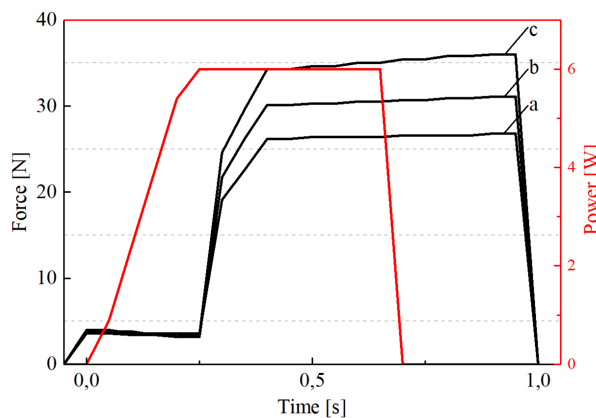

Fig. 8-2 Measured bonding profiles attained by sensors of FCB3 bonder for the averaged measured force values of 26.5 N (a), 30.6 N (b) and 35.2 N (c)

Measured pressure values (135, 156 and 180 MPa) and set bonding head temperature values (30, 90 and 150 °C) are used for presentation and discussion of the results in this study further on.

8.2 Inspection of the bonding tilt and its influence on the bonding area

8.2.1 Results and discussion

8.2.1.1 Characterization of the bonding tilt

Each bottom die received a mark in the right lower corner of the die in order to take into account its orientation (Fig. 8-3, (a)). The problem of planarity of bonding tool is essential since its tilting may influence the distribution of force on the dies and hence affect bonding yield and cause different deformation of the microbumps (Fig. 8-3, (b)). The bonding tilt comes from the non-planarity between the bonding tool and heating stage. Although the bonding machine is calibrated, the problem cannot be eliminated.

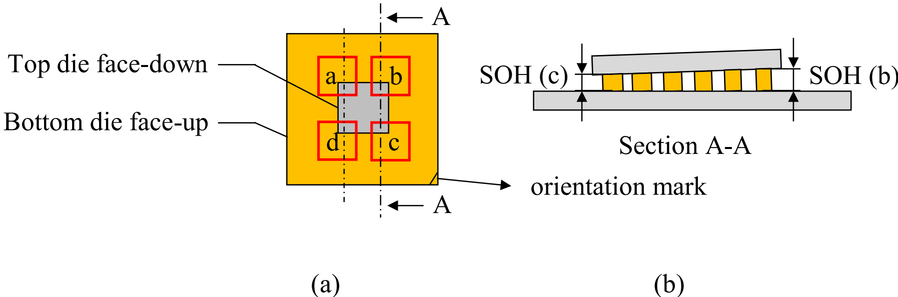

Fig. 8-3 Top view of bonded top and bottom dies with dotted lines showing the cross-section planes (a); exemplary cross-section A-A showing the differences of SOH between the corners *c* and *b* (b)

Bonding tilt was examined by SEM imaging of cross-sections in the target planes *c-b* and *d-a*, as shown in Fig. 8-3 and Fig. 8-4. SEM images provide values of standoff heights in four corners of a chip. Three chips were analyzed for this purpose: bonded at 135 MPa, 156 MPa and 180 MPa (bonding temperature 90 °C).

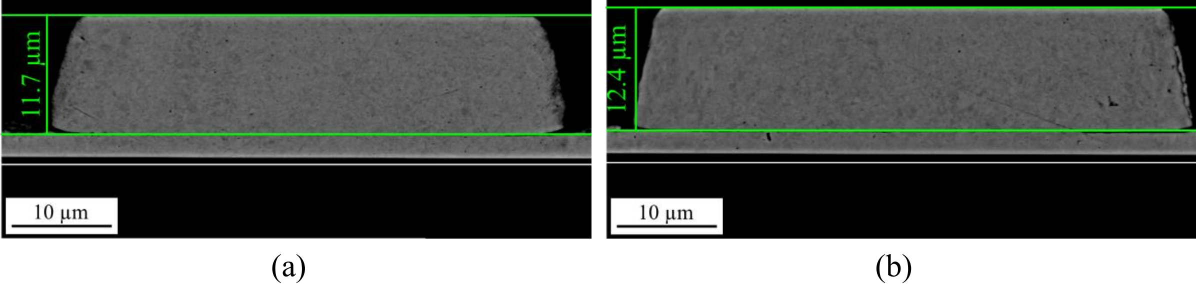

Fig. 8-4 Standoff height in the corner *c* (a) and corner *b* (b)

Maximal difference in standoff height was detected between corners *a* and *c* and was 1.34 µm. The correlation between bonding pressure and tilt was not found, which matches well with the literature [145, p. 55].

Fig. 8-5 shows a Si backside of a bonded top die from the top view (as shown in Fig. 8-3, a), scanned by confocal microscope µSurf with an objective 3200-S (5x) with *z*-axis resolution of

1.17 µm. Cu surface of bottom dies was leveled to “zero” height using µSurf software. One chip pair per parameter set was analyzed, which is 18 samples in total. The distribution of heights throughout the Si surface is well seen with the help of the color scale on the right side of the figures. Fig. 8-5 reveals that the right side of all chips (b-c) bonded at 135 MPa (a), 156 MPa (b) and 180 MPa (c) is lower than the left side (a-d) of the chips. The scales do not include minimum and maximum values. This is a fine scaling that shows the most frequently detected height values. The imprint of the bonding tool with a vacuum opening in the center is also detected in Fig. 8-5.

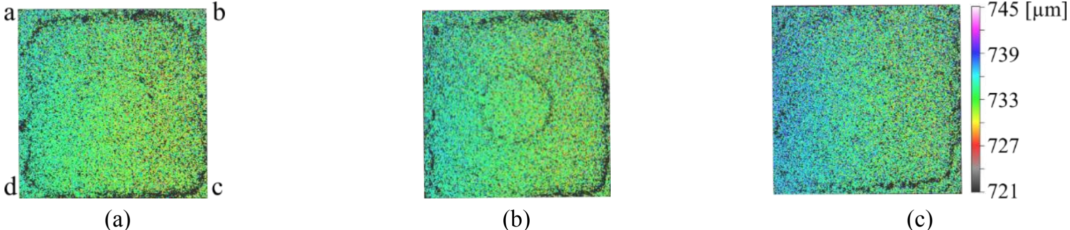

Fig. 8-5 Plane view of heights distribution on Si backside of the top dies after US bonding at (a) 135 MPa, (b) 156 MPa and (c) 180 MPa at 90 °C (fine scaling)

Fig. 8-6 shows the distribution of bump stamps on the bottom dies after shear strength tests. Coarse scaling with minimum and maximum values was used in this case. The heights values, higher than 12 µm, correspond to Si fractures. The results reveal that the amount of bumps is the highest in the right lower corner *c* and the lowest in the left upper corner *a*. These results correlate well with the results revealed by the cross-sectioning results and the results above. 18 samples were analyzed for this purpose.

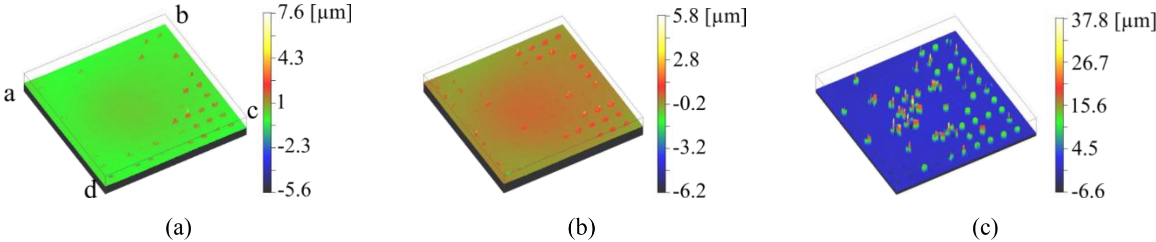

Fig. 8-6 3D view of heights distribution on bottom dies after shear strength tests on the example of samples bonded at 135 MPa (a), 156 MPa (b), 180 MPa (c) at 90 °C (coarse scaling)

8.2.1.2 Influence of the bonding tilt on the calculation of the bonding area

Microbump deformation causes the change of the total bonding area and, thus, influences the distribution of the bonding pressure and the shear strength. Exposure to bonding pressure, ultrasonic vibration and heating processes can cause deformation independently from the tilt [113]. It is important to analyze the maximal possible deformation of microbumps in this experiment in order to know if the influence of bonding tilt and deformation on the change of the bonding area is significant or can be neglected for further observations. Fig. 8-7 shows the influence of the bonding tilt on the bonding yield and the microbump deformation.

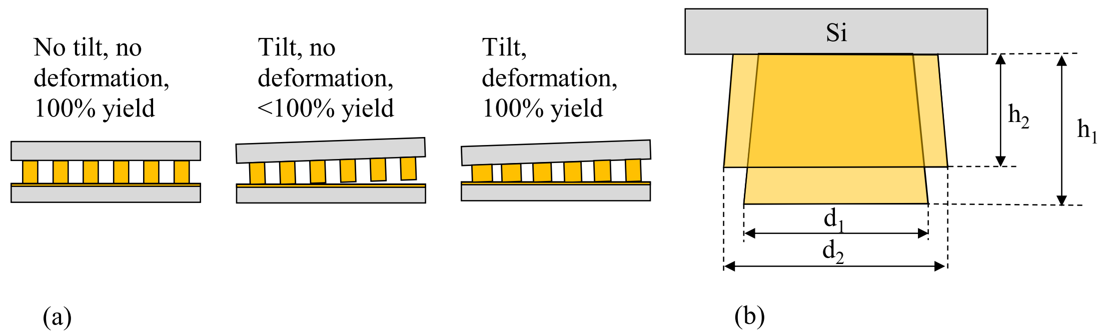

Fig. 8-7 Schematic representation of the effects of bonding tool planarity on bonding yield (a) and microbump deformation (b)

The initial diameter $d_1 = 50$ µm and the average height $h_1 = 12.7$ µm of a microbump are known (chapter 4.1) and schematically shown in Fig. 8-7. The minimal detected microbump height from the corner *c* (with the highest deformation) $h_2 = 11.4$ µm. Assuming that the volume of a single microbump stays constant before and after the deformation and that the microbump is a cylinder (for simplicity), the highest diameter value for the deformed bump can be approximately estimated using formula (8-1).

$$d_2 = d_1 \sqrt{\frac{h_1}{h_2}} \tag{8-1}$$

The maximal deformed microbump diameter is $d_2 = 52.8$ µm in this case. The corresponding bonding area (100 microbumps) with the maximally deformed bumps ($S_2 = 0.211$ mm^2) is approximately 10 % bigger than the initial one ($S_1 = 0.196$ mm^2). Since microbumps in other chip corners (*a*, *b*, *d*) and at lower bonding parameters are usually less deformed, this percentage is considered to be negligibly low and is not accounted for in the shear strength (in N/mm^2 = MPa) calculations.

Bonding tilt affects not only the distribution of force throughout a chip but also the distribution of power. Observing the bonding profiles in Fig. 8-2, during the first bonding stage, a low contact load (3.6 N) is applied, whereby ultrasonic power reaches its maximum set level (6 W). During this phase bumps come into contact, go through the cleaning phase and SAM is partially desorbed (chapter 3.3.1). The bonding force starts to increase after that and also reaches its maximum set level. During these 2 steps, due to the bonding tilt, part of the bumps is exposed to a higher bonding force than the other part. Afterward, the chips are exposed to the maximum values of power and force for 250 ms. When the power decreases to 0 W, the bonding force stays almost constant for a further 250 s. During this time the interconnects strengthen. The profiles in Fig. 8-2 are typical for a flip-chip US bonder [117], [149] and have been adjusted taking into account considerations of the device manufacturer Panasonic [150].

The planarity of the bonding head and stage plays a very important role, especially for the chosen bonding profile. If the contact load exposes a very low amount of bumps to US rubbing due to the tilt presence, the US power density may be too high and even destroy the interconnect. The highest detected tilt of the bonding tool in this study is 1.34 µm. The influence of this tilt

on the change of the bonding area is negligibly small. The tilt, however, influences the bonding yield, meaning the number of actually bonded microbumps, which will be discussed in the next chapters (8.3 - 8.4). Bonding parameters, used in this study, however, can compensate for the tilt problem and achieve a 100 % yield.

Luk et al. have investigated US flip-chip bonding of Au-Au interconnects and have found a tilt within the range of 7 μm [118]. Arai et al. have researched Cu-Cu US flip-chip bonding and claim that the planarity problem can be solved by using higher microbumps, for instance, with a height of 20 μm [115]. According to their findings, the deformation rate increases with the increase of the bump height. This can help to adjust planarity without the application of higher force or power.

The microbumps must come into contact as simultaneously as possible. For this purpose several methods can be used:

1. Calibration of planarity between the bonding head and stage
2. Minimizing the chip size
3. Increasing the height of bumps
4. Using such bonding tool size, which is matched precisely with a chip by size [150]

8.3 Characterization of the bonding interface by SEM and TEM analyses

8.3.1 Results and discussion

8.3.1.1 SEM analysis of Cu-Cu bonding interface

This subchapter presents the characterization of the bonding interface quality through SEM analysis of the interconnect cross-sections. In this evaluation, a good bonding quality is characterized by the absence of delamination, cracks, or voids at the bonding interface. Fig. 8-8 (c) presents a seamless bonding interface in the center of the interconnect and thin delamination lines at the bump edges ((a) and (b)).

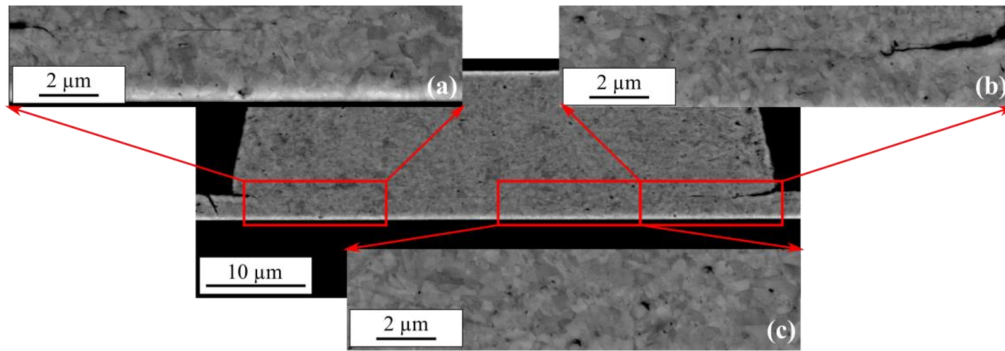

Fig. 8-8 Thin delamination lines at bump edges (a, b) and a seamless bonding interface in the middle (c) on the example of a sample with SAM passivation bonded at 30 °C at 180 MPa

Cross-sections were always made in the same plane *c-b* (Fig. 8-3) for better comparison. Each cross-section plane reveals 10 microbumps. Fig. 8-9 - Fig. 8-11 show cross-sections of interconnects with the best bonding quality from each parameter set.

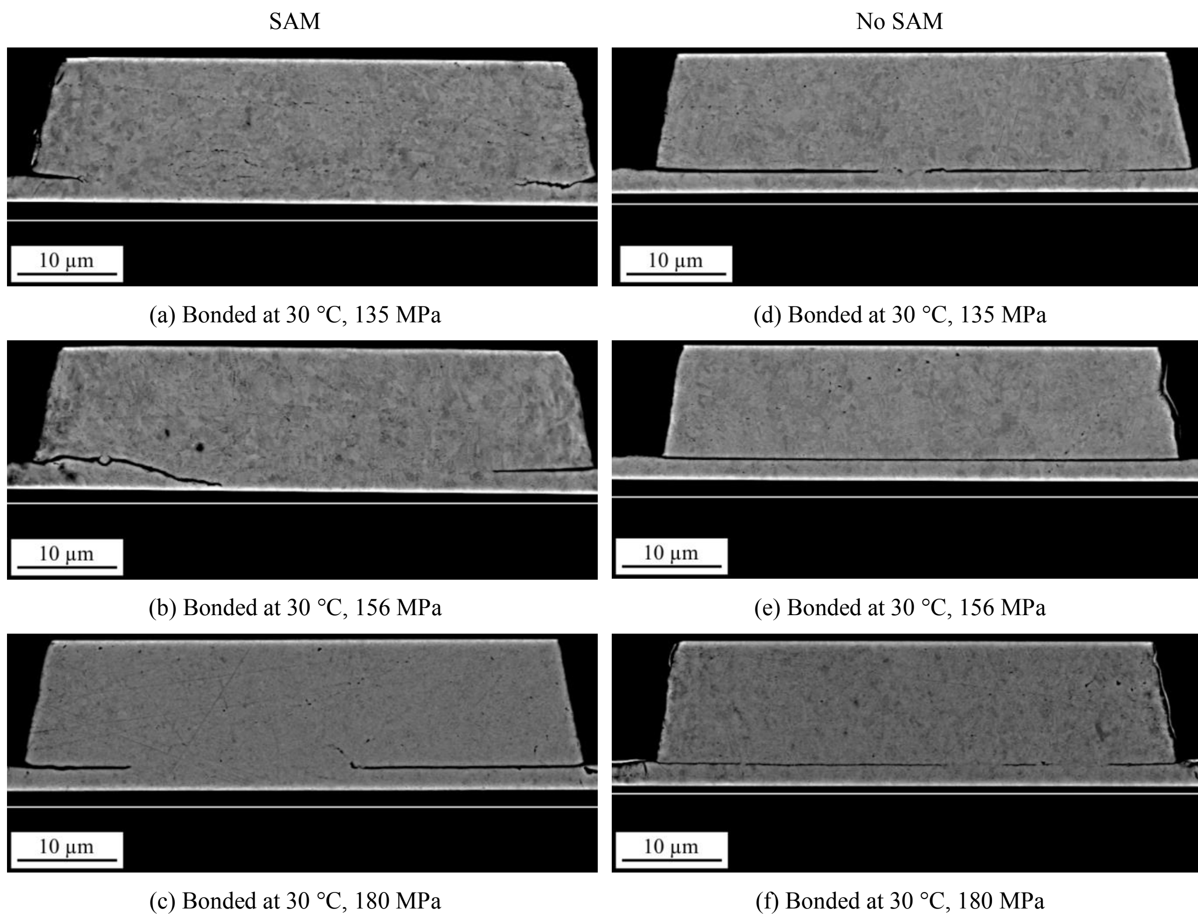

Fig. 8-9 SEM images of the interconnects cross-sections of the samples bonded at 30 °C, at 135 MPa (a, d), 156 MPa (b, e), 180 MPa (c, f)

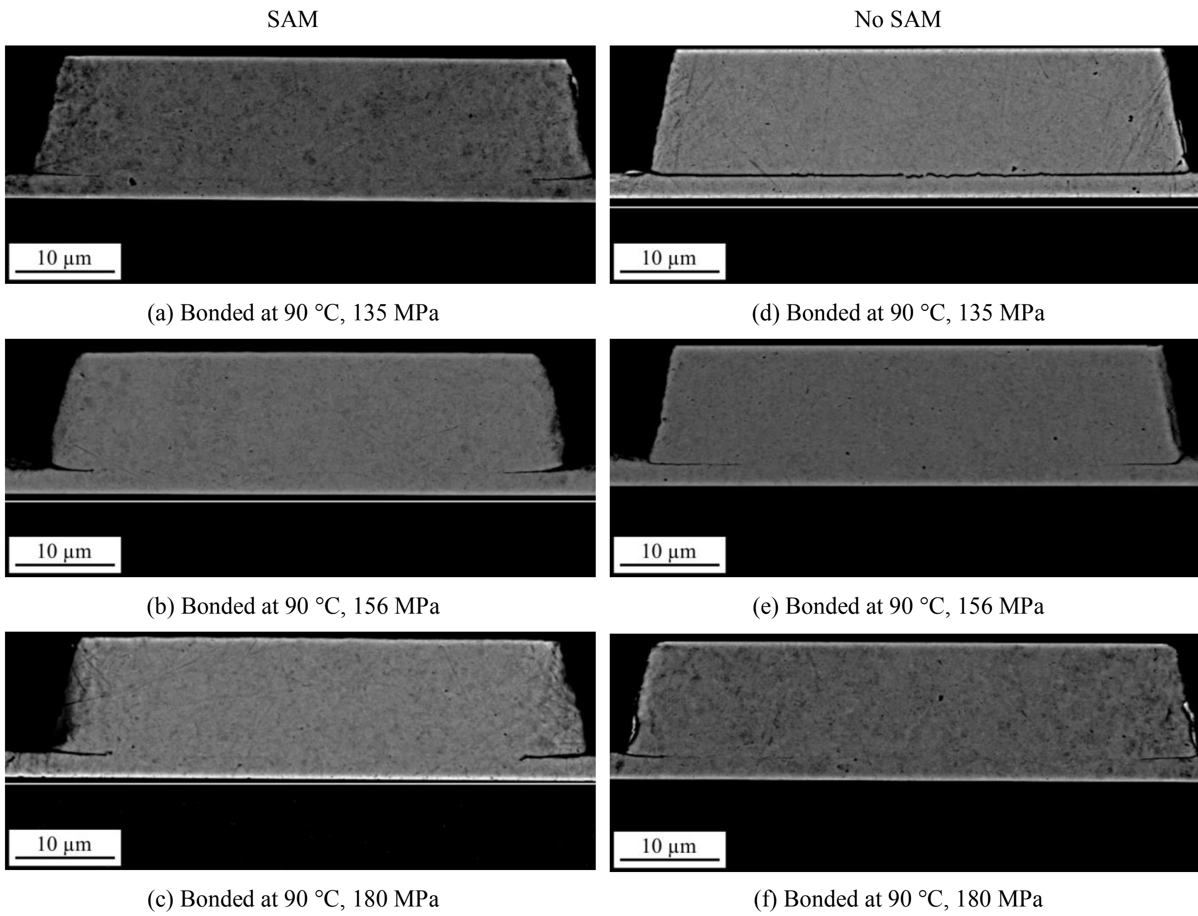

(a) Bonded at 90 °C, 135 MPa

(d) Bonded at 90 °C, 135 MPa

(b) Bonded at 90 °C, 156 MPa

(e) Bonded at 90 °C, 156 MPa

(c) Bonded at 90 °C, 180 MPa

(f) Bonded at 90 °C, 180 MPa

Fig. 8-10 SEM images of the interconnects cross-sections of the samples bonded at 90 °C, at 135 MPa (a, d), 156 MPa (b, e), 180 MPa (c, f)

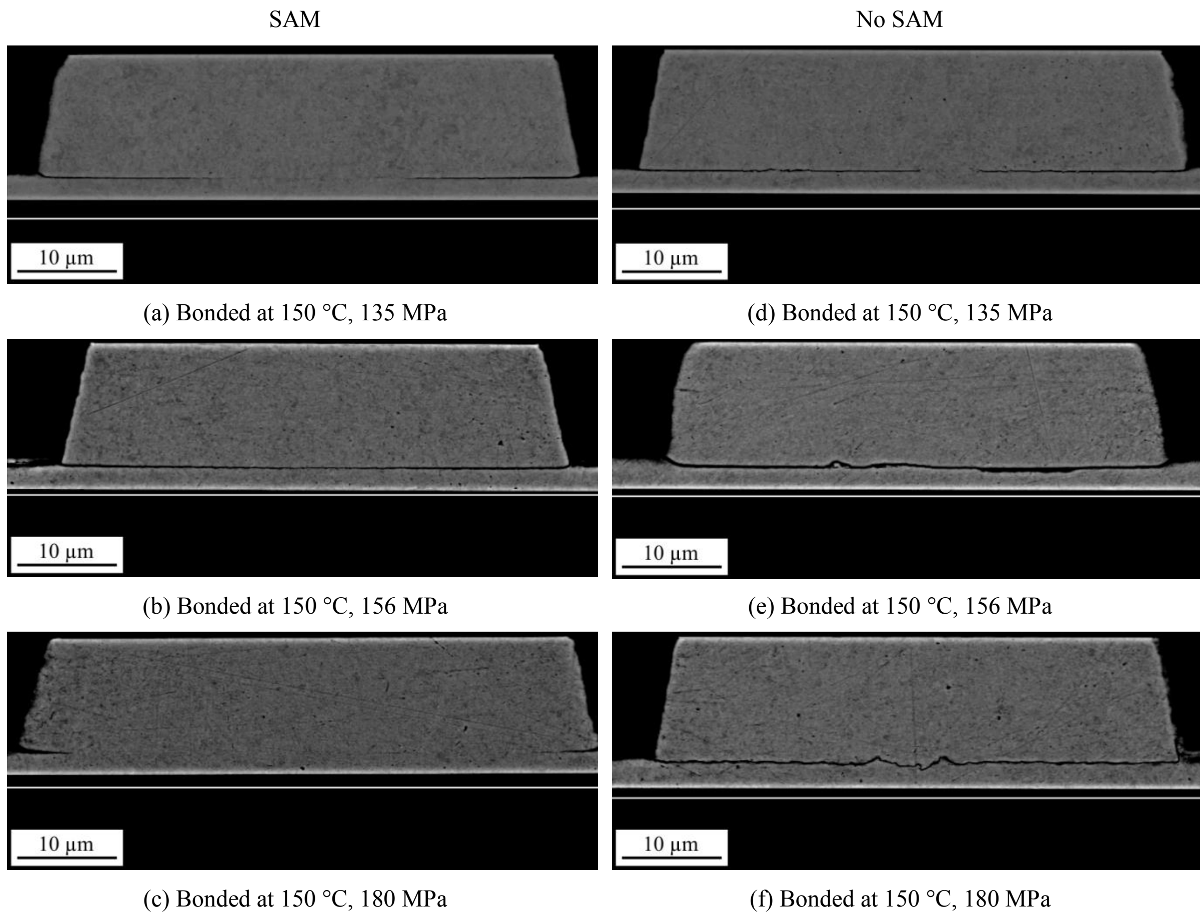

Fig. 8-11 SEM images of the interconnects cross-sections of the samples bonded at 150 °C, at 135 MPa (a, d), 156 MPa (b, e), 180 MPa (c, f)

Fig. 8-9 - Fig. 8-11 reveal that Cu-Cu interconnects with SAM have higher bonding quality in comparison to unprotected samples. This SEM analysis provides information only about one cross-section plane, not a 3D view of the interconnects. Therefore, the results should be evaluated together with shear strength and fracture surface analyses (subchapter 6.3). SEM method, however, yields a direct representation of the state of the bonding interface in contrast to other indirect characterization methods (shear strength, fracture surface analyses). The percentage of the bonding interface length, which is well bonded, is estimated for each bump (Fig. 8-12).

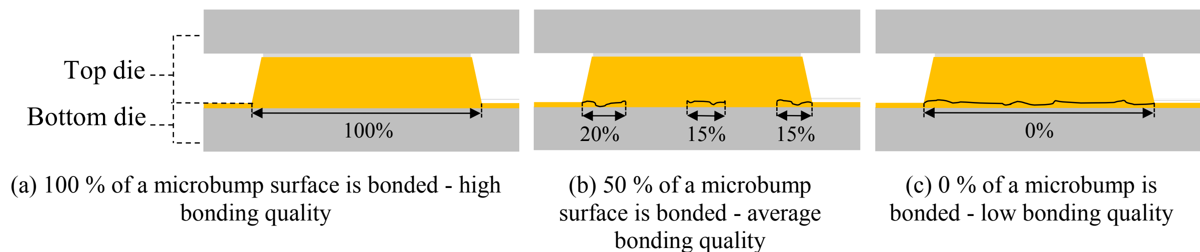

Fig. 8-12 Classification of bonding quality types based on evaluation of the bonding quality

The results are summarized in Fig. 8-13 - Fig. 8-18. In order to evaluate the influence of the bonding tilt, the results in each graph are shown sequentially from the first interconnect

(corner c) to the tenth interconnect (corner b). 10 bumps per parameter set, visible in a cross-section line, have been investigated.

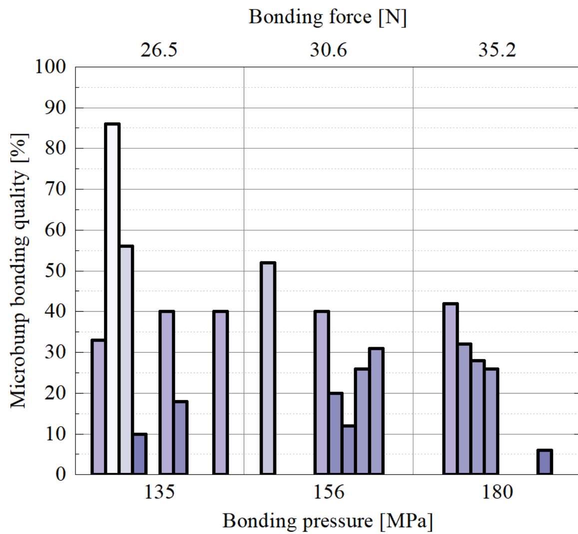

Fig. 8-13 Influence of bonding pressure on the bonding quality of the interconnects with SAM (SAM) passivation bonded at 30 °C

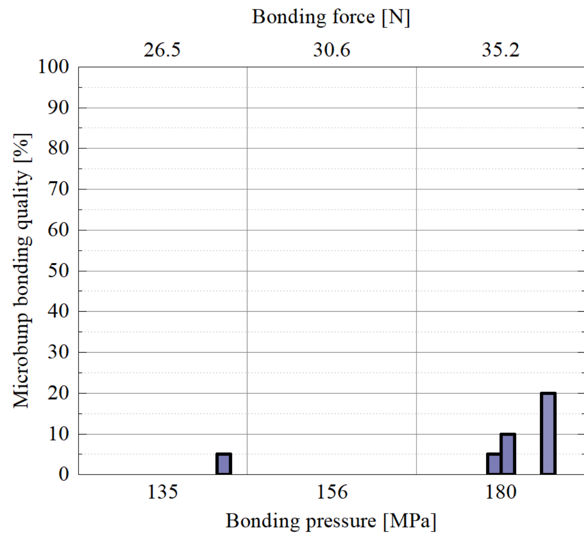

Fig. 8-14 Influence of bonding pressure on the bonding quality of the interconnects without SAM (no SAM) passivation bonded at 30 °C

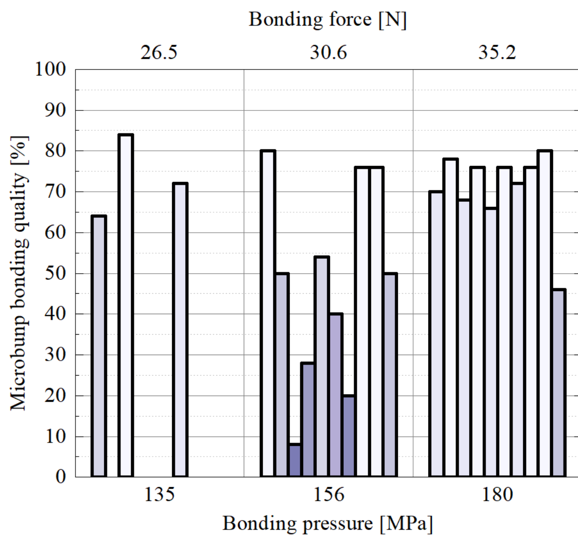

Fig. 8-15 Influence of bonding pressure on the bonding quality of the interconnects with SAM (SAM) passivation bonded at 90 °C

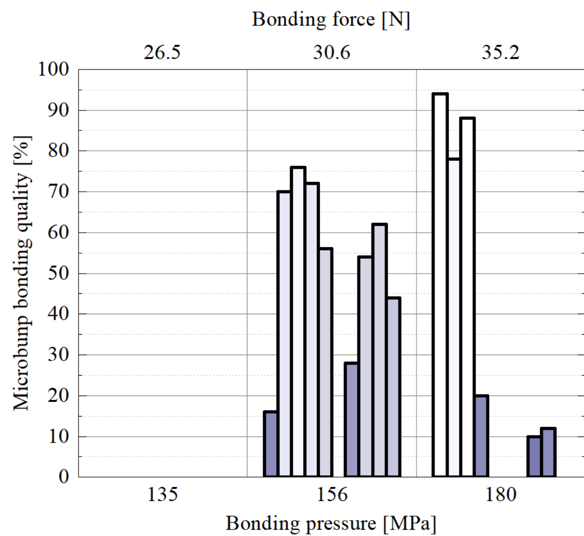

Fig. 8-16 Influence of bonding pressure on the bonding quality of the interconnects without SAM (no SAM) passivation bonded at 90 °C

SAM, 150 °C

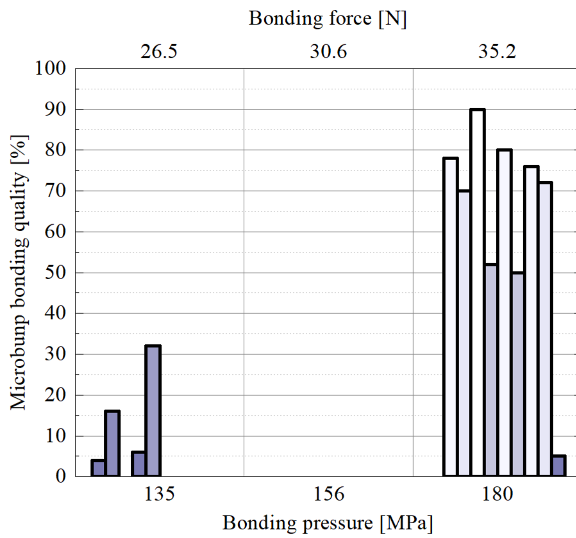

No SAM, 150 °C

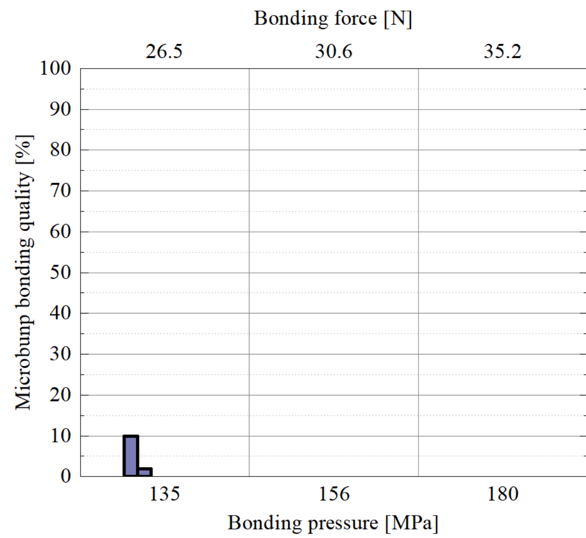

Fig. 8-17 Influence of bonding pressure on the bonding quality of the interconnects with SAM (SAM) passivation bonded at 150 °C

Fig. 8-18 Influence of bonding pressure on the bonding quality of the interconnects without SAM (no SAM) passivation bonded at 150 °C

Having analyzed SEM images of the bonding interfaces in Fig. 8-13 - Fig. 8-18, it can be stated that there is a tendency of decreasing interconnect quality from corner *c* to *b*, which can be caused by a tilt between the bonding head and stage, discussed in chapter 8.2.1.2. As corner *c* is exposed to the highest bonding load and power, this part of interconnects have often better bonding quality in comparison to interconnects from other chip sides.

Fig. 8-19 presents SEM images of the cross-sections with common types of interconnect defects. These defects can be divided into such categories: crack, thin delamination and no bonding. Some of the terms have already been used by Fushimi et al. [151], who also investigated Cu-Cu ultrasonic bonding.

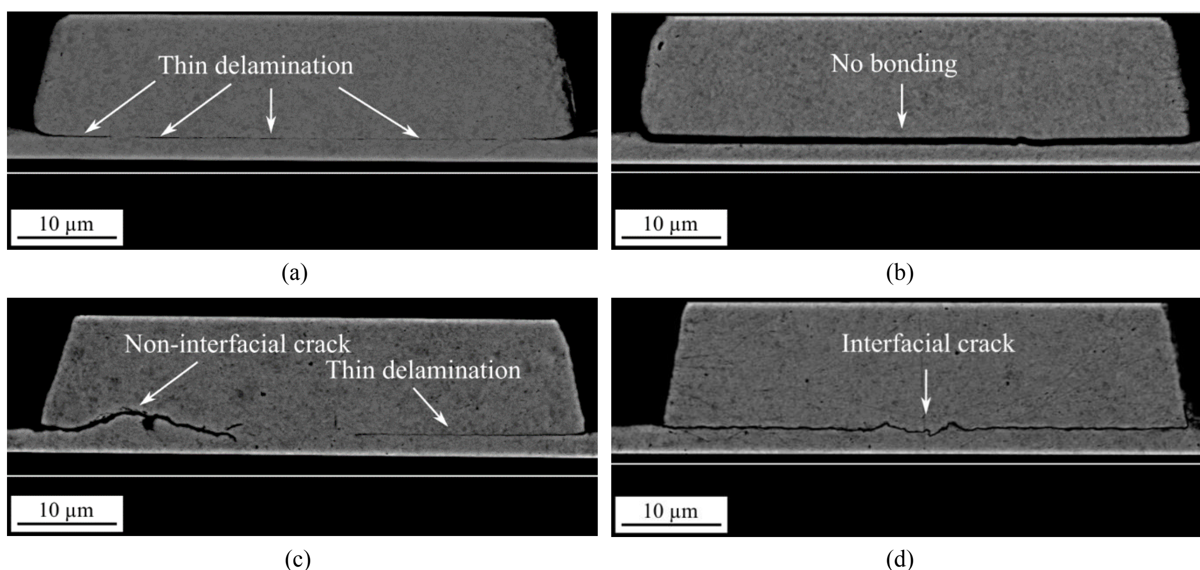

Fig. 8-19 SEM images of the cross-sections with exemplary types of bonding region defects: thin delamination (a), no bonding (b), non-interfacial crack (c) and interfacial crack (d)

The “no bonding” Cu-Cu interface can correspond to the lifted microbump, which can be the result of a weak bonding interface of this interconnect and the adjacent ones. If there are many adjacent bumps with the weak interface, it is possible that they slightly rise from the bonding interface when exposure to bonding pressure stops. The thickness of such a region commonly lies in the range of 0.65-0.75 µm. Maximum detected thickness equals 1.42 µm. Unbonded regions (thin delamination or no bonding) form as a result of underbonding: too low bonding pressure, too low received ultrasonic energy, too short bonding time, or too high contamination level.

The thin delamination lines usually have a thickness in the range of (10…15) nm (Fig. 8-19, (a)). These unbonded regions suggest that there are not many unbonded adjacent bumps. Therefore, they do not rise.

Cracks are characterized by deflecting and sometimes branched lines. These lines can be interfacial or non-interfacial. They reach a thickness of approximately 300 nm on the SEM images of the interconnects cross-sections. A non-interfacial crack is caused by the overbonding process. Geißler used terms “overbonded”, “optimal” and “underbonded” states of the interconnects in her Ph.D. thesis about wire bonding [112]. Underbonded state corresponds to lifted regions of a bonded wire. Straight black lines correspond to the underbonded region of a joint [151]. Overbonded state corresponds to a joint, which had a too low influence of force (hardening) and too high influence of ultrasonic energy (softening), which is characterized by low pull strengths. In this case, ultrasonic power destroys an already well-bonded interface. Lu et al. confirm that grain boundaries are an obstacle to crack propagation [152]. A refinement of Cu grains takes place during ultrasonic bonding. The crack propagates around the refined region. Therefore, deflected and meandered lines correspond to cracks [153, p. 408].

Using the proposed classification of the bonding regions, one bonded pair of chips per parameter set was evaluated. There are nine parameter sets for each passivation type (with/without SAM), which come from the variation of the bonding pressure (135 MPa, 156 MPa, 180 MPa) and the bonding temperature (30 °C, 90 °C, 150 °C). Each cross-section maintained 10 interconnects, hence, 90 interconnects with SAM and 90 interconnects without SAM were analyzed. Often one interconnect maintained several types of bonding regions. For instance, Fig. 8-19 (c) shows an interconnect with a non-interfacial crack, thin delamination and a seamless bonded interface. Fig. 8-20 shows the quantity of the interconnects, which contain a certain type of bonding region.

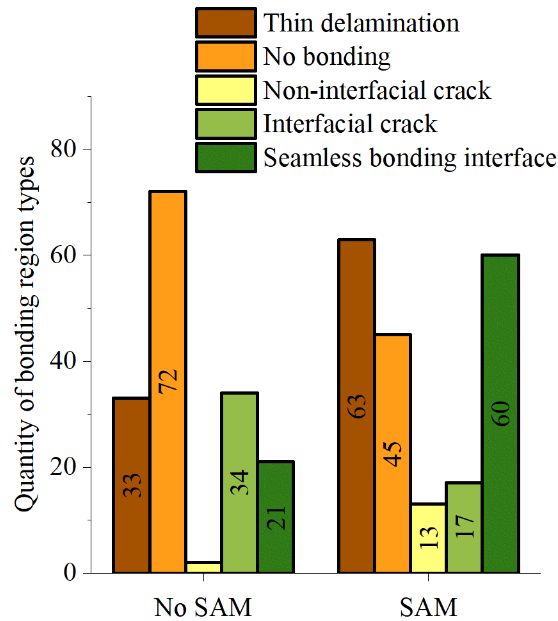

Fig. 8-20 Quantity of the interconnects with and without SAM, which maintains such types of bonding regions: thin unbonded region, thick unbonded region, non-interfacial crack, interfacial crack and seamless bonding interface

The results show that 60 out of 90 interconnects with SAM contain a seamless bonding interface, in contrast to 21 out of 90 interconnects without SAM passivation. There are 33 interconnects without SAM and 63 interconnects with SAM containing thin delamination. There are 72 interconnects without SAM and 45 interconnects with SAM containing "no bonding" regions. Non-interfacial crack is detected in two interconnects without SAM and in 13 interconnects with SAM coating. Interfacial cracks are detected in 34 interconnects without SAM and in 17 interconnects with SAM passivation.

Fig. 8-15 - Fig. 8-16 show that most of interconnects have a high joint quality for the samples with SAM bonded at 90 and 150 °C at 180 MPa. This correlates well with the results of the shear strength and fracture surface analyses (subchapter 8.4). Higher bonding force and temperature enhance the deformation process of microbumps. Deformation results from forming dislocations on the Cu surface [112, p. 92]. An interconnect starts to form as a result of activation of Cu surfaces and chemical interaction between them [113, p. 9].

Edge delamination is typical for all of the interconnects. It can be caused by bump deformation. Ultrasonic power is first applied to the initial microbump top surface. According to the comparison between the wire and microbump US bonding, an initial microbump surface can go through 4 phases: pre-deformation, cleaning, deformation and interdiffusion (subchapter 3.3.1). During the deformation time, the bump widens. Hence, the edges of the bump are exposed for a shorter period to the less density of ultrasonic power. Ye et al. report that microbump edges obtain the highest potential for delamination [154].

Fig. 8-20 shows that non-interfacial cracks are more often detected in the interconnects with SAM than without SAM (13 interconnects against 2). A non-interfacial crack appears commonly at higher bonding pressures and temperatures. The right side of the chip is exposed to a higher force, power density and longer bonding time due to the tilt between the bonding

head and stage. SAM passivation protects from oxidation and thus the cleaning phase is shorter [113]. Ultrasonic power is applied to clean Cu surfaces, which causes faster interconnect formation and in some cases its destruction due to too long exposure to US energy. Nevertheless, the ratio of such interconnects is < 20 %, which corresponds rather to a low level of overbonded interconnects.

Samples without SAM have 30 % more "no bonding" regions, which are slightly lifted . This suggests that there is a larger amount of weak interconnects without SAM in comparison to the passivated samples.

34 interconnects without SAM contain interfacial cracks, whereby samples with SAM comprise 17 of those. This suggests that samples without SAM have more regions in the early recrystallization phase and more adjacent unbonded regions (Fig. 8-19, (d)). These neighbor unbonded regions, as well as nearby unbonded microbumps, can cause additional tension in the region in an early recrystallization phase after US bonding stops. Thus, if the region is too weak, the crack propagates through it.

The amount and ratio of well-bonded regions (seamless bonding interface) increase with bonding pressure and temperature. 60 SAM interconnects contain a seamless bonding interface, in contrast to 21 interconnects without SAM.

Classification of bonding regions for US flip-chip bonding has not been done previously and, therefore, contributes to the investigation of the interconnect quality and further optimization of the bonding parameters.

Having characterized cross-sections of the US bonded Cu-Cu by SEM, the images with higher resolution by TEM can be taken.

8.3.1.2 TEM analysis of Cu-Cu bonding interface

Using SAM as a temporary passivation layer requires its removal before bonding in order to avoid the risks of low electrical and thermal conductivities, low mechanical strength, as well as corrosion issues in a long-term view. Mechanical rubbing is one of the possible SAM removal methods, along with thermal and electrical desorption methods [97]. Whether SAM can be removed during US bonding due to US rubbing, has not been investigated yet. For this purpose analyzing of Cu-Cu interface after US bonding using high-resolution TEM and EDX techniques is proposed in this study.

SEM characterization of the cross-section planes has shown that edges of microbumps are almost always unbonded or have poor bonding quality. This can be caused by the fact that the microbump center is exposed to the longest bonding time and highest ultrasonic power and bonding force. Due to the slight microbump deformation, the edges are bonded at lower bonding parameters and, therefore, can exhibit delamination. Hence, edge and central regions of the Cu-Cu interconnect were chosen for TEM analysis (Fig. 8-21, (a), (b)).

Fig. 8-21 presents SEM, TEM and dark-field STEM images of the edge and central regions of two Cu-Cu interconnects with SAM passivation bonded at 180 MPa at 150 °C. The interface in Fig. 8-21 (c) shows a straight line, which represents the bonding interface in the edge region.

A zig-zag or wave-shape line, on contrary, characterizes the interface of the central region (Fig. 8-21, (d)). The blue rectangle in the edge region marks the transition area from the straight line to a wave-shaped interface. This area is shown with higher magnification in Fig. 8-21 (f). The red rectangle in the central region is shown with higher magnification in Fig. 8-21 (e). The high-resolution dark-field STEM images show wave-shape interface and nanoscale voids for both of the magnified regions.

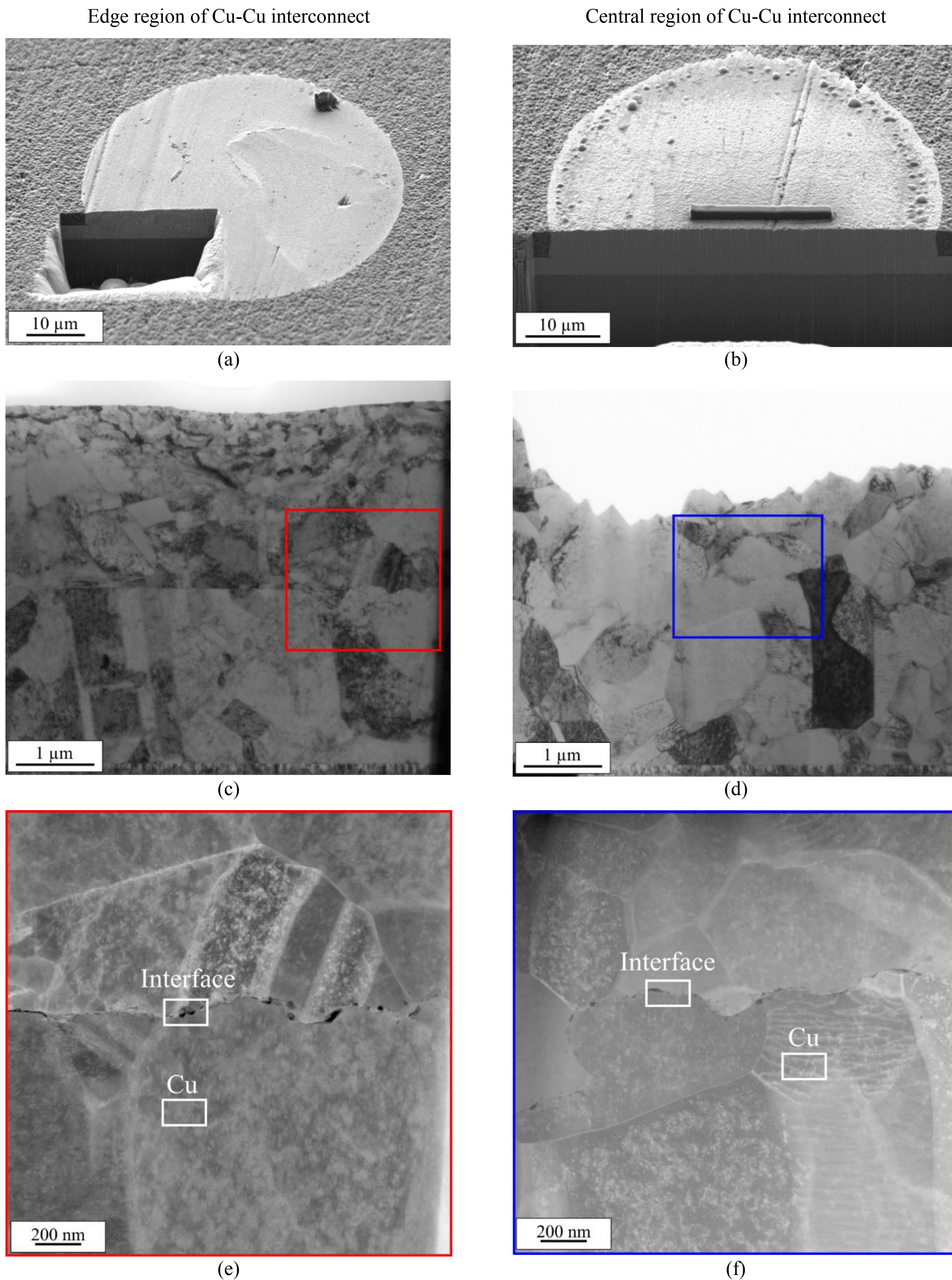

Fig. 8-21 SEM images of edge (a) and center (b) regions of Cu-Cu interconnects wherefrom thin TEM lamellae were cut out using FIB technique; TEM images of the edge (c) and central (d) cross-sectional regions with red and blue marks for the magnified view below; dark-field STEM images of the edge (e) and central (f) cross-section regions at higher magnification with white marked regions for EDX measurements

Chemical composition of the interfacial region (marked as "Interface") and of pure Cu surface (marked as "Cu") for edge and central regions (Fig. 8-21, (e-f)) is measured using EDX. Fig. 8-22 presents the results of the EDX measurements. Fig. 8-22 (a) shows that a low-intensity S peak can be indicated for the interface with nanovoids in the edge region. No S

species are detected in the Cu-Cu interface of the central region (Fig. 8-22, (b)). No S species are detected for the pure Cu surfaces of both regions, as expected. C and O species are detected for the Cu-Cu interface and pure Cu surface in the edge region (Fig. 8-22, (c)), which is probably caused by a short air exposure of TEM lamella during the transportation to the analysis chamber. O peaks are present in the Cu-Cu interface and on the pure Cu surface of the central region (Fig. 8-22, (d)). No differences are indicated between O intensities for the interface and pure Cu surface in the central region, which suggests that close to no oxidation occurs on the Cu-Cu interface after bonding with SAM.

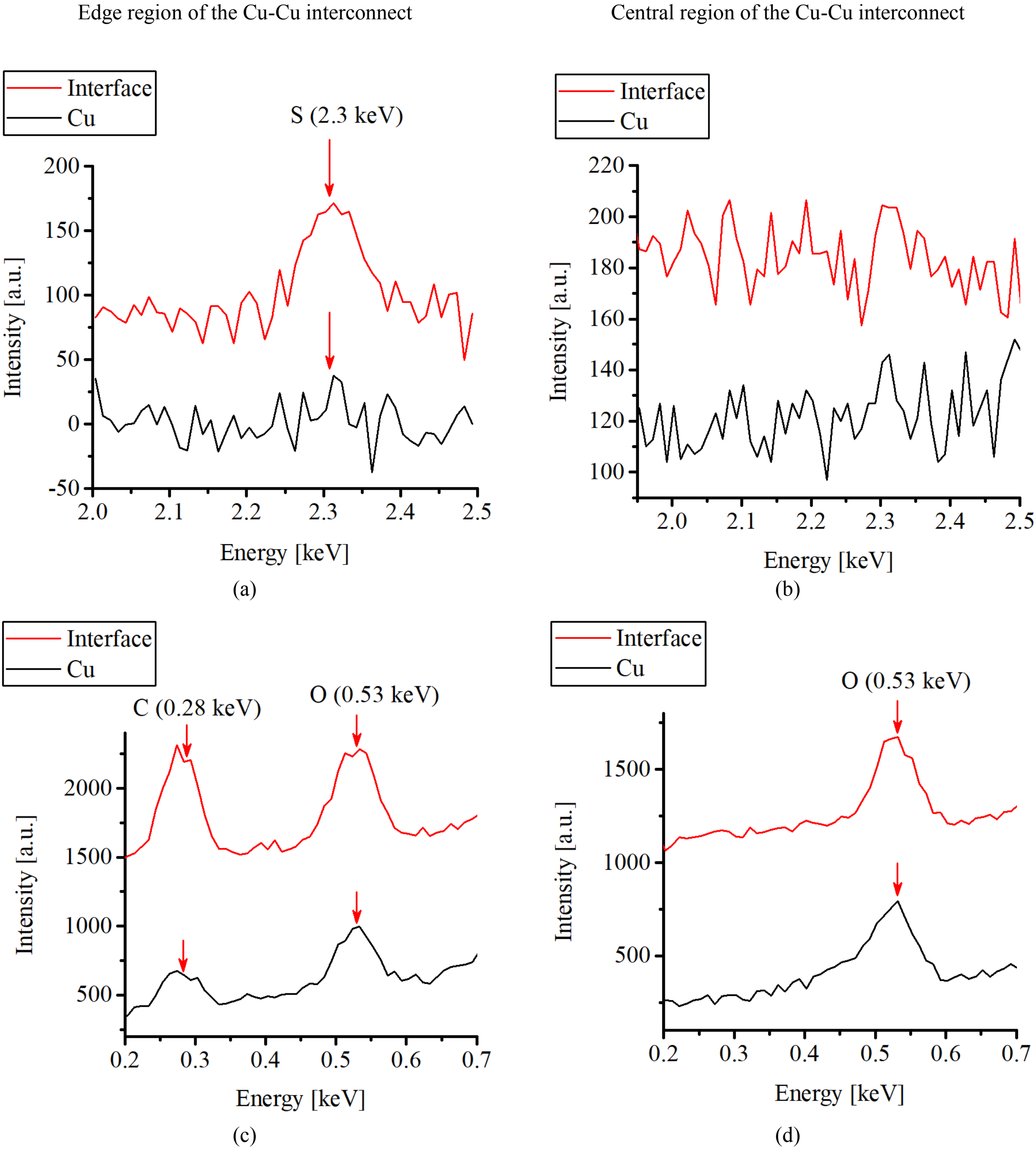

Fig. 8-22 EDX spectra of the Cu-Cu interface and pure Cu surface in the edge and central regions of the interconnects in the energy range between 2 keV and 2.5 keV for S spectrum detection (a, b) and the range between 0.2 keV and 0.7 keV (c, d) for the detection of O and C spectra (if present)

EDX analysis of TEM lamellae shows the presence of a weak S peak at the Cu-Cu bonding interface in the microbump edge region (samples passivated with SAM prior to bonding at

180 MPa at 150 °C). The center of a bump, on contrary, reveals no S residuals in the Cu-Cu bonding interface (Fig. 8-22, (a), (b)). These results confirm the theory that bonding (deformation) starts from the bump center, the edges are bonded at last. Therefore, lower interconnect quality is observed at the edge region and SAM residuals are present there, too. Most of the bonding area, nevertheless, is bonded well without or with barely detectable SAM species. Considering these results and the monolayer thickness (≤ 1.5 nm), the risk of Cu corrosion in connection to SAM application as a passivation layer in a long-term view can be estimated as negligibly low.

Zig-zag or wave shape form of the Cu-Cu interface (Fig. 8-21, (e), (f)), in contrast to a straight line form, is considered as a sign of a strong Cu-Cu interconnect in literature reports. Chua et al. observe a zig-zag form of the Cu-Cu interface in high-resolution TEM [155]. The research suggests a high mechanical strength of the interconnect. Rebhan et al. observe the zig-zag shape of the Cu-Cu bonding interface as well [156]. The research group suggests that interfacial voids can come from surface roughness, surface oxide, or from vacancy interdiffusion due to increased local stress. Room temperature Cu-Cu bonding without pressure, but with the following annealing, can also result in a zig-zag interface with some voids according to [18].

Bonding did not comprise annealing, was carried out in air, in a very short time (1 s), in a low-temperature range. The achieved zig-zag form of the Cu-Cu interconnects and the absence of SAM in the biggest part of the bonding area are valuable results, which indicate a high potential of the proposed technology for future microelectronic applications.

In order to fully characterize bonding quality, cross-sectional analysis has to be supported with mechanical strength tests. Therefore, shear strength tests and fracture surface analysis are presented and discussed in the next chapter.

8.4 Characterization of shear strength tests and fracture surface analysis

8.4.1 Results and discussion

8.4.1.1 Die shear strength tests and fracture surface analysis

This subchapter presents the results of the shear strength tests and fracture surface analysis for the samples with and without SAM passivation. 5 sample pairs were used for each bonding parameter set. Therefore, there were 90 sample pairs in total. Calculation of shear strength in MPa is done using the initial bonding area due to negligibly small deformations of the microbumps (discussed in subchapter 8.2.1.2).

There are four types of fracture surfaces after shear strength tests, common for both TC and US bonding processes: Si fracture, Ti fracture, Cu fracture and no contact. Details of each type definition are discussed in subchapter 7.1. Fig. 8-23 shows SEM images of the four fracture surface types and corresponding EDX measurements.

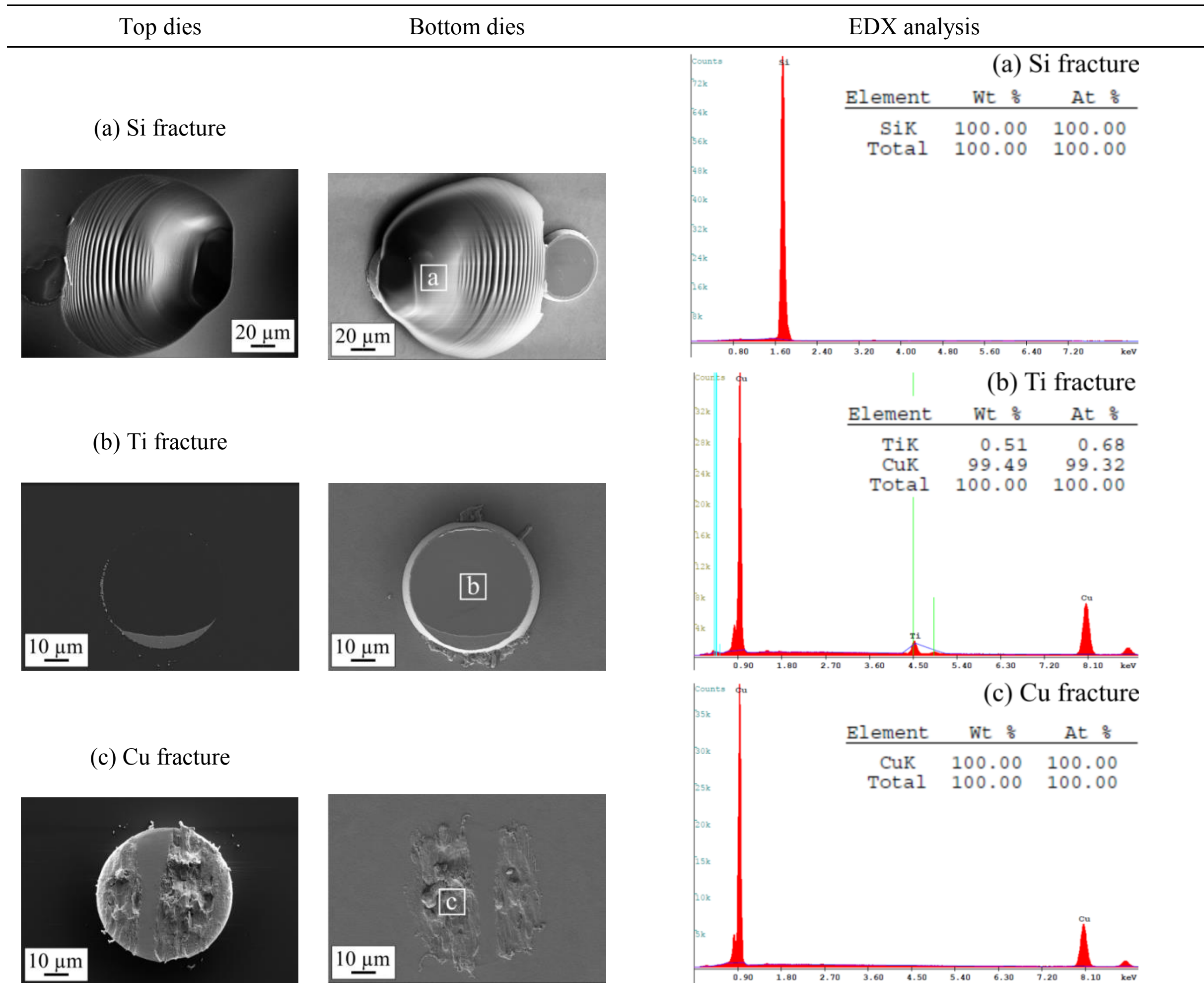

Fig. 8-23 Fracture surface types after shear strength tests by SEM and EDX: Si fracture (a), Ti fracture (b) and Cu fracture (c)

In order to evaluate fracture surfaces of 90 chips with 100 bumps per chip (five samples per parameter set) in a simple way, bottom dies were scanned by the µSurf confocal microscope. To evaluate the fracture surface, height profiling can be used. An example of fracture surface evaluation through height profiling is presented in Fig. 8-24.

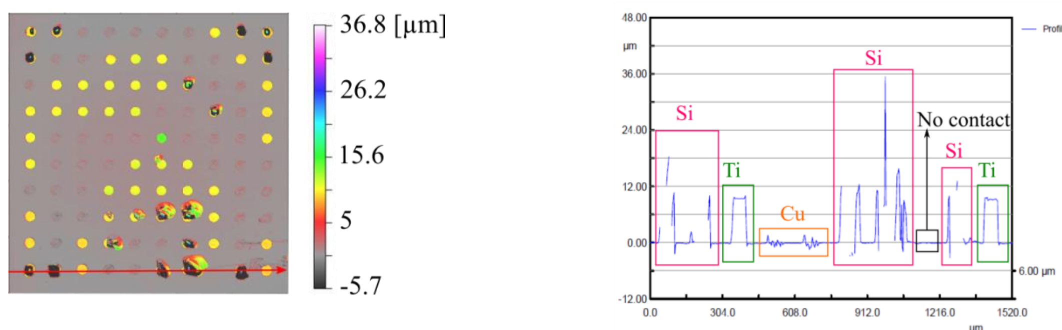

Fig. 8-24 Exemplary evaluation of fracture surfaces on a bottom die after shear strength test through height profiling: topographic data as a colored graphic in 2D-view with a red line (a), which marks a detailed height profile measurement (b)

Fig. 8-25 - Fig. 8-30 reveal the values of the shear strength with the corresponding percentage of Si, Ti, Cu fractures and of no contact places for the samples with and without SAM passivation, bonded at various parameters. The percentage of each fracture surface type has been conducted using height profiling, mentioned above. The values of shear strength are arranged in ascending order for each parameter set. Distributions of the fracture surface types correspond to each value of the shear strength above.

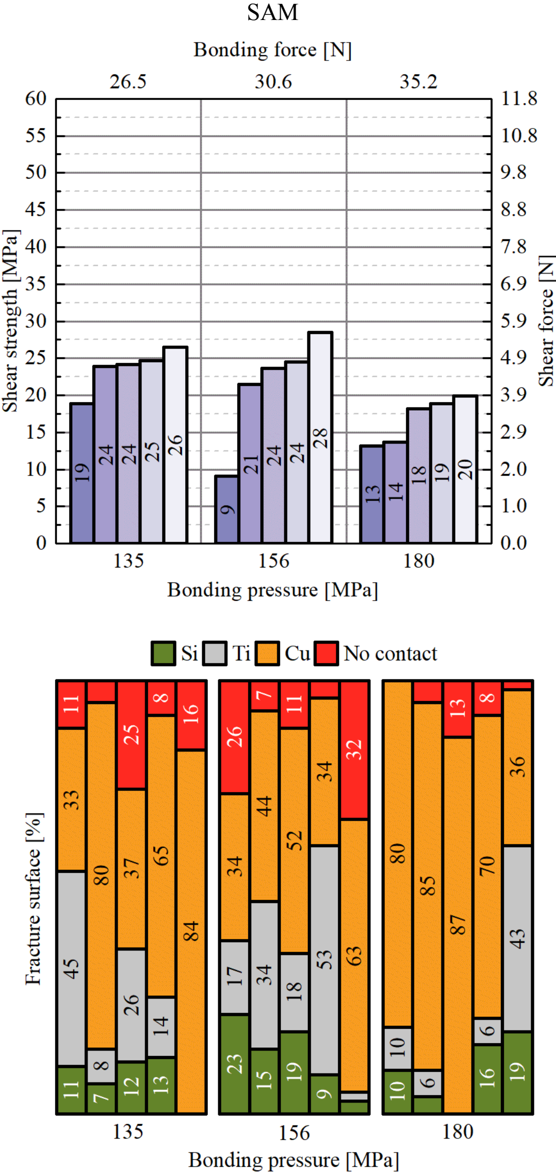

Fig. 8-25 Influence of bonding force/pressure on shear strength and percentage of fracture surface types for the samples with SAM (SAM) passivation bonded at 30 °C

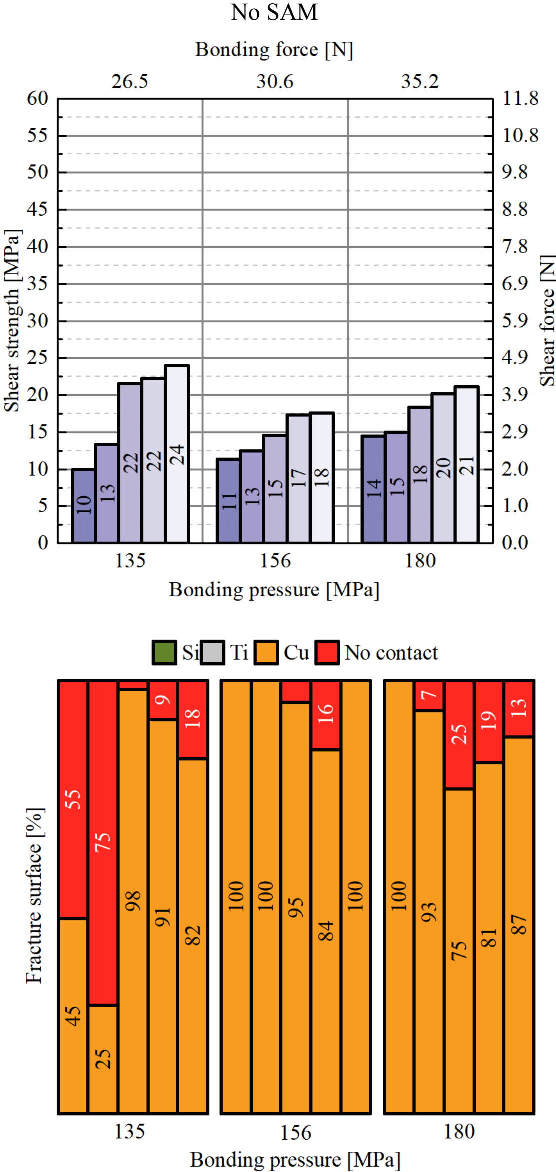

Fig. 8-26 Influence of bonding force/pressure on shear strength and percentage of fracture surface types for the samples without SAM (no SAM) passivation bonded at 30 °C

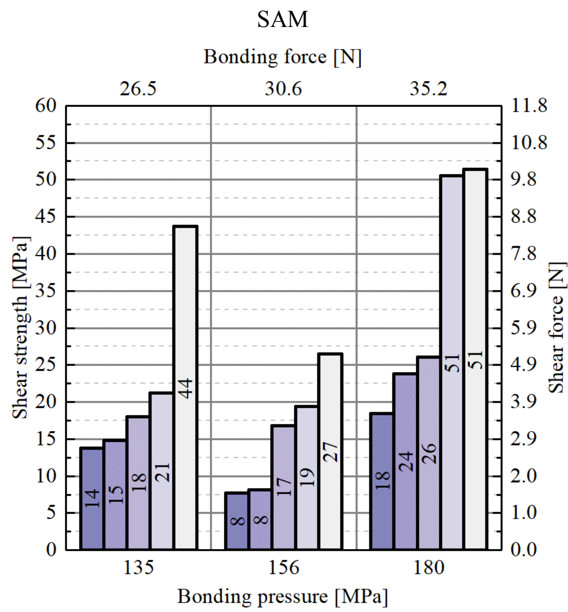

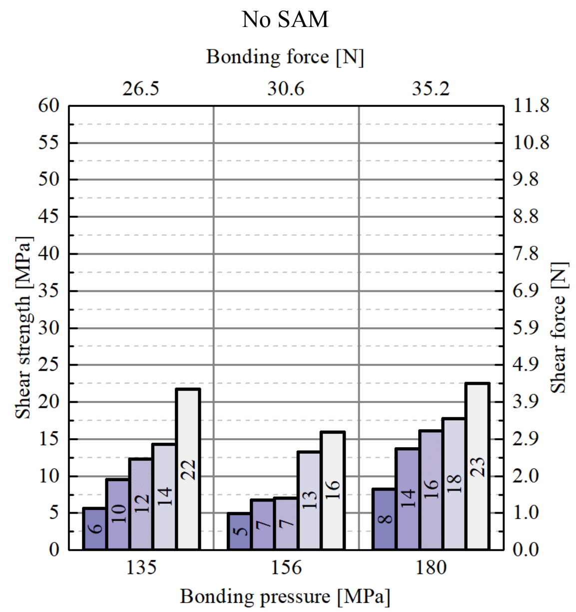

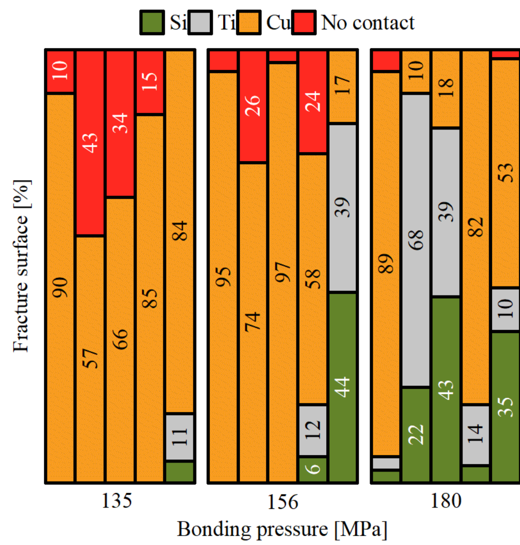

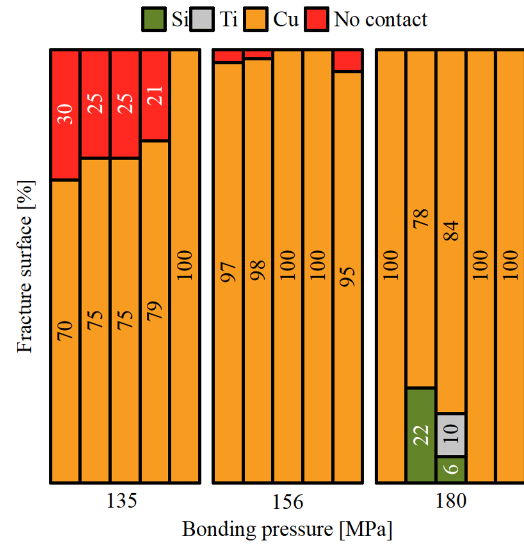

Fig. 8-27 Influence of bonding pressure on shear strength and percentage of fracture surface types for the samples with SAM (SAM) passivation bonded at 90 °C

Fig. 8-28 Influence of bonding pressure on shear strength and percentage of fracture surface types for the samples without SAM (no SAM) passivation bonded at 90 °C

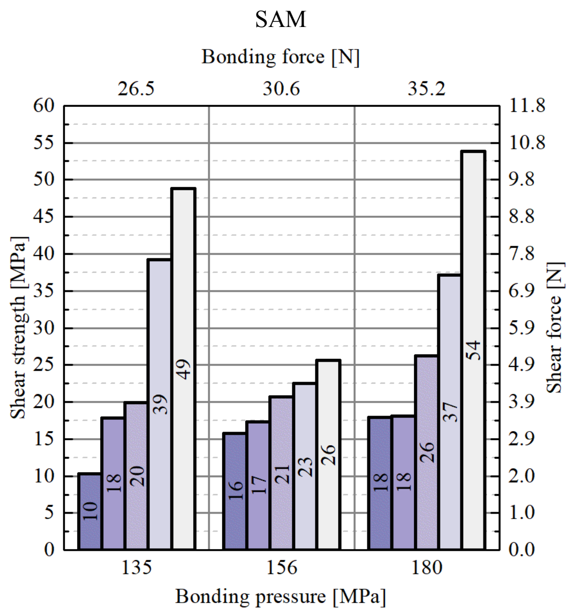

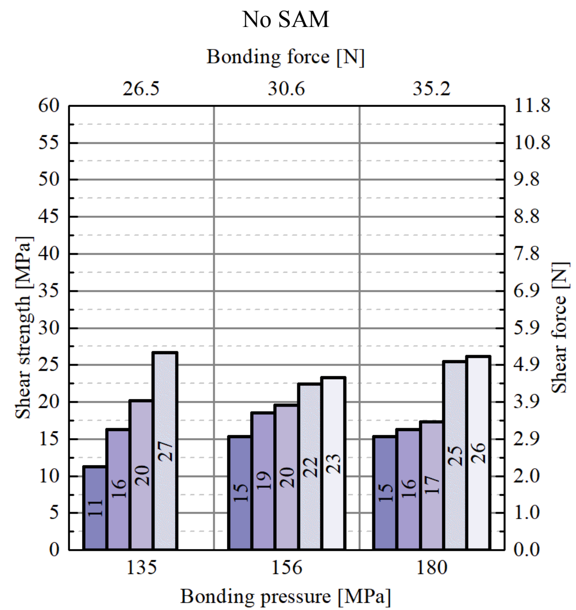

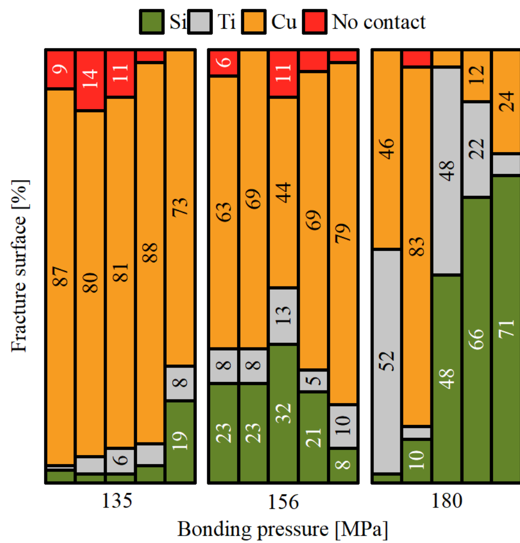

Fig. 8-29 Influence of bonding pressure on shear strength and percentage of fracture surface types for the samples with SAM (SAM) passivation bonded at 150 °C

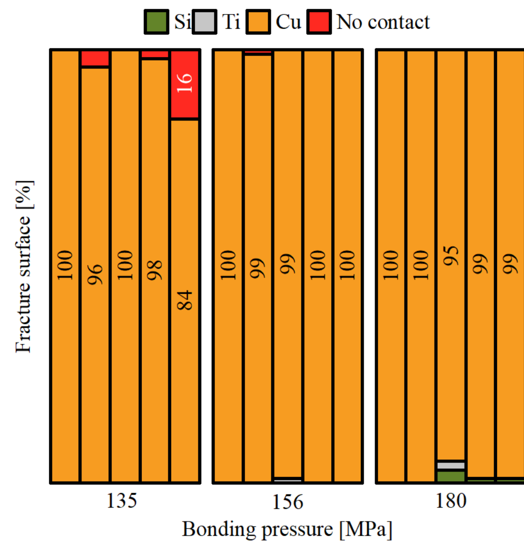

Fig. 8-30 Influence of bonding pressure on shear strength and percentage of fracture surface types for the samples without SAM (no SAM) passivation bonded at 150 °C

Fig. 8-25 and Fig. 8-26 reveal the shear strength of (9…28) MPa for the samples with and without SAM passivation bonded at 30 °C. The average mean shear strength values (averaged over all pressure values) for passivated samples are 20.6 MPa and 16.9 MPa for the uncoated samples. The difference appears clearly in the distribution of fracture surfaces. Si and Ti fractures are detected only for samples with SAM.

Fig. 8-27 and Fig. 8-28 exhibit higher shear strength for the surfaces with SAM (8…51) MPa in comparison to unprotected samples (5…23) MPa bonded at 90 °C. Samples with SAM exhibit higher scattering. The amount of Si and Ti fractures increases with bonding pressure. Almost no Si and Ti fractures were found on the samples without SAM passivation.

Fig. 8-29 and Fig. 8-30 show higher shear strength for the samples with SAM (10…54) MPa in comparison to the samples without SAM passivation (11…27) MPa bonded at 150 °C. The

amount of Si and Ti fractures increases and the percentage of "no contact" fractures decreases with bonding pressure for passivated samples.

It is valid for all the samples that the percentage of bumps, which have no contact with the substrate, decreases with increasing bonding pressure and temperature. Almost no Si and Ti fractures are detected for the samples without SAM passivation. 13 % of samples without SAM vs. 80 % of samples with SAM contain Si and Ti fractures. The shear strength of samples with SAM increases with temperature. The average shear strength (averaged over all pressures and temperatures) is 32 % higher for the interconnects with SAM in comparison to uncoated samples.

Comparing the results of the die shear strength tests, it can be stated that the resulting values of the samples with SAM are 32 % higher than those of samples without SAM, taking into account the mean values for all pressures and temperatures. Big variation in shear strength values is caused by the differences in the fracture surfaces and bonding tilt (max. 1.34 µm).

A dependency trend between the shear strength and the fracture surface types has been detected. Strong Cu-Cu interface results in Si and Ti fractures after die shear strength tests. The ratio of Si fractures reaches 71 % when die shear strength reaches its maximum value of 54 MPa for the samples with SAM passivation. The amount of Si fractures increases with shear strength, bonding pressure and temperature. Si fractures and Ti fractures systematically appear closer to the right side (*b* - *c*) of the chip, which proves that this side is exposed to the higher bonding force due to not ideal parallelism between the bonding head and stage (see chapter 8.2).

The fact that samples without SAM passivation show almost no Si and Ti fractures after the die shear test strongly suggests that these Cu-Cu interconnects, in contrast to the protected ones, can be oxidized and therefore have formed a week bond. This provides additional proof that SAM passivation can protect Cu from oxidation and positively affect the bonding results.

8.4.1.2 Microbump shear strength tests

In order to obtain information about the shear strength of separate bumps, peeling off of the Si layer from the top die after bonding was applied. The approach implies a new proposed in this study method of immersion of the bonded sample pair into the buffered oxide etchant (BOE) 10:1 (Sigma-Aldrich), which etches away the Ti layer between the bumps. As a result, the Si layer (Fig. 8-31, (b)) can be removed.

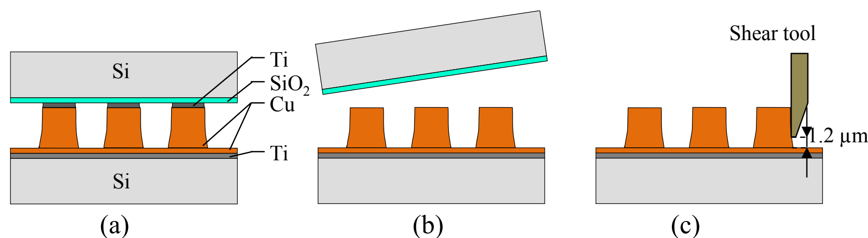

Fig. 8-31 Schematic view of the structure of bonded dies (a), etching away of Ti layer and removal of Si top die (b) and shearing of each bump separately (c)

The method of etching away the adhesive layer between Si and Cu of the top die with microbumps and peeling off the Si layer afterward has already been applied elsewhere, e.g. by etching the Al layer under the microbump [114], [157]. In this study, a new method of Ti etching has been proposed. Although this method gives a much more precise understanding of the bonding strength of the interconnects, there is not much literature data about it. Microbump shear test can be also named as a shear test of the Cu-Cu interconnect later on.

Fig. 8-32 presents the distribution of shear strength values across bonded dies with 10 × 10 microbump matrices for the sample pairs with and without SAM bonded at 30 °C depending on the bonding pressure. The details of the microbump shear test are provided in chapter 4.5.1. Orientation of dies during bonding could not be detected. The dies were slightly twisted during US bonding, possibly, due to low contact load (touch-down force) and room temperature bonding. Part of the microbumps did not stay on the bottom die after peeling off the Si layer from the top die. Due to complications in full removal of the Ti layer, a slight strain has been applied in order to peel off the Si layer, which could cause Cu fracture of the weak Cu-Cu interconnects and failure of their transfer on the bottom die. Fig. 8-32 shows "zero" shear strength values for such not transferred microbumps. Comparing die shear test values (Fig. 8-25 - Fig. 8-30) to these results, the shear strength of the Cu-Cu interconnects reaches much higher values (max. 54 MPa for die shear tests vs. 180 MPa for microbump shear tests).

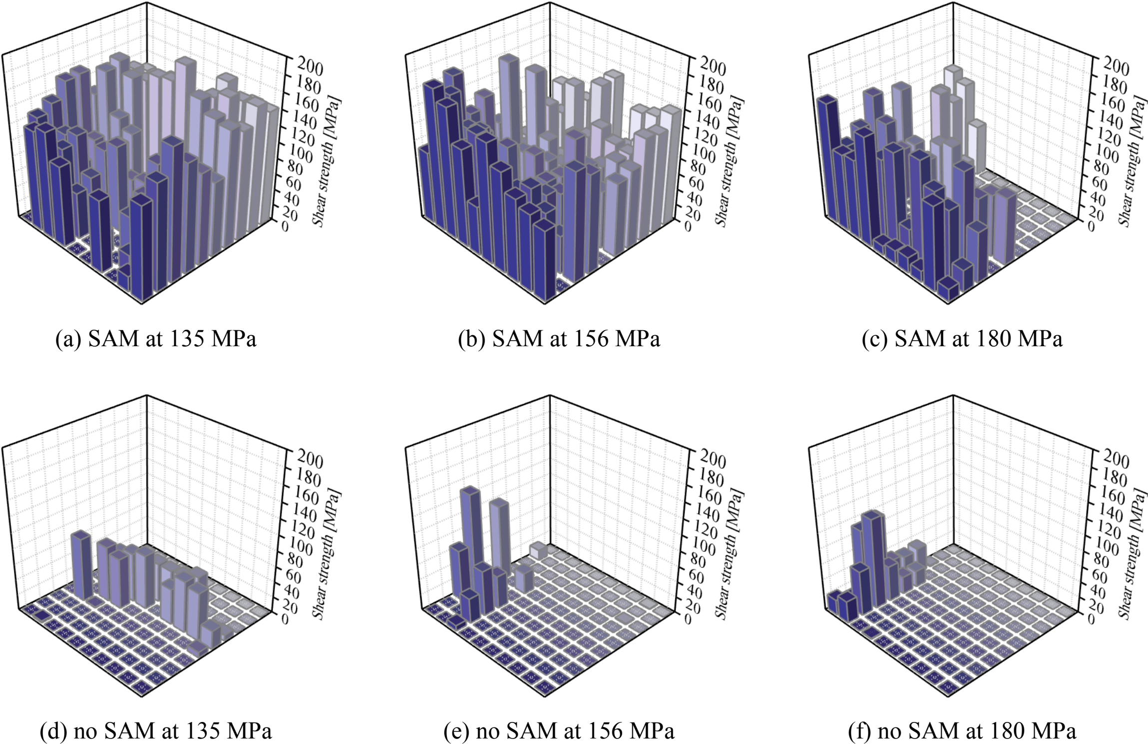

(a) SAM at 135 MPa (b) SAM at 156 MPa (c) SAM at 180 MPa

(d) no SAM at 135 MPa (e) no SAM at 156 MPa (f) no SAM at 180 MPa

Fig. 8-32 Distribution of shear strength across a bonded die with a matrix of 10 × 10 microbumps for samples with SAM bonded at 30 °C at 135 MPa (a), 156 MPa (b), 180 MPa (c) and for samples without SAM bonded at 135 MPa (d), 156 MPa (e), 180 MPa (f)

Fig. 8-32 shows the distribution of shear strength values for (100 microbumps per chip) throughout a chip. The variation of shear strength is, probably, connected to variation of the distribution of bonding force due to non-planarity between the bonding head and stage. The

fracture surface during shearing was a Cu-Cu bonding interface. The number of microbumps left on the bottom die after Ti etching is much higher for samples with SAM (max. 93 out of 100) in comparison to samples without SAM (max. 20 out of 100). The shear strength is much higher for samples with SAM (max. 181 MPa) in comparison to samples without SAM coating (max. 129 MPa). Nearly all bumps are transferred onto the bottom die after the peeling off for the samples with SAM passivation bonded at 135 MPa and 156 MPa. Cu with SAM bonded at 180 MPa have approximately half of all bumps left on the bottom die.

Fig. 8-33 presents the average shear strength (with corresponding standard deviation values) of the Cu-Cu interconnects, depending on the applied bonding pressure at 30 °C. The samples with SAM show significantly higher shear strength in comparison to uncoated samples. A high deviation and overlapping of the results is observed, which can be connected to the bonding tilt and, probably, not high enough touch-down force (caused twisting of chips bonded at 30 °C). The SAM-coated samples bonded at 135 MPa and 156 MPa feature a similar shear strength range. The microbump die shear strength decreases at 180 MPa, 30 °C.

The mean shear strength value (averaged over all pressures) for samples with SAM is 89.5 MPa and 40.5 MPa for samples without SAM, excluding microbumps that were not transferred on the bottom die.

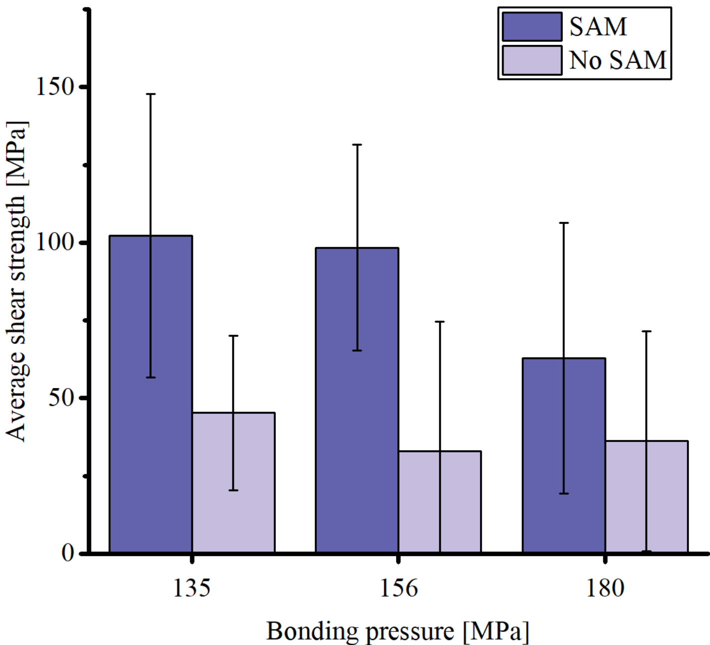

Fig. 8-33 Influence of the bonding pressure on the average shear strength and corresponding standard deviation values of the Cu-Cu interconnects (with and without SAM passivation) bonded at 30 °C after microbump shear tests

The number of the microbumps that did not come into contact with the bottom die decreases with increasing temperature and pressure for both sample types. A 100 % yield, whereby all 100 bumps are bonded, has been achieved for the samples bonded at 156 MPa and 180 MPa, at 90 °C and 150 °C. Bonding at 30 °C does not result in a 100 % yield and therefore features lower die shear strength. Nevertheless, the shear strength of the microbumps, which contacted the bottom die after bonding at 30 °C, is much higher and will be discussed later on. It confirms

that the planarity of the bonding tool is a crucial factor in order to decrease bonding temperatures and pressures, which correlates well with the literature [149].

Arai et al. have investigated the influence of the bump heights on US flip-chip Cu-Cu bonding using plasma pre-treatment. The researchers have used a similar method of etching the adhesive Al layer in order to shear each bump separately [110]. Microbumps with a height of 5 µm have been lifted after etching and have not adhered to the substrate. For the higher bumps, half of the whole amount had a strong bond with a substrate and have been transferred on it. The shear strength of 20 µm bumps reaches 198 MPa. These values correlate well with the yielded shear strength values in this work. This means that SAM passivation in Cu-Cu bonding can provide a high potential alternative for the plasma pre-treatment method.

The microbump mean shear strength has similar values after the bonding at 135 MPa and 156 MPa, and decrease at 180 MPa. Although the ranges of standard deviations overlap for different pressures, it can be suggested the decrease of the shear strength with increasing bonding pressure (Fig. 8-33). A similar effect can be seen for the die shear tests of the samples bonded at 30 °C (Fig. 8-25 - Fig. 8-26) if mean values are taken into account. This dependence, however, changes to the opposite after increasing the bonding temperature, which can be observed by the die shear strength results (Fig. 8-27 - Fig. 8-30). In this case, shear strength increases with bonding pressure. Decreasing of the shear with pressure at nearly room-bonding temperature can be explained by the material hardening due to too high pressure at low temperature, which restricts further deformation processes (see chapter 3.3.1). Furthermore, a high deviation of the microbump shear strength values is detected and is also caused probably by the presence of the bonding tilt, which means non-conformal distribution of the bonding pressure across the bonded dies.

8.4.1.3 Comparison of the shear strength of the SAM-protected interconnects with other pre-treatment methods from literature

Tab. 8-2 presents a comparison of the shear strength range values for Cu-Cu bonding with SAM passivation and other pre-treatments. Corresponding bonding parameters to the listed literature data with SAM passivation are provided in Tab. 2-3 (chapter 2).

The research of Qiu et al. presents US flip-chip bonding of Cu cone bumps to Cu electrodes, both passivated with SAM [12], [76]. The shear strength ranges are (26…115) MPa and (50…185) MPa for samples with and without SAM, respectively. The authors suggest that SAM prohibited strong interconnect formation and that it should be removed prior to bonding. These results contradict to conclusions of this thesis, which can be caused by the differences in passivation processes.

Literature data confirms that microbump shear strength is higher than die shear strength. Different fracture surface types appear during the die shear tests (Si, Ti, Cu fractures, no contact). This makes the estimation of the Cu-Cu bond strength complex. More precise information is expected from the shear strength test of each bump separately because only Cu fracture is evaluated in this case. The highest microbump shear strength is 181 MPa for the

sample with SAM, bonded at 135 MPa at 30 °C, which is not unusual as the tensile strength of Cu can reach 210 MPa or higher [158]–[164], depending on its deposition process.

The die shear strength of the US bonded samples is in the range of (9…54) MPa. This range is lower than of the TC bonded samples (58…80) MPa. This can be caused by the different bonding tilt, longer bonding time (30 min vs. 1 s), bonding atmosphere (Ar vs. air), bonding temperature (250 °C vs. 150 °C), etc. US bonding die shear strength results are comparable to several studies, where other pre-treatment methods, as plasma activation or pre-treatment with formic acid, have been used and present an excellent alternative for these methods.

Tab. 8-2 Comparison of the shear strength values for Cu-Cu bonding from this work with the literature results

Sample type	Bonding method	Shear strength test	Shear strength ranges	Reference
Pads and wire balls	Wire bonding with SAM	Ball shear strength test	(75…120) MPa	[54]
Chips with pads	TC bonding with SAM	Die shear strength test	(54…65.8) MPa	[59]
Top die with microbumps, bottom die with full Cu surface	TC bonding with SAM	Die shear strength test	(58…80) MPa	this work
Chips with microelectrodes	TC bonding with formic acid pre-treatment	Die shear strength test	(12.5…30) MPa	[120]
Polished full Cu surface	TC bonding with plasma surface pre-treatment	Die shear strength test	(12....57) MPa	[165]
Chip with cone-shaped bumps to chip with electrodes	US bonding with SAM	Microbump shear strength test	(26…115) MPa	[12], [76]
Top die with microbumps, bottom die with full Cu surface	US bonding with SAM	Die shear strength test	(9…54) MPa	this work
		Microbump shear strength test	(63…102) MPa	

8.5 Summary

Cu-Cu US flip-chip bonding in combination with SAM protective layer provides the benefit of short bonding time (1 s), low bonding temperature (down to room temperature) and bonding in the ambient air.

The interconnects with SAM revealed higher bonding quality in comparison to samples without SAM (bonded after Cu etching), which is proven as follows:

1. Cross-sectioning revealed that “no bonding” regions are more typical for unprotected samples, which indicates poor bonding quality of the analyzed and adjacent bumps. Interconnects with SAM contain a higher percentage of regions with the seamless bonding interface (60 %) in comparison to the uncoated Cu (21 %).
2. The shear strength increases with the bonding temperature. The higher bonding pressure causes better interconnect quality and higher shear strength for the bonding temperatures of 90 °C and 150 °C. The samples bonded at 30 °C reveal a slight

tendency of decreasing the shear strength with the bonding pressure based on the die and microbump mean shear strength values.

3. Si and Ti fractures after die shearing are detected almost only for samples with SAM passivation, which strongly suggests higher mechanical strength of such interconnects compared to uncoated samples.
4. The percentage of bumps, transferred onto the bottom die after Ti etching and peeling off the Si layer from the top die, is at least three times higher for the samples with SAM in comparison to the unprotected samples.
5. The microbump mean shear strength range for Cu-Cu interconnects with SAM is (63…102) MPa, which is comparable with the literature results.
6. SAM traces are detected at the interconnect edge region whereby the center of the microbump reveals almost no S residuals. Proposed explanation: a bond starts to form the bump center, the edges are exposed to less bonding power, force and time. SAM is rubbed away from the interconnect center to the edges using US energy.
7. A revealed zig-zag form of the bonding interface suggests high bonding quality of the samples with SAM bonded at 180 MPa at 150 °C.

D2D US flip-chip bonding with SAM passivation for Cu is a novel packaging technology that has not been systematically investigated and appears to have a high potential for implementation as a new bonding technology for 2.5D system integration.

9 Summary and outlook

2.5D and 3D system integration are quickly developing packaging technologies, which have a high potential of miniaturization and diversification of microelectronics while lowering manufacturing costs. Cu metal is a perfect choice for such packaging technologies because of its excellent electrical, mechanical, thermal properties, as well as cost-efficiency. The bottleneck of its implementation is Cu oxidation. The presence of Cu oxide layer requires bonding at longer durations, higher temperatures and pressures, using inert gas atmosphere during bonding. Therefore, the methods of Cu-Cu bonding with SAM passivation at lower bonding parameters (temperature, pressure, possibility of bonding in air) have been investigated in this thesis.

The work can be divided into three parts: microstructure characterization of the used samples in the initial state, characterization of SAM passivation effect and Cu-Cu bonding analysis.

The first part presents the main characteristics of the samples, as well as microstructural analysis of Cu before bonding. The grain size distribution and Cu texture have been analyzed using electron backscatter diffraction (EBSD) technology. The fraction of twin boundaries is dominant for all of the sample types and is in the range of (0.570…0.705). All of the sample types seem either to originate from or obtain a {0 0 1} texture. Correlation between the crystallographic orientation, Cu thickness and measured Young's Modulus has been detected.

The second part describes the effect of SAM passivation on Cu oxidation in air. In this part, SAM preparation has been carried out in a glove box system with $O_2 < 0.5$ ppm. The results show that Cu without SAM forms a higher amount of Cu oxide in comparison to the SAM protected sample after 12 hours of storage in air conditions. No oxidation of SAM (no sulfonates) has been found after this period. The results support literature discussions about not only the role of SAM as an oxidation inhibitor for Cu but also about Cu oxidation preceding the SAM oxidation (formation of sulfonates).

The SAM chain length has an important influence on its protective function. This has been proven using a relatively new approach of infrared spectroscopic ellipsometry (IRSE), which is particularly suitable for the characterization of thin organic films. The results suggest that the monolayer tilts gradually during air exposure, which is caused by the oxidation process. Long-chain SAMs degrade slower than short-chain ones. Nevertheless, long-chain species are hard to desorb from the Cu surface before bonding, which is required in order to achieve a strong Cu-Cu interconnect. Prolongation of the protective function of the short-chain SAMs (C6) has been achieved using storage at low temperatures. The approach has been proven to work not only for smooth sputtered surfaces but also for ECD Cu ($R_a = 9 \pm 0.75$ nm), which is commonly used for microbump manufacturing. Storage at -40 °C for one week in air has shown no Cu oxide formation on the ECD Cu with C6 SAM in contrast to the uncoated samples.

In the third part of the thesis, Cu-Cu bonding with SAM has been analyzed. In this case, SAM preparation has been carried out in air, using the addition of acetic acid into the SAM solution. This method has shown no Cu oxide formation either directly after the preparation, or

after the storage at -18 °C in a conventional freezer for three weeks. Die shear strength values achieve (58…80) MPa and (48…51) MPa for the samples with and without SAM, respectively. The mean shear strength value after 10 days of storage at -18 °C and TC bonding in the Ar gas atmosphere is 34 % higher for Cu/SAM in comparison to the bare Cu surface. A systematic fracture surface analysis has been conducted for the bonded samples after the die shear strength tests. Classification of fracture surface types (Si, Ti, Cu and no contact) has been proposed. The presence of Si and Ti fractures correlates well with the higher shear strength values of the Cu/SAM samples.

SAM desorption *in-situ* has been carried out at two different temperatures (200 °C and 250 °C). The chemical composition of the Cu surface has been analyzed at these desorption conditions. A decrease of S and increase of O contents with increasing temperature have been detected, which can be connected to the not ideal inert gas atmosphere in the bonding chamber. Optimal parameters for SAM desorption are found to be 200 °C and 30 min.

Another way of SAM removal from the Cu surface is mechanical rubbing using US energy of a US flip-chip bonder, which has not been systematically investigated in literature before. The advantages of this method are short bonding time (1 s), low-temperature range ((30…150) °C) and the possibility of bonding in air. The following bonding parameters have been varied: temperature (30 °C, 90 °C, 150 °C) and pressure (135 MPa, 156 MPa, 180 MPa). The die shear strength tests have shown definite domination for the samples with SAM. The die shear strength is in the range of (9…54) MPa and (5…27) MPa for the samples with and without SAM, respectively. Fracture surface analysis has shown Si and Ti fractures almost explicitly for Cu/SAM samples, as already observed for the TC bonding results. Bonding strength increases with pressure and temperature starting from 90 °C. The mean die shear strength decreases with the increasing pressure at 30 °C. This may be caused by the domination of hardening mechanisms at room temperature, which can lead to the destruction of the interconnects at elevated pressures.

Classification of bonding interface regions, based on cross-sections of the bonded interconnects, has been proposed. The results highlight that "no bonding" regions are more typical for samples without SAM. 60 % of Cu/SAM and 21 % of Cu interconnects without the protective coating contain a seamless bonding interface, which proves that using the SAM passivation increases the bonding quality.

New know-how of Ti etching and peeling off the Si top die after Cu-Cu bonding has been applied in order to make the shear test of each bonded microbump possible. At least three times higher amount of bumps has been transferred onto the bottom die for the samples with SAM in comparison to the unprotected samples. This suggests that not transferred interconnects have been too weak and, therefore, stayed on the top die after its peeling off. The achieved microbump mean shear strength lies in the range of (63…102) MPa. The microbump mean shear strength values over all pressures are approximately two times higher for Cu/SAM comparing to the samples without the protective monolayer. The microbump shear strength range has high deviation and overlapping and is similar for the samples bonded at 135 MPa and 156 MPa. The microbump shear strength range is slightly lower at 180 MPa for the samples

with SAM passivation. The decrease of microbump shear strength with increasing bonding pressures at 30 °C can be suggested due to the hardening mechanisms, which can occur at the low-temperature US bonding.

A novel investigation of the Cu-Cu bonding interface after US flip-chip bonding with SAM has been carried out using transmission electron microscopy (TEM). The results show almost no SAM traces in the microbump center and barely detectable S residuals at the bump edges. Since deformation of the microbump starts from its center, the edges are exposed to less US energy and pressure. This can explain why the SAM rests can be found in these regions. These findings suggest that there is a possibility of SAM desorption in air and that SAM is partially desorbed from the Cu surface. Moreover, the bonding interface features a zig-zag form (no straight line), which suggests a high bonding quality.

The application of the SAM passivation in US flip-chip bonding has a high potential for future implementations in microelectronic packaging. Development of a parameter window for a higher amount of dies for statistical accuracy, alternative microbump dimensions, bump-to bump bonding tests, aging tests and passivation of wafers for die-to-wafer bonding are the next steps to be done in order to optimize and adapt this technology for the future semiconductor applications.

Literature

[1] R. R. Tummala, *Fundamentals of microsystems packaging*. McGraw-Hill, 2001.

[2] M. M. Waldrop, “More Than Moore,” *Nature*, vol. 530, no. 7589. Nature Publishing Group, pp. 144–147, 09-Feb-2016, doi: 10.1038/530144a.

[3] J. Veres *et al.*, “Additive manufacturing for electronics ‘Beyond Moore,’” in *Technical Digest - International Electron Devices Meeting, IEDM*, 2017, pp. 25.6.1-25.6.3, doi: 10.1109/IEDM.2016.7838481.

[4] J. Kim *et al.*, “Architecture, chip, and package co-design flow for 2.5D IC design enabling heterogeneous IP reuse,” in *Proceedings - Design Automation Conference*, 2019, doi: 10.1145/3316781.3317775.

[5] X. Zhang *et al.*, “Heterogeneous 2.5D integration on through silicon interposer,” *Applied Physics Reviews*, vol. 2, no. 2. American Institute of Physics Inc., p. 21308, 01-Jun-2015, doi: 10.1063/1.4921463.

[6] Y. Li and D. Goyal, “Introduction to 3D Microelectronic Packaging,” Springer, Cham, 2017, pp. 1–15.

[7] S. H. Sharifi, “Exploration and optimization of different SAM (Self-Assembled Monolayer) deposition methods to passivate copper microbumps for 3D stacking,” Technical University of Dresden, Faculty of Physics, Institute of Applied Physics, 2017.

[8] D. F. Lim, J. Wei, K. C. Leong, and C. S. Tan, “Cu passivation for enhanced low temperature (⩽300 °C) bonding in 3D integration,” *Microelectron. Eng.*, vol. 106, pp. 144–148, 2013, doi: http://dx.doi.org/10.1016/j.mee.2013.01.032.

[9] L. Peng, H. Y. Li, D. F. Lim, S. Gao, and C. S. Tan, “Thermal reliability of fine pitch Cu-Cu bonding with self assembled monolayer (SAM) passivation for Wafer-on-Wafer 3D-Stacking,” in *2011 IEEE 61st Electronic Components and Technology Conference (ECTC)*, 2011, pp. 22–26, doi: 10.1109/ECTC.2011.5898485.

[10] J. C. Love, L. A. Estroff, J. K. Kriebel, R. G. Nuzzo, and G. M. Whitesides, “Self-Assembled Monolayers of Thiolates on Metals as a Form of Nanotechnology,” *Chem. Rev.*, vol. 105, no. 4, pp. 1103–1170, 2005, doi: 10.1021/cr0300789.

[11] R. G. Nuzzo, E. M. Korenic, and L. H. Dubois, “Studies of the temperature-dependent phase behavior of long chain n-alkyl thiol monolayers on gold,” *J. Chem. Phys.*, vol. 93, no. 1, pp. 767–773, 1990, doi: 10.1063/1.459528.

[12] L. Qiu, A. Ikeda, and T. Asano, “Effect of Coating Self-Assembled Monolayer on Room-Temperature Bonding of Cu Micro-Interconnects,” *Jpn. J. Appl. Phys.*, vol. 52, no. 6R, p. 68004, 2013.

[13] A. Huffman, J. Lannon, M. Lueck, C. Gregory, and D. Temple, “Fabrication and characterization of metal-to-metal interconnect structures for 3-D integration,” *J. Instrum.*, vol. 4, no. 03, pp. P03006–P03006, Mar. 2009, doi: 10.1088/1748-0221/4/03/P03006.

[14] J. M. Lannon, Jr. *et al.*, “Recent advances in high density area array interconnect bonding for 3D integration,” in *Technologies for Synthetic Environments: Hardware-in-the-Loop Testing XV*, 2010, vol. 7663, p. 766305, doi: 10.1117/12.850305.

[15] T. Suga, R. He, G. Vakanas, and A. La Manna, "Direct Cu to Cu Bonding and Other Alternative Bonding Techniques in 3D Packaging," in *3D Microelectronic Packaging*, 2017, pp. 129–155.

[16] Y.-S. Tang, Y.-J. Chang, and K.-N. Chen, "Wafer-level Cu–Cu bonding technology," *Microelectron. Reliab.*, vol. 52, no. 2, pp. 312–320, Feb. 2012, doi: 10.1016/J.MICROREL.2011.04.016.

[17] A. Shigetou, T. Itoh, M. Matsuo, N. Hayasaka, K. Okumura, and T. Suga, "Bumpless interconnect through ultrafine Cu electrodes by means of surface-activated bonding (SAB) method," *Adv. Packag. IEEE Trans.*, vol. 29, no. 2, pp. 218–226, 2006, doi: 10.1109/TADVP.2006.873138.

[18] H. Moriceau *et al.*, "Low temperature direct bonding: An attractive technique for heterostructures build-up," *Microelectron. Reliab.*, vol. 52, no. 2, pp. 331–341, Feb. 2012, doi: 10.1016/J.MICROREL.2011.08.004.

[19] L. Qiu, A. Ikeda, K. Noda, S. Nakai, and T. Asano, "Room-temperature Cu microjoining with ultrasonic bonding of cone-shaped bump," *Jpn. J. Appl. Phys.*, vol. 52, no. 4 PART 2, p. 04CB10, 2013, doi: 10.7567/JJAP.52.04CB10.

[20] E. Beyne *et al.*, "Scalable, sub 2μm pitch, Cu/SiCN to Cu/SiCN hybrid wafer-to-wafer bonding technology," in *Technical Digest - International Electron Devices Meeting, IEDM*, 2018, pp. 32.4.1-32.4.4, doi: 10.1109/IEDM.2017.8268486.

[21] M. Yamamoto, E. Higurashi, T. Suga, R. Sawada, and T. Itoh, "Properties of various plasma surface treatments for low-temperature Au–Au bonding," *Jpn. J. Appl. Phys.*, vol. 57, no. 4S, p. 04FC12, Apr. 2018, doi: 10.7567/JJAP.57.04FC12.

[22] Y. T. Yang *et al.*, "Low-Temperature Cu-Cu Direct Bonding Using Pillar-Concave Structure in Advanced 3-D Heterogeneous Integration," *IEEE Trans. Components, Packag. Manuf. Technol.*, vol. 7, no. 9, pp. 1560–1566, Sep. 2017, doi: 10.1109/TCPMT.2017.2720468.

[23] A. K. Panigrahy and K.-N. Chen, "Low Temperature Cu–Cu Bonding Technology in Three-Dimensional Integration: An Extensive Review," *J. Electron. Packag.*, vol. 140, no. 1, p. 010801, Mar. 2018, doi: 10.1115/1.4038392.

[24] E.-J. Jang, S. Hyun, H.-J. Lee, and Y.-B. Park, "Effect of Wet Pretreatment on Interfacial Adhesion Energy of Cu-Cu Thermocompression Bond for 3D IC Packages," *J. Electron. Mater.*, vol. 38, no. 12, pp. 2449–2454, Dec. 2009, doi: 10.1007/s11664-009-0942-9.

[25] B. Swinnen *et al.*, "3D integration by Cu-Cu thermo-compression bonding of extremely thinned bulk-Si die containing 10 μm pitch through-Si vias," in *2006 International Electron Devices Meeting*, 2006, pp. 1–4, doi: 10.1109/IEDM.2006.346786.

[26] K. N. Chen, C. S. Tan, A. Fan, and R. Reif, "Copper bonded layers analysis and effects of copper surface conditions on bonding quality for three-dimensional integration," *J. Electron. Mater.*, vol. 34, no. 12, pp. 1464–1467, Dec. 2005, doi: 10.1007/s11664-005-0151-0.

[27] B. Rebhan, S. Tollabimazraehno, G. Hesser, and V. Dragoi, "Analytical methods used for low temperature Cu–Cu wafer bonding process evaluation," *Microsyst. Technol.*, vol. 21, no. 5, pp. 1003–1013, May 2015, doi: 10.1007/s00542-015-2446-2.

[28] T. Sakai, N. Imaizumi, and T. Miyajima, “Low temperature Cu-Cu direct bonding for 3D-IC by using fine crystal layer,” in *2012 2nd IEEE CPMT Symposium Japan*, 2012, pp. 1–4, doi: 10.1109/ICSJ.2012.6523388.

[29] W. Yang, M. Akaike, and T. Suga, “Effect of Formic Acid Vapor In Situ Treatment Process on Cu Low-Temperature Bonding,” *IEEE Trans. Components, Packag. Manuf. Technol.*, vol. 4, no. 6, pp. 951–956, Jun. 2014, doi: 10.1109/TCPMT.2014.2315761.

[30] T. Sakai, N. Imaizumi, and S. Sakuyama, “A low temperature Cu-Cu direct bonding method with VUV and HCOOH treatment for 3D integration,” in *Electronics Packaging and iMAPS All Asia Conference (ICEP-IACC), 2015 International Conference on*, 2015, pp. 464–467, doi: 10.1109/ICEP-IAAC.2015.7111059.

[31] T. Suga, “Cu-Cu Room Temperature Bonding - Current Status of Surface Activated Bonding(SAB) -,” in *ECS Transactions*, 2006, vol. 3, no. 6, pp. 155–163, doi: 10.1149/1.2357065.

[32] C. Wang and T. Suga, “A novel room-temperature wafer direct bonding method by fluorine containing plasma activation,” in *Electronic Components and Technology Conference (ECTC), 2010 Proceedings 60th*, 2010, pp. 303–308, doi: 10.1109/ECTC.2010.5490955.

[33] S. Yamamoto, E. Higurashi, T. Suga, and R. Sawada, “Low-temperature hermetic packaging for microsystems using Au–Au surface-activated bonding at atmospheric pressure,” *J. Micromechanics Microengineering*, vol. 22, no. 5, p. 55026, 2012.

[34] R. He, M. Fujino, M. Akaike, T. Sakai, S. Sakuyama, and T. Suga, “Combined surface activated bonding using H-containing HCOOH vapor treatment for Cu/Adhesive hybrid bonding at below 200°C,” *Appl. Surf. Sci.*, vol. 414, no. Supplement C, pp. 163–170, 2017, doi: https://doi.org/10.1016/j.apsusc.2017.03.168.

[35] H. Lei and Y.-J. Tang, “Stress-induced stacking faults in the Cu/Au interface,” *J. Phys. Condens. Matter*, vol. 16, no. 43, p. 7823, 2004.

[36] J. A. Borders, “Ion back-scattering analysis of interdiffusion in Cu-Au thin films,” *Thin Solid Films*, vol. 19, no. 2, pp. 359–370, 1973, doi: http://dx.doi.org/10.1016/0040-6090(73)90072-2.

[37] C. Lang, “Heterogene Interdiffusion Von nanokristallinen Cu/Co/Au-Schichten,” Georg-August-Universität zu Göttingen, 2001.

[38] Y.-P. Huang, Y.-S. Chien, R.-N. Tzeng, and K.-N. Chen, “Demonstration and Electrical Performance of Cu–Cu Bonding at 150 °C With Pd Passivation,” *IEEE Trans. Electron Devices*, vol. 62, no. 8, pp. 2587–2592, Aug. 2015, doi: 10.1109/TED.2015.2446507.

[39] M. R. Pinnel, “Diffusion-related behaviour of gold in thin film systems,” *Gold Bull.*, vol. 12, no. 2, pp. 62–71, 1979, doi: 10.1007/BF03216542.

[40] V. Smet, M. Kobayashi, T. Wang, P. M. Raj, and R. Tummala, “A new era in manufacturable, low-temperature and ultra-fine pitch Cu interconnections and assembly without solders,” in *2014 IEEE 64th Electronic Components and Technology Conference (ECTC)*, 2014, pp. 484–489, doi: 10.1109/ECTC.2014.6897328.

[41] X. Wu, D. Cullen, G. Brist, and O. M. Ramahi, “Surface Finish Effects on High-Speed Signal Degradation,” *Adv. Packag. IEEE Trans.*, vol. 31, no. 1, pp. 182–189, Feb. 2008, doi: 10.1109/TADVP.2007.914962.

[42] L. Cha, "A metastable HCP intermetallic phase in Cu-Al bilayer films," Universität Stuttgart, 2006.

[43] B. Boettge, J. Braeuer, M. Wiemer, M. Petzold, J. Bagdahn, and T. Gessner, "Fabrication and characterization of reactive nanoscale multilayer systems for low-temperature bonding in microsystem technology," *J. Micromechanics Microengineering*, vol. 20, no. 6, p. 64018, 2010.

[44] J. Li, J. W. Mayer, and E. G. Colgan, "Oxidation and protection in copper and copper alloy thin films," *J. Appl. Phys.*, vol. 70, no. 5, pp. 2820–2827, Sep. 1991, doi: 10.1063/1.349344.

[45] M. M. Sung, K. Sung, C. G. Kim, S. S. Lee, and Y. Kim, "Self-Assembled Monolayers of Alkanethiols on Oxidized Copper Surfaces," *J. Phys. Chem. B*, vol. 104, no. 10, pp. 2273–2277, 2000, doi: 10.1021/jp992995h.

[46] P. E. Laibinis, G. M. Whitesides, D. L. Allara, Y. T. Tao, A. N. Parikh, and R. G. Nuzzo, "Comparison of the structures and wetting properties of self-assembled monolayers of n-alkanethiols on the coinage metal surfaces, copper, silver, and gold," *J. Am. Chem. Soc.*, vol. 113, no. 19, pp. 7152–7167, Sep. 1991, doi: 10.1021/ja00019a011.

[47] C. Yang, "Corrosion protection of copper by self-assembled monolayer," University of Alberta, 2002.

[48] M. D. Porter, T. B. Bright, D. L. Allara, and C. E. D. Chidsey, "Spontaneously organized molecular assemblies. 4. Structural characterization of n-alkyl thiol monolayers on gold by optical ellipsometry, infrared spectroscopy, and electrochemistry," *J. Am. Chem. Soc.*, vol. 109, no. 12, pp. 3559–3568, Jun. 1987, doi: 10.1021/ja00246a011.

[49] F. Schreiber, "Structure and growth of self-assembling monolayers," *Prog. Surf. Sci.*, vol. 65, no. 5–8, pp. 151–257, 2000, doi: 10.1016/S0079-6816(00)00024-1.

[50] Y. Xia, X.-M. Zhao, and G. M. Whitesides, "Pattern transfer: Self-assembled monolayers as ultrathin resists," *Microelectron. Eng.*, vol. 32, no. 1–4, pp. 255–268, Sep. 1996, doi: 10.1016/0167-9317(95)00174-3.

[51] A. Kumar, H. A. Biebuyck, and G. M. Whitesides, "Patterning Self-Assembled Monolayers: Applications in Materials Science," *Langmuir*, vol. 10, no. 5, pp. 1498–1511, May 1994, doi: 10.1021/la00017a030.

[52] Y. Sun *et al.*, "Optimization and upscaling of spin coating with organosilane monolayers for low-k pore sealing," *Microelectron. Eng.*, vol. 167, pp. 32–36, Jan. 2017, doi: 10.1016/j.mee.2016.10.011.

[53] B. R. Murthy, W. M. Yee, A. Krishnamoorthy, R. Kumar, and D. C. Frye, "Self-Assembled Monolayers as Cu Diffusion Barriers for Ultralow-k Dielectrics," *Electrochem. Solid-State Lett.*, vol. 9, no. 7, p. F61, Jul. 2006, doi: 10.1149/1.2201988.

[54] C. M. Whelan, M. Kinsella, L. Carbonell, H. M. Ho, and K. Maex, "Corrosion inhibition by self-assembled monolayers for enhanced wire bonding on Cu surfaces," *Microelectron. Eng.*, vol. 70, no. 2–4, pp. 551–557, 2003, doi: http://dx.doi.org/10.1016/S0167-9317(03)00283-1.

[55] G. K. Jennings and P. E. Laibinis, "Self-assembled monolayers of alkanethiols on copper provide corrosion resistance in aqueous environments," *Colloids Surfaces A Physicochem. Eng. Asp.*, vol. 116, no. 1–2, pp. 105–114, 1996, doi: http://dx.doi.org/10.1016/0927-7757(96)03626-6.

[56] J. Scherer, M. R. Vogt, O. M. Magnussen, and R. J. Behm, “Corrosion of Alkanethiol-Covered Cu(100) Surfaces in Hydrochloric Acid Solution Studied by in-Situ Scanning Tunneling Microscopy,” *Langmuir*, vol. 13, no. 26, pp. 7045–7051, 1997, doi: 10.1021/la970372u.

[57] D. F. Lim, J. Wei, K. C. Leong, and C. S. Tan, “Cu passivation for enhanced low temperature (⩽300°C) bonding in 3D integration,” *Microelectron. Eng.*, vol. 106, pp. 144–148, Jun. 2013, doi: 10.1016/j.mee.2013.01.032.

[58] M. Lykova *et al.*, “Characterization of self-assembled monolayers for Cu–Cu bonding technology,” *Microelectron. Eng.*, vol. 202, 2018, doi: 10.1016/j.mee.2018.09.008.

[59] C. S. Tan, D. F. Lim, X. F. Ang, J. Wei, and K. C. Leong, “Low temperature Cu-Cu thermo-compression bonding with temporary passivation of self-assembled monolayer and its bond strength enhancement,” *Microelectron. Reliab.*, vol. 52, no. 2, pp. 321–324, 2012, doi: http://dx.doi.org/10.1016/j.microrel.2011.04.003.

[60] D. F. Lim, J. Wei, K. C. Leong, and C. S. Tan, “Surface Passivation of Cu for Low Temperature 3D Wafer Bonding,” *ECS Solid State Lett.*, vol. 1, no. 1, pp. P11–P14, 2012, doi: 10.1149/2.013201ssl.

[61] D. F. Lim, S. G. Singh, X. F. Ang, J. Wei, C. M. Ng, and C. S. Tan, “Application of Self Assembly Monolayer (SAM) in lowering the process temperature during Cu-Cu diffusion bonding of 3D IC,” *IMPACT Conf. 2009 Int. 3D IC Conf. - Proc.*, pp. 68–71, Oct. 2009, doi: 10.1109/IMPACT.2009.5382311.

[62] D. F. Lim, S. G. Singh, X. F. Ang, J. Wei, C. M. Ng, and C. S. Tan, “Achieving low temperature Cu to Cu diffusion bonding with self assembly monolayer (SAM) passivation,” in *2009 IEEE International Conference on 3D System Integration*, 2009, pp. 1–5, doi: 10.1109/3DIC.2009.5306545.

[63] A. Paul, E. Laibinis, and G. M. Whitesides, “Self-Assembled Monolayers of n-Alkanethiolates on Copper Are Barrier Films That Protect the Metal against Oxidation by,” *J. Am. Chem. Soc*, vol. 114, pp. 9022–9028, 1992.

[64] A. B. Horn, D. A. Russell, L. J. Shorthouse, and T. R. E. Simpson, “Ageing of alkanethiol self-assembled monolayers,” *J. Chem. Soc. Faraday Trans.*, vol. 92, no. 23, p. 4759, Jan. 1996, doi: 10.1039/ft9969204759.

[65] M. H. Schoenfisch and J. E. Pemberton, “Air stability of alkanethiol self-assembled monolayers on silver and gold surfaces,” *J. Am. Chem. Soc.*, vol. 120, no. 18, pp. 4502–5413, 1998, doi: 10.1021/ja974301t.

[66] T. M. Willey, A. L. Vance, T. van Buuren, C. Bostedt, L. J. Terminello, and C. S. Fadley, “Rapid degradation of alkanethiol-based self-assembled monolayers on gold in ambient laboratory conditions,” *Surf. Sci.*, vol. 576, no. 1–3, pp. 188–196, 2005, doi: http://doi.org/10.1016/j.susc.2004.12.022.

[67] T. Ghosh, A. Dutta, E. Lingareddy, C. Subrahmanyam, and S. G. Singh, “Room temperature desorption of Self Assembly Monolayer (SAM) passivated Cu for lowering the process temperature Cu-Cu bonding of 3-D ICs,” in *Emerging Electronics (ICEE), 2012 International Conference on*, 2012, pp. 1–4, doi: 10.1109/ICEmElec.2012.6636262.

[68] D. A. Hutt and C. Liu, “Oxidation protection of copper surfaces using self-assembled monolayers of octadecanethiol,” *Appl. Surf. Sci.*, vol. 252, no. 2, pp. 400–411, 2005, doi: http://dx.doi.org/10.1016/j.apsusc.2005.01.019.

[69] M. R. S. Shirazy, S. Blais, and L. G. Fréchette, "Mechanism of wettability transition in copper metal foams: From superhydrophilic to hydrophobic," *Appl. Surf. Sci.*, vol. 258, no. 17, pp. 6416–6424, 2012, doi: http://doi.org/10.1016/j.apsusc.2012.03.052.

[70] C. Liu and D. A. Hutt, "Fluxless Soldering of Copper Substrates Using Self-Assembled Monolayers for Preservation," *IEEE Trans. Components Packag. Technol.*, vol. 29, no. 3, pp. 512–521, Sep. 2006, doi: 10.1109/TCAPT.2005.853177.

[71] G. H. Yang, Y. Zhang, E. T. Kang, K. G. Neoh, A. C. H. Huan, and D. M. Y. Lai, "Plasma polymerization of allylpentafluorobenzene on copper surfaces," *J. Mater. Chem.*, vol. 12, no. 3, pp. 426–431, Feb. 2002, doi: 10.1039/b108895p.

[72] T. Ghosh, E. Krushnamurthy, C. Subrahmanyam, V. SivaRamaKrishna, A. Dutta, and S. G. Singh, "Room temperature desorption of Self Assembled Monolayer from Copper surface for low temperature amp; low pressure thermocompression bonding," in *Electronic Components and Technology Conference (ECTC) , 2015 IEEE 65th*, 2015, pp. 2200–2204, doi: 10.1109/ECTC.2015.7159908.

[73] S. Ebbens, D. Hutt, and C. Liu, "The Thermal Stability of Alkanethiol Self-Assembled Monolayers on Copper for Fluxless Soldering Applications," *IEEE Trans. Components Packag. Technol.*, vol. 33, no. 2, pp. 251–259, 2010, doi: 10.1109/TCAPT.2010.2041779.

[74] C. M. Whelan, M. Kinsella, H. M. Ho, and K. Maex, "In-situ cleaning and passivation of oxidized Cu surfaces by alkanethiols and its application to wire bonding," *J. Electron. Mater.*, vol. 33, no. 9, pp. 1005–1011, Sep. 2004, doi: 10.1007/s11664-004-0027-8.

[75] L. Carbonell, C. M. Whelan, M. Kinsella, and K. Maex, "A thermal stability study of alkane and aromatic thiolate self-assembled monolayers on copper surfaces," *Superlattices Microstruct.*, vol. 36, no. 1–3, pp. 149–160, Jul. 2004, doi: 10.1016/J.SPMI.2004.08.033.

[76] A. Ikeda, L. J. Qiu, K. Nakahara, and T. Asano, "Surface passivation of Cu cone bump by self-assembled-monolayer for room temperature Cu-Cu bonding," in *2013 IEEE International 3D Systems Integration Conference (3DIC)*, 2013, pp. 1–4, doi: 10.1109/3DIC.2013.6702317.

[77] H. M. Ho, W. Lam, S. Stoukatch, P. Ratchev, C. J. Vath III, and E. Beyne, "Direct gold and copper wires bonding on copper," *Microelectron. Reliab.*, vol. 43, no. 6, pp. 913–923, 2003, doi: http://dx.doi.org/10.1016/S0026-2714(03)00074-X.

[78] K. W. Lam *et al.*, "Fine pitch copper wire bonding on copper bond pad process optimization," in *Electronic Materials and Packaging, 2002. Proceedings of the 4th International Symposium on*, 2002, pp. 63–68, doi: 10.1109/EMAP.2002.1188814.

[79] C. Kodama, T. Hayashi, and H. Nozoye, "Decomposition of alkanethiols adsorbed on Au (1 1 1) at low temperature," *Appl. Surf. Sci.*, vol. 169–170, pp. 264–267, Jan. 2001, doi: 10.1016/S0169-4332(00)00664-4.

[80] J. B. Schlenoff, M. Li, and H. Ly, "Stability and Self-Exchange in Alkanethiol Monolayers," *J. Am. Chem. Soc.*, vol. 117, no. 50, pp. 12528–12536, Dec. 1995, doi: 10.1021/ja00155a016.

[81] "Aluminium - online catalogue source - supplier of research materials in small quantities - Goodfellow." [Online]. Available: http://www.goodfellow.com/E/Aluminium.html. [Accessed: 23-Sep-2020].

[82] "Gold - online catalog source - supplier of research materials in small quantities - Goodfellow." [Online]. Available: http://www.goodfellow.com/A/Gold.html. [Accessed: 23-Sep-2020].

[83] "Copper - online catalogue source - supplier of research materials in small quantities - Goodfellow." [Online]. Available: http://www.goodfellow.com/E/Copper.html. [Accessed: 23-Sep-2020].

[84] N. Kanani, *Kupferschichten: Abscheidung, Eigenschaften, Anwendungen*. Bad Saulgau: Eugen G. Leuze Verlag, 2000.

[85] M. Mueller, J. Kriz, D. Meinhold, and T. Zerna, "Influence of liner-system and Cu-layer thickness on the grain structure of electroplated Cu," in *2012 4th Electronic System-Integration Technology Conference, ESTC 2012*, 2012, doi: 10.1109/ESTC.2012.6542072.

[86] W. D. Callister, *Materials science and engineering : an introduction*. John Wiley & Sons, 2003.

[87] G.-T. Lui, D. Chen, and J.-C. Kuo, "EBSD characterization of twinned copper using pulsed electrodeposition," *J. Phys. D. Appl. Phys.*, vol. 42, no. 21, 2009.

[88] D. Xu, H.-P. Chen, K. N. Tu, E. Zschech, S. Ogawa, and P. S. Ho, "Improved Interconnect Properties For Nano-Twinned Copper: Microstructure And Stability," in *AIP Conference Proceedings 11th Int. Workshop on Stress-Induced Phenomena in Metallization*, 2010, vol. 1300, pp. 23–32, doi: 10.1063/1.3527132.

[89] G. Gottstein, *Materialwissenschaft und Werkstofftechnik*. Berlin, Heidelberg: Springer Berlin Heidelberg, 2014.

[90] J. F. Nye, *Physical Properties of Crystals*. Clarendon Press, 1985.

[91] R. P. Carreker and W. R. Hibbard, "Tensile deformation of high-purity copper as a function of temperature, strain rate, and grain size," *Acta Metall.*, vol. 1, no. 6, pp. 654–663, 1953, doi: https://doi.org/10.1016/0001-6160(53)90022-4.

[92] F. A. Holleman, E. Wiberg, and N. Wiberg, *Lehrbuch der Anorganischen Chemie (German Edition)*. Walter de Gruyter, 2007.

[93] Z.-J. Zuo, J. Li, P.-D. Han, and W. Huang, "XPS and DFT Studies on the Autoxidation Process of Cu Sheet at Room Temperature," *J. Phys. Chem. C*, vol. 118, no. 35, pp. 20332–20345, Sep. 2014, doi: 10.1021/jp504977p.

[94] A. W. Adamson and A. P. Gast, *Physical chemistry of surfaces*. Wiley, 1997.

[95] J. Rainer, "Funktionspolymere," 2017.

[96] "ACD/ChemSketch (Freeware)." Advanced Chemistry Development, Inc., Toronto, ON, Canada, 2019.

[97] J. C. Love *et al.*, "Formation and Structure of Self-Assembled Monolayers of Alkanethiolates on Palladium," 2003, doi: 10.1021/JA028692.

[98] A. Ulman, "Formation and Structure of Self-Assembled Monolayers Abraham," *Chem. Rev*, 1996.

[99] J. F. Kang, A. Ulman, R. Jordan, and D. G. Kurth, "Optically induced band shifts in infrared spectra of mixed self-assembled monolayers of biphenyl thiols," *Langmuir*, vol. 15, no. 17, pp. 5555–5559, Aug. 1999, doi: 10.1021/la9904051.

[100] J. García-Antón, J. Monzó, and J. L. Guiñón, "Effect of Elemental Sulfur and Mercaptans on Copper Strip Corrosion and Use of the ASTM D 130 Test Method," *CORROSION*, vol. 51, no. 7, pp. 558–566, 1995, doi: 10.5006/1.3294376.

[101] G. M. Whitesides, J. K. Kriebel, and J. C. Love, "Molecular engineering of surfaces using self-assembled monolayers.," *Science progress*, vol. 88, no. Pt 1. pp. 17–48, 2005, doi: 10.3184/003685005783238462.

[102] G. E. Poirier and M. J. Tarlov, "The c(4×2) Superlattice of n-Alkanethiol Monolayers Self-Assembled on Au(111)," *Langmuir*, vol. 10, no. 9. Academic Press, pp. 2853–2856, 01-Sep-1994, doi: 10.1021/la00021a001.

[103] Badin, "Self-Assembled Monolayers on Gold Substrates made from Functionalized Thiols and Dithiols," Ruhr-Univeristät Bochum, 2007.

[104] A. Ulman, *Self-assembled monolayers of thiols*. Academic Press, 1998.

[105] S. Xu *et al.*, "In situ studies of thiol self-assembly on gold from solution using atomic force microscopy," *J. Chem. Phys.*, vol. 108, no. 12, pp. 5002–5012, Mar. 1998, doi: 10.1063/1.475908.

[106] N. Nishida, M. Hara, H. Sasabe, and W. Knoll, "Thermal desorption spectroscopy of alkanethiol self-assembled monolayer on Au(111)," *Japanese J. Appl. Physics, Part 1 Regul. Pap. Short Notes Rev. Pap.*, vol. 35, no. 11, pp. 5866–5872, Nov. 1996, doi: 10.1143/jjap.35.5866.

[107] L. Kankate, A. Turchanin, and A. Gölzhäuser, "On the Release of Hydrogen from the S−H groups in the Formation of Self-Assembled Monolayers of Thiols," *Langmuir*, vol. 25, no. 18, pp. 10435–10438, Sep. 2009, doi: 10.1021/la902168u.

[108] J. Braeuer, "Erarbeitung eines Raumtemperatur-Waferbondverfahrens basierend auf integrierten und reaktiven nanoskaligen Multilagensystemen," Technischen Universitaet Chemnitz, 2014.

[109] K. Meißner, "Reduzierung der Belastung eines Chips beim Ultraschall-Flipchip-Bonden durch Einführung einer zweidimensionalen Ultraschallanregung," Universität Paderborn.

[110] Y. Arai, M. Nimura, and H. Tomokage, "Vibration for Flip-chip Interconnection," pp. 468–472, 2015.

[111] S. Gao and A. S. Holmes, "Thermosonic Flip Chip Interconnection Using Electroplated Copper Column Arrays," *IEEE Trans. Adv. Packag.*, vol. 29, no. 4, pp. 725–734, Nov. 2006, doi: 10.1109/TADVP.2006.884812.

[112] U. Geißler, "Verbindungsbildung und Gefügeentwicklung beim Ultraschall-Wedge-Wedge-Bonden von AlSi1-Draht," TU Berlin, 2008.

[113] F. Osterwald, "Verbindungsbildung beim Ultraschall-Drahtbonden : Einfluß der Schwingungsparameter und Modellvorstellungen," Technische Universität Berlin, Berlin, 1999.

[114] Y. Arai, M. Nimura, and H. Tomokage, "Evaluation of Ultrasonic Vibration Energy on Cu-Cu Direct Bonding for Flip-Chip Interconnection," *Trans. Japan Inst. Electron. Packag.*, vol. 7, no. 1, pp. 8–13, 2014, doi: 10.5104/jiepeng.7.8.

[115] Y. Arai, M. Nimura, and H. Tomokage, "Cu-Cu direct bonding technology using ultrasonic vibration for flip-chip interconnection," in *2015 International Conference on Electronic Packaging and iMAPS All Asia Conference (ICEP-IAAC)*, 2015, pp. 468–472, doi: 10.1109/ICEP-IAAC.2015.7111060.

[116] K. Tanida *et al.*, “Au bump interconnection with ultrasonic flip-chip bonding in 20 μm pitch,” *Japanese J. Appl. Physics, Part 1 Regul. Pap. Short Notes Rev. Pap.*, vol. 42, no. 4 B, pp. 2198–2203, 2003, doi: 10.1143/JJAP.42.2198.

[117] S. Yamatsu, K. Watanabe, N. Kanagawa, T. Ishikawa, and T. Kojio, “3D Stacking Process with Thermo-Sonic Bonding Using Non-conductive Film,” in *2018 IEEE 68th Electronic Components and Technology Conference (ECTC)*, 2018, pp. 2049–2054, doi: 10.1109/ECTC.2018.00307.

[118] C. . Luk, Y. . Chan, and K. . Hung, “Development of gold to gold interconnection flip chip bonding for chip on suspension assemblies,” *Microelectron. Reliab.*, vol. 42, no. 3, pp. 381–389, Mar. 2002, doi: 10.1016/S0026-2714(01)00256-6.

[119] K. Iwanabe, T. Shuto, K. Noda, S. Nakai, and T. Asano, “Room-temperature microjoining using ultrasonic bonding of compliant bump,” in *2012 3rd IEEE International Workshop on Low Temperature Bonding for 3D Integration*, 2012, pp. 167–170, doi: 10.1109/LTB-3D.2012.6238081.

[120] W. Yang, M. Akaike, M. Fujino, and T. Suga, “A Combined Process of Formic Acid Pretreatment for Low-Temperature Bonding of Copper Electrodes,” *ECS J. Solid State Sci. Technol.*, vol. 2, no. 6, pp. P271–P274, Apr. 2013, doi: 10.1149/2.010306jss.

[121] F. Iker, T. Funaya, R. C. Teixeira, and W. Ruythooren, “Diamond bit cutting as alternative to polymer patterning for 3D interconnections technologies,” in *2009 59th Electronic Components and Technology Conference*, 2009, pp. 1284–1288, doi: 10.1109/ECTC.2009.5074176.

[122] P. Limaye and W. Zhang, “Micro Bump Assembly,” in *Ultra-thin Chip Technology and Applications*, New York, NY: Springer New York, 2011, pp. 185–192.

[123] M. Godin *et al.*, “Surface stress, kinetics, and structure of alkanethiol self-assembled monolayers,” *Langmuir*, vol. 20, no. 17, pp. 7090–7096, 2004, doi: 10.1021/la030257l.

[124] J. F. Moulder, W. F. Stickle, P. E. ’ Sobol, K. D. Bomben, and J. Chastain, *Handbook of X-ray Photoelectron Spectroscopy*. Pekin-Elmer Corporation, 1993.

[125] T. Du, D. Tamboli, V. Desai, and S. Seal, “Mechanism of Copper Removal during CMP in Acidic H[sub 2]O[sub 2] Slurry,” *J. Electrochem. Soc.*, vol. 151, no. 4, p. G230, Apr. 2004, doi: 10.1149/1.1648029.

[126] G. Deroubaix and P. Marcus, “X-ray photoelectron spectroscopy analysis of copper and zinc oxides and sulphides,” *Surf. Interface Anal.*, vol. 18, no. 1, pp. 39–46, Jan. 1992, doi: 10.1002/sia.740180107.

[127] S. Tajima, S. Tsuchiya, M. Matsumori, S. Nakatsuka, and T. Ichiki, “Reduction of Copper Oxide Films by an Atmospheric-Pressure Inductively Coupled Plasma Microjet,” *Trans. Mater. Res. Soc. Japan*, vol. 35, no. 3, pp. 621–625, 2010, doi: 10.14723/tmrsj.35.621.

[128] W. Wurth, C. Schneider, R. Treichler, E. Umbach, and D. Menzel, “Evolution of adsorbate core-hole states after bound and continuum primary excitation: Relaxation versus decay,” *Phys. Rev. B*, vol. 35, no. 14, pp. 7741–7744, May 1987, doi: 10.1103/PhysRevB.35.7741.

[129] B. V. Crist, *Handbook of monochromatic XPS spectra*. Wiley, 2000.

[130] M. C. Biesinger, “Advanced analysis of copper X-ray photoelectron spectra,” *Surf. Interface Anal.*, vol. 49, no. 13, pp. 1325–1334, Dec. 2017, doi: 10.1002/sia.6239.

[131] H. Peisert, T. Chassé, P. Streubel, A. Meisel, and R. Szargan, "Relaxation energies in XPS and XAES of solid sulfur compounds," *J. Electron Spectros. Relat. Phenomena*, vol. 68, pp. 321–328, May 1994, doi: 10.1016/0368-2048(94)02129-5.

[132] A. M. de Jong *et al.*, "Sulfidation mechanism by molybdenum catalysts supported on silica/silicon(100) model support studied by surface spectroscopy," *J. Phys. Chem.*, vol. 97, no. 24, pp. 6477–6483, Jun. 1993, doi: 10.1021/j100126a024.

[133] T. P. Ang, T. S. A. Wee, and W. S. Chin, "Three-Dimensional Self-Assembled Monolayer (3D SAM) of n-Alkanethiols on Copper Nanoclusters," 2004, doi: 10.1021/JP049006R.

[134] M. El-Desawy, "Characterization and application of aromatic self-assembled monolayers," University of Bielefeld, 2007.

[135] X.-R. Yu, F. Liu, Z.-Y. Wang, and Y. Chen, "Auger parameters for sulfur-containing compounds using a mixed aluminum-silver excitation source," *J. Electron Spectros. Relat. Phenomena*, vol. 50, no. 2, pp. 159–166, Jan. 1990, doi: 10.1016/0368-2048(90)87059-W.

[136] "XPS Interpretation of Carbon." [Online]. Available: https://xpssimplified.com/elements/carbon.php. [Accessed: 26-Sep-2020].

[137] K. Hinrichs, M. Gensch, and N. Esser, "Analysis of organic films and interfacial layers by infrared spectroscopic ellipsometry," *Appl. Spectrosc.*, vol. 59, no. 11, pp. 272A-282A, Nov. 2005, doi: 10.1366/000370205774783106.

[138] K. Hinrichs and K.-J. Eichhorn, *Ellipsometry of Functional Organic Surfaces and Films*, vol. 52. Berlin, Heidelberg: Springer, 2014.

[139] M. A. Gosálvez, I. Zubel, and E. Viinikka, "Wet Etching of Silicon," in *Handbook of Silicon Based MEMS Materials and Technologies: Second Edition*, Elsevier Inc., 2015, pp. 470–502.

[140] M. Stangl, "Charakterisierung und Optimierung elektrochemisch abgeschiedener Kupferdünnschichtmetallisierungen für Leitbahnen höchstintegrierter Schaltkreise," Technische Universität Dresden, Dresden, 2008.

[141] I. Panchenko *et al.*, "Grain Structure Analysis of Cu/SiO2 Hybrid Bond Interconnects after Reliability Testing," in *Proceedings - 2020 IEEE 8th Electronics System-Integration Technology Conference, ESTC 2020*, 2020, doi: 10.1109/ESTC48849.2020.9229743.

[142] R. Ihnfeldt and J. B. Talbot, "Effect of CMP Slurry Chemistry on Copper Nanohardness," *J. Electrochem. Soc.*, vol. 155, no. 6, p. H412, Apr. 2008, doi: 10.1149/1.2903293.

[143] R. Arnold, A. Terfort, and C. Wöll, "Determination of molecular orientation in self-assembled monolayers using IR absorption intensities: The importance of grinding effects," *Langmuir*, vol. 17, no. 16, pp. 4980–4989, Aug. 2001, doi: 10.1021/la010202o.

[144] G. S. Hwang, Y. Nam, E. Fleming, P. Dussinger, Y. S. Ju, and M. Kaviany, "Multi-artery heat pipe spreader: Experiment," *Int. J. Heat Mass Transf.*, vol. 53, no. 13–14, pp. 2662–2669, Jun. 2010, doi: 10.1016/j.ijheatmasstransfer.2010.02.046.

[145] I. Panchenko, "Process-dependent microstructure changes in solid-liquid interdiffusion interconnects for 3D integration," TU Dresden, 2013.

[146] K. Tanaka *et al.*, "Investigation of Surface Pre-Treatment Methods for Wafer-Level Cu-Cu Thermo-Compression Bonding," *Micromachines*, vol. 7, no. 12, p. 234, Dec. 2016, doi: 10.3390/mi7120234.

[147] L. Peng, "Wafer-level fine pitch Cu-Cu bonding for 3-D stacking of integrated circuits.," Nanyang Technological University, 2012.

[148] T. Ghosh, V. S. R. Krishna, and S. G. Singh, "Low temperature Cu-Cu thermocompression bonding assisted by electrochemical desorption of a self-assembled monolayer," in *Emerging Electronics (ICEE), 2014 IEEE 2nd International Conference on*, 2014, pp. 1–4, doi: 10.1109/ICEmElec.2014.7151165.

[149] T. Ishikawa, M. Okazaki, and T. Sakai, "Mounting method of bump-equipped electronic component and mounting structure of the same," US 2005/0127141 A1, 2005.

[150] "E-mail communication with Mr. Reinhard Windemuth and Mr. Bernhard Oberhofer from Panassonic in Ottobrunn," 2018.

[151] T. Fushimi *et al.*, "Thermal Fatigue Properties of Ultrasonically Bonded Copper Joints," *Appl. Sci.*, vol. 9, no. 8, p. 1556, Apr. 2019, doi: 10.3390/app9081556.

[152] W. Lu, S. S. Chakravarthula, J. Chen, and Y. Qiao, "Propagation of a cleavage crack front across a field of persistent grain boundaries," *Int. J. Solids Struct.*, vol. 49, no. 3–4, pp. 584–589, Feb. 2012, doi: 10.1016/J.IJSOLSTR.2011.11.003.

[153] R. W. Hertzberg, R. P. Vinci, and J. L. Hertzberg, *Deformation and fracture mechanics of engineering materials*. John Wiley & Sons, Inc, 2012.

[154] H. Ye, M. Lin, and C. Basaran, "Failure modes and FEM analysis of power electronic packaging," *Finite Elem. Anal. Des.*, vol. 38, no. 7, pp. 601–612, May 2002, doi: 10.1016/S0168-874X(01)00094-4.

[155] S. L. Chua, G. Y. Chong, Y. H. Lee, and C. S. Tan, "Direct copper-copper wafer bonding with Ar/N2 plasma activation," in *Electron Devices and Solid-State Circuits (EDSSC), 2015 IEEE International Conference on*, 2015, pp. 134–137, doi: 10.1109/EDSSC.2015.7285068.

[156] B. Rebhan, T. Plach, S. Tollabimazraehno, V. Dragoi, and M. Kawano, "Cu-Cu wafer bonding: An enabling technology for three-dimensional integration," in *Electronics Packaging (ICEP), 2014 International Conference on*, 2014, pp. 475–479, doi: 10.1109/ICEP.2014.6826724.

[157] J.-Y. Juang, C.-L. Lu, Y.-J. Li, K. N. Tu, and C. Chen, "Correlation between the Microstructures of Bonding Interfaces and the Shear Strength of Cu-to-Cu Joints Using (111)-Oriented and Nanotwinned Cu," *Materials (Basel).*, vol. 11, no. 12, p. 2368, Nov. 2018, doi: 10.3390/ma11122368.

[158] "Overview of materials for Gold Alloy." [Online]. Available: http://www.matweb.com/search/DataSheet.aspx?MatGUID=b9639c2f4ed84006923b2956f90cc13c&ckck=1. [Accessed: 18-Feb-2020].

[159] "Properties: Aluminum - Advantages and Properties of Aluminum." [Online]. Available: https://www.azom.com/properties.aspx?ArticleID=1446. [Accessed: 18-Feb-2020].

[160] "Properties: An Introduction to Copper." [Online]. Available: https://www.azom.com/properties.aspx?ArticleID=597. [Accessed: 18-Feb-2020].

[161] "ASM Material Data Sheet." [Online]. Available: http://asm.matweb.com/search/SpecificMaterial.asp?bassnum=MA6061T6. [Accessed: 18-Feb-2020].

[162] "OFHC Copper - online catalog source - supplier of research materials in small quantities - Goodfellow." [Online]. Available: http://www.goodfellow.com/A/OFHC-Copper.html. [Accessed: 18-Feb-2020].

[163] "Gold - online catalog source - supplier of research materials in small quantities - Goodfellow." [Online]. Available: http://www.goodfellow.com/A/Gold.html. [Accessed: 18-Feb-2020].

[164] "Aluminium alloy 7075 - online catalogue source - supplier of research materials in small quantities - Goodfellow." [Online]. Available: http://www.goodfellow.com/E/Aluminium-alloy-7075.html. [Accessed: 18-Feb-2020].

[165] P.-H. Chiang, S.-Y. Liang, J.-M. Song, S.-K. Huang, Y.-T. Chiu, and C.-P. Hung, "Enhanced Cu-to-Cu direct bonding by controlling surface physical properties," *Jpn. J. Appl. Phys.*, vol. 56, no. 3, p. 35503, 2017.

List of figures

Fig. 1-1 Schematic cross-section view of a 2.5D integrated logic die and a 3D stack of memory dies, connected by TSVs and microcontacts (adapted from [5]) 1

Fig. 1-2 Schematic presentation of one SAM chain of 1-hexanethiol (C6) with tilt angle α and twist angle β (a); schematic view of the ordered SAM chains on Cu surface and their structure (b) 2

Fig. 1-3 Schematic overview of the influencing factors on the Cu-Cu bonding technology with SAM passivation 4

Fig. 2-1 Proposed classification of common bonding technologies, interconnect forms and Cu pre-treatment methods for diffusion bonding using Cu as interconnect material 5

Fig. 2-2 Types of die topologies for Cu-Cu bonding: with microbumps (a), with bumpless interconnects (b) and concave-pillar interconnects (c) 6

Fig. 2-3 Schematic view of Cu-Cu TC bonding with thermal SAM desorption...................... 12

Fig. 2-4 Schematic representation of US bonding using SAM passivation of planar (on the bottom die) and cone-shaped (on the top die) bumps 13

Fig. 3-1 Ordering of atoms in a face-centered cubic (fcc) elemental cell of Cu (a), Miller indices and (1 1 1) close-packed plane with [1 1 1] vector (b) (adapted from [83]).......................... 14

Fig. 3-2 Schematic view of IPF plot with the distribution of Young's modulus for cubic crystal system of Cu depending on crystal orientation 16

Fig. 3-3 Mechanism of Cu oxides growth according to [92] 17

Fig. 3-4 3D Model of a 1-hexanethiol molecule with distances and angles between the atoms made in ACD/Labs software [95] (a) and schematic symbol of 1-hexanethiol (b) 19

Fig. 3-5 Classification of SAM by head groups, terminal groups and by the molecular backbone structure (according to [94]).. 21

Fig. 3-6 Possible types of defects in SAM caused by (a) gauche conformations, (b) Au grain boundaries, (c) SAM crystal edges, (d) Au vacancy islands, (e) surface contaminations and (f) Au monoatomic step-edges (adapted from [10], [100]) 22

Fig. 3-7 Schematic illustration of intermolecular and intramolecular energies of the adsorbed SAM where ΔE_{corr} is corrugation substrate potential, ΔE_g is gauche defect energy or variation from the energy of a stretched chain, ΔE_{hyd} is the energy between the organic backbones, ΔE_{ads} is adsorption energy (according to [102]) 23

Fig. 3-8 Phases of C6 SAM formation on Cu surface: mobile phase (a), immobile lying-down or striped phase (b), the coexistence of stand-up and lying-down phases (c) and completed monolayer (d). Adapted from [103], [104]... 24

Fig. 3-9 Schematic representation of chemical compounds taking part in adsorption and desorption processes 24

Fig. 3-10 The adsorption and desorption mechanisms of the alkanethiols on Au (according to [105], [106]) showing the immersion of samples and the SAM adsorption from the solution (a), the rinsing of the samples with a solvent (b), the heating of the samples and the desorption of the weakly adsorbed species (c), the increasing temperature, the formation of disulfides and their desorption from the metal surface (d) 25

Fig. 4-1 Schematic top view of the bottom (a) and top (b) dies, cross-sectional view of the bottom (c) and top (d) dies 29

Fig. 4-2 Arrangements of bumps on the top dies A (a) and B (b) 29

Fig. 4-3 Zig-zag measurement profiles of microbumps roughness of the microbump A (a) and microbump B (b) according to DIN EN ISO 4288 and ASME B46.1 31

Fig. 4-4 Layer thicknesses of the top dies with Cu microbumps and bottom dies fully covered with Cu with standard deviations 32

Fig. 4-5 SEM images of Cu microbumps from the top view (a, b, d, e) and of Cu microbumps from the cross-sectional view (c, f) 33

Fig. 4-6 Stages of through-mask plating to fabricate Cu microbumps (according to [121]) with a following fly cutting procedure 34

Fig. 4-7 Distribution of bump heights (in µm) on the wafer with samples A (a) and one chip (b) from the wafer middle 35

Fig. 4-8 Distribution of bump heights (in µm) on the wafer with samples B (a) and one chip (b) from the wafer middle 35

Fig. 4-9 A drop of liquid on the highly hydrophobic Cu surface with SAM (left) and the hydrophilic surface of freshly sputtered Cu surface (right) 37

Fig. 4-10 Wide XPS spectrum of an exemplary Cu surface (*y*-axis represents intensity in counts/second) 38

Fig. 4-11 Narrow XPS spectrum of O1s for an exemplary Cu surface 38

Fig. 4-12 Characteristic parameters of the ellipsometric measurements: orthogonal field components of the incident electromagnetic wave (E_{pi}, E_{si}), reflected electromagnetic wave (E_{pr}, E_{sr}), angle Ψ and phase shift Δ of the elliptically polarized wave (adapted from [136]) 41

Fig. 4-13 Alpha Design TC bonder with Ar-gas atmosphere in the bonding chamber 43

Fig. 4-14 FCB 3 bonder (Panasonic) 44

Fig. 4-15 Cross-sectional view of sample fixation in the polymer form (Ø25 mm) before filling it with epoxy resin mixture (a); epoxy resin sample with graphite powder after curing, grinding, polishing and painting it with Ag conductive varnish for SEM inspections (b) 45

Fig. 4-16 Cross-section view of the top and bottom dies with a grinding direction after underfilling (a), top view of the top and bottom dies after grinding (b), magnified top view of one of the bumps with unbonded and well-bonded regions (c) and magnified view of the TEM lamella (d) 48

Fig. 5-1 Sample arrangement for EBSD measurements: (a) schematic representation of the EBSD measurement setup with inserted sample coordinate system defined by normal (ND), rolling (RD) and transverse (TD) direction, (b) sample orientation for the cross-sectional view of a microbump, (c) sample orientation for the top view of the bottom die (fully covered with Cu) 51

Fig. 5-2 Processing of an EBSD measurement for analysis (IPF map with accumulated filter progress in the left column; IQ map with red highlighting of excluded data points from the raw dataset in the right column): IPF map of the raw dataset (a); image quality filter (IQ > 500) (b); EDX filter for Si (EDX_{Si} < 20 counts) (c); grain size filter, which excludes grains with a size of 1 point and more than 5 ° deviation from adjacent points (d); cleanup grain dilation whereby single points with more than 5 ° deviation are included into the neighboring grain (e) 52

Fig. 5-3 Deviation from the ideal cross-section plane during EBSD measurements: manual sample preparation may introduce a rotation around RD (a); manual sample alignment on tilted sample holder introduces a rotation around ND (b) 53

Fig. 5-4 Correction of the sample misalignment of an EBSD measurement by rotating a Si single crystal into its ideal position given by (001) wafer orientation: initial misalignment (a), correction by rotation around ND (b), correction by rotation around TD (c) 54

Fig. 5-5 Correction of the image alignment by rotation around ND, calculated rotation is not perfect and approx. 0.5 ° larger compared to manual image correction 55

Fig. 5-6 Drift during EBSD measurements: SEM image of a cross-sectioned Cu microbump (a), IQ image of the respective EBSD measurement showing drift in x and y direction (b), Drift during a top view measurement obtained from a tilt corrected SEM image (c) 56

Fig. 5-7 Influence of the surface pre-treatment on the image quality (IQ) 58

Fig. 5-8 Grain size distribution and unique grain maps for of the top die A for TC bonding and top die B for US bonding 60

Fig. 5-9 Grain size distribution and unique grain maps for 50 × 50 μm^2 measurement areas of bottom die A (ECD Cu after CMP) for TC bonding and bottom die B (ECD Cu) for US bonding 61

Fig. 5-10 Grain size distribution and unique grain maps for 250 × 250 μm^2 measurement areas of the bottom die A (ECD Cu after CMP) for TC bonding and bottom die B (ECD Cu) for US bonding 62

Fig. 5-11 Positions of twins of the 1st – 3rd orders (4th order is not shown) in the IPF plots and schematic representation of twin formation till the 4th order from the original {0 0 1} and {1 1 1} orientations 63

Fig. 5-12 Characteristic texture plots showing the qualitative distribution of grain orientations for top die A (a, b), top die B (d, e), bottom die A (c) and bottom die B (f)............................ 64

Fig. 5-13 Characterization of grain boundaries for top die A and top die B, bottom die A and bottom die B before bonding... 65

Fig. 5-14 Typical textures for the top die A (a, b) and top die B (d, e), bottom die A (c) and bottom die B (f) with the corresponding Young's modulus overlay....................................... 66

Fig. 6-1 Experimental setup for characterization of SAM protective effect depending on its chain length, storage temperature and time... 69

Fig. 6-2 Atomic concentrations of C1s (a), O1s (b) and $Cu2p_{3/2}$ (c) on Cu surface without (-) and with H_2SO_4 10 % etching (Etching) in the initial state (initial state), after Ar^+ ion bombardment for 2 min at 600 eV (cleaning step), after 20 s at 2 keV (20s 2keV), after 60 s at 2 keV (60s 2keV) and after 140 s at 2keV (140s 2keV) 71

Fig. 6-3 IRSE spectra of Cu with C6-SAM (C6), C16-SAM (C16), without SAM (no SAM) and without SAM after storage for two weeks at room temperature in air (no SAM, 2 weeks) 73

Fig. 6-4 Referenced IRSE spectra of Cu with C6-SAM (C6), C16-SAM (C16), after storage for 43 - 236 h at room temperature in air divided by IRSE spectra of Cu with C6 or C16, respectively, stored for 17 h in same conditions 73

Fig. 6-5 Schematic view of the orientation of C6 SAM (left) and the transition dipole moments of some of the CH_2 and CH_3 vibrations (right). Θ, Φ and Ψ angles define the orientation of the C6 chain as follows: initially, a CCC backbone is normal to the surface and parallel to the z-x plane; then the chain is tilted by the angle Θ relative to the z-axis, then the chain is twisted by the angle Ψ and rotated around the z-axis by the angle Φ (adapted from [142])................... 74

Fig. 6-6 Influence of storage at room temperature (a) and -40 °C (b) in air on the wettability (contact angle) of the samples with SAM (SAM) and without SAM (no SAM) passivation.. 76

Fig. 6-7 XPS spectra of C1s for the samples with (SAM) and without SAM (no SAM) passivation after 12 hours at room temperature in air in the initial state (a, c) and after the cleaning step (b, d) 77

Fig. 6-8 XPS spectra of O1s for the samples with (SAM) and without SAM (no SAM) passivation after 12 hours at room temperature in air in the initial state (a, c) and after the cleaning step (b, d) 78

Fig. 6-9 XPS spectra of S2p for the samples with (SAM) passivation after 12 hours at room temperature in air in the initial state (a) and after the cleaning step (b).................................. 79

Fig. 6-10 Atomic concentrations of O1s (a), Cu2p (b), S2p (c) and C1s (d) for the samples with (SAM) and without SAM (no SAM) before and after storage for 7 days at -40 °C (7 days, -40 °C) before and after the cleaning step (Ar^+ ion bombardment) 80

Fig. 7-1 Experimental setup for the investigation of the influence of desorption and storage conditions on the quality of Cu-Cu interconnects 83

Fig. 7-2 Set bonding profile for TC bonding in Ar in Alpha Design bonder 84

Fig. 7-3 Schematic layer stack of the bonded interconnect 85

Fig. 7-4 Types of fracture surfaces in schematically presented cross-sections 85

Fig. 7-5 Types of fracture surfaces after shear strength tests on the bottom dies A: Si and Ti fracture surfaces (a); Si, Ti, Cu fracture surfaces and no contact (b) 85

Fig. 7-6 Schematic top view of a bonded sample pair with orientation mark (left image) and a confocal microscope image of a bottom die after the shear strength test (right image)........... 86

Fig. 7-7 XPS spectra of C1s before and after SAM desorption procedure at 200 °C and 250 °C for 30 min 88

Fig. 7-8 XPS spectra of S2p3/2 before and after SAM desorption procedure at 200 °C and 250 °C for 30 min 89

Fig. 7-9 XPS spectra of O1s before and after SAM desorption procedure at 200 °C and 250 °C for 30 min 90

Fig. 7-10 XPS spectra of Cu LMM before and after SAM desorption procedure at 200 °C and 250 °C for 30 min 91

Fig. 7-11 Atomic concentrations of C1s (a), S2p (b), O1s (c) and Cu2p (d) of the samples with SAM before and after desorption at 200 °C and 250 °C 92

Fig. 7-12 Influence of desorption temperature on the shear strength (a) and fracture surface (b) of the bonded samples 94

Fig. 7-13 Proposed schematic model of SAM desorption at 200 °C for 30 minutes with such stages: initial state (a), desorption of physisorbed SAMs and oxidation of free surface (b), formation and desorption of disulfides (c), the state of the Cu surface with partial SAM desorption after 30 minutes (d) 96

Fig. 7-14 XPS spectra of C1s for the samples with and without SAM passivation after 3 weeks of storage at -18 °C in air 97

Fig. 7-15 XPS spectra of O1s for the samples with and without SAM passivation after 3 weeks of storage at -18 °C in air 98

Fig. 7-16 XPS spectra of Cu LMM for the samples with and without SAM passivation after 3 weeks of storage at -18 °C in air 99

Fig. 7-17 Atomic concentrations of C1s (a), Cu2p (b) and O1s (c) of Cu surface with SAM (SAM) and without SAM (no SAM) passivation after 3 weeks storage at -18 °C in air 100

Fig. 7-18 Bonding interface types on SEM images of cross-sections of Cu-Cu interconnects after TC bonding in Ar inert gas atmosphere: seamless bonding interface (a), bonding interface with nanovoids (b), bonding interface with thin delamination (c), no bonding (d) 101

Fig. 7-19 Shear strength (a) and fracture surfaces (b) after TC bonding of samples with SAM in Ar after different storage times at -18 °C: 0, 1 and 10 days... 102

Fig. 7-20 Shear strength (a) and fracture surfaces (b) after TC bonding of samples without SAM in Ar after different storage times at -18 °C: 0, 1 and 10 days 103

Fig. 8-1 Schematic overview of experiments for Cu-Cu US bonding with SAM passivation 106

Fig. 8-2 Measured bonding profiles attained by sensors of FCB3 bonder for the averaged measured force values of 26.5 N (a), 30.6 N (b) and 35.2 N (c) 107

Fig. 8-3 Top view of bonded top and bottom dies with dotted lines showing the cross-section planes (a); exemplary cross-section A-A showing the differences of SOH between the corners *c* and *b* (b) 108

Fig. 8-4 Standoff height in the corner *c* (a) and corner *b* (b) 108

Fig. 8-5 Plane view of heights distribution on Si backside of the top dies after US bonding at (a) 135 MPa, (b) 156 MPa and (c) 180 MPa at 90 °C (fine scaling) 109

Fig. 8-6 3D view of heights distribution on bottom dies after shear strength tests on the example of samples bonded at 135 MPa (a), 156 MPa (b), 180 MPa (c) at 90 °C (coarse scaling) ... 109

Fig. 8-7 Schematic representation of the effects of bonding tool planarity on bonding yield (a) and microbump deformation (b) 110

Fig. 8-8 Thin delamination lines at bump edges (a, b) and a seamless bonding interface in the middle (c) on the example of a sample with SAM passivation bonded at 30 °C at 180 MPa 112

Fig. 8-9 SEM images of the interconnects cross-sections of the samples bonded at 30 °C, at 135 MPa (a, d), 156 MPa (b, e), 180 MPa (c, f) 112

Fig. 8-10 SEM images of the interconnects cross-sections of the samples bonded at 90 °C, at 135 MPa (a, d), 156 MPa (b, e), 180 MPa (c, f) 113

Fig. 8-11 SEM images of the interconnects cross-sections of the samples bonded at 150 °C, at 135 MPa (a, d), 156 MPa (b, e), 180 MPa (c, f) 114

Fig. 8-12 Classification of bonding quality types based on evaluation of the bonding quality 114

Fig. 8-13 Influence of bonding pressure on the bonding quality of the interconnects with SAM (SAM) passivation bonded at 30 °C 115

Fig. 8-14 Influence of bonding pressure on the bonding quality of the interconnects without SAM (no SAM) passivation bonded at 30 °C 115

Fig. 8-15 Influence of bonding pressure on the bonding quality of the interconnects with SAM (SAM) passivation bonded at 90 °C 115

Fig. 8-16 Influence of bonding pressure on the bonding quality of the interconnects without SAM (no SAM) passivation bonded at 90 °C 115

Fig. 8-17 Influence of bonding pressure on the bonding quality of the interconnects with SAM (SAM) passivation bonded at 150 °C 116

Fig. 8-18 Influence of bonding pressure on the bonding quality of the interconnects without SAM (no SAM) passivation bonded at 150 °C 116

Fig. 8-19 SEM images of the cross-sections with exemplary types of bonding region defects: thin delamination (a), no bonding (b), non-interfacial crack (c) and interfacial crack (d)..... 116

Fig. 8-20 Quantity of the interconnects with and without SAM, which maintains such types of bonding regions: thin unbonded region, thick unbonded region, non-interfacial crack, interfacial crack and seamless bonding interface 118

Fig. 8-21 SEM images of edge (a) and center (b) regions of Cu-Cu interconnects wherefrom thin TEM lamellae were cut out using FIB technique; TEM images of the edge (c) and central (d) cross-sectional regions with red and blue marks for the magnified view below; dark-field STEM images of the edge (e) and central (f) cross-section regions at higher magnification with white marked regions for EDX measurements 121

Fig. 8-22 EDX spectra of the Cu-Cu interface and pure Cu surface in the edge and central regions of the interconnects in the energy range between 2 keV and 2.5 keV for S spectrum detection (a, b) and the range between 0.2 keV and 0.7 keV (c, d) for the detection of O and C spectra (if present).. 122

Fig. 8-23 Fracture surface types after shear strength tests by SEM and EDX: Si fracture (a), Ti fracture (b) and Cu fracture (c) 124

Fig. 8-24 Exemplary evaluation of fracture surfaces on a bottom die after shear strength test through height profiling: topographic data as a colored graphic in 2D-view with a red line (a), which marks a detailed height profile measurement (b) 124

Fig. 8-25 Influence of bonding force/pressure on shear strength and percentage of fracture surface types for the samples with SAM (SAM) passivation bonded at 30 °C 125

Fig. 8-26 Influence of bonding force/pressure on shear strength and percentage of fracture surface types for the samples without SAM (no SAM) passivation bonded at 30 °C 125

Fig. 8-27 Influence of bonding pressure on shear strength and percentage of fracture surface types for the samples with SAM (SAM) passivation bonded at 90 °C 126

Fig. 8-28 Influence of bonding pressure on shear strength and percentage of fracture surface types for the samples without SAM (no SAM) passivation bonded at 90 °C 126

Fig. 8-29 Influence of bonding pressure on shear strength and percentage of fracture surface types for the samples with SAM (SAM) passivation bonded at 150 °C 127

Fig. 8-30 Influence of bonding pressure on shear strength and percentage of fracture surface types for the samples without SAM (no SAM) passivation bonded at 150 °C 127

Fig. 8-31 Schematic view of the structure of bonded dies (a), etching away of Ti layer and removal of Si top die (b) and shearing of each bump separately (c)..................................... 128

Fig. 8-32 Distribution of shear strength across a bonded die with a matrix of 10 × 10 microbumps for samples with SAM bonded at 30 °C at 135 MPa (a), 156 MPa (b), 180 MPa (c) and for samples without SAM bonded at 135 MPa (d), 156 MPa (e), 180 MPa (f)......... 129

Fig. 8-33 Influence of the bonding pressure on the average shear strength and corresponding standard deviation values of the Cu-Cu interconnects (with and without SAM passivation) bonded at 30 °C after microbump shear tests 130

List of tables

Tab. 2-1 Common chemical formulas and terminology of used alkanethiols and their derivatives in this study (R = C_nH_{2n+1}) [10] 9

Tab. 2-2 Indication of chemical composition changes of the Cu surface depending on Cu type and storage conditions 9

Tab. 2-3 Wire, thermocompression and ultrasonic Cu-Cu bonding with SAM 11

Tab. 3-1 Comparison of the main properties of the commonly used metals in diffusion bonding 14

Tab. 4-1 Characteristic parameters of the designs and measured microbump properties for the top die A and top die B 30

Tab. 4-2 Characteristic parameters of the bottom die A and bottom die B 30

Tab. 4-3 Main measurement parameters of the used XPS systems 37

Tab. 4-4 Binding energies of Cu LMM and corresponding to it O1s and S2p bindings with references 39

Tab. 4-5 Peak positions assigned to molecules in the XPS spectra of C 1s 40

Tab. 4-6 Binding energies of S bindings with references 40

Tab. 4-7 Peak positions of C-H stretching modes for thiols and thiolates adsorbed on the metal, where $\nu_s(CH_2)$ is CH_2 symmetrical and $\nu_a(CH_2)$ is CH_2 asymmetrical vibration modes, $\nu_{a,ip}(CH_3)$ is CH_3 asymmetrical in-plane vibration mode, $\nu_{s,FR}(CH_3)$ are CH_3 asymmetrical vibration modes connected to Fermi resonance interactions 42

Tab. 4-8 List of the main parameters for bonders used in this thesis 42

Tab. 4-9 Characteristic parameters of the lenses for the analysis of the surface roughness and topology 45

Tab. 4-10 Main parameters for the grinding and polishing 47

Tab. 4-11 Parameters for SEM imaging of the cross-sections of the Cu-Cu interconnects 48

Tab. 5-1 Overview of the EBSD measurements in the initial state for all investigated sample types 50

Tab. 7-1 Parameters for TC bonding used in this chapter 83

Tab. 8-1 Set and measured bonding parameters 107

Tab. 8-2 Comparison of the shear strength values for Cu-Cu bonding from this work with the literature results 132

Appendix

A.1 Additional information for EBSD measurements

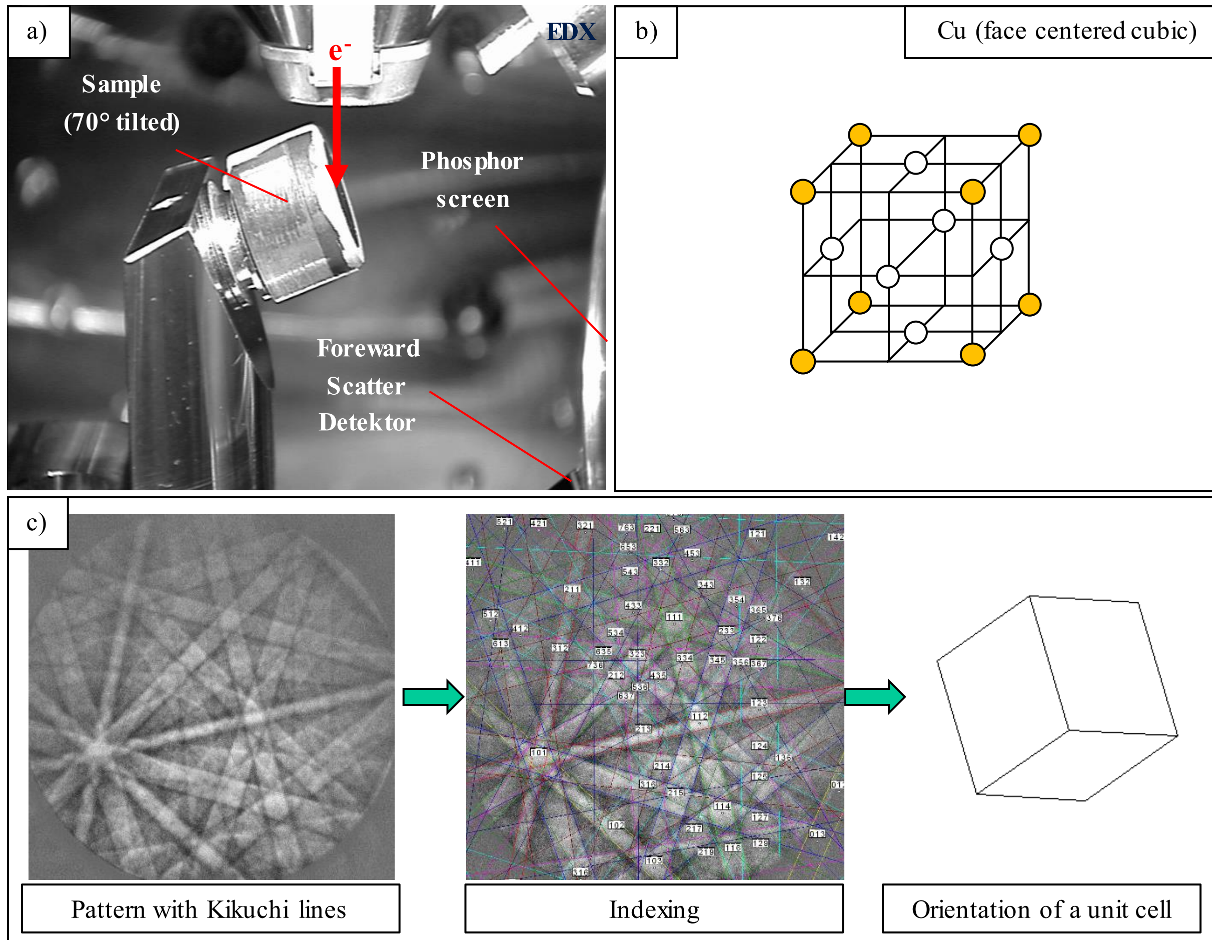

Fig. A. 1 Experimental setup for EBSD measurements (a), representation of cubic face centered Cu unit cell (b), a Cu unit cell orientation determination using indexing of patterns with Kikuchi lines (c)

Tab. A. 1 Parameters for EBSD data acquisition and pattern indexing (via Hough transformation)

SEM/Detector Parameters	Values	Hough parameters	Values
Micrsocope:	Supra 40 VP (Zeiss)	Indexed lattice cell:	Face-centered cubic
Aperture:	60 µm	Active reflectors:	(1 -1 -1); (0 -2 0); (0 -2 2); (1 -3 1); (1 -3 -3); (0 -4 2)
Excitation Voltage:	20 kV		
Working Distance	16 mm	Binned pattern size:	96
High Vacuum/High Current	On/On	θ step size:	1 °
EBSD Camera:	DigiView IV (EDAX.)	Rho fraction:	90 %
Binning/Resolution:	4x4 / 348x260 pixel	Peak count (min./max.):	3 / 7
Acquisition speed (Pattern):	30-60 fps	Hough Type / Resolution:	Classic / Low
Image processing (Pattern):	Background Substraction / Normalize Histogramm	Convolution mask:	Medium (9x9)
EDX-Detector:	Octane Elect Plus (EDAX)	Min. peak magnitude:	5
Mapped Elements:	C, O, N, Al, Si, Ti, Cu, Ag	Min. peak distance:	20
		Peak symmetrie:	0.5

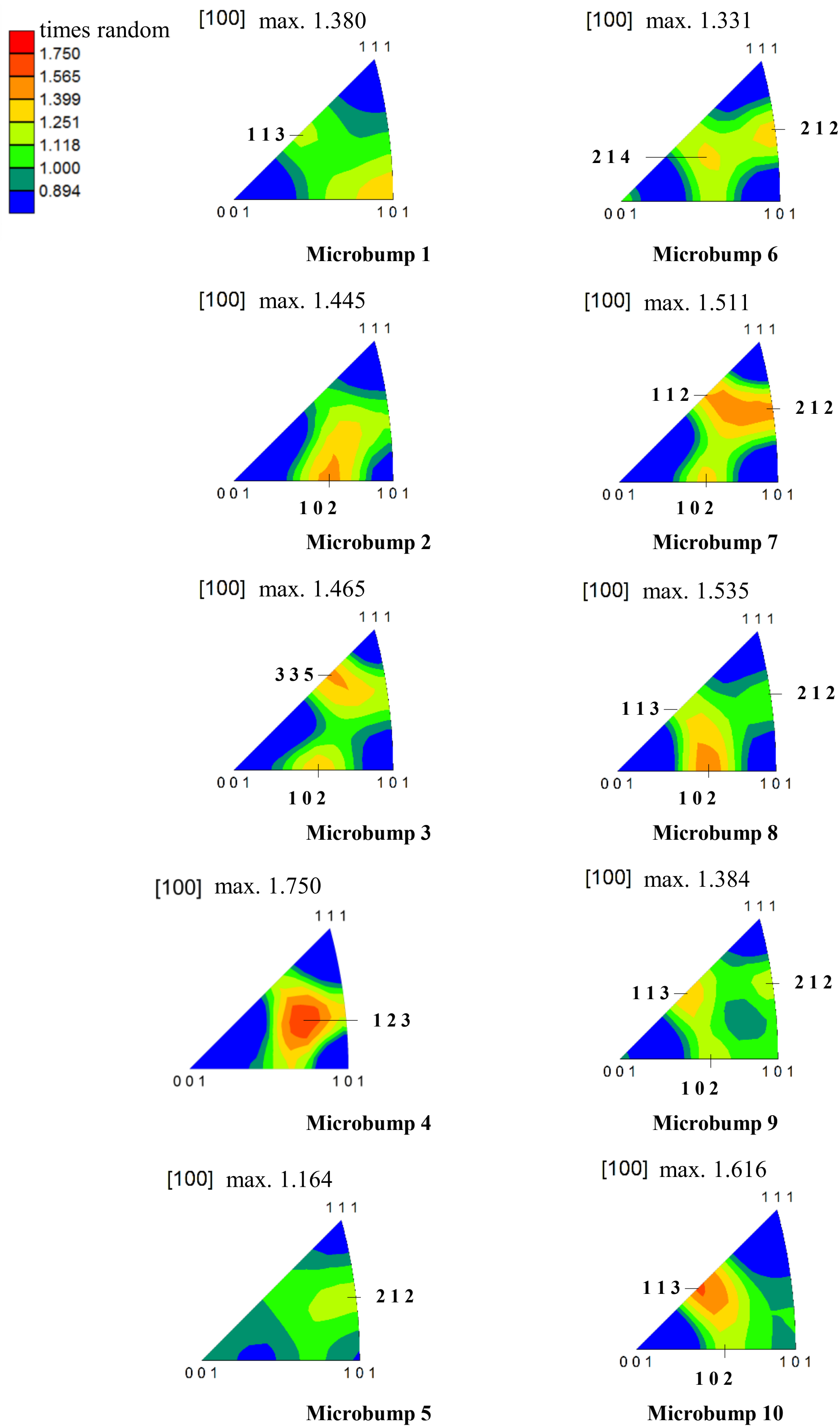

Fig. A. 2 Texture plots of 10 bumps in a cross-section raw for the top die A

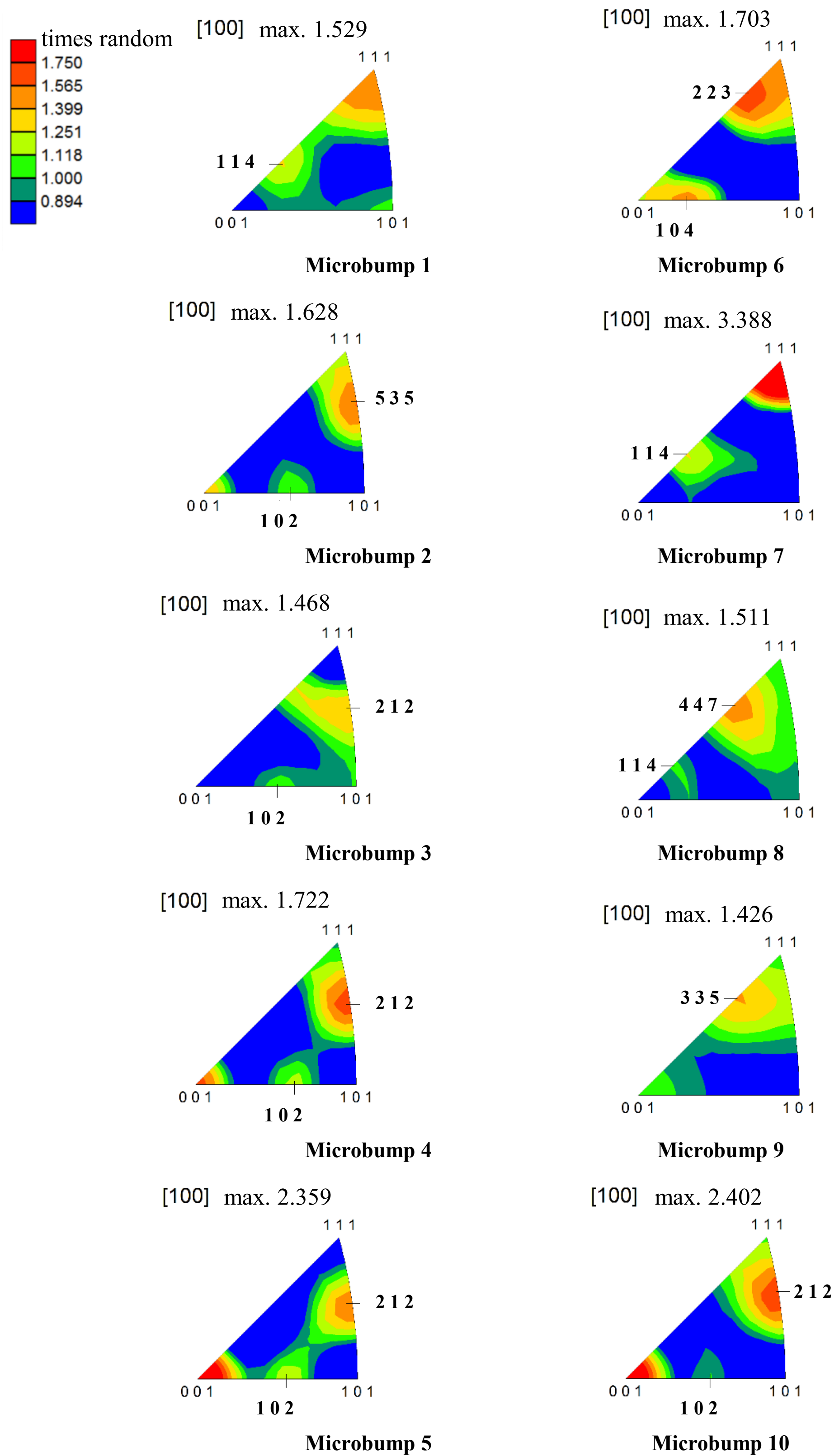

Fig. A. 3 IPF plots representing Cu textures of 10 bumps in a cross-section raw for the top die B

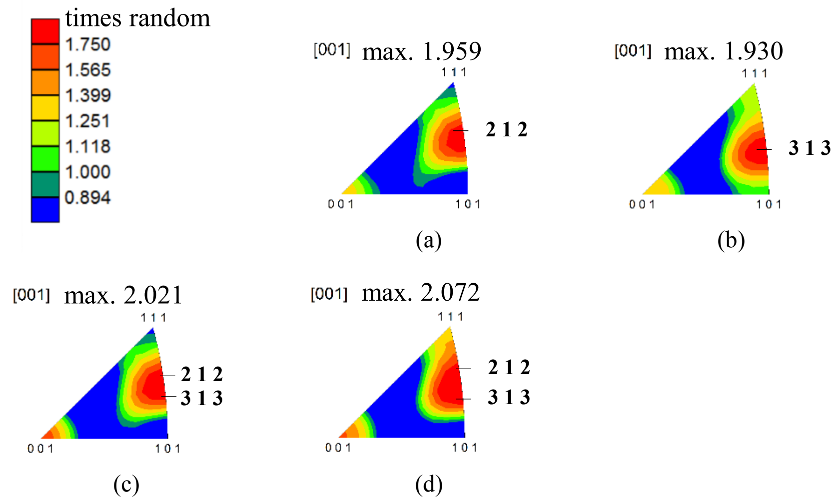

Fig. A. 4 IPF plots representing typical Cu textures for the measured area (50×50) μm^2 of the bottom die A (a) and the bottom die B (b), for the measured area (250×250) μm^2 of the bottom die A (c) and the bottom die B (d)